Numerical Modeling of Crustal Deformation and Pore-Pressure Changes Associated with the 1999 Chi-Chi Earthquake, Taiwan

by

Gregory Bryce Dyer

A thesis submitted to the Graduate Faculty of
Auburn University
in partial fulfillment of the
requirements for the Degree of
Master of Science

Auburn, Alabama
December 13, 2010

Approved by

Ming-Kuo Lee, Co-chair, Professor of Geology
Lorraine Wolf, Co-chair, Professor of Geology
James Saunders, Professor of Geology

Abstract

A new 3D time-dependent pore-pressure diffusion model PFLOW is used to investigate the response of pore fluids to the crustal deformation generated by strong earthquakes in heterogeneous geologic media. Using a carefully calibrated finite fault-rupture model (Ma et al., 2005), the coseismic pore pressure changes and diffusion induced by volumetric strain were calculated for the 1999 Chi-Chi earthquake (M_w = 7.6) in Taiwan. The Chi-Chi earthquake provides a unique opportunity to investigate the spatial and time dependent poroelastic response of near-field rocks and sediments because extensive field data of water level changes and crustal deformation are well documented and readily available. The integrated model provides a means to explore the various mechanisms responsible for hydrologic anomalies observed in Taiwan's western foothills and the Choshui River alluvial plain.

Of special interest is identifying which of the observed hydrologic changes can be explained by a coseismic strain hypothesis and whether the pore-pressure diffusion model can account for observed recovery (dissipation) rates of seismically induced water-level changes in the alluvial fan. Coupled strain-pore pressure modeling results show a strong correlation between areas of coseismic dilatational strain and water-level decline in regions where consolidated rocks are present in the foothills. However, in the Choshui River alluvial fan, water-level rises are observed in regions of dilatational strain, suggesting that other mechanisms, such as seismic shaking, compaction, or faulting-

enhanced gravity flow may be responsible for hydrologic changes. Assuming pre-seismic hydraulic conductivity values, our modeling results also show that water-level recovery rates cannot be explained by simple diffusion processes, suggesting that seismic loading may have caused significant re-arrangement and compaction of sediments in the alluvial plain.

Acknowledgements

The author would like to thank Dr. Ming-Kuo Lee for his support and guidance in the field of hydrogeology and geologic modeling. I would also like to thank Dr. Lorraine Wolf for guidance in the field of geophysics, seismology, and manuscript writing. This thesis would not be nearly as well written without her careful critiquing. Special thanks go out to Dr. Amnon Meir for his PFLOW codes and guidance in the field of numerical modeling and taking the time to sit down with me whenever I had a question. I would like to thank Dr. James Saunders for his role as committee member. Many thanks go out to the staff and rest of the faculty in the geology department for their guidance and support. Specifically, I would like to thank Sheila Arrington, John Simms, and Dr. Uddin. A very special thanks go out to my parents, Edward and Diane Dyer, for their love and encouragement through these last two years. I would not have made it this far without them and I owe much of my success to them. Also, I would like to thank my lovely fiancée, Ann Robbins, for all her love, support, and encouragement, and furthermore for providing me with the all the motivation in the world to achieve the most I can. Finally, I would like to thank the USGS, GSA, and APPG for their support and funding of this project.

Table of Contents

List of Tables

List of Figures

Introduction

The damages from earthquakes can be extensive in terms of money required to repair structures and more importantly the lives lost to these catastrophic events. For these reasons, geoscientists have dedicated much research to understanding the mechanisms that produce mainshocks and aftershocks. The dynamics of earthquake triggering mechanisms are highly variable and intrinsically related to the regional tectonic stress environment as well as to hydrologic changes (e.g., Healy et al., 1968; Simpson et al., 1988; Lin and Stein, 2004). Major breakthroughs relating stress transfer generated by earthquakes to neighboring faults and associated hydrologic changes has increased geoscientists' abilities to locate potential areas of seismic activity, yet many aspects of these predictions rely on knowledge and understanding of the seismic history for a given area (Stein, 1999).

An unparalleled opportunity to study earthquake dynamics and associated hydrological responses arose on September 21, 1999. On this date a magnitude M_w= 7.6 earthquake occurred near the town of Chi-Chi in central Taiwan. The epicenter was located at 23.85ºN, 120.82ºE, with a focal depth of approximately 8 km. The seismic event occurred along the Chelungpu thrust fault, which trends north-south for 100 km (Ji et al., 2005). The Chelungpu fault is a bedding-parallel thrust that separates central Taiwan's foothills and coastal plains (Lee et al., 2002). The rupture generated dual slip components, having both a reverse dip-slip and also a strike-slip motion. Horizontal

displacements along the hanging wall increased from 1 m in the south to 9 m at the fault's northern terminus. Vertical displacements along the hanging wall were greatest near the fault trace, where a maximum value was found to be around 4.4 m. Along the footwall, smaller horizontal displacements were observed to be from 0.2 m to 1.5 m, and subsidence was observed to 0.32 m (Johnson et al., 2001). The effects of the Chi-Chi earthquake's large surface rupture were devastating to the population in the region. Official casualty reports indicate that 2470 people died, 11,305 others were injured, and greater than 100,000 buildings were damaged (Shin and Teng, 2001).

During this catastrophic event, a network of 60 broadband strong-motion stations recorded ground-motion data (Lee et al., 2001; Shin and Teng, 2001; Wang et al., 2003) and 70 hydrological stations with 188 monitoring wells documented considerable changes in water levels across the large sedimentary basin to the west of the fault (Chia et al., 2001; Wang et al., 2001; Wang et al., 2003). The availability of such data provides researchers with a rare opportunity to investigate possible correlations between coseismic crustal deformation and hydrological changes, such as pore pressure diffusion, water-level change, increases in stream discharge, and liquefaction (Wang et al., 2003).

Despite a large number of investigations on the source mechanisms of the Chi-Chi earthquake and on rupture propagation, little attention has been given to possible poroelastic coupling in this large earthquake event. In general, the role and interactions of pore fluids with large magnitude earthquakes and aftershocks is still a deficient aspect of earthquake investigation. However, this realm of investigation should not be ignored, as the expulsion or diffusion of overpressured fluids out of the fault zone could significantly impact the pore-pressure distribution and aftershock activity in the seismic zone.

Similarly, the study of coseismic water-level changes and pore- pressure diffusion is also important because of its relation to other earthquake-related natural hazards, such as landslides and debris flows, liquefaction of soil, and groundwater pollution caused by the mixing of radioactive wastes or other hazardous wastes (Lai et al., 2004). Thus understanding the mechanisms that generate hydrologic anomalies and being able to quantify these relationships is important for many reasons.

Three plausible hypotheses have been proposed to explain the possible mechanisms accounting for field observations that indicate a strong relationship between hydrological changes and coseismic crustal deformation and ground motion. The first hypothesis claims that water can be expelled from the crust as a result of coseismic elastic strain (Muir-Wood and King, 1993). The rupturing of faults transfers stress to other areas of the crust, and therefore generates areas of strain, which may be of a compressional or dilatational nature. Pore fluids flow from areas of compression to areas of dilatation, accounting for some of the hydrological variations associated with large magnitude earthquakes. The second hypothesis states that the properties of the fluid-containing matrix can be altered by seismic activity. Fractures opened during an earthquake could increase the permeability and conductivity of the rock as long as these fractures are well-connected (Briggs, 1991; Rojstaczer and Wolf, 1992). This increase in permeability can lead to both changes in flow direction as well as increased flow and thus possibly account for observed hydrological anomalies. A third hypothesis claims that water can be released from storage through coseismic liquefaction or sediment compaction by strong ground-motion (Manga, 2001; Manga et al., 2003; Montgomery et

al., 2003). The expulsion of pore fluids caused by a reduction in pore space could account for rises in water-table and increasing base flow to streams.

This research project explores the three major hypotheses for explaining time-dependent changes in stress/strain and pore-pressure associated with the 1999 Chi-Chi, Taiwan, earthquake. Results from poroelastic modeling are compared with field data to examine the relationship between pore pressure build-up/relaxation and crustal deformation during and after the earthquakes. Of special interest are (1) which of the observed water-level changes can be explained by the coseismic strain model and (2) whether the pore-pressure diffusion model can adequately explain the various recovery (dissipation) patterns of seismically induced excess pore-pressure in the alluvial fan. These results have significance for understanding hydrologic anomalies related to other large magnitude earthquakes.

Background

Geologic History

The island of Taiwan developed as the result of the complex interactions between the Philippine Sea plate and the Eurasian plate over the last 12 Ma (Teng, 1990). Geographically, Taiwan is located at the convergent boundary between these two plates. The island's formation began when the ongoing consumption of the oceanic crust of the South China Sea led to the oblique collision of the Eurasian continental margin with the Luzon Arc around 6.5 Ma (Lin et al., 2003). Seismological studies have shown that this region is one of the most complex consumptive plate boundaries in the world (Katsumata and Sykes, 1964). To the south, the Eurasian plate subducts underneath the Philippine Sea plate along an east-dipping seismic zone; however, to the northeast, the polarity of subduction reverses and the tectonic style reflects the subduction of the Philippine Sea plate along a north-dipping seismic zone (Shin and Teng, 2001). In between these subduction zones, the island of Taiwan developed as a small fold-and-thrust belt as the result of oblique collision between the northern Luzon Arc Complex and the South China Sea rifted margin. Taiwan can be broken down into five major geological provinces, the Coastal Range, the Longitudinal Valley, the Central Range, the Western Foothills, and the Coastal Plane, described below from east to west (Fig. 1).

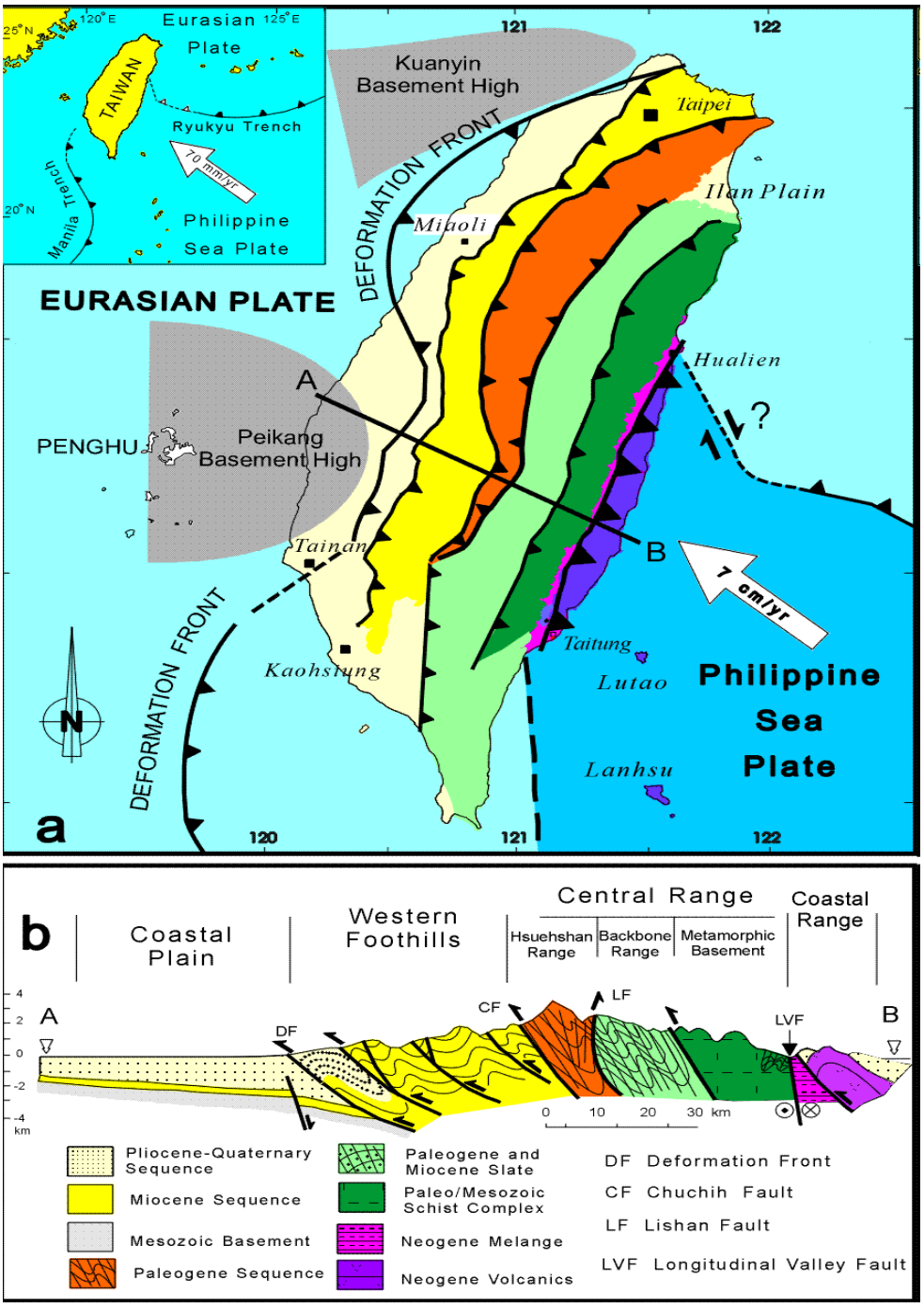

Figure 1. (a) Geologic map of Taiwan shows the five major geological provinces developed from the oblique collision of the Philippine Sea plate with the Eurasian plate. (b) Geologic cross-section provides a generalized view of changes in lithology and structure along the transect A-B (after Shin and Teng, 2001).

The Coastal Range

The Coastal Range in eastern Taiwan was formed from the collision of the northern Luzon arc and fore-arc basin with the Eurasian margin during the Miocene (Ho, 1986). The lithology is dominated by basal andesitic volcanic units and vertically grading volcaniclastic deposits. Volcaniclastic deposits are composed mainly of turbiditic sandstones, mudstones, siltstones, and conglomerates containing large amounts of disseminated volcanic fragments. Found within the upper sections of volcaniclastic units are mélange type deposits (Ho, 1986). These mélange deposits are composed of detritus from the Luzon arc and the Eurasian margin. Ophiolites derived from the uppermost mantle of the South China Sea are commonly found within these mélange deposits (Page and Suppe, 1981). Generally, the structure of the Coastal Range is dominated by NNE-trending anticlines and synclines, and low-angle east-dipping imbricate thrust faults (Ho, 1986).

Longitudinal Valley

The Longitudinal Valley separates the eastern Coastal Range and the Central Range. This zone is approximately 6 km wide and trends N-S for 150 km. Geologically, it is considered to be the suture zone associated with the Luzon Arc-Eurasian margin collision, where the Eurasian margin corresponds to the western boundary and the Luzon Arc of the Philippine Sea Plate is the eastern boundary (Chai, 1972).

The Central Range

The Central Range forms the core of the island and rises to a height of 4000 m. The Central Range is dominated by unroofed pre-Tertiary continental basement and Cenozoic sedimentary and metasedimentary cover. The eastern flank is dominated by pre-Tertiary metamorphic basement complexes, made up of mostly schists, marble, gneiss, and amphibolites bodies (Ho, 1986). The western flanks and highest ridges are underlain by argillite, slate, and phyllite (Ho, 1975).

The Western Foothills

The Western Foothills are part of the modern day foreland fold-and-thrust belt formed from pre-collisional Cenozoic siliciclastic deposits including Oligocene to Miocene continental margin sequences and Pliocene to Quaternary synorogenic foreland basin deposits (Chou, 1973; Covey, 1986; Teng, 1987a). Continental margin sequences consist mostly of shallow marine siliciclastic sediments (i.e., shale, siltstone, and sandstone) derived from the Asian continent and correspond to the original depositional setting on the continental margin (Teng, 1990). The Cenozoic sediments in the western Taiwan basin were deformed into mountains during the Plio-Pleistocene by a combination of folds and thrust faults (Ho, 1986).

The Coastal Plain

The Coastal Plain, west of the Western Foothills, consists of alluvial sediments and well-bedded, but poorly consolidated, clastic deposits. The Neogene sediments underneath the alluvial cover have a regional dip towards the east (Ho, 1986). The lithologies of the Coastal Plain mimic that of the tectonic development of Taiwan and the foreland basin. Foreland basin deposits are underlain by passive margin siliciclastic sediments and syn-rift deposits originating from the rifting of the South China Sea. Foreland basin deposits show a generally coarsening and shallowing up sequence. Deeper marine deposits are overlain by more shallow water and coastal deposits as the orogenic front migrated forelandward during the Plio-Pleistocene. In general, facies show a trend from more coarse in the north to fine in the south, indicating the relative direction of the collision is propagating towards the south as new depocenters evolve with the migrating orogenic front. A major unconformity separates the foreland sequences from the Miocene passive margin sequences. The stratigraphic gap increases westward into the distal portions of the foreland basin and provides evidence for uplift and erosion caused by a migrating forebulge during the last 3 m.y (Yu, 2001).

The 1800 km^2 Choshui River alluvial fan lies within the Coastal Plain province and provides the southwest Taiwan with its main source of freshwater. It is composed mainly of alluvial and shallow-marine deposits of Holocene to Pleistocene age, overlying a sedimentary basin containing alternating layers of Pleistocene to Miocene sandstone and shale (Chen and Yuan, 1999). The Western Foothills also contain these same alternating layers; however, they have been faulted and folded (Wang et al., 2004). The Choshui River alluvial fan contains four interfingering aquifers separated by three clay-

rich confining aquitards (Fig. 2) (Water Resources Bureau, 1999). The aquifers extend to a depth of approximately 300 m. The aquitards consist of thin, fine-grained sand, silt and mud that pinch out towards the fan's eastern edge (e.g., Wong and Wung, 2007). Layer F1, the shallowest aquifer, is an unconfined or partially confined aquifer, whereas Layers F2 through F4 are mostly well-confined aquifers (Hsu et al., 2000). The Choshui River alluvial fan is also divided into the upper-fan, middle-fan and lower-fan areas, based on the different hydrological and geological settings. The upper-fan (proximal) is closest to the Western Foothills and is comprised of thick gravel layers with high hydrological conductivities (10.81×10^{-4} to 8.37×10^{-4} m/d). The middle-fan is composed of thick sands and gravels with some interbedding of silts and muds to the north and mostly medium to fine-grained sands and silts to the south. The distal-fan is mostly composed of marine facies silt and mud deposits of low hydrologic conductivity (5.99×10^{-4} to 1.52×10^{-4}), with a few thin layers of sands and gravels in the north-central area (Water Resources Bureau, 1999).

Chelungpu Fault Geology

Most of Taiwan's seismic activity is attributed to rapid northwest convergence of the Philippine Sea plate towards the Eurasian plate (e.g., Shin and Teng, 2001). The average rate of convergence is believed to be approximately 82 mm/yr (Wong and Wung, 2007). Seismicity coincides with the growth of the Central Range and Western Foothills by frontal accretion and internal thickening as the convergence between the two plates continues. The 1999 Chi-Chi earthquake was the result of rupture along the Chelugpu

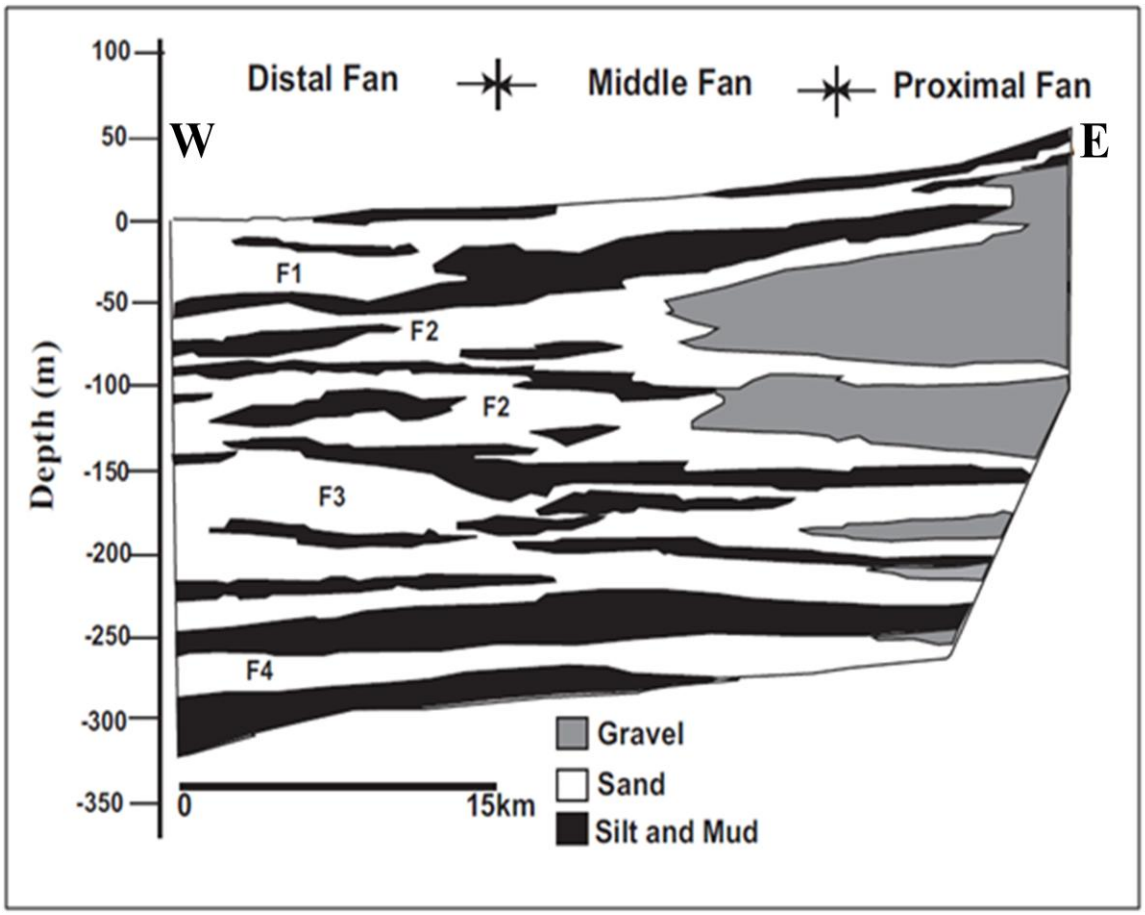

Figure 2. Geologic cross-section of the Choshui River Alluvial Fan (after Baird, 2002)

fault in west-central Taiwan (Fig. 3). The Chelungpu fault is part of the foreland basin fold-and-thrust belt that accommodates this internal shortening of the island, and also marks an important geological boundary between the Western Foothills and Coastal Plains provinces (Shih et al., 2000). It is considered to be a bedding-parallel thrust (Fig. 3) that follows and slips along the 150 to 300 m-thick Chinshui shale layer (Wang et al., 2004). The fault strikes roughly N-S for approximately 75 km, and then bends to the east for another 25 km; it dips towards the east at approximately 30 degrees (Chen et al., 2001). At greater depths the Chelungpu fault is thought to be a basal decollement in the critical wedge-type mountain belt and thin-skinned model (e.g., Barr and Dahlen, 1989; Barr et al., 1991, and Wang et al., 2000). Early studies suggest that the Chi-Chi event involved multiple fault planes with variable slip and strike components.

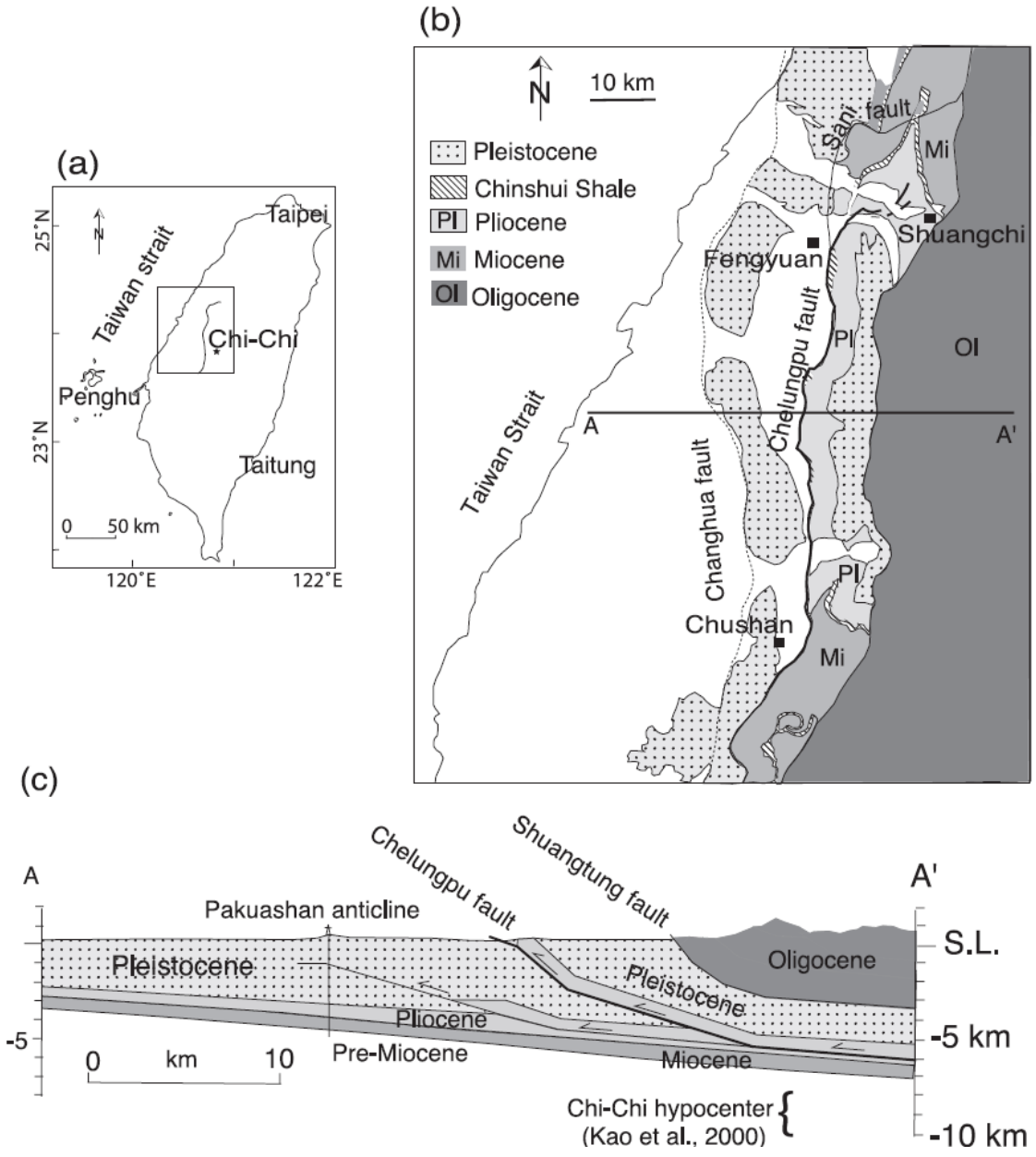

Figure 2. (a) Location of the Chelungpu fault and Chi-Chi epicenter. (b) A generalized geologic map of the fault zone area. (c) Cross-section of the Chelungpu fault zone shows that the Chelunpgu fault dips towards the east at approximately 29 degrees along the underlying Chinshui shale layer (after Johnson and Segall, 2003)

Previous Work

A significant amount of research has been aimed at understanding the mechanisms that trigger anomalous hydrologic variations observed with the onset of seismic events. A fundamental understanding of these mechanisms proves vital as earthquakes have been observed to disturb groundwater supplies, change pore-water chemistry, and drastically alter pore-pressures. Advances in geodetic observation tools, hydrologic monitoring stations, and computer modeling software, combined with a practical importance to understand the link between crustal deformation and hydrologic anomalies, have provided the assets necessary to explore poroelastic coupling in great detail.

Coseismic Volumetric Strain Hypothesis

Muir-Wood and King (1993) first proposed the volumetric strain hypothesis. This hypothesis investigates how stress resulting from fault ruptures is transferred to pore fluids. When a fault slips, it relieves a portion of the regional tectonic shear stress. Because of heterogeneities and the finite length of the break, strain created by the earthquake includes substantial components of compression and dilatation, as well as shear (Nur and Booker, 1972). Therefore, for a given seismic event, stress is relieved along the fault plane, but is transferred to the near and far fields via the propagation of seismic waves. This propagation of energy provides stress to the surrounding regions, which undergo deformation or volumetric strain. Depending on the focal mechanism and kinematics of slip, these regions become zones of induced compression or dilatation. Pore

pressure will change by an amount proportional to the volumetric shear stress change, and pore-fluids will flow from areas of compression to those of dilatation.

The focal mechanism for each earthquake provides the key constraints for the poroelastic response. Different kinematics of slip result in unique stress transfer conditions and resultant strain patterns. Generally associated with normal faulting is a dilatation of pore-spaces and cracks during the interseismic periods, followed by reduction in porosity and fracture size with the onset of an earthquake. This results in the expulsion of pore-fluids during the seismic event (Muir-Wood and King, 1993). Reverse faulting results in the opposite response. As stress builds up on the fault region during the interseismic periods, porosity and fractures become reduced. During the fault rupture, the pore spaces and fractures open up, serving to draw down the fluids towards the fault zone as a pump (Muir-Wood and King, 1993). Strike-slip and oblique slip faults have been shown to be very complex with regards to kinematics and thus may be difficult to be described by such an idealized coseismic strain model.

Therefore, the key component to this hypothesis is what happens to the individual pore-spaces and existing fractures following the fault rupture. If the deformation due to rupture results in compression, then pore-fluids will be forced out of voids from the reduction in pore-space and an increase in pore pressure. If the region undergoes dilatation, the pore-space becomes expanded and thus fluid pressures drop with the onset of an earthquake. This resultant drop in fluid pressure theoretically corresponds also to a drop in water-table elevation. In summary, one should expect to see a net increase in water-table elevation with compression due to an expulsion of pore-fluids out of the pore-space and a decrease in water-table elevation with dilatation due to a decrease in pore-

pressure. This response is thus a viable mechanism for inducing hydrologic anomalies such as rapid changes in well monitor readings and variations in stream discharges following an earthquake.

Fracture-Induced Permeability Enhancement

Rojstaczer and Wolf (1994) and Wang et al. (2010) proposed an alternative mechanism to explain invoked hydrologic anomalies associated with seismic events. Both explored in detail the response of stream discharges to earthquakes. They found that stream discharges commonly increased post-earthquake, after a lag time of minutes up to a few weeks following the rupture. They argued that these pronounced increases in stream discharge are related to fracturing of rocks controlling the groundwater flow system.

Following the 1989 Loma Prieta earthquake, data from stream-gauging stations indicated significant increases in stream discharge within 15 minutes of the rupture. Similarly, Rojstaczer and Wolf (1994) found ionic concentrations and the calcite saturation index of the stream water had also increased. Stream flow and solute concentration decreased significantly over a period of several months following the earthquake. An increase in solute concentrations and calcite saturation index in the surface waters provides compelling evidence that excess water must have interacted with the rock units along a flow path that originated from the nearby mountainous regions (Rojstaczer and Wolf, 1994). Furthermore, it was observed that in the highland portions of the basin, groundwater levels were lowered by as much as 21 m within weeks to months after the earthquake. From these data, they surmised that fracturing generated by

the earthquake had increased the rock permeability and enhanced groundwater flow and dewatering from the higher portion of the mountains and basins (i.e., recharge areas) towards lower elevations discharge areas through increased base-level contribution.

Similar increases in stream discharge were observed following the 1999 Chi-Chi earthquake, Taiwan. Discharge values obtained from stream gauging stations near the Western Foothills displayed rapid coseismic increases. Base flow analysis of these streams, however, revealed that no significant changes in horizontal hydraulic diffusitivity resulted from the earthquake (Manga, 2001; Manga et al., 2003). Similarly, no significant precipitation events occurred during this time frame to cause the increased discharges. It was hypothesized by Wang et al. (2010) that vertical fracturing caused by the seismic event could be a mechanism for increase in stream discharge.

Well-lithified shale and sandstone units of the Western Foothills provide the possibility of perched water-tables. Sandstone reservoirs could be confined by underlying relatively impermeable shale units. However, if these shale units become fractured by the tensile stresses generated from the drop of the hanging wall (Lee et al., 2002) or by strong seismic shaking, then new flow paths from higher elevations in the foothills towards lower elevations may develop. Evidence of decreased water-levels in perched water-tables could provide more scientific evidence that such processes may be occurring. Therefore, Wang et al. (2010) concluded that increased fracturing in the Western Foothills region of Taiwan created a connection between perched water-tables and streams at lower elevations.

Fracturing-induced permeability by tensile stresses or extreme seismic shaking can be a viable hypothesis if the resultant fractures are well connected to permeable

geologic layers. If the fractures remain poorly connected, new pathways for fluid flow are not possible, and increases in base flow and stream discharge would not likely result. Seismic shaking can also lead to the removal of particles or gas bubbles that may have otherwise blocked fluid flow through these fractures, providing yet another way that fracturing can increase permeability (Brodsky et al., 2002).

Compaction

Manga (2001) studied stream flow response to the Chi-Chi earthquake in the Choshui River alluvial fan region of Taiwan as well as the response of several California streams to seismic events. He argued that a third plausible mechanism is responsible for increased water-tables and stream discharge rates. Manga (2001) postulated that for the studied stream systems, the coseismic increase of discharge required increased hydraulic head gradients resulting from the rapid release of water from some storage source in the shallow crust. He hypothesized that a change of fluid pressure in the matrix materials by transient dynamic strain created elevated stream discharges. If the seismic waves propagating through the layers contain enough energy to surpass a threshold resistance then the sediments generally will preferentially re-orient themselves into a new configuration. This agitation brought about by seismic shaking or transient dynamic strain generally results in a tighter packed sediment configuration reducing the pore-space and increasing grain-to-grain contacts. As a direct result, pore-waters would be expulsed, providing a source for increases in water-table elevations or stream discharge values. Following the Loma Prieta earthquake, water temperatures of streams were found to be lower than normal with excess flow from a shallow source (Manga, 2001). This is

somewhat contrary to the coseismic volumetric strain hypothesis in that Muir-Wood and King (1993) suggested that the source water most likely came from the mid-crust. Compaction is most commonly seen in alluvial fans or regions dominated by relatively unconsolidated sediments near the fault zone.

Numerical Modeling

Baird (2002) researched the interplay of coseismic strain and pore pressure for the 1999Chi-Chi earthquake. He created a one-way coseismic deformation fluid-pressure diffusion model. His results showed a promising correlation between induced strain fields andthe behavior of pore fluids, supporting the mechanism for coseismic volumetric strain (Muir-Wood and King, 1993) as the trigger for some hydrologic anomalies observed in Taiwan. Baird's research shows that some coseismic drops in water-table were found to be located in dilatational zones. Pore-pressure modeling revealed that these zones showed cosesimic decreases in pore pressure and thus water-table drops would be consistent with a coseismic volumetric strain hypothesis. However, Baird's (2002) finite fault rupture model was not calibrated against field data . Contrastingly, this study improved Baird's model by making use of a published finite-fault rupture model (Ji et al., 2005) and thus pore-pressure models will be integrated with well calibrated spatially-dependent stress and strain values for the Chi-Chi earthquake.

Observed Hydrologic Anomalies

Water-Table Changes

A network of 58 monitoring wells documented the coseismic and post-seismic responses of the Choshui River alluvial fan aquifers to the 1999 Chi-Chi earthquake (Fig. 4). The observed hydrologic anomalies following the Chi-Chi earthquake varied widely. Coseismic variations in water-table elevations were found to range from a decrease of -11.1 m to an increase of 7.42 m within the Choshui River alluvial fan and slope region. The magnitude of change corresponded relatively well to the proximity of well location to the Chelungpu fault. Generally, the largest variations occurred near the rupture zone, with diminishing values farther from the fault. Two types of hydrologic responses were observed in the well logs: (1) persistent changes and (2) oscillatory changes. Persistent changes were commonly found within the Choshui River alluvial fan and slope regions. These persistent changes are characterized by step-wise coseismic changes in the water levels and gradual diffusion towards a pre-seismic water-table elevation. Oscillatory changes occurred mainly in the shallow, unconfined aquifer and are the result of passing seismic waves through the water column. These changes lasted only while the shear waves originating from the Chi-Chi earthquake propagated through the well locations.

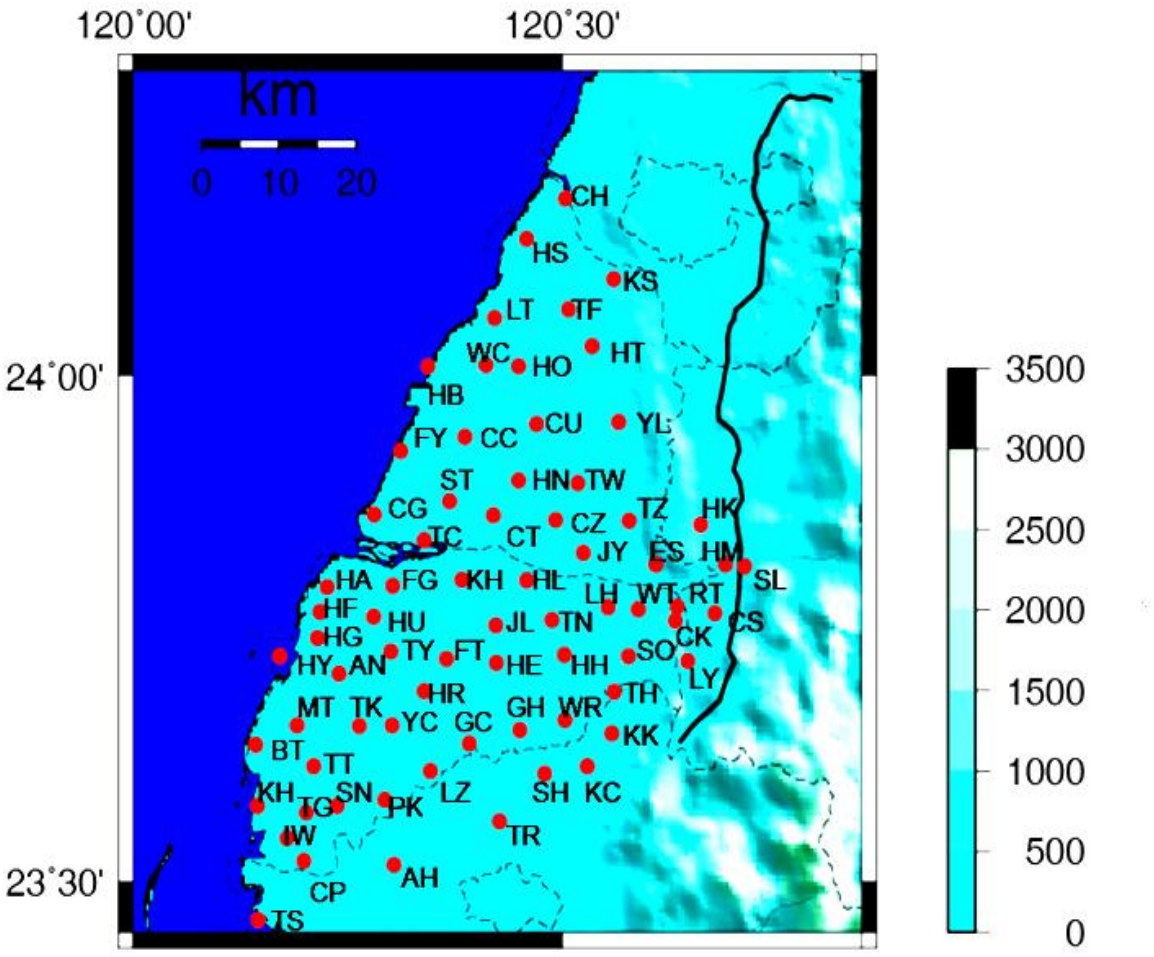

Figure 3. Map showing the locations of monitoring wells within the Choshui River alluvial fan and Western Foothills upper-slope region. Red dots indicate well locations. Black line represents the Chelunpgu fault.

Persistent Water-Table Variations

Persistent water-table variations showed two general trends with regards to proximity to the seismogenic zone. Coseismic water-table falls were observed in regions nearest the fault zone, mainly on the edge of the Western Foothills and slope regions of the Choshui River alluvial fan. These drops were generally located in consolidated sedimentary rocks and located within 5 km distance from the Chelungpu fault. Farther away from the fault zone (<15 km), within the middle and lower portions of the Choshui River alluvial fan, strong coseismic water-table rises were observed. In between these zones, a mixture of rises and falls were observed within the monitoring well network. Of the 58 total monitoring wells recorded readings, the predominant response was a coseismic rise (50 wells) following the earthquake.

Piezometric readings can be grouped into four distinct diffusion patterns within the wells: (1) a up-up response (Fig. 5a), (2) down-down response (Fig. 5b), (3) up-down response (Fig. 6a), and (4) down-up response (Fig. 6b) (Wang et al., 2004). These responses were characterized by Wang et al. (2004) to be related to the local geology of the well and also the redistribution of stress fields in the shallow subsurface due to fault rupture (Chia et al., 2008). This research focuses on two responses: (1) rise-fall and (2) fall-rise as these are the only responses that can be investigated by a coseismic volumetric strain mechanism. Rise-rise and fall-fall responses could be attributed to outside factors such as local irrigation or pumping or possibly attributed to be the response due to another mechanism altogether (e.g., fracturing).

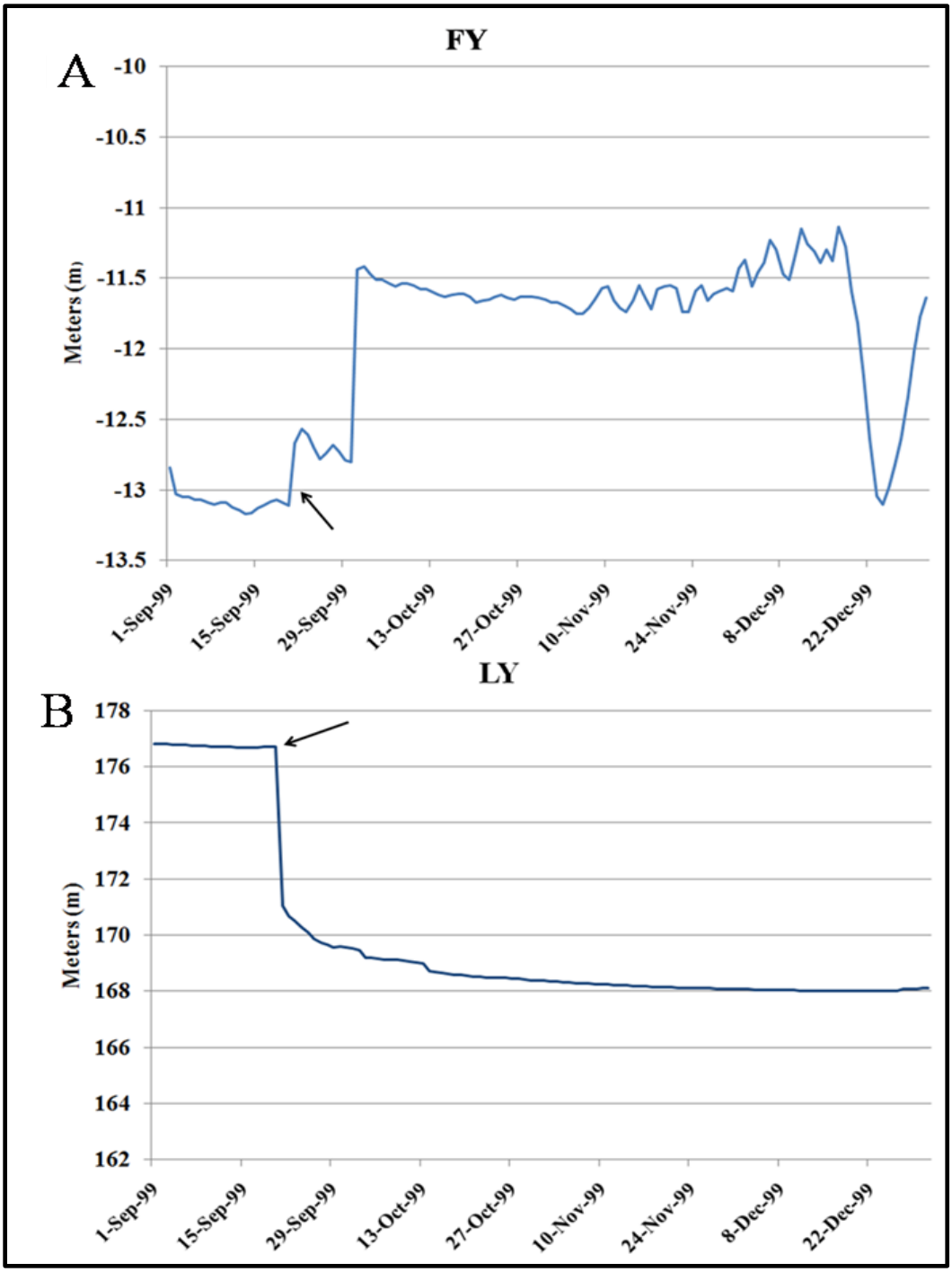

Figure 5. (a) Well FY shows a up-up response following the Chi-Chi earthquake. (b) Well LY shows a down-down response following the earthquake. Black arrows indicate timing of the earthquake event.

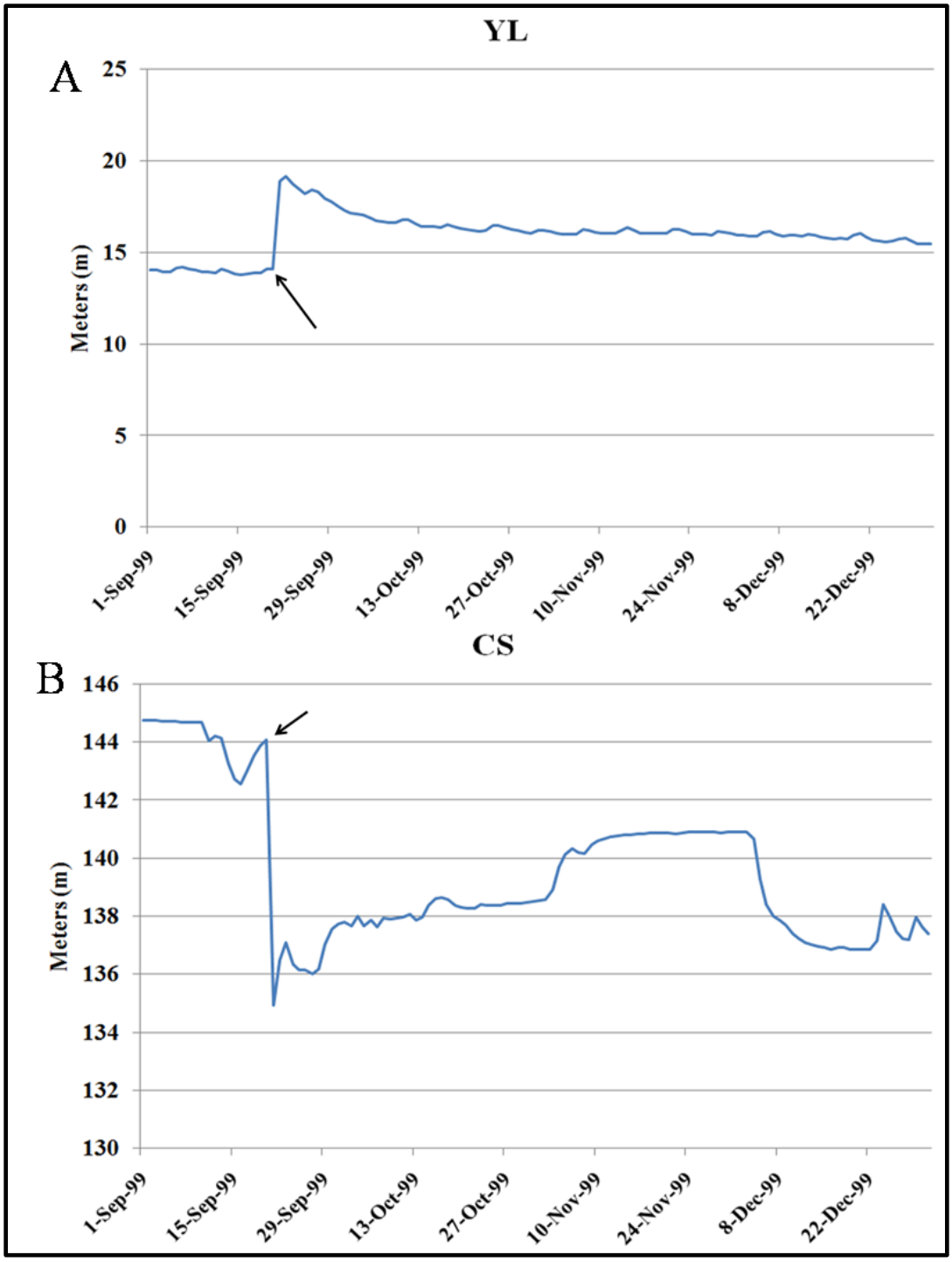

Figure 6. (a) Well YL shows an up-down response to the Chi-Chi earthquake. (b) Well CS shows a down-up response to the earthquake event. Black arrow indicates timing of the earthquake.

Coseismic Response of Aquifer F2

Aquifer F2 is mostly confined by clay and silt layers above and below. It is composed mostly of medium-to-coarse grained sands in the central and western regions of the fan and gravel sized sediments (Fig. 2) to more consolidated sedimentary rock in the upper fan and slope regions (Lai et al., 2004). Careful investigation of all the major aquifers in the region revealed that aquifer F2 showed the largest magnitude changes and thus is the most useful aquifer to study for the purposes of this research.

The fan is divided into three segments based upon distance from the fault zone (Fig. 7). The proximal zone extends roughly 15 km westward from the Chelungpu fault zone. This zone includes the slope region of the Western Foothills and upper portion of the Choshui River alluvial fan. Aquifer F2 in this region is generally regarded to be composed of gravel-to-sand sized sediments as well as consolidated sandstone (Fig. 2). The second zone, the middle fan, ranges from 15 km to 30 km west of the Chelungpu fault. Aquifer F2 in this zone reflects a gradation from more coarse sands and gravels in the east to medium grained sands in the west (Fig. 2). The final zone, the distal fan, extends from 30 km west of the fault to the coast. The sediments constituting the F2 aquifer in the distal zone grade from medium to fine-grained sands before pinching out beneath the Taiwan Strait (Fig. 2).

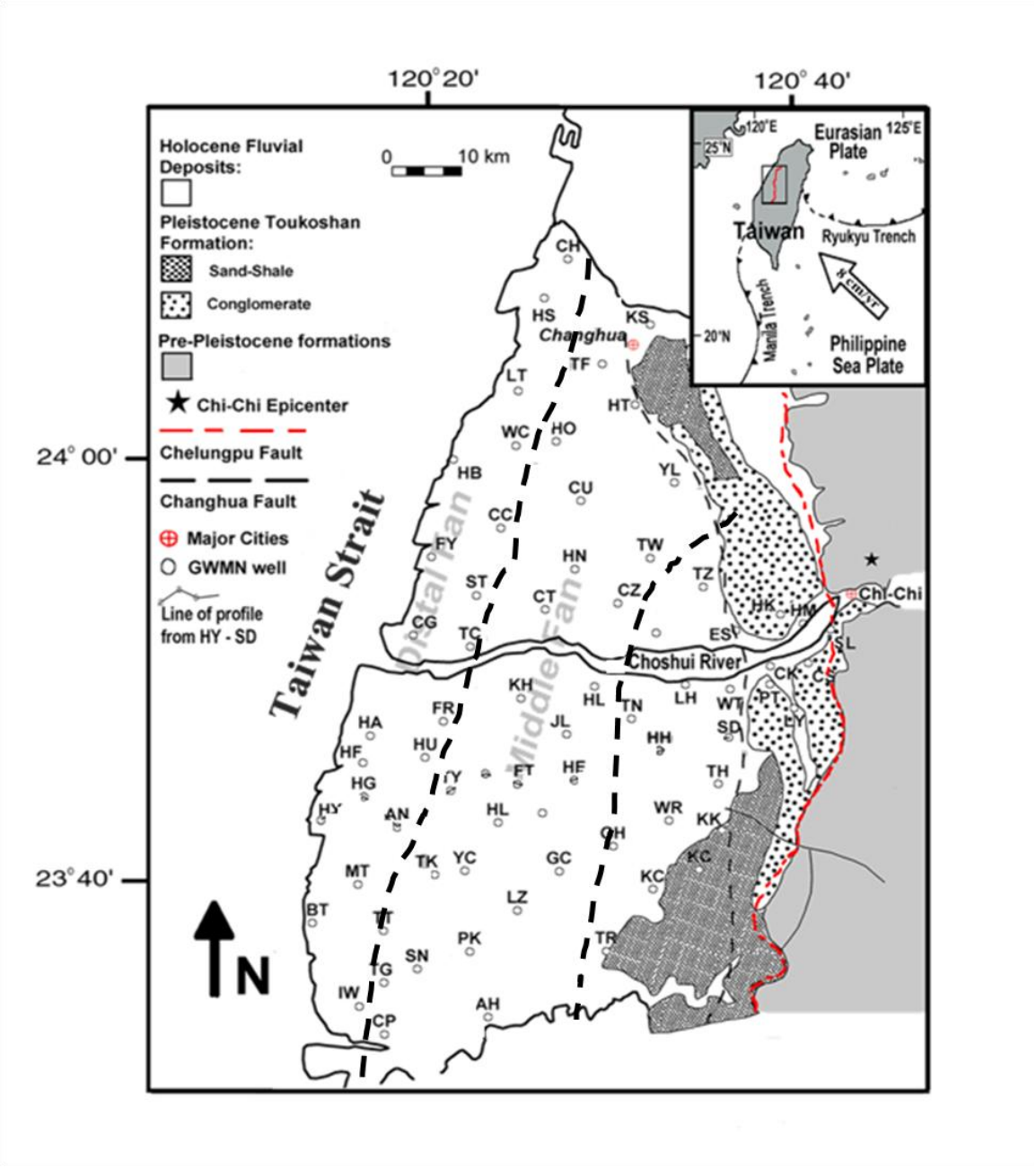

Figure 7. Well locations are divided into three categories based on proximity to fault. Proximal < 15 km. Middle Zone 15 to 30 km. Distal Zone > 30 km. Chelungpu fault is highlighted by solid dashed line (after Baird, 2002).

Distal Response

In total *25* wells were located in the distal zone (Fig. 8). The dominant coseismic response (21 wells) was observed to be an increase in water-table elevation . The largest magnitude changes occurred in the northern portion of the distal zone (north of Choshui River), averaging an approximate increase of 3 m. The largest documented changes occurred in the far northern section of the zone in wells CC, HO, LT, and HS (Fig. 9a), where changes were 5.4 m, 5.28 m, 5.22 m, and 4.28 m, respectively. South of the Choshui River, the magnitude of coseismic changes diminished. A majority of the wells south of the river exhibited small coseismic increases, averaging less than 1 m. Three wells documented minute coseismic decreases, however, these decreases in water-level were found to average less than 0.1 m.

Middle Fan Response

A total of 24 wells are located within the middle portion of the Choshui River alluvial fan (Fig. 8). Water-table change maps illustrating the coseismic water-table elevation response at each well location were made with GMT®. Of these *24* wells, only two (TZ and KS) displayed coseismic decreases in water-table elevation. Wells *TZ* and *KS* are located within 5 km of the gproximal zone and responded with coseismic drops of -2.47 m and -0.07 m, respectively. The remaining 22 wells exhibited increases in water-table elevation, ranging from 0.02 to 7.42 m. The largest coseismic increases were observed within the central portion of the middle fan around 17 to 25 km away from the

fault zone. Wells HE, YL, and JL (Fig. 9b) showed the largest increases with values of 7.42 m, 6.46 m, and 4.21 m, respectively. Anomalously, many of the wells located in this zone showed no coseismic response, often located near wells exhibiting large magnitude changes.

Proximal Response

Eight wells are located within the proximal zone (Fig. 8). Five of these wells showed strong drops in water-table elevation following the Chelungpu fault rupture. Two wells (ES, KC) showed small coseismic increases of 0.08 m and 0.29 m respectively. One well (WT*)* showed no change following the Chi-Chi earthquake. The largest decreases in water-table elevation were found to occur within 5 km of the Chelungpu fault, with the largest observed decrease of -11.09 m (CS) (Fig. 9c) occurring within 2 km. The other decreases in water-table elevation were found to range from -0.8 m to -5.94 m within the proximal zone.

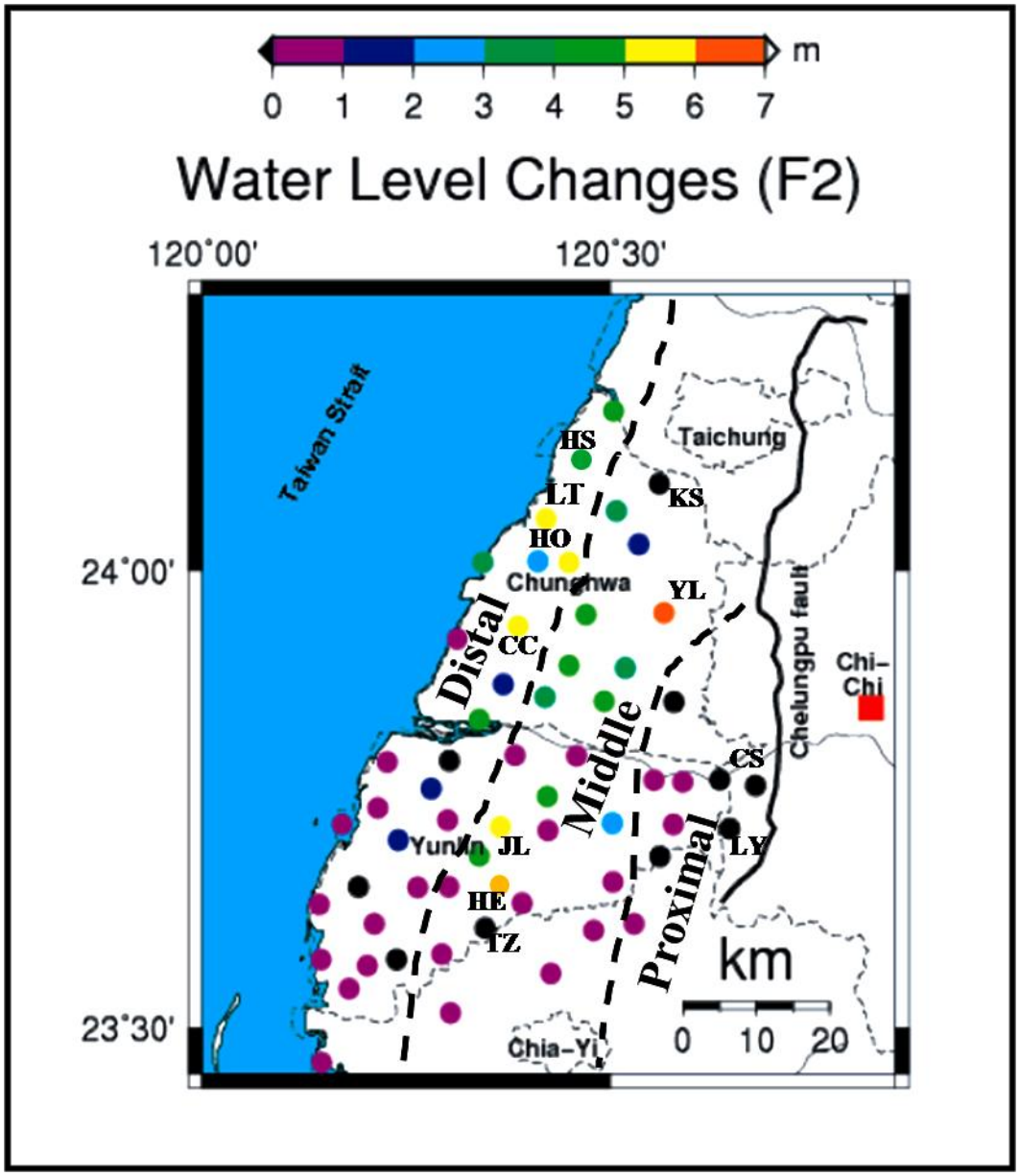

Figure 8. Coseismic well response of aquifer F2 to the Chi-Chi earthquake. Black dashed lines mark zone boundary. Solid black line represents Chelungpu fault. Red square is the epicenter. Black dots indicate coseismic decreases in water-level. Key wells discussed in text are labeled**.**

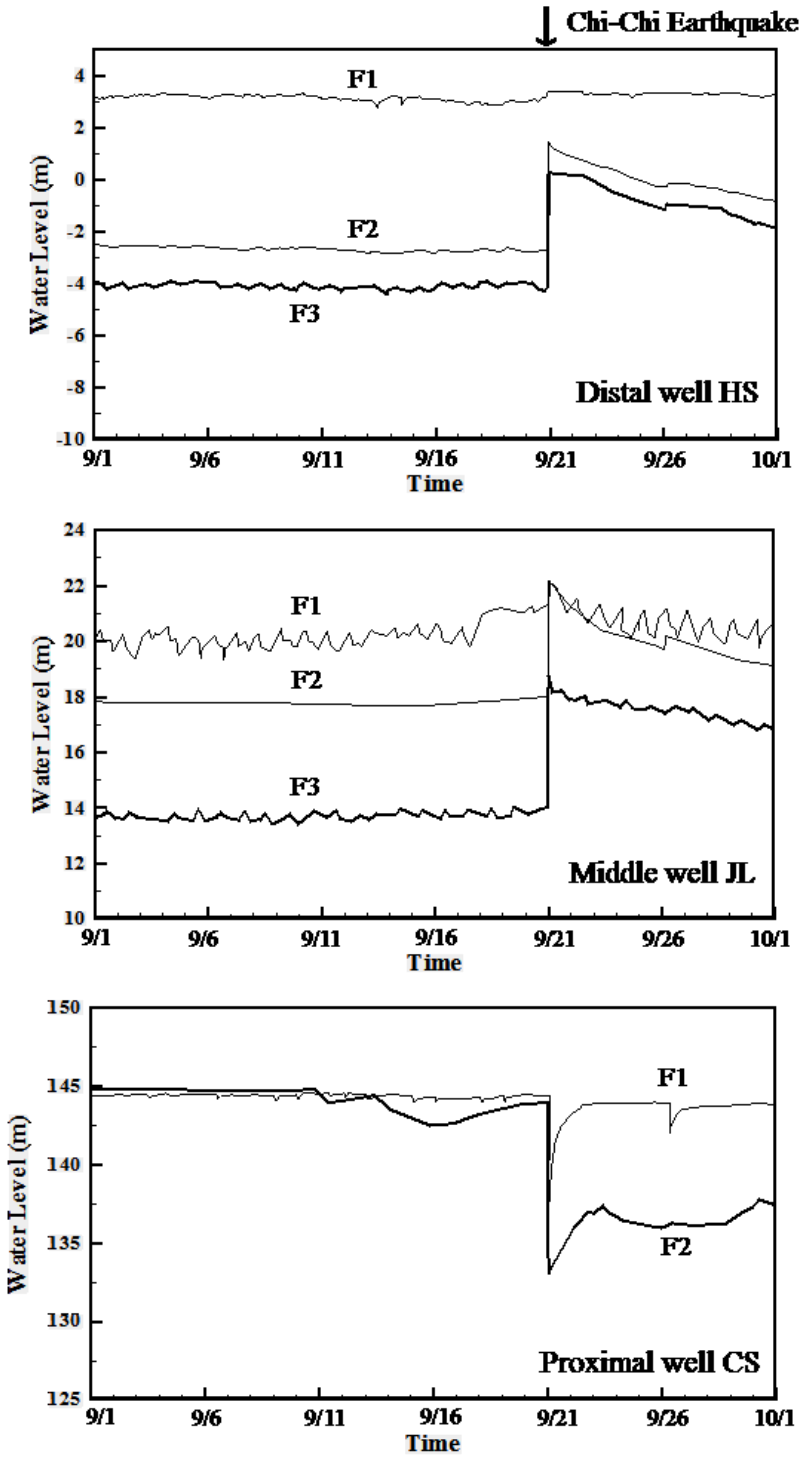

Figure 9. (a) Coseismic response of well HS, located in the distal zone of the Choshui River alluvial fan. (b) Coseismic response of well JL, located in the middle zone of the alluvial fan. (c) Coseismic response of well CS, located in the proximal zone.

Post-Seismic Responses

After 50 days, the water-levels in the F2 aquifer show a different pattern of changes (Fig. 10). Wells found in the distal zone, primarily showed a decrease in water-level, below that of pre-seismic levels. In total, 16 of the 25 wells located in the distal fan illustrated this pattern. Geographically, the majority of the decreases were found in the southern portion of the distal zone, where coseismic increases were found to be on average only around 1 m. Seasonal variations (i.e., rainfall decrease, irrigation pumping, etc) may therefore be the cause for this response.

In the middle zone, a total of 6 wells were found to have dropped below pre-seismic levels. Anomalously, all of these wells showed strong coseismic increases in water-level of 1 to 3 m. Geographically, these wells are generally located within 10 km of the proximal zone and near the southeastern corner of the zone. The two wells that exhibited coseismic decreases in water-level were found to have rebounded over the 50 day time-span, responding with increased levels above that of pre-seismic level. The remaining wells (16), illustrated average decreases of 1 to 2 m from strong coseismic increases,indicating a slow recovery back to pre-seismic levels.

Seven of the nine wells located in the proximal zones were found to have water-levels below that of pre-seismic water-table. Two wells that exhibited coseismic increases were found to have dropped below pre-seismic levels. One well, that showed a coseismic decrease in water-level, was found to have increases above pre-seismic level after 50 days.

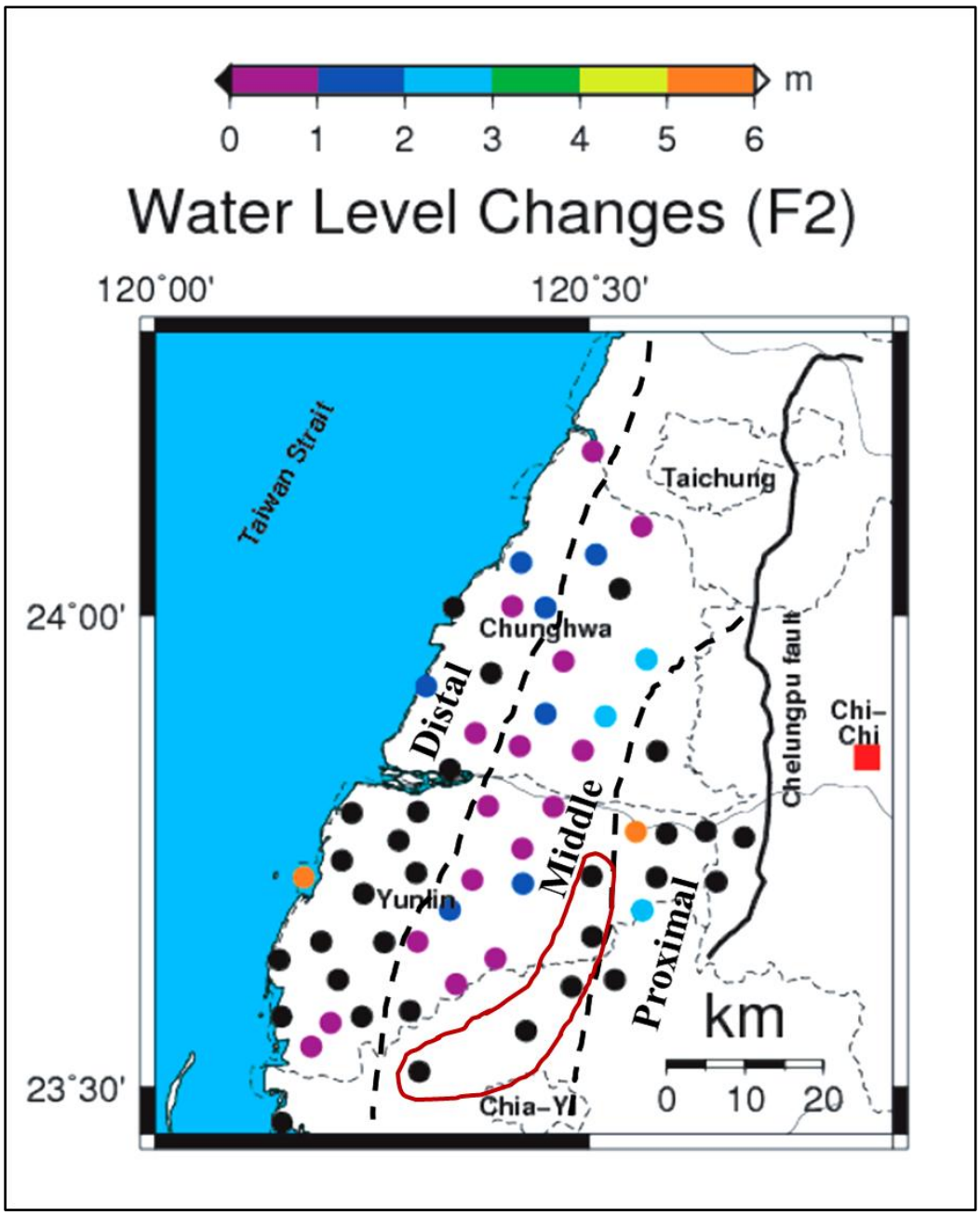

Figure 10. Post-seismic (50-day) water-level changes show that a majority of the wells located in the distal zone show drops below pre-seismic levels. Within the southeastern section of the middle zone, a group of wells that showed strong coseismic increases, responded with decreases over the next 50 days (red outline). Wells located in the proximal zone continue to show decreased water-levels. Black dots indicate negative levels.

The water-levels after 100 days (Fig. 11) show yet a different pattern than that of the coseismic and 50-day pattern. The number of wells displaying negative responses (below pre-seismic levels) decreased from 16 wells to 9 wells within the distal zone. The remaining wells (16) exhibited water-levels above that of pre-seismic conditions, but averaging only an increased head of 0 to 1 m.

Wells located within the middle zone illustrated a similar pattern to that of the 50-day pattern. In total 7 wells were found to be negative. The remaining wells (16) had positive levels, but averaged an increased hydraulic head of 0 to 1 m. Only two wells had hydraulic head increases greater than 2 m. Wells located within the proximal zone continued to show decreased water-levels. In total 7 wells were found to have negative levels. The remaining two wells had positive levels; however, neither had levels that were 1 m above that of pre-seismic level.

In general, the wells located in the Choshui River alluvial fan showed sporadic 100-day responses to the Chi-Chi earthquake (Table 1). It appears that wells located in the proximal zone show a more permanent trend of decreased water-level. Yet, many of the wells located farther out in the fan show an oscillating pattern, in which water-levels swing above and below those of pre-seismic conditions.

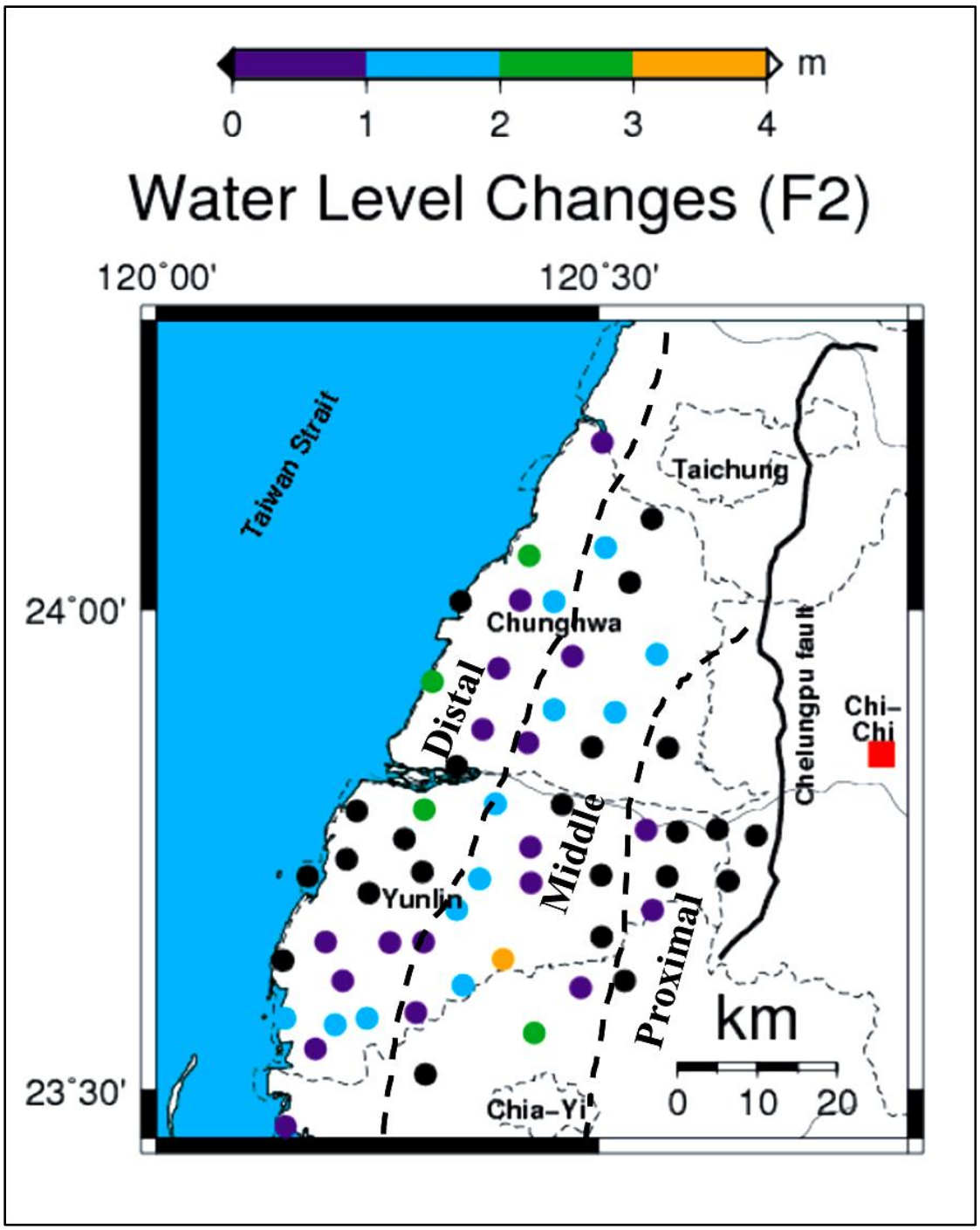

Figure 11. Post-seismic (100-day) response of wells located within the Choshui River alluvial fan shows that wells generally recover with a sporadic and oscillating pattern. Wells located in the proximal zone show a more permanent pattern of decreases water-level over the 100-day span. Black dots indicate negative water-levels.

Table 1. Co- to Post-seismic water-levels for monitoring wells located in the Choshui River alluvial fan. Levels are taken at three steps: (1) Coseismic, (2) 50-day, and (3) 100-day. Water-levels are plotted in Figures 8, 10, and 11.

Well Abbrev	Coseismic (m)	50-Day (m)	100-Day (m)	Well Abbrev	Coseismic (m)	50-Day (m)	100-Day (m)
CZ	4.75	0.16	-0.46	LH	0	5.04	0.37
CT	3.86	0.33	0.29	HH	2.57	-0.38	-0.91
TC	4.01	-0.17	-0.4	IW	0.21	0.38	0.42
TZ	-2.47	-1.29	-3.21	KH	0.02	-0.25	1.92
FY	0.49	1.5	2.01	TY	0.72	-3.18	-1.3
CC	5.4	-0.09	0.2	HL	0.03	0.08	-0.1
YL	6.46	2.12	1.58	KH	0.02	0.8	1.28
CU	4.76	0.93	0.78	HA	0.48	-1.09	-1.5
HB	3.23	-1.2	-1.24	HG	0.74	-1.53	-2.17
HT	1	-2.29	-2.37	KC	0.02	-2.12	-1.17
HO	5.28	1.65	1.89	PK	0.97	-0.1	0.9
KS	-0.07	0.7	-0.12	BT	0.56	-2	-1.86
CS	-11.09	-3.63	-6.77	FG	-0.09	-1.68	2.11
LY	-5.94	-8.45	-8.6	WT	0	-1.19	-2.56
CK	-2.23	-1.41	-1.84	SH	0	-1.55	0.69
CH	4.66	0.66	0.37	WR	0.32	-2.19	-0.55
LT	5.22	1.97	2.38	JL	4.11	0.46	0.39
TF	3.73	1.62	1.45	TG	0.5	0.02	1.09
WC	2.76	0.59	0.64	HU	1.13	-2.78	-2.23
ST	1.59	0.74	0.19	LZ	-0.02	0.19	1.93
TW	3.95	2.23	1.33	TT	0.52	-1.26	0.56
HN	4.43	1.81	1.11	SN	-0.01	-0.38	1.47
SO	0.24	-1.88	-3.99	YC	0.02	0.62	0.55
FT	5.8	0.14	1.07	MT	-0.01	-1.33	0.52
AN	1.44	-1.57	-1.7	HR	4.55	1.31	1.17
HY	0.4	5.4	-1	TR	0.03	-0.83	2.97
HE	0.87	1.07	0.89	TK	0.99	-1.53	0.02
TH	-2.96	2	0.01	GC	0.01	0.48	3.56
AH	0.09	-1.16	-0.18	TS	0.01	-0.92	0.6

Stream Response

Stream discharge data gathered from the Ta'ang, Wu, and Choshui rivers (Fig. 12) show dynamic coseismic and post-seismic changes in stream flow within west-central Taiwan. Generally, the trend of these streams was a coseismic increase in discharge followed by a slow post-seismic recovery back to normal gauging levels. Precipitation is likewise measured at these stations, providing the data necessary to make distinctions between changes caused by rainfall and changes brought upon by earthquake.

The Ta'ang River borders the northern portion of the Chelungpu fault zone, flowing from central Taiwan to the strait of Taiwan (Fig. 12). Along the Ta'ang River, three gauging stations monitored stream flow (SS, TL, YL). Gauging station SS (Fig. 13a), located near the border of the Western Foothills and east of the Chelunpgu fault, recorded a coseismic increase of 0.5 m. This coseismic increase took approximately 2 months to recover back to a pre-seismic level. Station TL (Fig. 13b) is located north of the fault tip, within the Western Foothills. Data retrieved from this station show a larger coseismic increase in stream level (~0.7 m). This increase took approximately 8 days to achieve maximum levels (Fig. 13b). Following its peak, the stream recovered nearly to pre-seismic level within 2 months. Station YL (Fig. 13c) is located northwest (~ 10 km) of the fault. This station shows a coseismic increase of approximately 0.5 m, followed by an oscillating recovery back to pre-seismic levels. Within a couple days of fault rupture, stations TL and YL, received around 50 mm of precipitation. Based upon plotted pre-seismic stream responses to rainfall, however, the rainfall does not appear to significantly affect the stage levels.

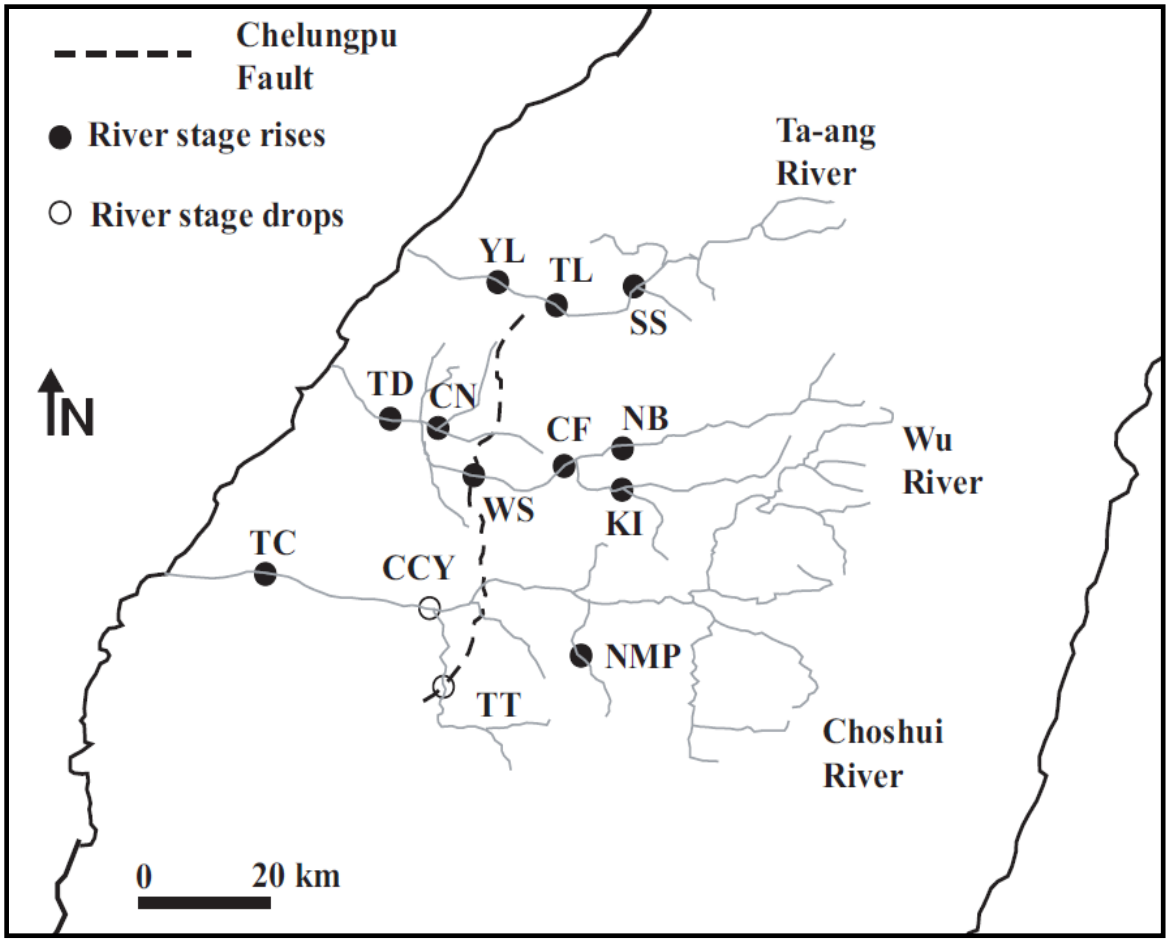

Figure 12. Stream gauging station location map for streams located in the fault zone. Chelungpu fault is highlighted with dashed black line.

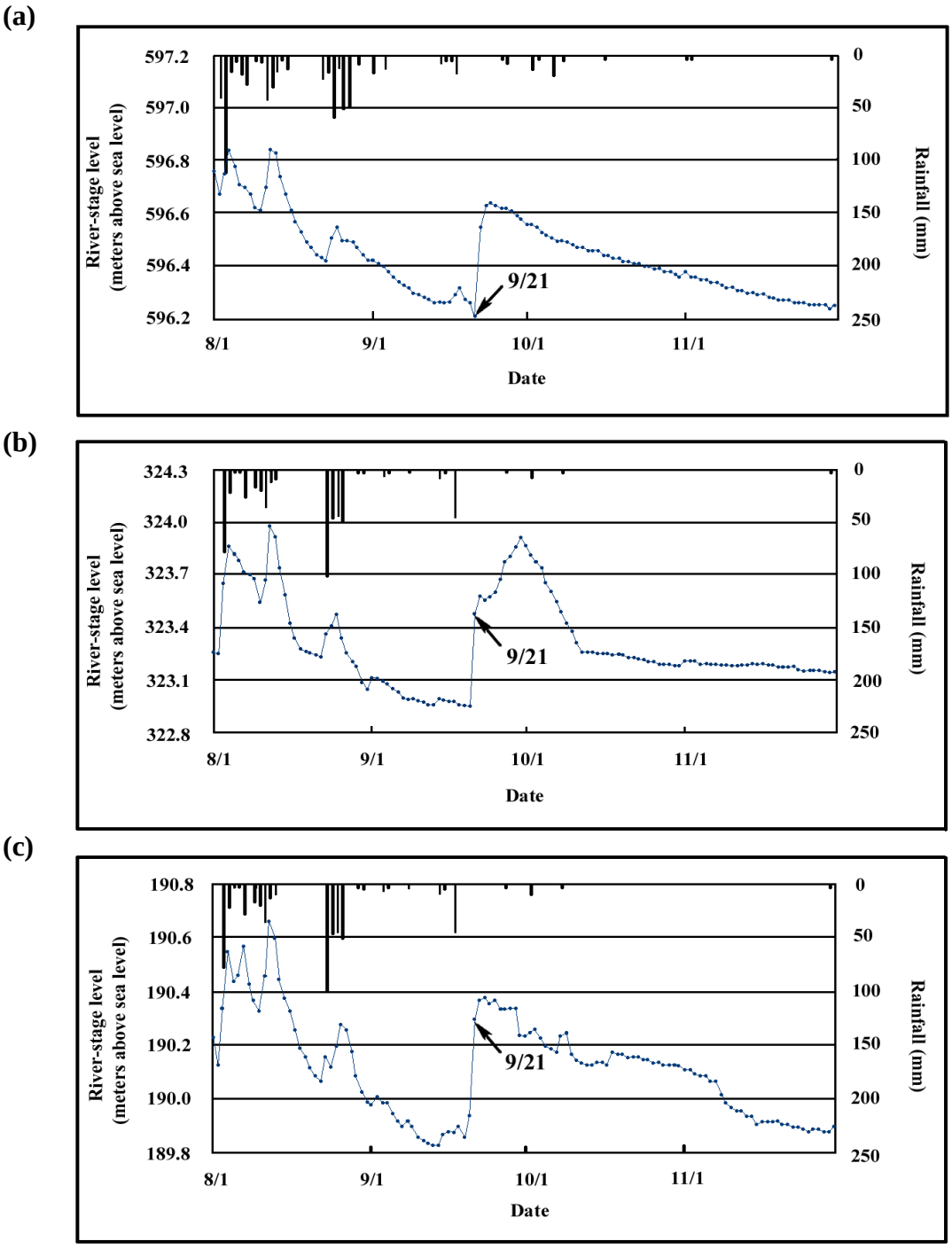

Figure 13. Pre- to post-seismic surface (river) water level changes observed at monitoring stations SS (a), TL (b), and YL (c) along the Ta-ang River (as shown on Fig. 12). The arrow marks the Chi-Chi earthquake. Rainfall amounts are shown by the vertical bars (left Y-axis) (modified after Water Resource Bureau of Taiwan, 2000).

The Wu River transverses the northern part of the Chelungpu fault (Fig. 12). Three gauging stations located to the east of the fault recorded data as well as three stations located to the west. One of these stations (WS) is located very near the fault zone. All of these stations recorded coseismic increases (1 or 2 days post-event). Generally, stations located farther than 10 km away from the fault zone displayed coseismic increases of less than 1 m and recovered back to pre-seismic levels within two months (Figs. 14 and 15). Station WS (Fig. 14c), is the exception to these observations. This station recorded an abrupt (Fig. 14) coseismic increase in stream level of over 4.5 m. In the two months following the earthquake, the station did not recover back to pre-seismic levels, but showed a continuous increased stream level. Precipitation data show that rainfall did not play a significant role in any coseismic or post-seismic changes in stream flow.

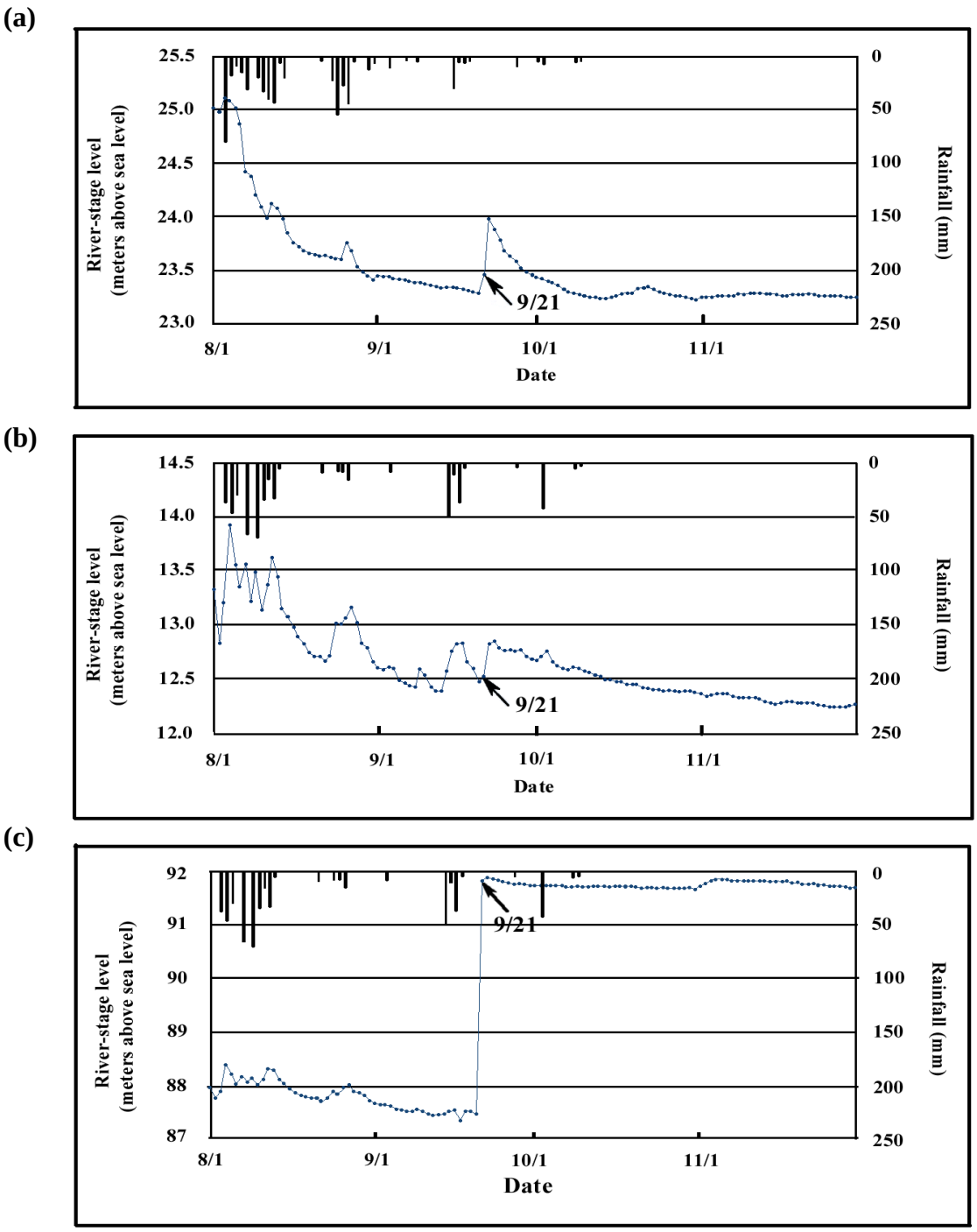

Figure 14. Pre- to post-seismic surface (river) water level changes observed at monitoring stations CN (a), TD (b), and WS (c) along the Wu River (as shown on Fig. 11). The arrow marks the Chi-Chi earthquake (modified after Water Resource Bureau of Taiwan, 2000).

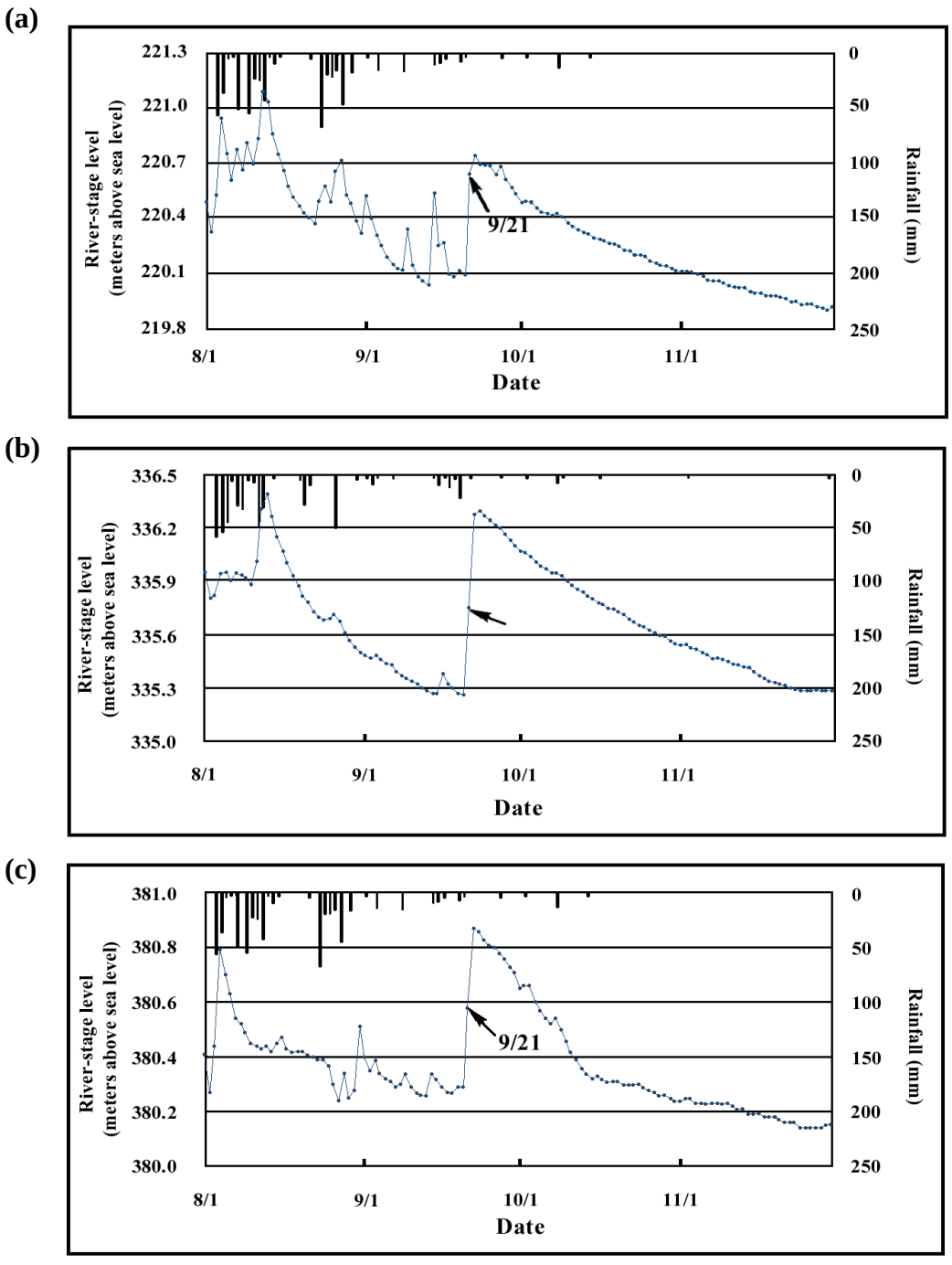

Figure 15. Pre- to post-seismic surface (river) water level changes observed at monitoring stations CF (a), NB (b), and KI (c) along the Wu River (as shown on Fig. 11). The arrow marks the Chi-Chi earthquake (modified after Water Resource Bureau of Taiwan, 2000).

The Choshui River transverses the southern portion of the Chelungpu fault (Fig. 12). Four gauging stations monitor stream levels in the area (Figs. 16 and 17). Two are located to the west of the fault (TC and CCY), one is located near the fault zone TT (Fig. 16a), and one to the east, NMP (Fig. 16b). Two stations show coseismic increases of less than 1 m, TC (Fig. 16a) and NMP (Fig. 16b), one shows no coseismic change, CCY (Fig. 17b), and one shows a coseismic decrease, TT (Fig. 17a). Stations that display a coseismic increase generally recover back to pre-seismic levels within a month. Station TT (Fig 17a), located along the fault zone illustrated a coseismic decrease of approximately 1 m. Similar to station WS (Fig. 14c) along the Wu River, the gauge showed no recovery and the stream remained at 1 m lower for at least two months.

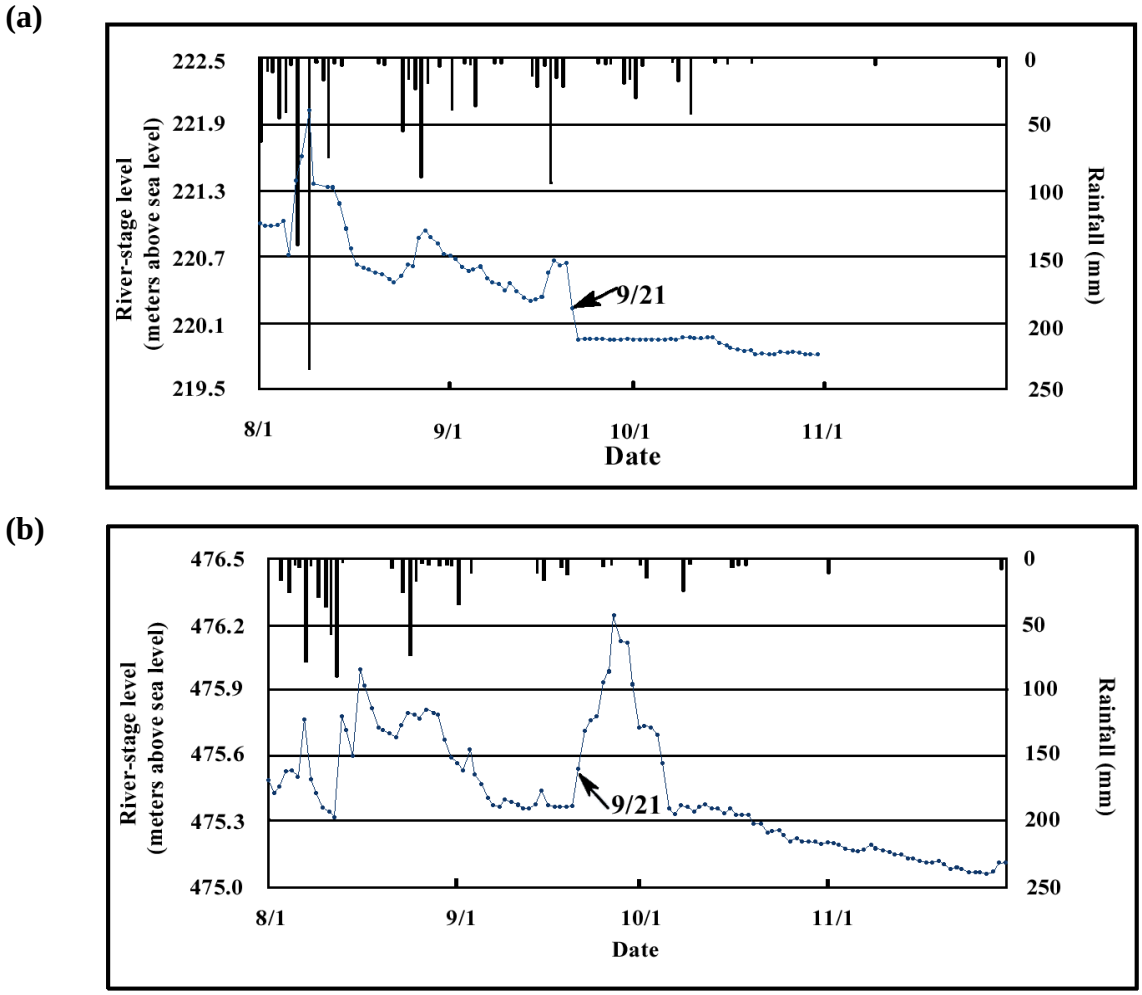

Figure 16. Pre- to post-seismic surface (river) water level changes observed at monitoring stations TT (a) and NMP (b) along the Choshui River (as shown on Fig. 11). The arrow marks the Chi-Chi earthquake (modified after Water Resource Bureau of Taiwan, 2000).

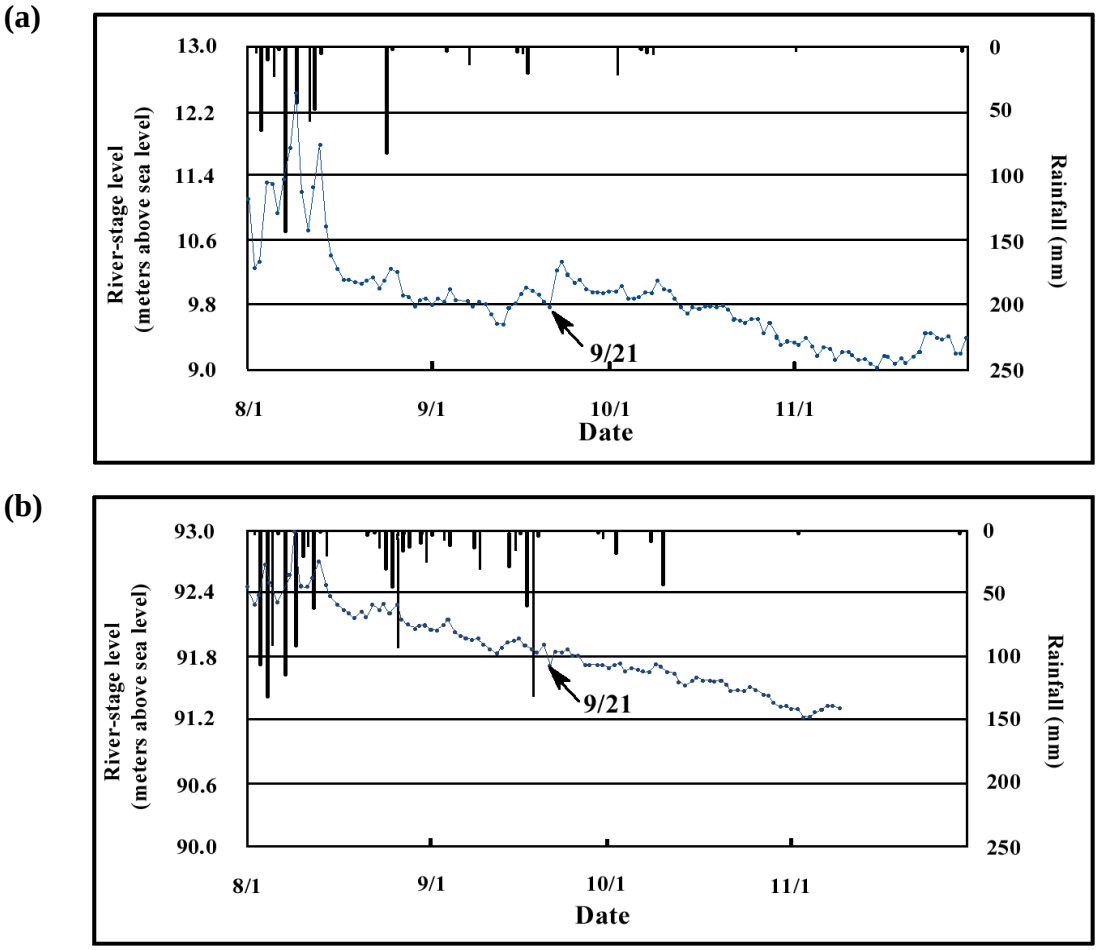

Figure 17. Pre- to post-seismic surface (river) water level changes observed at monitoring stations TC (a) and CY (b) along the Choshui River (as shown on Fig. 11). The arrow marks the Chi-Chi earthquake (modified after Water Resource Bureau of Taiwan, 2000).

Theory of Poroelasticty

Poroelasticity is a continuum theory for the analysis of a porous media consisting of an elastic matrix containing interconnected fluid-saturated pores (Wang and Anderson, 1982). The theory states that when a porous medium is subjected to an applied stress, the resulting deformation causes volumetric changes in the pores. Because the pores are fluid-filled, the presence of the fluid not only acts to make the material more rigid, but also leads to the flow of pore-fluids between regions of elevated and decreased pressure. Fluid flow is found to occur in order to dissipate the excess pore-pressure. Biot (1941) founded the theory of poroelasticity on two linear constitutive equations: (1) changes in applied stress and pore-pressure produce a fractional volume change and (2) changes in applied stress and pore-pressure require fluid to be added or removed from storage.

Solid-to-fluid coupling occurs when a change in applied stress produces a change in volumetric strain and fluid pressure. In this research, crustal strain generated by Coulomb stress changes following large magnitude earthquakes forms the basis for inducing pore-pressure change. Pore-pressure is defined as the pressure of the fluid occupying the pore space. Generally, the pore-pressure initial condition for poroelastic problems is often based on an equilibrium applied boundary load (e.g., hydrostatic condition), which induces the starting distribution of pore-pressure. Due to the complex nature of fault kinematics and rupture, these applied stresses are non-uniform in distribution and thus lead to intrinsically complex spatial variations in pore-pressure distribution. Scientifically important to this concept is that a non-uniform pore-pressure distribution will lead to fluid flow through the geologic media (Wang and Anderson, 1982).

The magnitude of the solid-to-fluid coupling depends largely on the compressibility of the geologic framework, the fluid compressibility, and the porosity of the media. Compressibility (α in 1/Pa), in this sense, is the resistance of volume change in a geologic media to an applied stress while pore-pressure is held constant. When considering a poroelastic problem, the compressibility of the pore, the compressibility of the grains, and the compressibility of the fluid occupying the pore-spaces should be defined (Wang and Anderson, 1982). A highly compressible skeletal framework will lead to larger reduction in pore volume and thus impart more stress upon the fluids occupying the pores. More compressible fluids will result in more significant volumetric changes of the pore-fluids. Thus, the volumetric response of the framework and pore-fluids could instigate a migratory diffusion of fluids in or out of the pores.

Specific storage, S_s (L^{-1}), also known as the elastic storage coefficient, is another important parameter in determining the pore-fluid response to applied stress. Specific storage is defined as the amount of water per unit volume of a saturated formation that is stored or expelled from storage owing to the compressibility of the mineral skeleton and the pore-water per unit change in head. This coefficient links dynamic changes of fluid content in an aquifer to compressibility and pressure change. With increased pressure or hydraulic head, water exerts more pressure on the pore walls and framework grains, causing a volumetric expansion of the pores. Decreases in pressure or hydraulic head will have the opposite effect, leading to a contraction of pore-spaces and an expansion of pore-fluids. The specific storage coefficient will determine how much fluid will be stored or expulsed from each aquifer in relation to the change in pore-pressure for a given

compressibility. Higher specific storage coefficients would indicate that the aquifer is more likely to undergo a drastic change in fluid volume.

Skempton's coefficient (*B*) relates the ratio of induced pore-pressure change to change in applied stress. Specifically, it is a measure of how the applied stress is distributed between the skeletal framework and the fluids. A value for pore-pressure can be obtained by multiplying the Skempton's coefficient by the applied stress. Skempton's coefficient varies between zero and one, with more compressible materials (e.g., clay) being closer to one and uncompressible materials estimated to be zero. Therefore, scientists generally regard a Skempton's coefficient of one to correspond to a completely fluid supported load and Skempton's coefficient of zero to correspond to a gas supported load.

The hydraulic conductivity *K* (m/d) of the sediments plays a major role in determining the rate of pore-pressure diffusion and fluid flow. Hydraulic conductivity is directly proportional to the density of the fluid and inversely proportional the viscosity of the fluid. The conductivity of the material also depends upon the intrinsic permeability k (m^2 or darcy) of the geologic media. Permeability is the measure of the geometry and size of the pore structure. The more well connected the pores, the greater the hydraulic conductivity. It can be assumed that higher values of hydraulic conductivity would correspond to faster diffusion rates, because the fluid flow can proceed with less restriction. Thus, groundwater should recover back to steady-state with higher values of conductivity.

Generally speaking, the linear poroelastic response to coseismic volumetric deformation can be constrained to three material constants: (1) bulk modulus, (2)

poroelastic expansion coefficient, and (3) specific storage. The bulk modulus (Pa) for each geologic material is the resistance to uniform compression. It is defined as the pressure increase needed to cause a given relative decrease in volume. The poroelastic expansion coefficient (1/L) is opposite to the bulk modulus in that it is the materials susceptibility to undergoing expansion. Specific storage dictates the relationship between pore-fluid volume to induced pressure. The first two constants govern the amount of volumetric deformation a material will experience due to an applied stress. The last constant implies how much fluid will be stored or expulsed due to pressure changes. Together, these material constants can be used to derive other parameters such as compressibility.

Objectives and Research Significance

The extensive hydrologic and ground-motion data gathered from the 1999 Chi-Chi earthquake presents an opportunity to examine the plausible mechanisms proposed to explain observed earthquake-induced hydrologic anomalies. The objectives of this research are: (1) to test the newly developed 3-D pore-pressure diffusion code (PFLOW), (2) to examine the mechanisms using Coulomb 3.1™ and PFLOW in one-way coupling for exploring the observed anomalies created by the Chi-Chi earthquake, and (3) using PFLOW to examine the importance of hydraulic conductivity (K) in dissipating induced excess pore-pressures resulting from the earthquake.

The results of this study could shed light and provide a better understanding of the dynamic relationship between volumetric strain and induced pore pressure diffusion in seismic zones and furthermore could help researchers understand: (1) predicting the effects induced fluid flow can have on solute and hazardous pollutant transport, (2) determining good locations for the storage of hazardous material, (3) the ability of pore pressure diffusion to trigger earthquakes or inhibit them, and (4) discovering the role of pore fluids in aftershock temporal and spatial distribution.

In addition to providing valuable insight as to how coseismic deformation and resulting changes in pore pressure can account for hydrological variations observed

during strong earthquakes, this research will result in a new tool for exploring pore-pressure development and dissipation as a function of time.

Methodology

Observed Field Data

For this study, hydrologic data from 1999 to 2004 were acquired from the Water Resources Bureau of Taiwan. A dense network of 73 hydrologic stations, along with 188 individual monitoring wells, was installed within the Choshui River alluvial fan beginning in 1992 (Chia et al., 2001). Each monitoring station is equipped with one to five wells, ranging in depth from 14 to 300 meters. The monitoring stations provide good spatial coverage for investigating the hydrologic response of the alluvial fan to the crustal deformation generated from the Chi-Chi earthquake; the stations range from within 2 km of the fault zone to over 50 km from the fault zone near the coastal areas. These wells provide a complete hourly record of the coseismic and post-seismic responses of the major aquifers located in the Choshui river alluvial fan. Discharge data (stream level) gathered from gauging stations (Water Resources Bureau of Taiwan, 2002) along the Ta' ang, Wu, and Choshui Rivers provide added insight into coseismic and post-seismic hydrologic responses.

Water-Table Data Analysis

This research project focuses solely on the F2 aquifer response because it showed the most pronounced response to the earthquake among four major aquifers in the alluvial fan. Due to its confined condition, the F2 aquifer maintained changes longer, providing the best opportunity to study the diffusion of excess pore pressures.

The analysis followed the previously described divisions of the alluvial fan: (1) proximal, (2) middle, and (3) distal (Fig. 4). The proximal zone extends 10 km westward from the Chelungpu fault and encompasses the slope and upper fan regions. The middle fan extends westward from the proximal zone for 20 km and is comprised of upper fan and middle fan lithologies as described by Lai et al. (2004). The distal fan extends approximately another 20 km westward from the middle fan until it reaches the Taiwan Strait. Water-table data for this study were organized based upon distance from the Chelungpu fault in the alluvial fan (i.e. proximal, etc). Data were plotted as graphs to show the temporal evolution of the water column at each location.

Coseismic piezometric well readings were used to test pore-pressure diffusion from coseismic volumetric strain as a mechanism for generating the observed hydrologic anomalies. In the coseismic volumetric strain hypothesis, the calculated resultant strain generated from the Chelungpu fault rupture should dictate the style of aquifer response immediately following the event. Specifically, if the wells are in areas of compressional strain, then the pore-fluids should be expulsed due to a reduction in net pore volume. This would lead to elevated piezometric readings following the earthquake. If the wells are in

areas of dilatation, then pore-fluids would be drawn in due to an increase in pore volume and correspond to lower piezometric readings.

Post-Seismic Water-Table Analysis

A 100-day time-series was prepared for each obtained monitoring well (Appendices A to C). These time-series plots were prepared in Microsoft® Excel® and grouped based upon proximity to the fault zone. Well data were then analyzed to determine whether or not proximity to the fault zone or local geology plays a role in fluid diffusion processes. Lastly, the observed water level recovery pattern for well JL was compared with the modeled diffusion pattern (assuming pre-earthquake hydraulic conductivity values) for well JL. The program, 3PFLOW (Lee and Wolf, 1998) was used to model the recovery of well JL with pre-seismic hydraulic conductivity values (K). This analysis tested whether the permeability of the sediments was permanently or temporarily altered by the earthquake. Themis-match between calculated and observed diffusion rates would suggest the possibility that the hydraulic properties of the sediments were changed permanently due to the propagation of seismic waves following the earthquake.

The post-seismic response or diffusion patterns of the piezometric readings also provide a test of the pore-pressure diffusion model. Regardless of the well response, whether the water table rises or falls, there should be a return of the well reading back to a steady-state condition, if no permanent deformation has taken place. If coseismic volumetric strain is the only mechanism responsible for the observed hydrologic anomalies pore fluids should diffuse back to a pre-earthquake level over time. Thus, if the piezometric reading showed an increase, the water-table should show a relatively smooth

recovery back to a base-line, re-established the height of the water-table before fault rupture occurred. Conversely, if the piezometric reading showed a decrease in water-table, then there should be a smooth and continuous rise back to steady-state elevation.

Stream Discharge Analysis

Stream discharge data from the Choshui River alluvial fan, slope, and Western Foothills were used to test the volumetric strain hypothesis. Total stream discharge in most areas is the composite of contributions by surface flow and base-flow. Surface flow is the contribution made by surface runoff due to precipitation events or snowmelt at higher elevations through a drainage basin, whereas base flow is dominated by the contribution of the groundwater discharge into the streams. The mountainous regions in the foothills of Taiwan, where most streams have their headwaters, consist of mainly consolidated sedimentary rocks. As Muir-Wood and King (1993) proposed, the strain generated by fault rupture can initiate pore volume reduction or expansion dependent upon the strain regime. For consolidated regions, this strain could either open up fractures or close them. In thrust faulting, such as in the Chi-Chi earthquake, the pore spaces and fractures close up during interseismic periods due to buildup of stresses. During rupture these fractures can open up providing conduits for groundwater to flow. Therefore, if an induced hydraulic gradient is created by the strain regime, or permeability along flow path is enhanced by seismic fracturing, groundwater can flow from mountains towards lower elevations. This would result in a significant increase in base-level contribution and a resultant increase in stream discharge.

Stream gauge readings from three rivers in the alluvial fan, slope, and Western Foothills regions were used. The nature of the coseismic responses and post-seismic recoveries are used in conjunction with water-table data to shed light on whether or not coseismic strain is responsible for invoking the hydrologic change.

Numerical Modeling

Numerical modeling was used to investigate the poroelastic response of the Choshui River alluvial fan to crustal deformation generated by the Chi-Chi earthquake. This study makes use of a published finite fault rupture model (Ji et al., 2005) for 3D strain modeling, thus expanding on the model developed by Baird (2002). This finite fault rupture model has been carefully calibrated to match field observations and slip kinematics. Coulomb 3.1™, a Coulomb stress change/deformation modeling program (Toda et al., 2005), was used to perform the 3D strain modeling. The program writes an output file of resultant coseismic strain values and also provides graphic output for the calculated strain fields. The strain values calculated from the deformation code are used as an initial disturbance in the poroelastic medium. PFLOW, a 3D, finite-element pore-pressure diffusion model, was then used to calculate the resultant coseismic pore-pressure response and diffusion pattern over a specified time frame.

Coulomb 3.1™ Strain Modeling

Coulomb 3.1™ is a Matlab-based deformation modeling program that makes use of finite fault rupture models to calculate Coulomb stress changes or strain resulting from fault dislocation (Lin and Stein, 2004). The program converts elastic dislocation and

crustal deformation values to strain, and results can be compared with seismograms and GPS data.

A carefully calibrated finite fault rupture model provides the basis for accurate strain modeling. Recent advances in technology have resulted in the development of geodetic observational tools. These tools range from satellite-derived GPS devices to regional and global scale seismic monitoring stations equipped with broadband digital strong motion stations. Researchers combine static GPS measurements with strong motion data sets and teleseismic P-waves to model the complexities inherent in fault dislocation. GPS stations provide the location and displacement measurements generated by the fault rupture, while seismic stations provide the arrival times for the passing seismic waves. The seismic data can be used to help define the temporal evolution of the fault rupture (Ji et al., 2005). Teleseismic P-waves are often used to test the validity of the model in replicating the release in energy required to produce the observed dislocation fields.

Explanation and Application of Finite Fault Models

Elastic dislocation theory present faults as discontinuities or dislocations in an otherwise perfectly continuous elastic medium (Okada, 1992). Specifically, faults are represented as surfaces across which there is defined to be a discontinuity in the elastic displacement field. The surrounding medium can be modeled as a uniform elastic half-space with boundary conditions of zero normal and shear tractions at the free surface and zero displacement at an infinite distance from any dislocation or as a more detailed layered earth half-space model which incorporates more realistic geologic heterogeneities

into the surrounding elastic medium. Okada's (1992) formulation expresses the displacement field generated by rupture at any given point as a function of fault locations, dimension, geometry, slip and the elastic constraints (Healy et al., 2004).

Fault Parameters and Input File

Coulomb input files are constructed from parameters grouped into three different sections. The first section includes (1) source data, (2) elastic parameters, (3) friction coefficient, and (4) regional stress tensors. Specifically, this section provides parameters and constraints for an elastic half-space medium. Two elastic parameters are added to the input file: (1) Poisson's ratio and (2) Young's Modulus. Poisson's ratio (ν) is an elastic constant that gives the relationship between contraction and extension of a geologic material and is given by $\nu = -\varepsilon_1/\varepsilon_3$, where ε_1 is the strain in the principle stress direction and ε_3 are the strains in mutually orthogonal directions. Young's Modulus (E) relates the ratio of tensional stress to the resulting tensional strain. It is given by $E = \sigma/\varepsilon$, where σ is the applied stress and ε is the resulting strain. These two values show how the elastic medium will deform when rupture occurs. The coefficient of friction, along with compressive normal stress, determines how easily fault motion will be achieved. Higher coefficients of friction require more frictional force and result in lower displacements. Regional stress tensor information gives the directions of principle stresses acting upon the source faults.

The second section of the Coulomb input file provides: (1) fault geometry, (2) source fault positions and slip, and (3) grid information. This section contains the necessary source or receiver fault parameters for modeling. The model geometry consists

of the x and y locations at which calculations are made and the grid information in which the calculations proceed. Also included are dip angles and slip sense for each point listed in the input file.

The third section of the input file provides: (1) graphical representation parameters and (2) plotting parameters. Grid parameters constrain the size of the modeled area with regards to two dimensions and also control the increment of size for each grid. Size parameters control the size of the graphic output. Shade and color parameters control the increment for dilatation and stress values, and exaggeration parameters control the values for displacement, distorted grid, and slip line. Cross-section parameters control the size and increments for any cross-sections run in Coulomb.

Earthquakes occur as a result of localized stress concentrations at suitably oriented anisotropies (Lin and Stein, 2004). Fault rupture occurs when the accumulation of stress exceeds the yield point. Within the modeling process there are two important types of faults mentioned: (1) source fault(s) and (2) receiver fault(s). Source faults are those faults that have slip components and impart stress on the surrounding region; in this case the Chelungpu fault serves as the source. Receiver faults are those faults that do not slip and receive stress from the source rupture. They can be moved closer to or further away from failure by the changes in Coulomb stress.

Fault Model and Geometry

This study uses the fault model developed by Ji et al. (2005). This fault model uses three planar fault segments to approximate the rupture plane during the Chi-Chi mainshock (Fig 18). Fault 1 is located along the north-south trending Chelungpu fault and

has a strike of N3ºE. Fault 2 is connected to fault 1 in the north and follows along the eastward trending rupture for approximately 13 km with a strike of N80ºE. Fault 3 matches the bend in the surface break at the southern end and has a strike of N45ºE. All of the fault segments have a dip angle of 29º and all fault segments were extended down to a dip width of 17 km (Ma et al., 2005).

To simulate the slip distribution accurately along the fault segments, Ma et al. (2005) divided each fault into smaller rectangular regions of equal area, or subfaults. All of the subfaults have the same dimension of 3.8 x 3.7 km. There are a total of 360 subfaults (Fig. 18); however, not all of them are used to generate the synthetic fault rupture. Because most of the slip attributed to rupture was located to the surface of the "wedge-shaped" block formed at the intersection of fault 1 and 2. Ji et al. (2003) found it a plausible assumption to set the slip amplitudes of the subfaults below the surface of the "wedge-shaped" block to zero. Thus, the actual number of contributing subfaults used in the generation of the synthetic fault rupture is only 324.

Within the modeling process each subfault was allowed to have a slip amplitude ranging from 0 to 24 m. For fault segments 1 and 3 the rake angle was fixed between 0º and 180º to suppress downward slip not observed during the rupture. Fault 2 was allowed to have a rake angle ranging from 0º to 360º because there were some observations of normal faulting and associated downward slip along this segment of the rupture. Average rupture velocity as calculated from the GPS measurements and waveform data, was allowed to vary between 1.5 to 3.0 km s^{-1}.

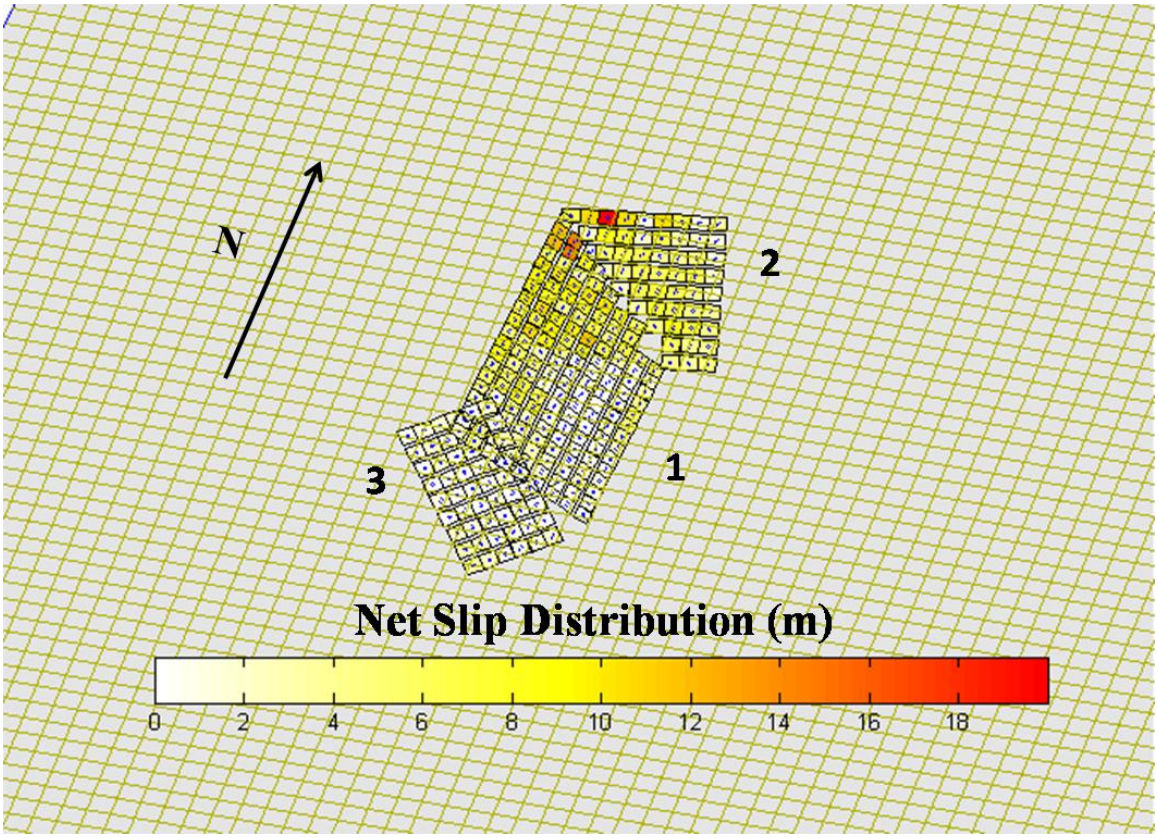

Figure 18. The Chelungpu fault is divided into three segments (1 to 3) to account for the geometry and the slip pattern logged by GPS stations. Slip varied from 0 to 18 m. The largest amounts of slip occurred near the intersection of fault segment 1 and 2. Fault model from Ji et al. (2005).

PFLOW Modeling

Output values of strain calculated from the deformation models provide the initial conditions to relate strain to pore-pressure. Pore-pressure diffusion evolves according to spatial characteristics of the elastic medium and the governing equations. PFLOW fluid pressure modeling results can then be compared to the observed water-level change and stream discharge data to test the coseismic volumetric strain hypothesis. Unique to the PFLOW algorithm is the ability to spatially vary the hydraulic conductivity of the modeled area in three dimensions. This application allows users to explore more realistic heterogeneous geological models.

Input parameters for PFLOW include calculation area and depth, diffusion time, number of time steps, Skempton's coefficient, compressibility, boundary conditions, and hydraulic conductivities of the modeled space. PFLOW calculates the flux gradient and pore-pressure at the time steps specified.

Poroelastic Governing Equations

Systems of partial differential and algebraic equations can be used to describe the relationship between stress (σ), strain (ε), pore pressure (P), and increment of fluid content (ζ) in a deformed porous media (refer to Wang and Anderson, 1982). The following governing equation describes the diffusion of induced excess pore pressure,

$$S_s \frac{\partial P}{\partial t} - \nabla \cdot (\frac{k}{\mu} \nabla P) = Q \qquad (1)$$

where S_s is the hydrogeologic specific storage of rock, k is the permeability, μ is the viscosity, and Q is a fluid source term, as induced by seismic faulting.

PFLOW was developed to investigate the first-order evolution of pore-pressure changes induced by changes in Coulomb stress and their possible relation to water-level changes in wells or changes in stream discharge. It utilizes linear or quadratic finite elements for spatial discretization and first or second order, explicit or implicit finite difference discretization in time.

PFLOW uses finite difference discretization to evaluate the pressure at each node with respect to time. After temporal discretization is performed the equation which solves for pressure becomes a semi-discrete (discrete in time, continuous in space) formulation

$$S_\sigma \frac{P^{n+1} - P^n}{\Delta t} - \theta \nabla \cdot \left(\frac{k}{\mu} \nabla P^{n+1}\right) = \theta Q^{n+1} + (1-\theta)\mathrm{Q}^{\mathrm{n}} + (1-\theta)\nabla \cdot (\frac{\mathrm{k}}{\mu}\nabla \mathrm{P}^{\mathrm{n}}) \quad (2)$$

where the superscript n represents the discrete time level at which the function is evaluated and Δt is the specified time step. The parameter θ determines the type of discretization. For $\theta = 0$, the discretization is an explicit first-order (known as a forward Euler). Explicit discretization relies on previous time steps to calculate future ones. Specifically, use of the explicit scheme implies that the values of the space derivatives at the old time level (n) is the best approximation for the future time step. For $\theta = 1$, the discretization is an implicit first order (known as a backward Euler). Implicit discretization is not expressed explicitly in terms of known quantities and requires that pressure at the future time level be obtained as the solution of a system of linear equation. The space derivatives are thus approximated at the advanced time level (n+1) and it is assumed that value of the space derivative at the future time is the best approximation.

The use of $\theta = ½$, it is presumed that the best value lies halfway between time levels (n) and (n+1). This is termed the Crank-Nicolson method and it is an implicit second-order discretization.

After spatial (finite element) discretization, equation (1) becomes a system of linear algebraic equations, with very sparse matrices. Once the initial (coseismic) pressure P^0 caused by faulting is obtained from a deformation modeling program, such as Coulomb, the system can be solved for P^n for n≥1. At each time, the system is solved using a sparse direct solver, a built-in function of Matlab™.

PFLOW offers a tool to explore how changes in Coulomb stress can influence pore-pressure through time following an earthquake. Coulomb stress transfer (ΔCFS) can be caused by fault rupture and can have significant impact on the fault zone region. It is defined as

$$\Delta CFS = \Delta\sigma_s + m(\Delta P - \Delta\sigma_n) \tag{3}$$

where $\Delta\sigma_s$ is the change in shear stress, m is the coefficient of friction, ΔP is the change in pore pressure, and $\Delta\sigma_n$ is the change in normal stress. Positive Coulomb stress changes promote failure, whereas negative changes in Coulomb stress discourage failure along a fault. A positive increase in normal stress or a decrease in pore-pressure therefore will lead to negative Coulomb stress change and discourage failure along specified faults.

Stress (σ) can then be related to strain (ε) by Young's modulus. Strain generated by stress leads to net changes in volume of the media. The fractional volume change generated by these fault ruptures can be expressed by the equation

$$\frac{\Delta V}{V} = \varepsilon(1 - 2v) = -\beta\Delta\sigma \tag{4}$$

where ν is Poisson's ratio and β is the bulk compressibility. The strain derived from Coulomb stress will initiate the development of excess pore pressure (overpressure development), pressure gradients, and corresponding flux. In this research (one-way coupling), the pore pressure change is calculated in the main PFLOW driver script by multiplying the calculated stress change by the Skempton's coefficient (B)

$$\Delta P = B\Delta\sigma \tag{5}$$

Since variations in pore-pressure will lead to a net gradient, pore-fluids will flow to alleviate overpressure and restore a steady-state equilibrium condition. The equation that describes fluid flow in a 3D heterogeneous media is described by

$$S_s \frac{\partial h}{\partial t} = \frac{\partial}{\partial x}\left[K_x \frac{\partial h}{\partial x}\right] + \frac{\partial}{\partial y}\left[K_y \frac{\partial h}{\partial y}\right] + \frac{\partial}{\partial z}\left[K_z \frac{\partial h}{\partial z}\right] \tag{6}$$

where K_x, K_y, and K_z are the hydraulic conductivities in the x, y, and z directions, h represents the hydraulic head, and S_s is the specific storage for the aquifer. Therefore, since induced pressure changes will lead to the development of hydraulic gradients and expulsion of fluids out of storage, flow will take in place in three dimensions and be dictated by the hydraulic conductivity in the respective directions. The net pore pressure change over time depends on the magnitudes of the volumetric strain and also the hydraulic conductivity (higher conductivity equals faster diffusion).

Numerical Modeling Results

Introduction

This chapter provides the results of three individual case studies for investigation into the relationship between crustal deformation and pore-pressure changes. The first case study uses a simplified fault model to explore the basic relationships between strain and induced pore-pressure and evolution. Hydraulic conductivity (*K*) values are then changed for each simplified model to determine the effect of the type of geology and hydraulic conductivity (*K*) on pore-pressure evolution with time. Building off these simplified fault models, a second case study is performed to illustrate the pore-pressure response of the pore-fluids within the island of Taiwan in response to the crustal deformation generated by the 1999 Chi-Chi earthquake. In this case study, the finite-fault model of Ji et al. (2005) is used to replicate the dynamic strains and rupture kinematics associated with the large magnitude earthquake. This Chi-Chi case study is divided into two distinct models. The first model is fixed with a homogeneous geology or uniform hydraulic conductivity (*K*), whereas the second model contains a more complex layered geologic medium with spatially varying values of conductivity. A third case study solely targets the poroelastic response of the Choshui River alluvial fan to the crustal deformation generated by the earthquake. This study involves the most complexly layered geologic media and was modeled off of the stratigraphy presented by Lai et al.

(2004). The modeled results for the Choshui River alluvial fan and the island of Taiwan as a whole form the basis for comparison with the observed hydrologic changes.

Case Study 1: Simplified Right-Lateral Strike-Slip Fault

The simplified strike-slip fault was constructed using Coulomb 3.1™. The fault plane trends due north for 30 km and has a homogenous slip of 3 m (i.e., strain = 1.0×10^{-4}). Rupture occurs with a pure strike-slip motion. The fault plane dips 90° and downwards to a depth of 10 km. Poisson's ratio (ν) was specified to be 0.25 and the Young's Modulus set to 8×10^5 bars. The coefficient of friction was set to 0.4, meaning that the fault plane contains some fluid lubrication.

Modeling of this simplified right-lateral fault rupture shows a distinct four-lobe strain pattern (Fig. 19). Generally, compressional strain (blue zones) occurred in the direction of fault slip, whereas opposite to the sense of slip, positive dilatational strain occurred (red zones). Near the northern fault tip, maximum compressional strain develops (-1.0×10^{-4}). Similarly, at the southern fault tip maximum dilatational strain occurs (1.0×10^{-4}). Away from these localized zones, the strain field diminishes.

Two cross-sections constructed for the modeled area perpendicular to the fault plane down to a depth of 10 km are shown in Figure 19. The first cross-section transverses 3 km north of the northern fault tip and extends west to east for 32 km. This section shows that west of the fault plane, compressional strain occurs. Conversely to the east of the fault plane, dilatational strain occurs. At the center of the cross-section, a zone of compressional strain is found. This zone correlates well to the compressional zone near the fault tip in the plane view strain map. The second cross-section transverses 3 km

south of the southern fault tip and extends west to east for 32 km. This section shows that to the west of the fault plane, dilatational strain occurs. To the east of the fault plane, compressional strain occurs. At the center of the cross-section, a zone of dilatational strain occurs. This zone corresponds to the zone of maximum dilatational strain, found on the plane view strain map.

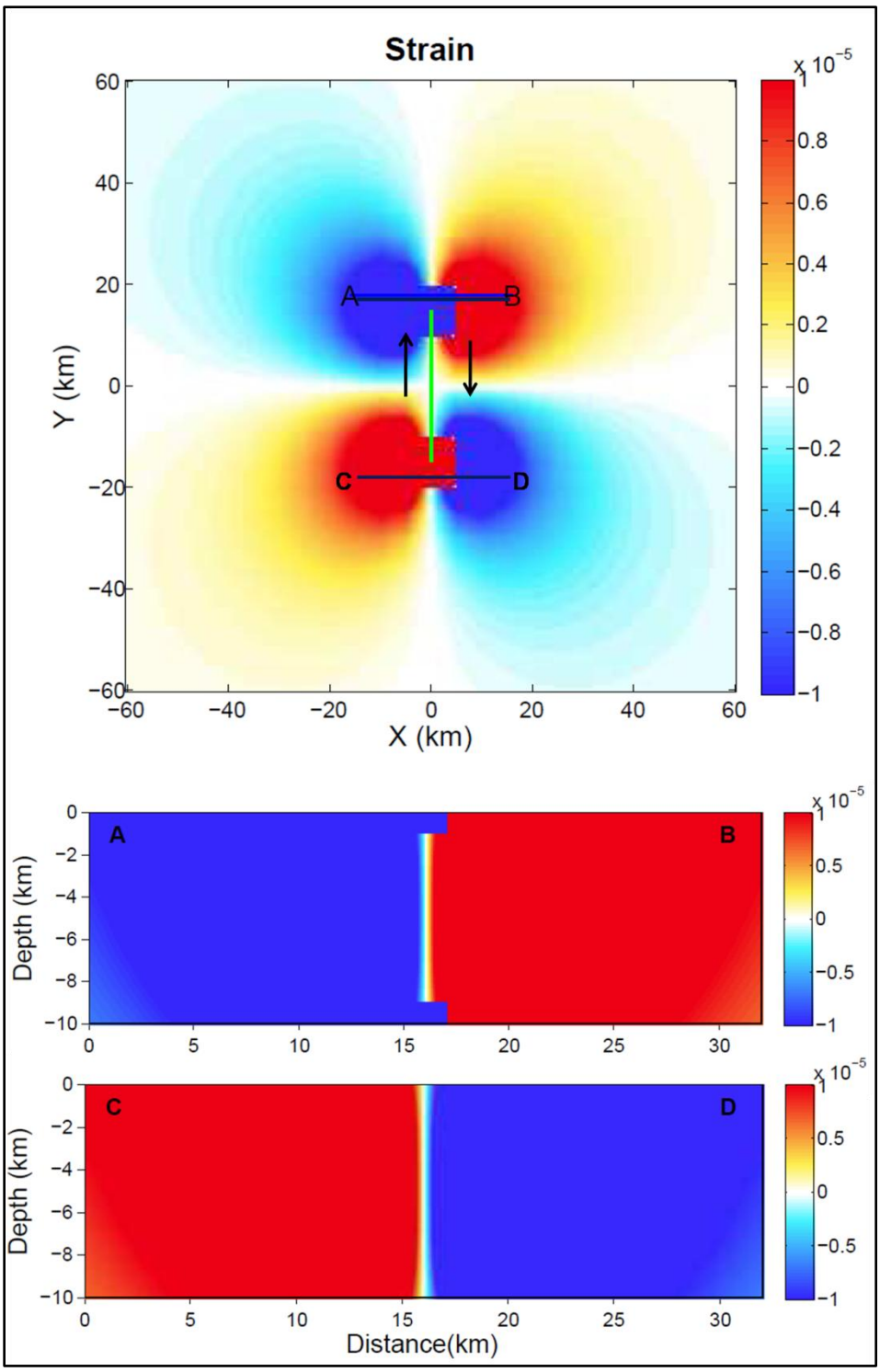

Figure 19. (top) Plane view strain map shows that zones of compressional (blue) and dilatational (red) strain develop along a right-lateral strike-slip fault (green). (bottom) Cross-sections show the resultant strain field calculated at the northern and southern fault tips. Black arrows indicate sense of motion.

Pore-Pressure Response to Simplified Right-lateral strike-slip faultt

Coupled coseismic pore-pressure modeling mimics the calculated strain pattern observed for this simplified right-lateral strike-slip fault, but opposite in sign (Fig. 20). Two coseismic pressure figures were generated for the right-lateral strike-slip model (Figs. 20 and 21). Maximum induced excess and decreased pore-pressure changes reached 5.0×10^7 Pa and -5.0×10^7 Pa respectively. These values correlate well with localized zones of maximum strain ($+/- 1.0 \times 10^4$) located near the fault tips (Fig. 19). In contrast, Figure 20 shows that the four-lobed coseismic pressure field generated farther away from the fault tips reaches maximum magnitudes of 10^5 Pa and -10^5 Pa. Thus, there is a contrast of two orders of magnitude between the induced pressure fields located near the fault tips, and those within the four lobes away from the fault.

Two pore-pressure diffusion models were generated for the right-lateral strike-slip fault. The first model has a homogeneous hydraulic conductivity value of 3×10^{-4} m/d and boundary conditions were set so that flow could only be achieved through the surface (elevation = 0 m). By not spatially varying hydraulic conductivity, the model space assumes a constant geology. In this case, a hydraulic conductivity of 3×10^{-4} m/d is consistent with that of a sandstone.

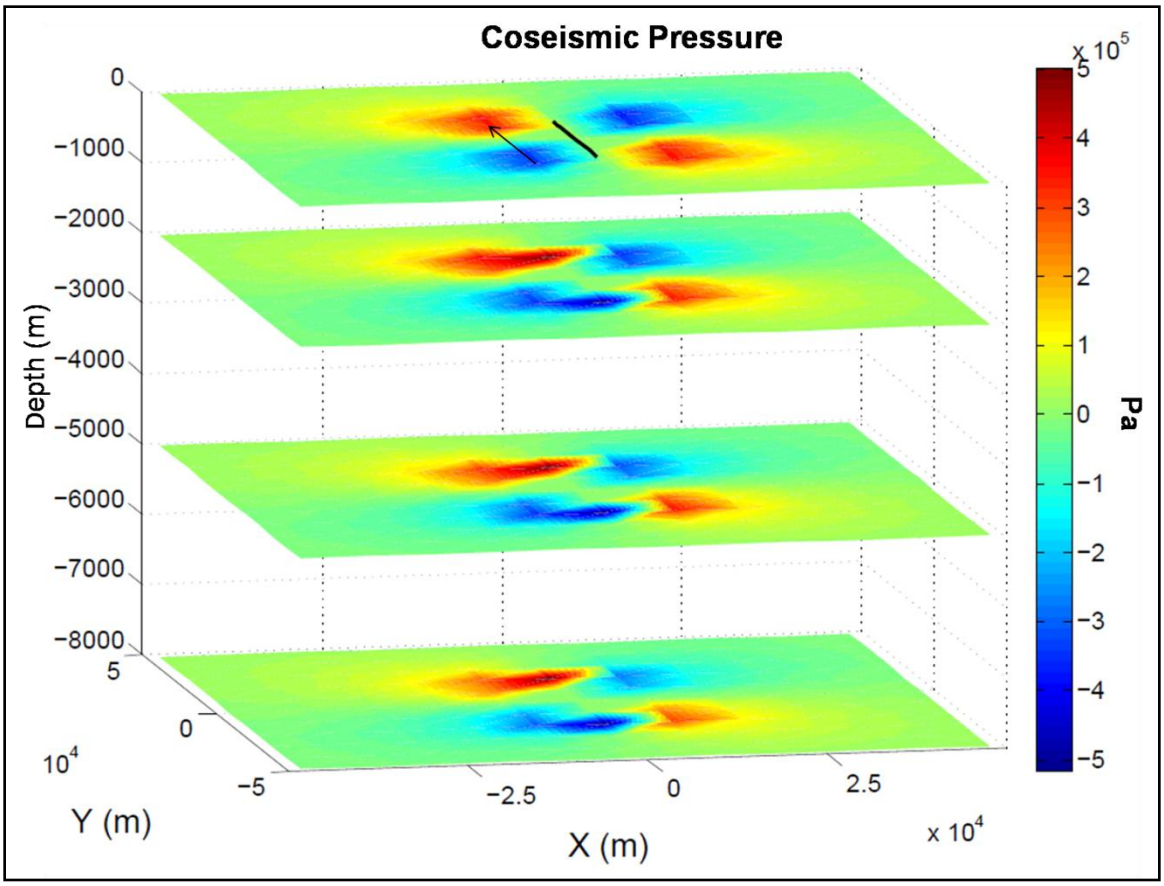

Figure 20. Coseismic pore-pressure field for simplified right-lateral strike-slip fault. Excess pore-pressure developed in the direction of fault slip (red). Under-pressure developed opposite the sense of fault motion (blue). Black arrow indicates fault motion.

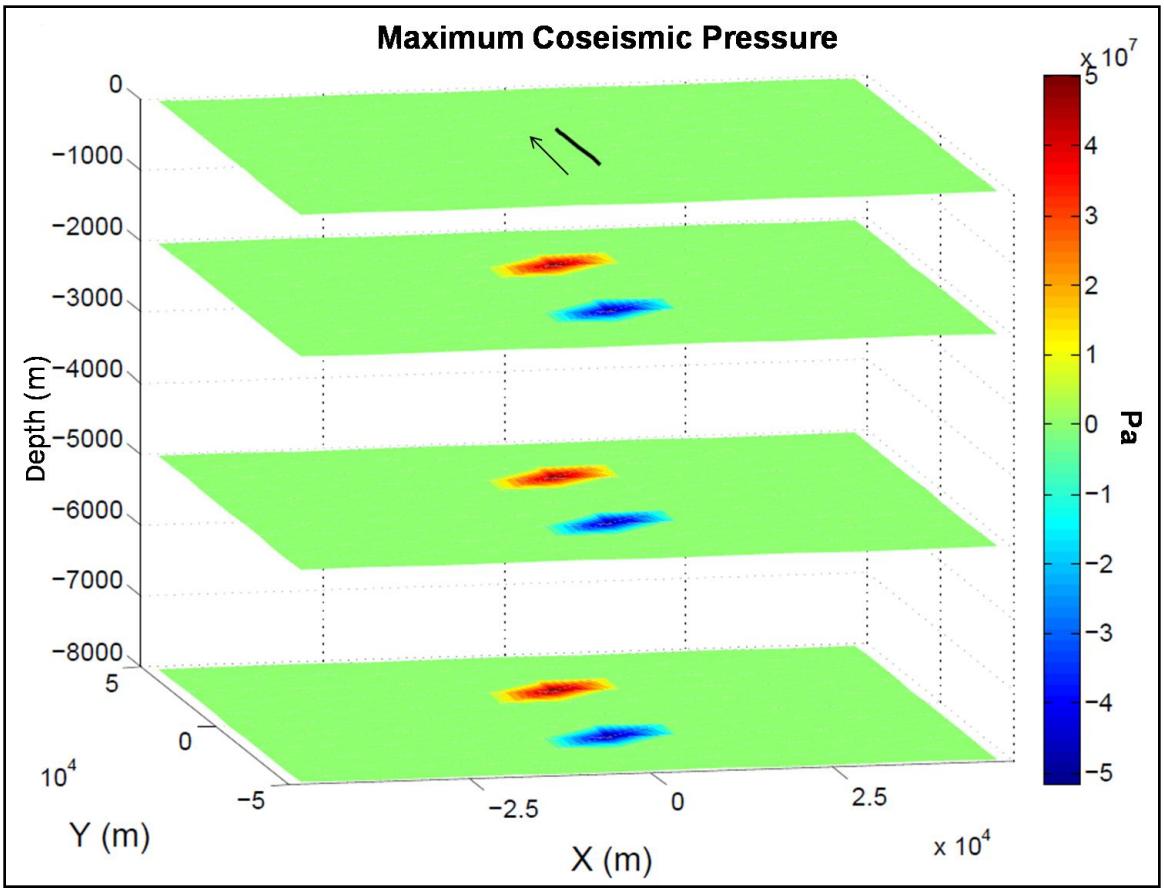

Figure 21. Coseismic pore-pressure map illustrating only? zones where maximum pore-pressure developed. Near the northern fault tip, maximum excess pore-pressure developed. Near the southern fault tip, maximum under-pressure developed. These zones are two orders of magnitude greater the rest of the pressure field (Fig. 15). Black arrow indicates sense of motion.

After a time window of 1 day, the diffusion model changes distinctly. Instead of the expected gradual diffusion of the four-lobes back towards pre-seismic conditions, the modeled pattern shows that the northern half of the grid is dominated by induced excess pressure. Conversely, the southern half of the grid is dominated by underpressure (Fig. 22). Modeling shows that maximum overpressure and underpressure zones remain localized near the fault tips (+/-1.0 x 10^6 Pa). In the northern half of the grid, excess pore-pressure zones surrounding the fault tip reaches a maximum of 5.0 x 10^5. Similarly, in the southern half, maximum underpressure surrounding the southern fault tip is maintained around -5.0 x 10^5 Pa.

In this case-study, modeling results suggest that the zones of maximum pressure change near the fault tips dictate the corresponding diffusion pattern. Large differences of excess pressure establish high pressure gradients in the northern and southern segments, which control the direction of flow and resulting pore pressure pattern (Fig. 23). These strong gradients reduce diffusion from taking place in a north to south direction in large areas away from the fault. The pressure gradient established between the northern maximum excess pressure zone and the adjacent zone of under-pressure (to the east) is 3.33 x 10^6 Pa/km. Comparing this to the pressure gradient calculated between the zones of excess pressure and under-pressure east of the fault (3.33 x 10^3 Pa/km), it can be deduced that groundwater will flow in the direction of maximum gradient. Similarly, the pore-pressure front will migrate in the direction of maximum gradient. Therefore, the modeled pattern to the north is linked to the node of maximum overpressure near the fault tip. Initially the northeast quadrant is dominated by underpressure or decreased pore pressure (Fig. 20). Very quickly over-pressure spreads to the northeast quadrant (Fig. 22)

as fluid flow and the migrating pressure-front move down gradient. In the south, groundwater flow and the pressure gradient is dictated by the maximum underpressure near the southern fault tip. Overpressure in the southeast quadrant dissipates quickly and drops below pre-seismic condition as water there moves quickly toward the underpressure center.

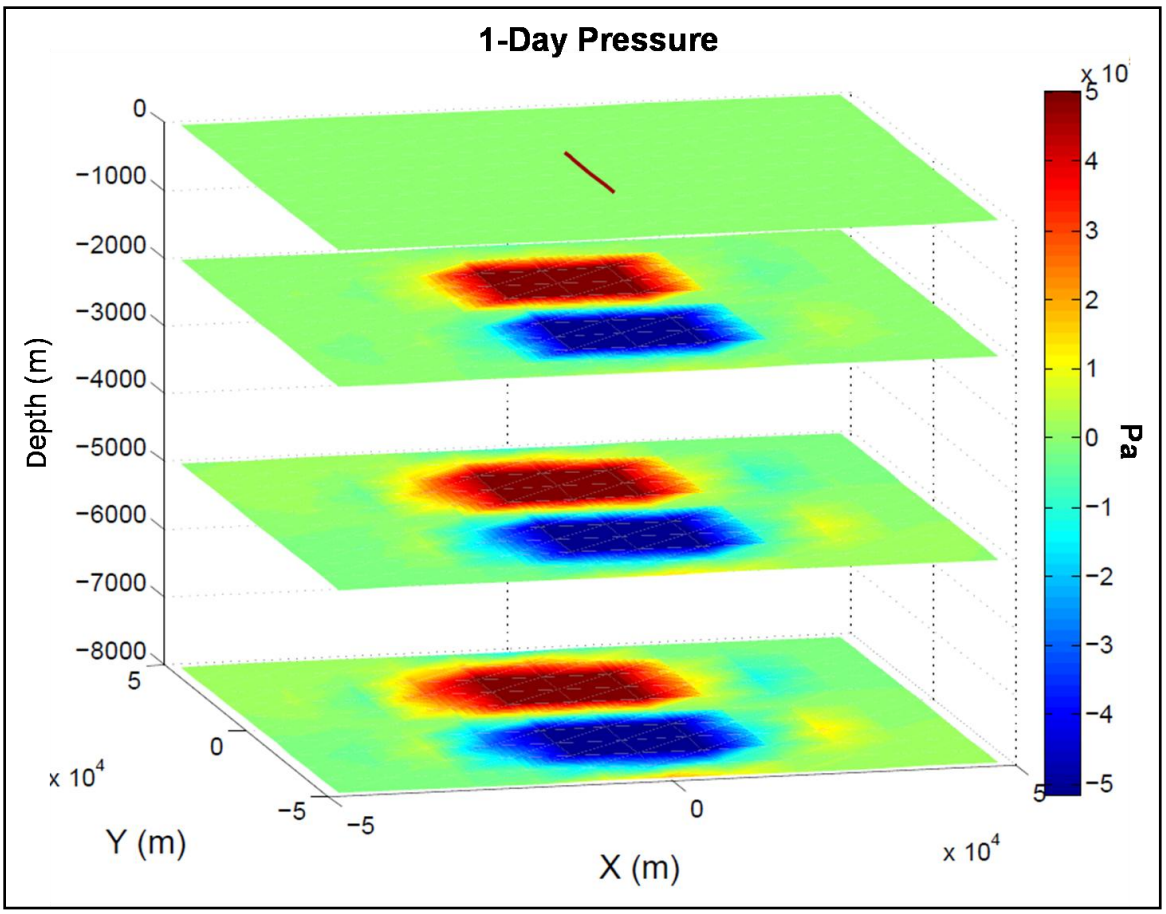

Figure 22. 1-day pressure map shows that the northern section of the grid is dominated by excess pressure and the southern section is dominated by under-pressure. Zones of maximum pressure dominate the diffusion pattern.

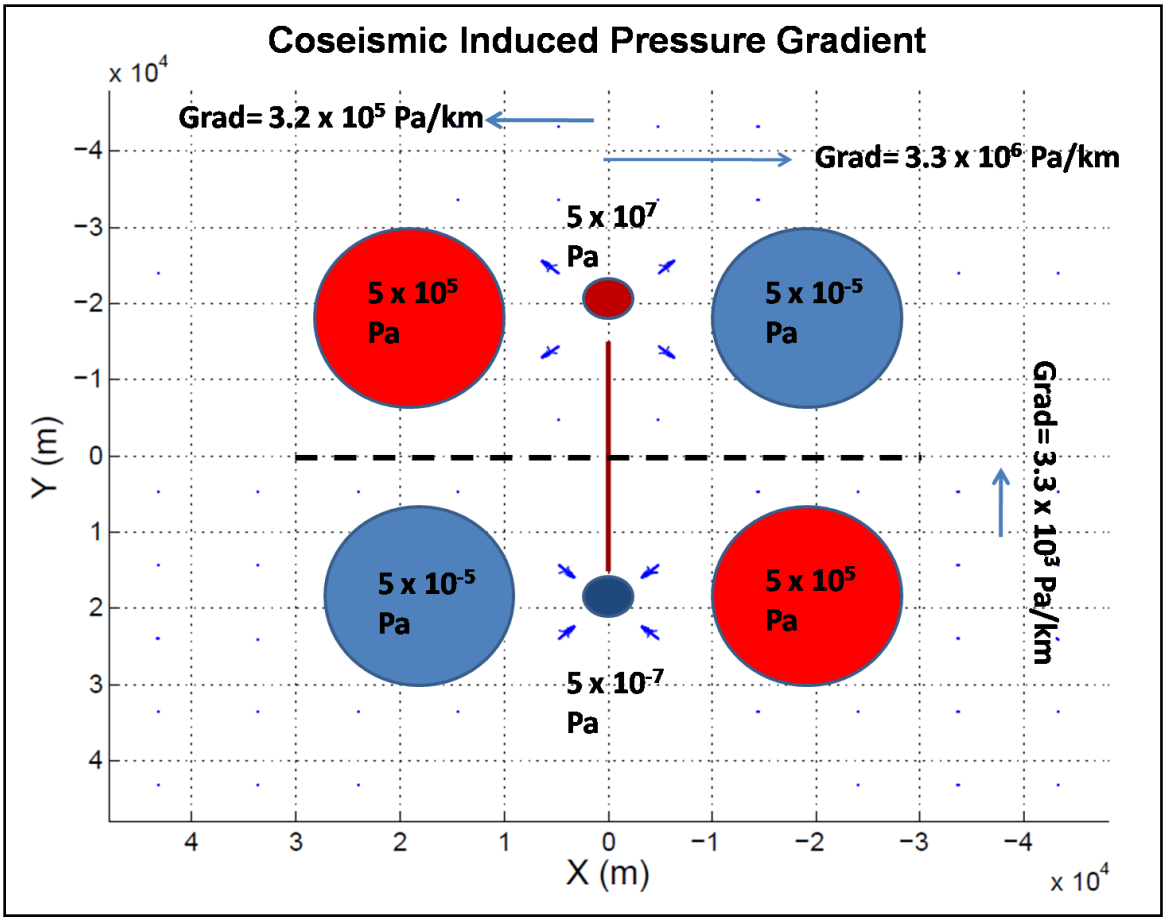

Figure 23. Coseismic pressure gradient field shows that the zones of maximum pressure (near fault tips) dictate the diffusion pattern. Gradients are orders of magnitude greater in an east to west direction than in a north to south direction. Thus the pressure-front and pore fluids migrate in the direction of maximum gradient. Dotted black-line indicates no-flux. Large gradients also exist between the zones of maximum overpressure and underpressure near the fault tips. Arrows indicate gradient.

After 10 days (Fig. 24), the pore-pressure pattern and distribution remain similar to that of the 1-Day pattern, but are smaller in magnitude. Maximum zones of overpressure exist to the north at depth, but have been dissipated to 5.0×10^{3} Pa. Similarly, maximum zones of underpressure exist to the south with depth, but have been reduced to 5.0×10^{-3} Pa. In the upper 2 km, overpressure has further diminished to 1.0×10^{3} Pa, while under-pressure had dissipated to -1.0×10^{3} Pa. The east-west pressure gradient established by the induced coseismic pressure field has reduced pressure changes by two orders of magnitude. Large north-south gradients exist between the zones of maximum overpressure and underpressure near the fault tips. Flow from north fault tip toward south fault tip allows continuous dissipation of excess and decreased pore pressure.

After 20 days (Fig. 25), the pore-pressure pattern still resembles that of the Day 1 pattern. However, maximum values of pore-pressure change have been reduced by over 99%. At depth, overpressure is present, but only reaches a maximum of 5 Pa. Under-pressured zones show a similar pattern,existing to a greater extent at depth, but only to a maximum of -5 Pa. In the upper 2 km, overpressure and underpressure has been reduced to 2 Pa and -2 Pa, respectively. Thus, a homogeneous hydraulic conductivity (K) of 3.0×10^{-4} m/d dissipates the maximum pressure changes ($+/- 5.0 \times 10^{7}$ Pa) associated with the right-lateral strike-slip rupture within 20 days.

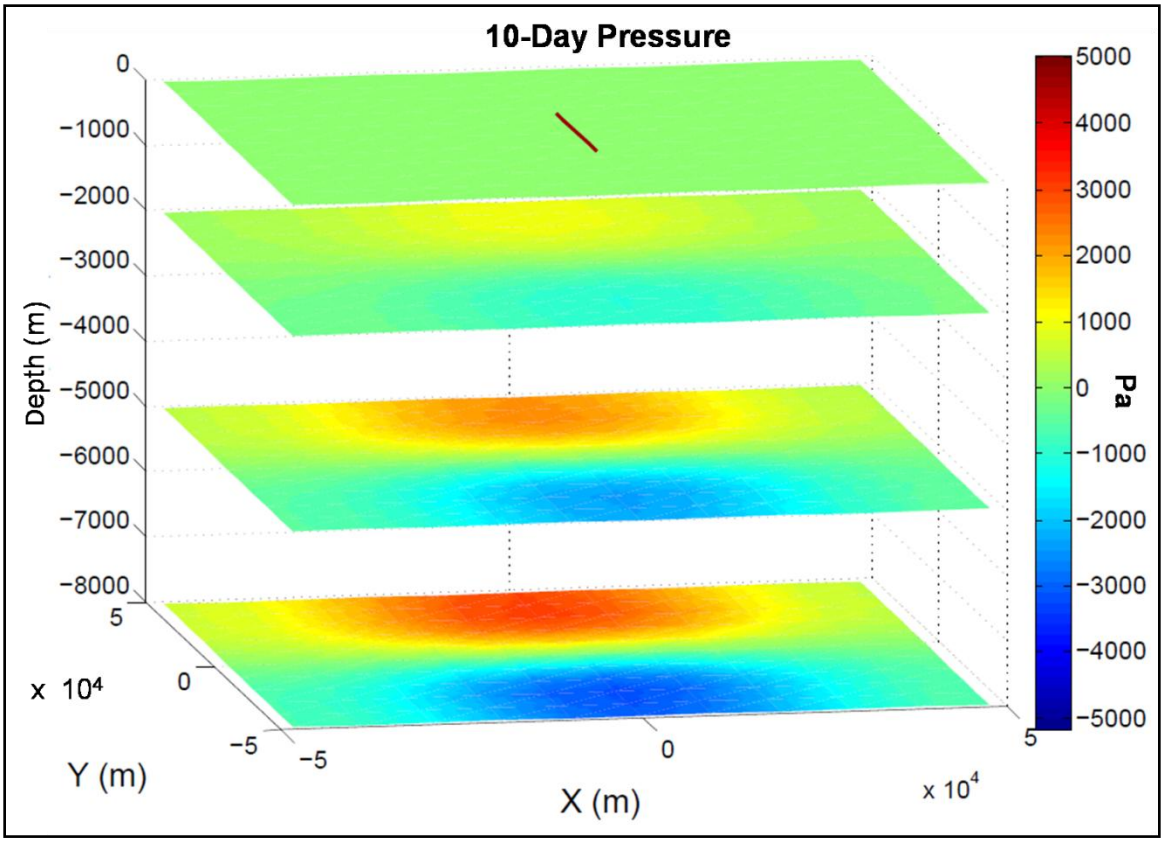

Figure 24. 10-day pore-pressure map shows a similar pore-pressure pattern to that of the 1-day map (Fig. 17). However, maximum pressure changes have dissipated by 2 orders of magnitude. The greatest values of overpressure and underpressure exist at depth.

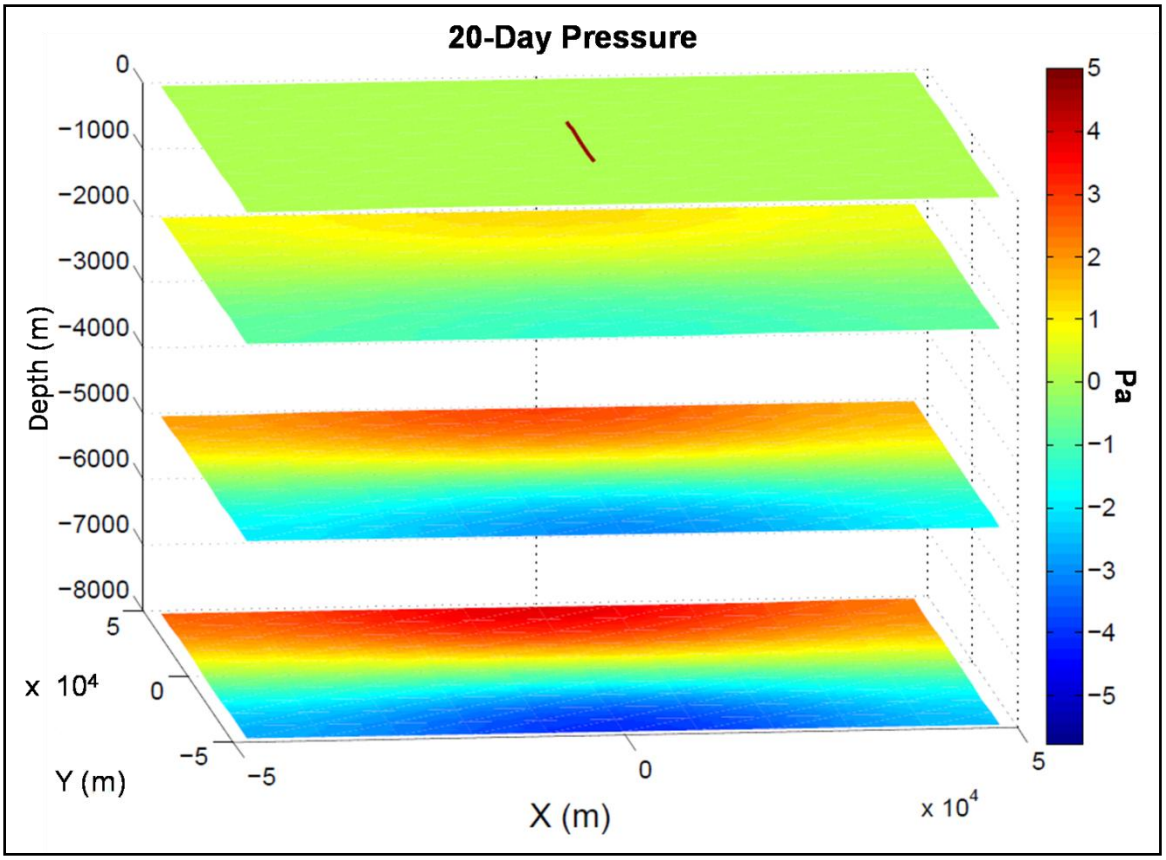

Figure 25. Pore-pressure model shows that a hydraulic conductivity value of 3.0 x 10-^{4} m/d is enough to dissipate the induced pressure-change field in 20 days. Overpressure and underpressure remain; however, they have been reduced to below +/- 5 Pa.

.

The second model features a reduced hydraulic conductivity (3×10^{-5} m/d). Similar to the first model, hydraulic conductivity (K) was not allowed to vary within the modeling space and boundary conditions only allowed flow through the top surface. Because hydraulic conductivity does not affect the initial pore-pressure distribution, the induced coseismic pressure field is the same as that of Model 1 (Figs. 20 to 21). Similarly, the induced pressure gradient remains the same as Model 1 (Fig. 23). After 1 day (Fig. 26), the pore-pressure pattern and distribution is more complex than that of the first model (see Fig. 22 for comparison). The northern section of the grid is still dominated by induced excess pressure; however, localized zones of underpressure are found. Excess pressure is mostly on the order of 10^5 Pa. Maximum overpressure occurs near the northern fault tip and is on the order of 10^6 Pa (not shown). Underpressure in the north, exists on the order of -10^5 Pa. To the south, the pressure field is symmetrical to that of the north, but opposite in magnitude. Maximum underpressure is found near the southern fault tip and is on the order of -10^6 Pa (not shown). The south is dominated by underpressured zones, yet a few localized zones of overpressure exist. Generally, under-pressure zones are around -10^5 Pa and excess pressure is on the order of 10^5 Pa. In comparison to the Day 1 results from Model 1 (Fig. 17), this model (Fig. 26) shows that the excess pore-pressure field has not dissipated as rapidly. Reducing the hydraulic conductivity one order of magnitude has retained the coseismic pore-pressure distribution better over a 1-day period of time, despite the same induced pressure gradient. Lower conductivity reduces the ease of fluid-flow and thus the pressure-front cannot migrate as quickly through the model space.

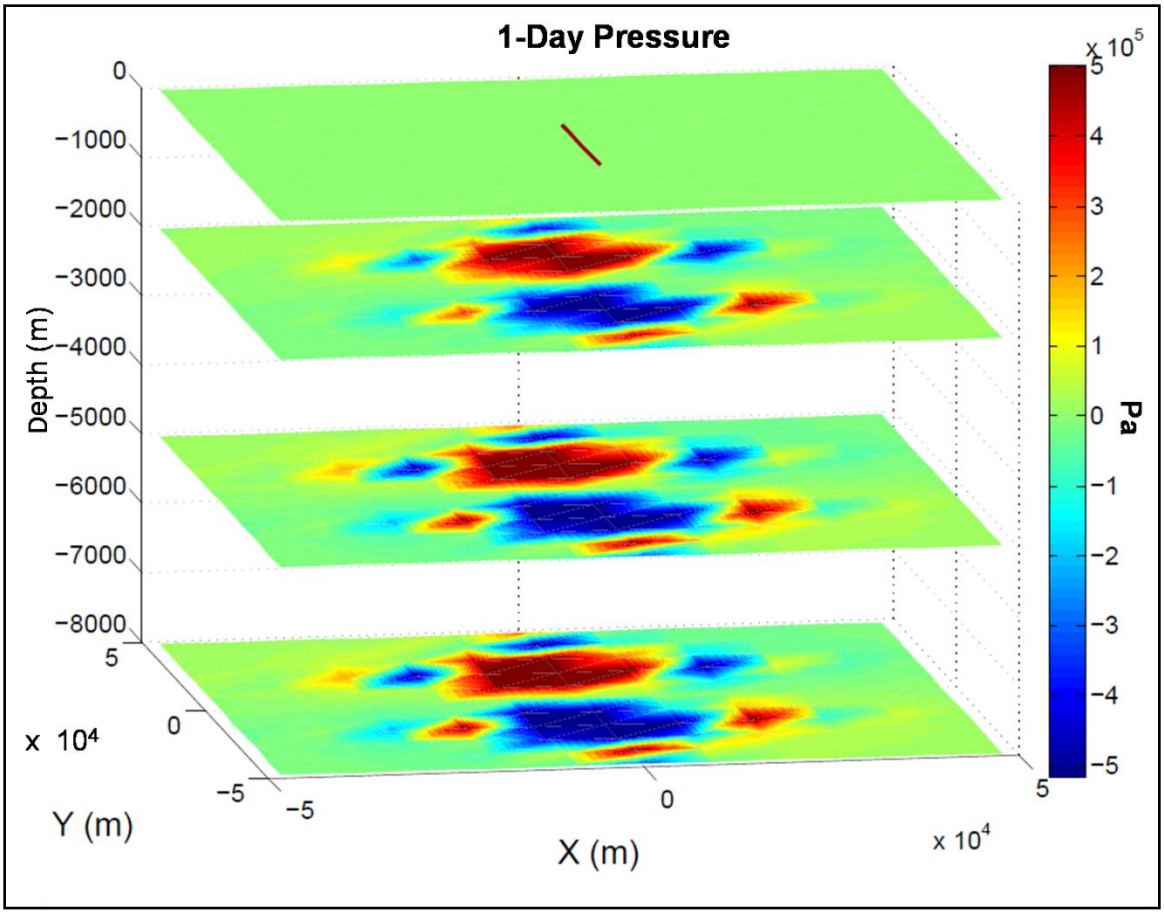

Figure26. 1-day pressure map for the low-K model shows that coseismic pore-pressure changes are retained better over a 1-day time span. Overpressure dominates the northern section (red) and under-pressure dominates the southern section (blue).

After 10 days (Fig. 27), the calculated pore-pressure resembles that of the 1-day map from model 1 (Fig. 22). The northern section is dominated by excess-pressure, centered around the northern fault tip. Maximum over-pressure reaches 5.0×10^5 Pa near the fault tip and grades laterally to approximately 3.0×10^5 Pa within 15 km. Small zones (Fig. 21) of underpressure still persist after 10 days in the north. These zones are localized and generally do not exceed -0.5×10^{-5} Pa. To the south, the pressure field shows a similar pattern. However, it is dominated by under-pressure. Localized zones of overpressure are observed and show a similar distribution to localized under-pressure zones in the north. Maximum under-pressure reaches -5.0×10^5 Pa. Also evident from this map is that pressure changes are maintained better at depth.

In the next 10 days, the pressure field dissipates very little (Fig. 28). The only major difference between 10 days (Fig. 27) and 20 days (Fig. 28) is that the isolated zones of under-pressure and over-pressure have dissipated. Maximum overpressure is centered around the northern fault tip and remains to be 5.0×10^5 Pa. This zone diminishes radially to around 0.5×10^5 Pa after 30 km. In the south, maximum under-pressure is centered around the southern fault tip and diminishes radially, values are similar to that of the northern section, but opposite invalue. With depth, zones of induced pressure change are better maintained and occupy a larger area.

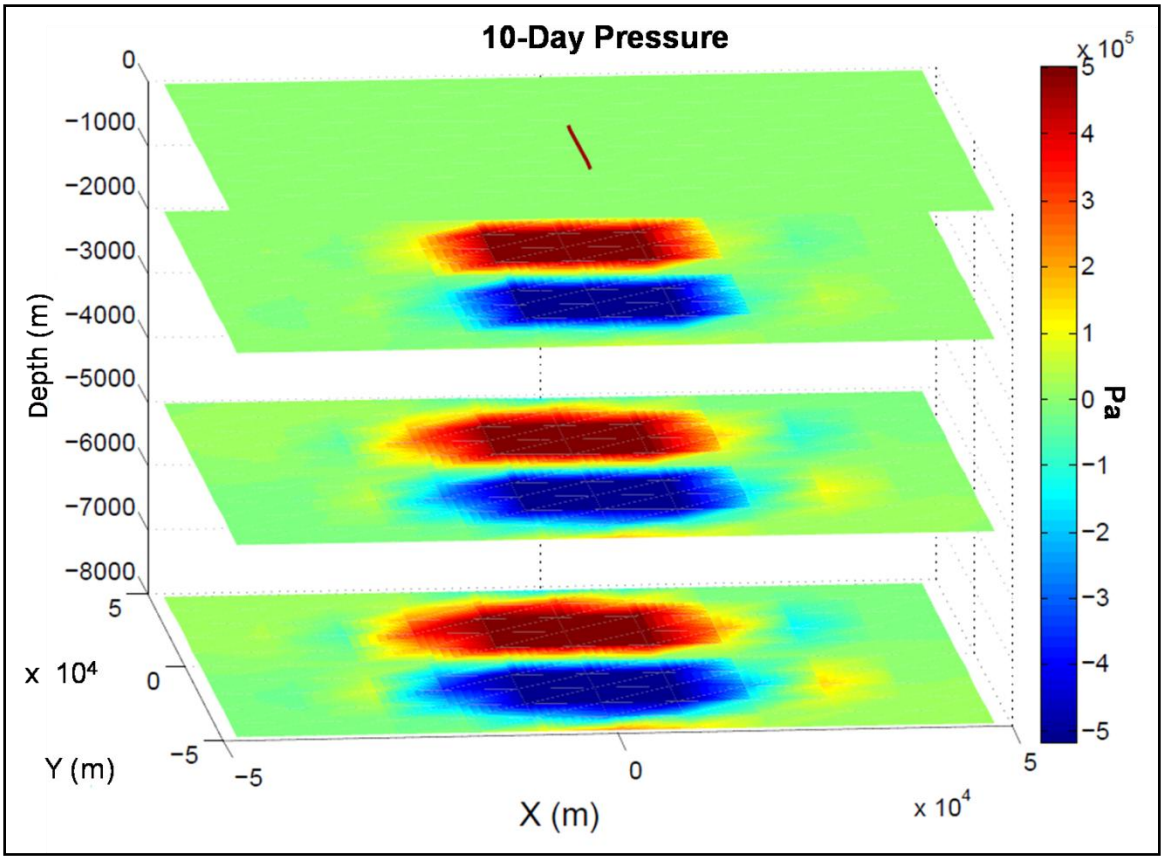

Figure 27. 10-day pressure map shows a similar pattern to that observed in Figure 17. Maximum over-pressure is centered around the northern fault tip and maximum under-pressure is centered around the southern fault tip. Isolated patches of under-pressure and overpressure remain in the northern and southern sections, respectively. Induced pressure changes are better maintained at depth.

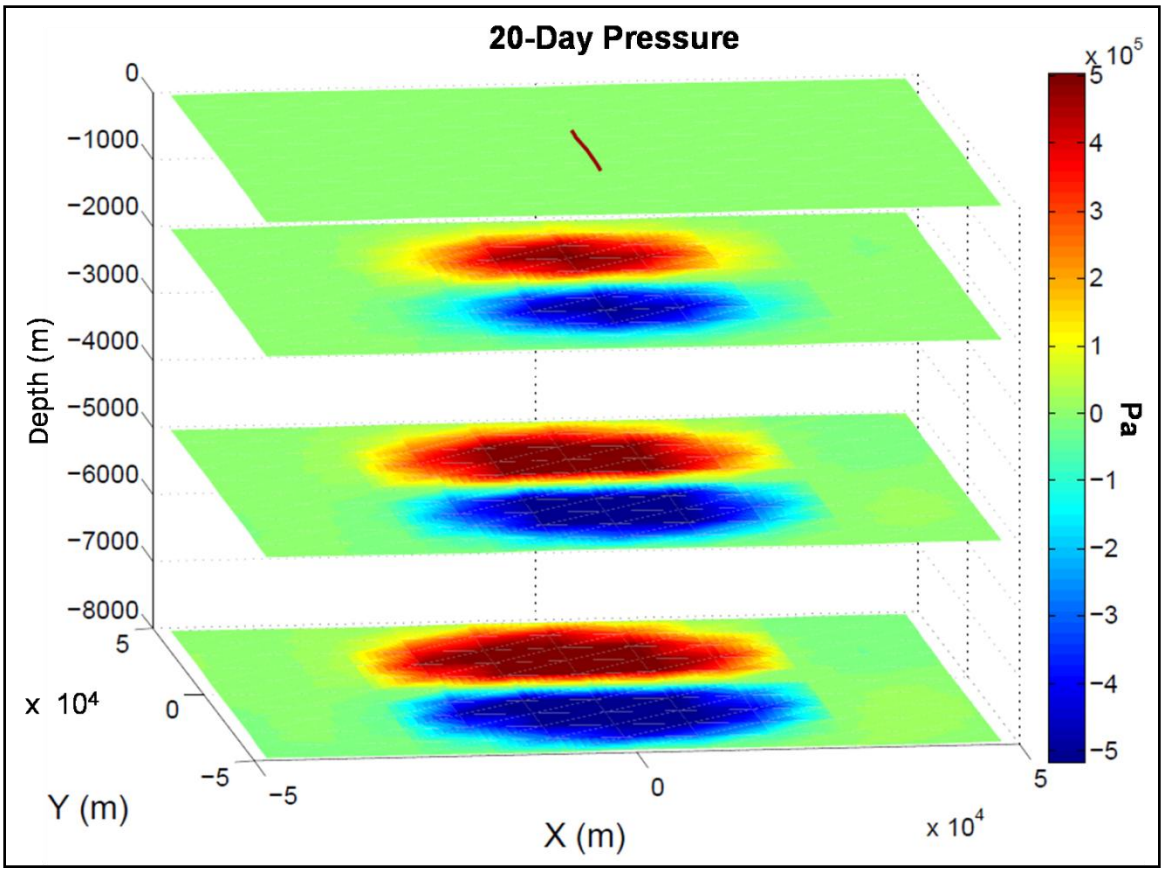

Figure 28. 20-day pressure map shows that very little dissipation has occurred since the 10-day map. The only noticeable difference is that isolated zones of under-pressure and overpressure have dissipated completely. Pressure changes are maintained better at depth.

After 100 days (Fig. 29), the pressure field resembles that of the 10-day map from Model 1 (Fig. 24). Excess-pressure in the upper 2 km of the northern section remains, but only on the order of 1.0×10^3 Pa. Similarly, underpressure exists in the upper 2 km of the southern section, but reaches only to -1.0×10^3 Pa. Pressure changes at depth are better maintained; however, these zones have dissipated to $+/- 3.0 \times 10^3$ Pa.

There is a strong correlation between Model 1 ($K = 3.0 \times 10^{-4}$ m/d) and Model 2 ($K = 3.0 \times 10^{-5}$ m/d). By decreasing the conductivity by exactly one order of magnitude, the dissipation time increases by about ten-fold. Therefore, with a hydraulic conductivity of 3.0×10^{-5} m/d, the recovery time for the same initial pore-pressure disturbance (from Model 1), increases from 20 days to 200 days. This case study highlights the importance of hydraulic conductivity as the most important variable for determining the recovery rate of pore-pressure in response to strain generated from earthquakes. The result also indicates that the induced coseismic pressure gradient dictates the direction of fluid-flow and thus the distribution of excess and decreased pore pressure, which could potentially affect the spatial distribution of aftershock activities in the fault zone.

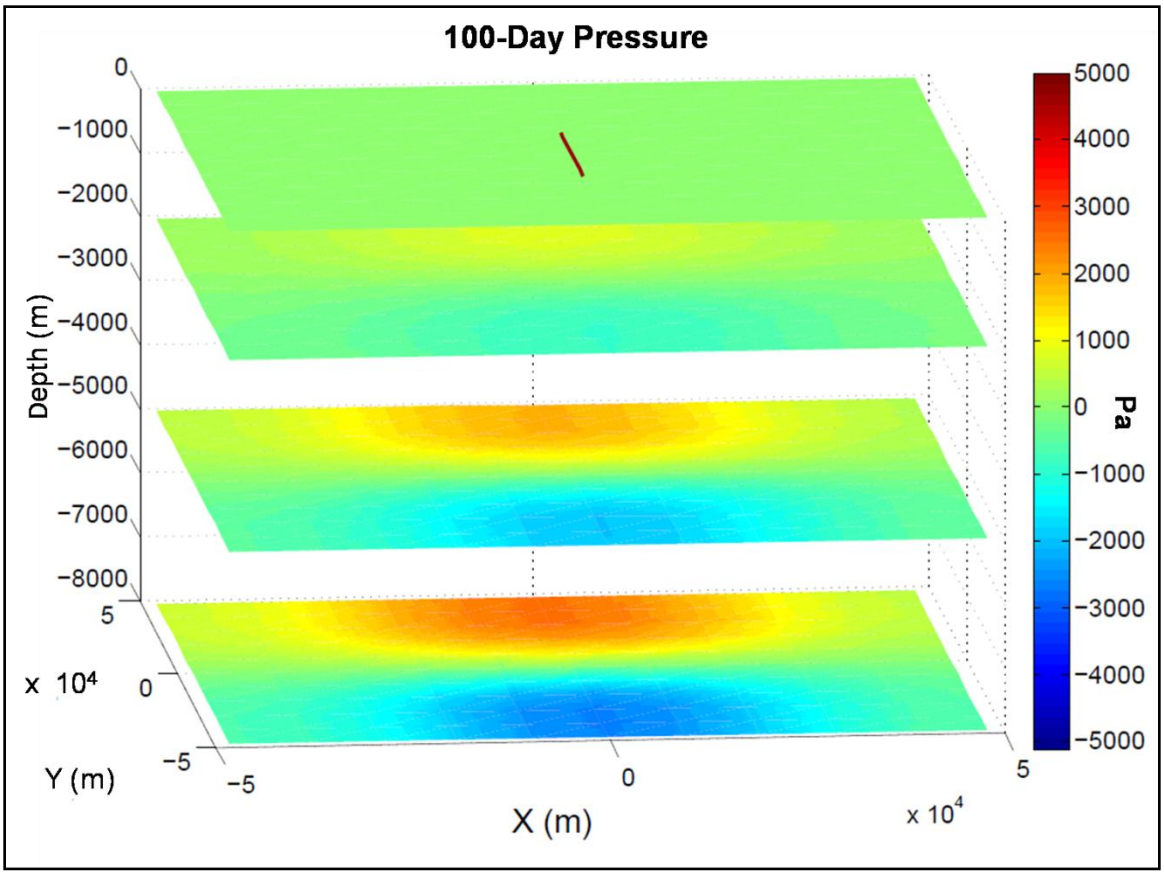

Figure 29. 100-day pressure map resembles that of the 10-day map from model 1. Overpressure remains to the north on the order of 105 Pa. Under-pressure remains in the south on the order of 10^5. Decreasing the hydraulic conductivity by one order of magnitude increases the recovery time by ten-fold.

Case Study 2: Chi-Chi Earthquake

The second case study numerically models the strain fields generated by the Chi-Chi earthquake (Ma et al., 2005) and corresponding pore-pressure fields that resulted. The Chelungpu fault rupture is much more complex than the example described previously. The fault contains several compressional bends where thrusting motion transforms into more oblique slip (Ji et al., 2005). Also, different from the simplified strike-slip fault model is differential slip on the fault plane. Specifically, different parts of the fault slip more than others, leading to eccentricities in the overall strain pattern. Using the fault model of Ji et al. (2005) for the Chi-Chi earthquake, the calculated strain pattern is consistent with what was observed in the field (Ji et al., 2005).

Like the first case study , this study examines the role hydraulic conductivity (K) plays in dissipating pore-pressure. The models examined are (1) a homogeneous geologic model (conductivity does not vary spatially) and (2) a more realistic heterogeneous geology in which the hydraulic conductivity (K) is allowed to vary spatially.

Strain modeling for the Chi-Chi earthquake reveals a complex strain pattern (Fig. 30). The hanging-wall block (east of fault trace) initially slipped near the fault southern terminus. As rupture progressed northward, fault slip gained momentum and at fault bends the kinematics of rupture, switching to a more left-lateral strike-slip (Ji et al., 2005). These factors led to increased deformation along northern sections of the fault and also larger horizontal displacements.

The rupture generated large zones of dilatational strain (red) parallel to fault segment 1 (Fig. 30). Near the rupture zone, positive dilatation reaches a maximum value of 1×10^{-5}. Positive dilatational strain gradually decreases to the east and west away from the fault plane, diminishing to 0.2×10^{-5} approximately 50 km from the rupture zone (Fig 23). Near the northern (segment 2) and southern terminus (segment 3), compression occurs (blue) (Fig 30). Compressional strain reaches a maximum of 1×10^{-5} nearest the fault tips, but diminishes quickly to 0.2×10^{5} approximately 25 km from the tips. Strong zones of compression (negative dilatation) occur on the leading edge of the hanging-wall (near surface). As the hanging-wall move upwards, the top edge of the fault block is compressed. Local nodes of either compression or dilatation can be found throughout the fault plane; these anomalous zones are most likely the result of differing amounts of frictional resistance. (slip) as well as differential stress build-up on the fault plane before rupture (i.e., different principle directions) (Ji et al., 2005).

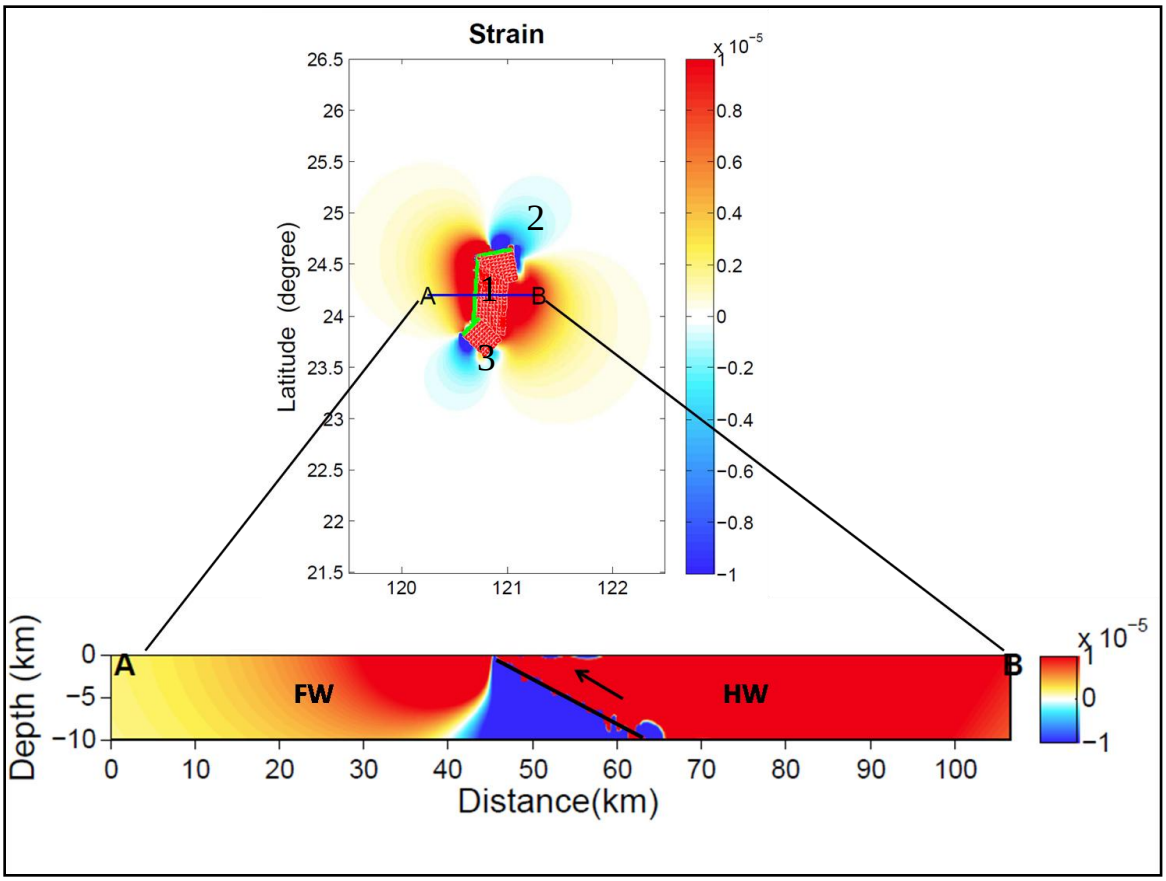

Figure 30. Plane view of the strain field calculated for the Chi-Chi earthquake (top) from rupture model of Ji et al. (2005). The model shows that zones of dilatational strain (red) developed mostly parallel to fault segment 1 (middle). Zones of compression develop near the northern (segment 2) and southern fault tips (segment 3) (blue). Cross-section (bottom) shows compression along the footwall (blue) and dilatation along the hanging-wall (red). Black arrows indicate sense of motion. Green (top) and black (bottom) lines illustrate the fault.

Pore-Pressure modeling of Chi-Chi earthquake

For this study, pore-pressure models for the Chi-Chi earthquake were constructed using two distinct spatial distributions of hydraulic conductivity (*K*). The first pore-pressure model used a uniform hydraulic conductivity of $K = 3 \times 10^{-4}$ m/d throughout the grid space. Boundary conditions allow for flow to be achieved out of the top of the model space (surface). The coseismic pore-pressure response (Fig. 31) mimicked the strain field calculated from the deformation modeling program (Fig. 30), but opposite in convention. Parallel to fault segment 1, zones of under-pressure developed (blue) in response to the dilatational strain field. Coseismic decreases in pore-pressure reached -6×10^{4} Pa, while zones of overpressure exceeded 2×10^{4} Pa. Increased magnitudes of pore-pressure with depth are in good agreement with strain modeling, as deformation was calculated to be more extensive near the hypocenter (Ji et al., 2005).

After 4 days (Fig. 32), the pressure field had decreased by approximately 3 orders of magnitude. Induced zones of overpressure are located parallel to the fault trace (blue), but have diminished to around 6×10^{3} Pa. Figure 32 illustrates that at depth, these zones are maintained longer, but could be a function of Neumann's boundary conditions. Localized zones of underpressure remain near the fault tips at depth, but likewise had diminished to around -3×10^{3} Pa. At the surface, a state of zero pressure had already been achieved within 4 days, most likely by fluid-flow through the surface.

After 25 days (Fig. 33), the four lobed pore-pressure patterns had changed. Most of the excess pore-pressure has dissipated to below 2×10^{-2} Pa by this time. Zones of underpressure remain more prevalent to the east of the fault and with increasing depth.

These zones occur because the fault dips towards the east and regions proximal to the fault plane underwent the most extensive deformation. However, modeling shows that these zones of underpressure correspond to only about -8×10^{-2} Pa. Induced pressure changes in areas farther away from the fault zone (10-15 km) had diminished to below $+/- 1 \times 10^{-2}$ Pa (Fig. 33). Therefore, after 25 days a constant hydraulic conductivity of $K = 3 \times 10^{-4}$ m/d was enough to dissipate the induced pressure fields back to near zero.

After 50 days (Fig. 34), pressure changes are reduced back to zero. The model shows that no zones of underpressure or overpressure remain. With this hydraulic conductivity ($K = 3 \times 10^{-4}$ m/d), pore-pressure modeling shows that all anomalous hydrologic changes associated with changes in pore pressure should have ceased by 50 days.

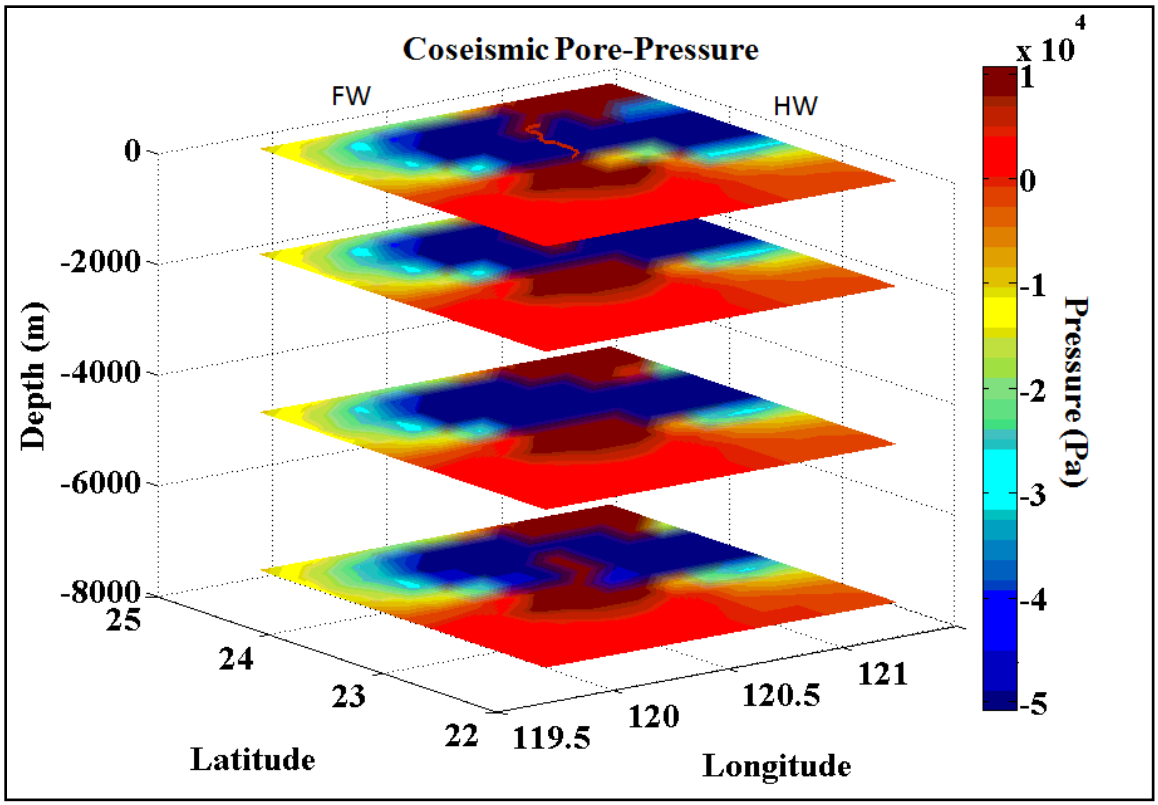

Figure 31. Coseismic pore-pressure calculated for the Chi-Chi earthquake. Model shows that the resultant pore-pressure field mimics that of the strain field, but opposite in sign. Zones of induced under-pressure developed parallel to fault segment 2, while zones of overpressure develop near the northern and southern tips of the fault. Underpressure was calculated to reach -6 x 10^4 Pa and overpressure around 2 x 10^4 Pa. Red line indicates fault trace. Hanging-wall is located to the east of the fault plane.

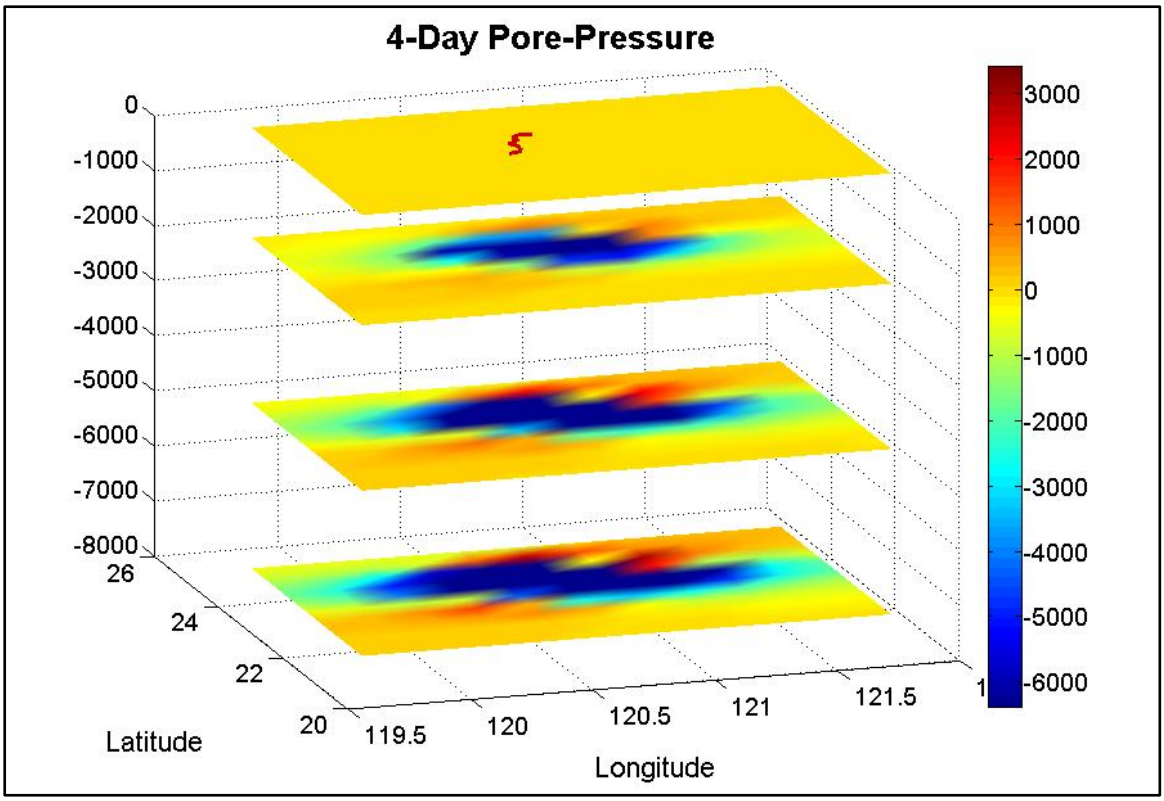

Figure 32. 4-day pressure map shows that all induced coseismic pressure changes had been reduced by three orders of magnitude. Zones of overpressure remain parallel to the fault trace and are maintained better at depth (blue). Localized zones of underpressure remain near the fault tips, especially with depth (red).

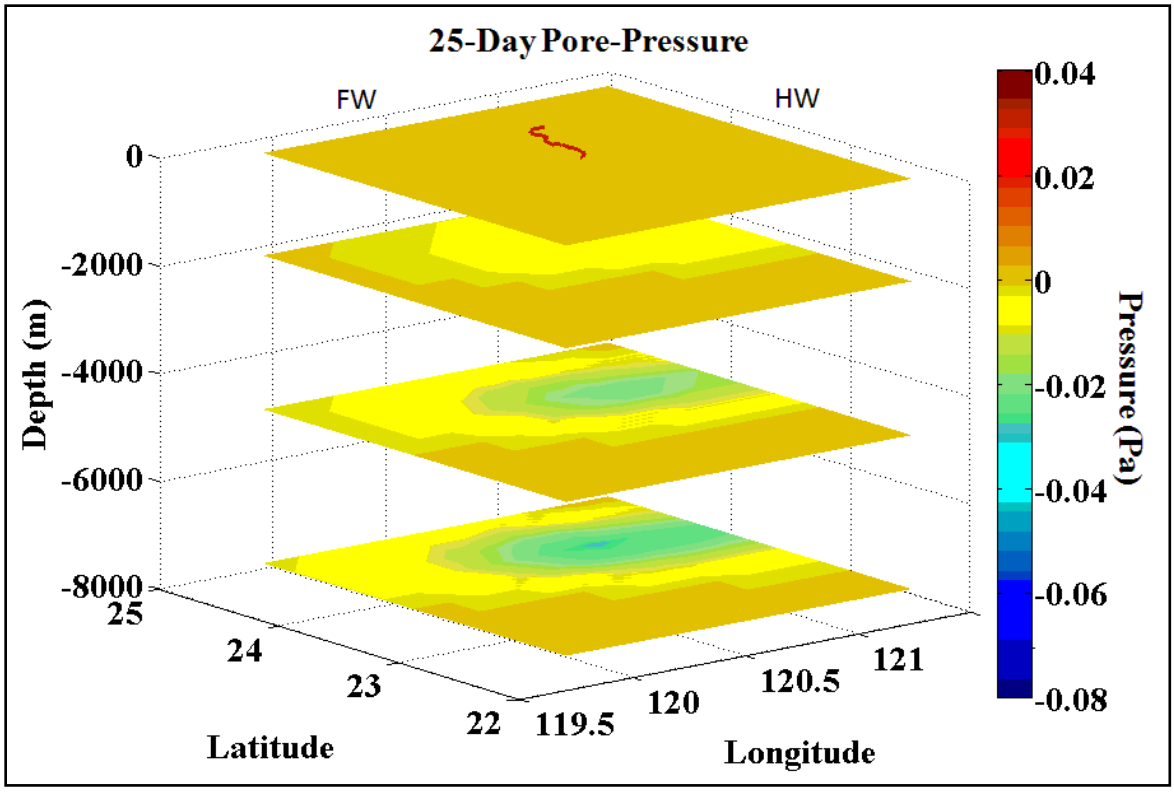

Figure 33. Resultant pore-pressure fields after 25 days. Zones of over-pressure are highly localized and reduced to less than 2 x 10^{-2} Pa. This suggests that a hydraulic conductivity of K = 3x10^{-4} m/d was enough to dissipate the induced over-pressure over this time-span. Circular zones of under-pressure remain throughout the sub-surface, however these zones correspond to less than -6 x 10^{-2} Pa. Red line indicates the fault trace. Hanging-wall is located to the east of the fault plane.

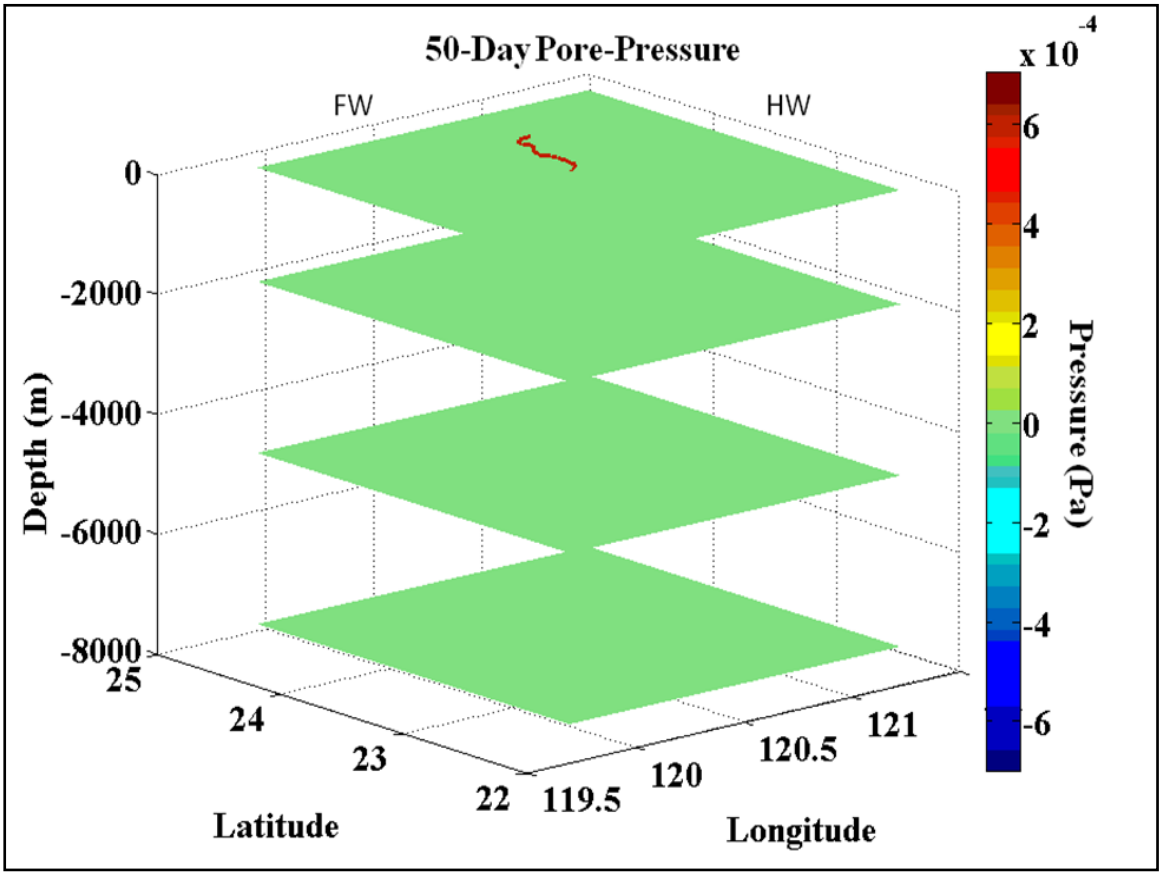

Figure 34. Resultant pore-pressure field 50 days after the Chi-Chi earthquake. All induced zones of pore-pressure caused by deformation had completely dissipated by this time. Thus, a hydraulic conductivity (K) of $3x10^{-4}$ m/d was enough to dissipate these zones via fluid-flow. Red line indicates surface fault trace. Hanging-wall is to the east of the fault plane.

The complex geology of the island of Taiwan cannot be represented in a numerical model. However, a simplified fault model can provide insight into pore-pressure changes. Thus, a second, three-layer model was created to represent a generalized geology of the island of Taiwan (Fig. 35). The hydraulic conductivity (*K*) decreases with depth and each successive layer. A hydraulic conductivity of 2.74×10^{-4} m/d was assigned for strata in the first 4 km. This value is the average appropriate for the lithologies and sediments that dominate the Choshui River alluvial fan and Western Foothills region. The second layer extends down from 8 km and has a hydraulic conductivity value of 3.0×10^{-5} m/d. This layer is consistent with a silt- to fine-grained sandstone. The third layer extends to 10 km depth and was assigned a hydraulic conductivity value of 3×10^{-7} m/d. This value is consistent with a well-consolidated mudrock or bedrock. The last layer extends down to 10 km and was given a conductivity of 1.0×10^{-8} m/d (consistent with bedrock).

The layered Chi-Chi model illustrates a slower recovery pattern. The more conductive upper layers dissipate induced pore-pressure more rapidly than those of the lower layers. Coseismic induced excess pressure (refer to Fig. 31) reached 2.0×10^{4} Pa, while underpressure zones reached -6.0×10^{4} Pa, as in the homogeneous model. After 25 days (Fig. 36), the excess pore-pressure field was reduced to below 500 Pa near the surface and to around 1.0×10^{3} Pa with increasing depth. Underpressured zones remained and generally increased with depth, reaching -2.5×10^{3} Pa at 8 km. This model shows that lower values of conductivity retain induced pressure-changes longer. Fluid flow is not as easily achieved with low conductivities and thus the excess cannot be relieved as rapidly.

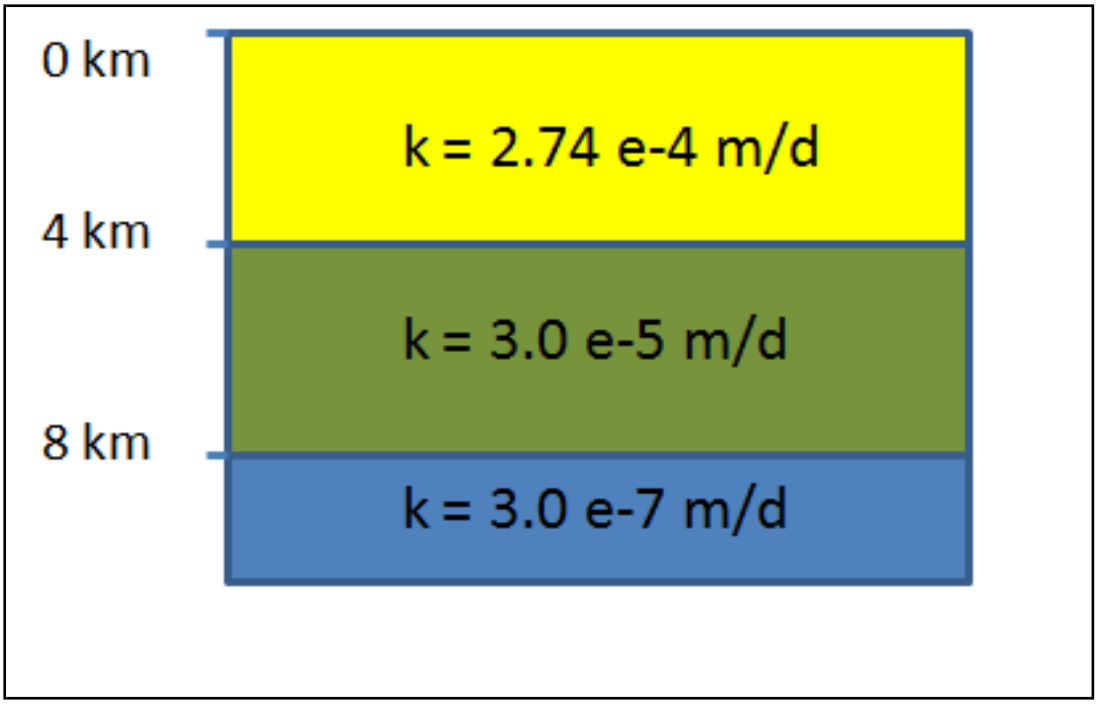

Figure 35. Schematic diagram of the hydraulic conductivity used for the layered Chi-Chi pore-pressure model.

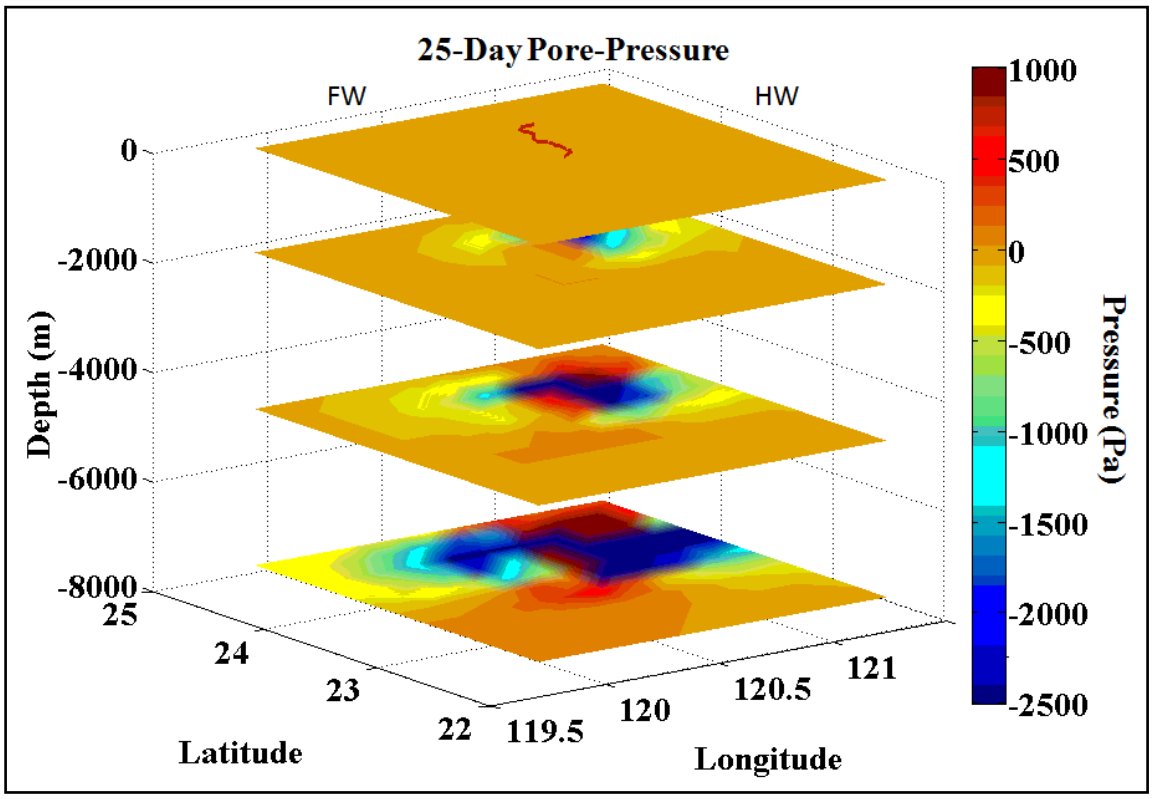

Figure 36. Resultant strain field after 25 days. Near the surface, induced pressure changes are reduced to less than -100 Pa. Coseismic overpressured zones near the surface had effectively dissipated. With depth, induced pore-pressure changes persist, ranging from 1.0 x 10^3 Pa to -2.5 x 10^3 Pa. Increasing depth also corresponds to decreased hydraulic conductivity in this model and thus, lower conductivity values trap induced pressure changes and make fluid flow more to difficult to achieve dissipation. Red line indicates fault trace. Hanging-wall is to the east of the fault plane.

After 50 days, overpressured zones near the surface had effectively decayed to zero (Fig. 37). However, at depth, pressure remained around 1.0×10^2 Pa in the less conductive layers. Underpressure zones near the surface returned to zero pressure within this time span as well, suggesting that fluid flow from zones of high pressure to zone of lower pressure dissipated the induced pressure changes. With depth (4 to 8 km), under-pressured zones are sustained and ranged from approximately -100 to -500 Pa. In less conductive layers, fluid flow and the migration of the pressure front could not be achieved to re-equilibrate the pressure.

In the next 50 days pore-pressure continued to dissipate steadily. After 100 days (Fig. 38), the overpressured zones remaining at depth (4 to 8 km) had recovered to about 10 Pa. Zones of under-pressure at these same depths had dissipated to -50 Pa. Two hundred days after the Chi-Chi earthquake (Fig. 39), pressure had normalized back to pre-seismic conditions (zero excess pressure). In the more realistic layered geology model, dissipation took between 100 and 200 days. Also, of special interest, the regions pertaining to the Choshui fan and Western foothills had completely dissipated all induced pressure changes in the upper 2 km by 50 days. Therefore, any hydrologic anomalies generated by coseismic strain, in general, should not persist past 50 days in these regions although excess pore pressure may maintain within localized low-conductivity zones.

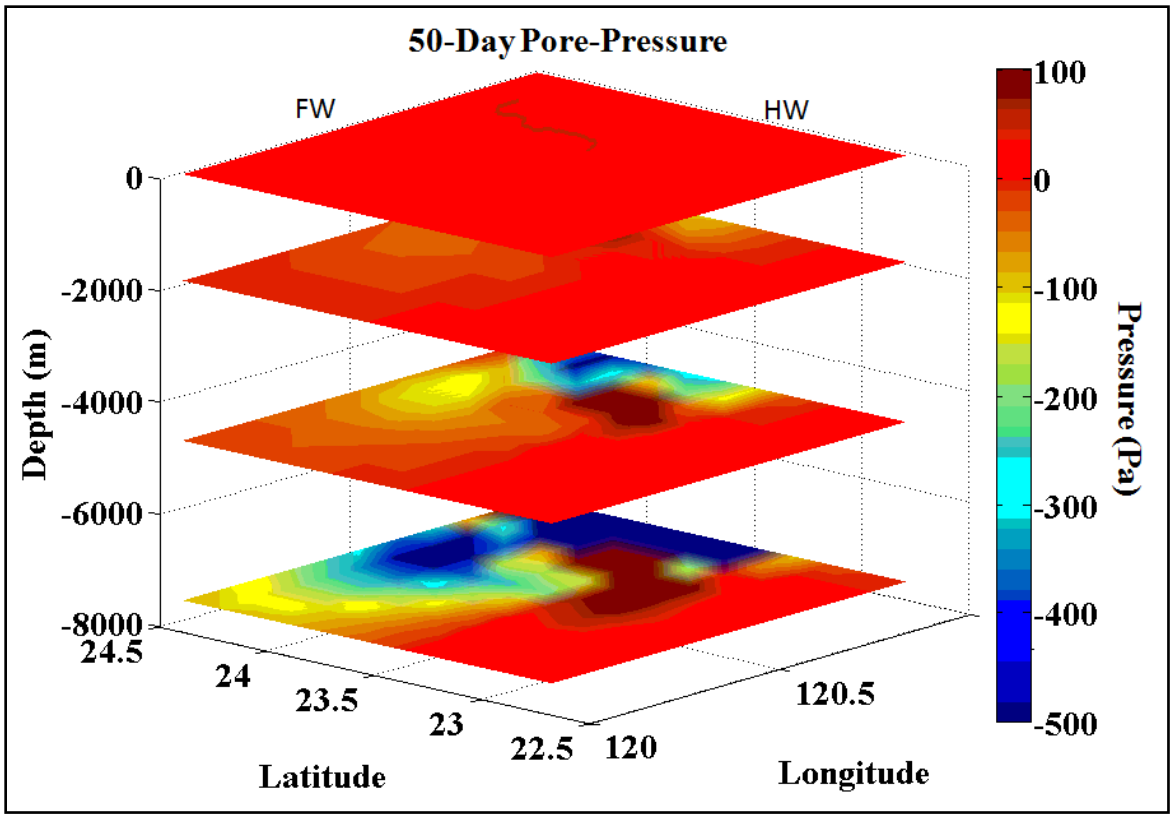

Figure 37. Resultant pore-pressure field after 50 days shows that zones of excess pore-pressure remain intact from 4 to 8 km depth, but does not exceed 100 Pa. Zones of decreased pore-pressure remain to be around -500 Pa at 8 km depth. Only small amounts of decreased pore-pressure remain at 2 km depth. Red line indicates fault plane. Hanging-wall is to the east of the fault plane. Boundary conditions were set so that flow could be achieved out of the top of the model.

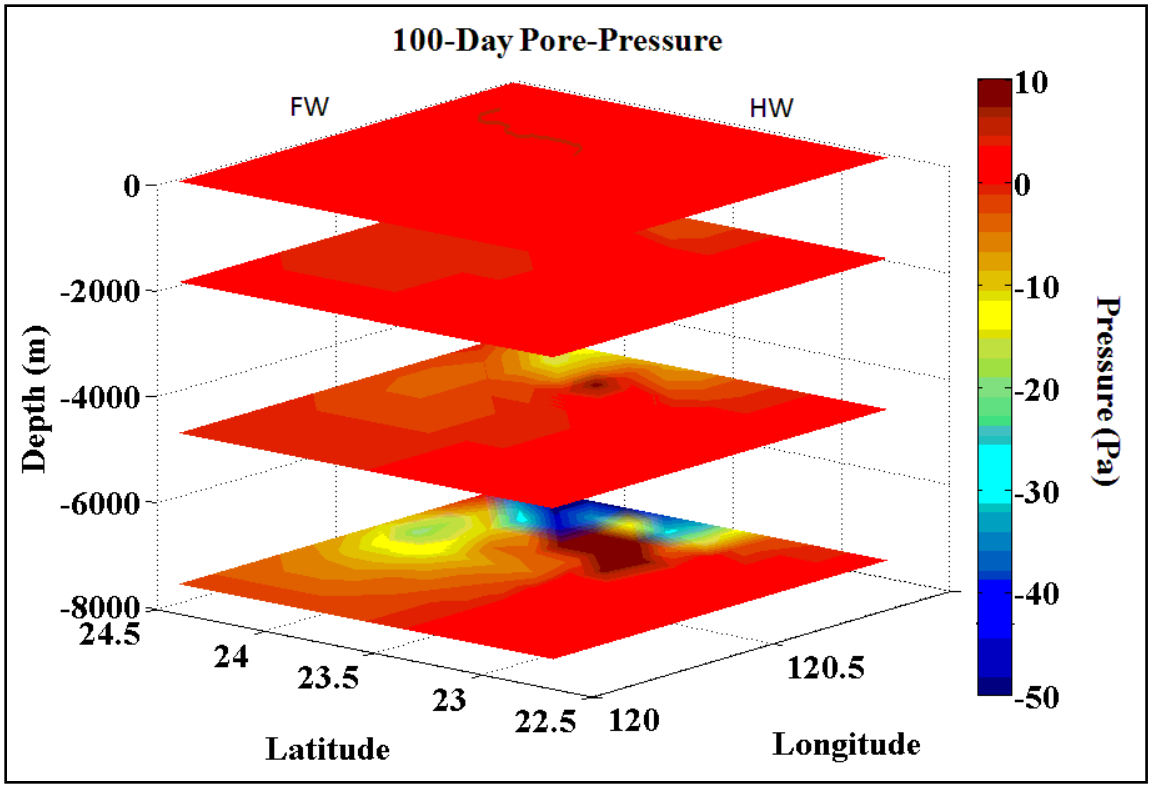

Figure 38. Resultant pore-pressure field after 100 days. Pressure changes are only maintained at depth in less conductive layers. Overpressure exists at 8 km depth and is calculated to be around 10 Pa. Underpressured zones range from -25 to -50 Pa within the fault zone at 8 km depth. Red line indicates fault trace. Hanging-wall is to the east of the fault trace. Boundary conditions only allow for flow out of the surface.

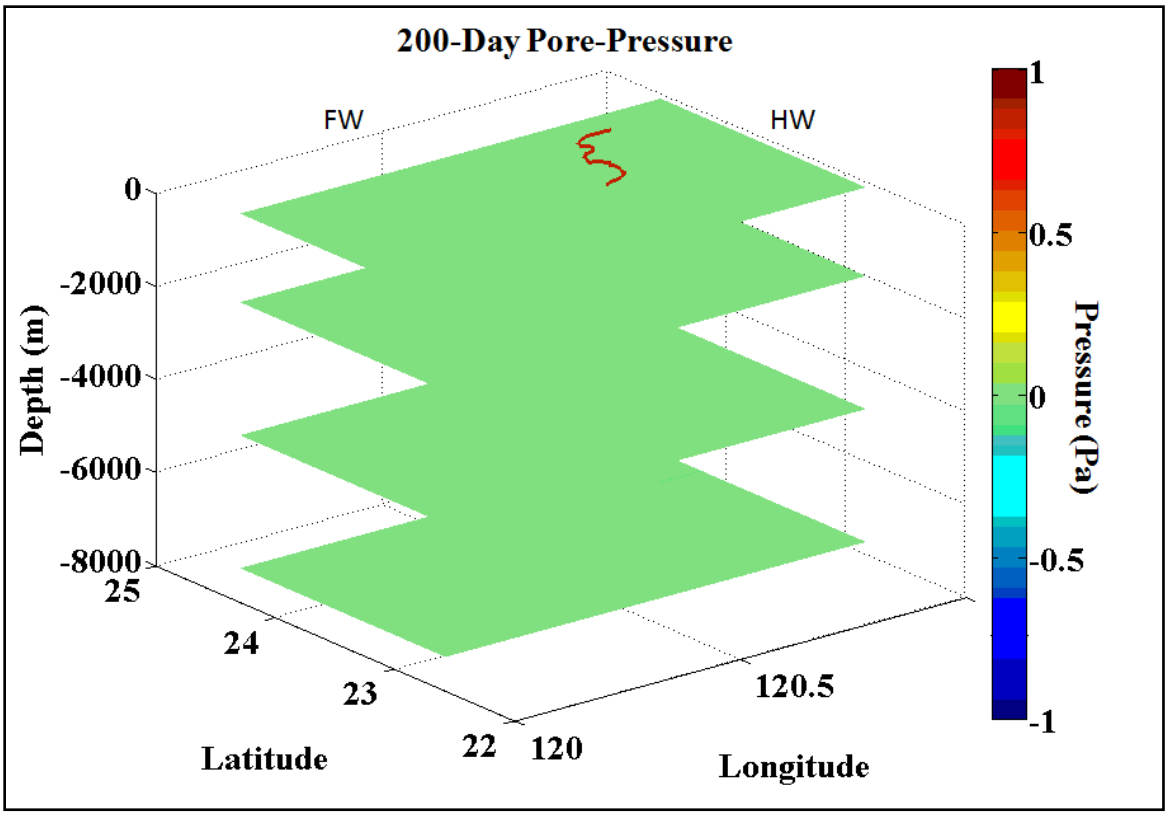

Figure 39. Resultant pore-pressure field after 200 days shows that all induced pressure changes dissipated to pre-seismic conditions. Modeling suggests that complete recovery took between 100 and 200 days. Red line indicates fault trace. Hanging-wall is located to the east of the fault plane. Boundary conditions allow for flow to be achieved through the surface of the box.

Case Study 3: Choshui River Alluvial Fan

Choshui Strain Model

The final case study focuses solely on the Choshui River alluvial fan region located directly east of the Western Foothills. This region is of the utmost importance as the bulk of the observed hydrological changes were monitored therein. Thus, this model is a very diagnostic test to determine whether or not coseismic volumetric strain could generate the observed hydrologic anomalies. The model covers an area directly to the west of the intersection between fault segments 1 and 3 (Fig. 40) (Ji et al., 2005). The strain pattern calculated for the Choshui River alluvial fan is relatively simple (Fig. 40). The far southeastern portion of the fan, located near the Chelungpu fault's southern terminus, corresponds to a zone of compressional strain. Compressional strain reaches a maximum of 1×10^{5} in the areas surrounding the southern fault tip and grades to 0.5×10^{5} Pa approximately 15 km west. The remaining portions of the fan, bordering fault segment 1, are zones of dilatation. Dilatational strain grades from 1.0×10^{-5} Pa near fault segment 1 to 0.1×10^{-5} Pa near the coastline (Figs. 40 and 41).

A cross-section through the alluvial fan (Fig. 41) illustrates that the entire hanging-wall block of fault segment 3 was dilated (1×10^{-5}) by the rupture event. However, the footwall block is shown to have been compressed by the rupture (-1×10^{-5}). West of the footwall, the alluvial fan underwent positive dilatation, ranging from a maximum of 1×10^{-5} near the surface trace to 0.2×10^{-5} approximately 20 km west (Fig. 41).

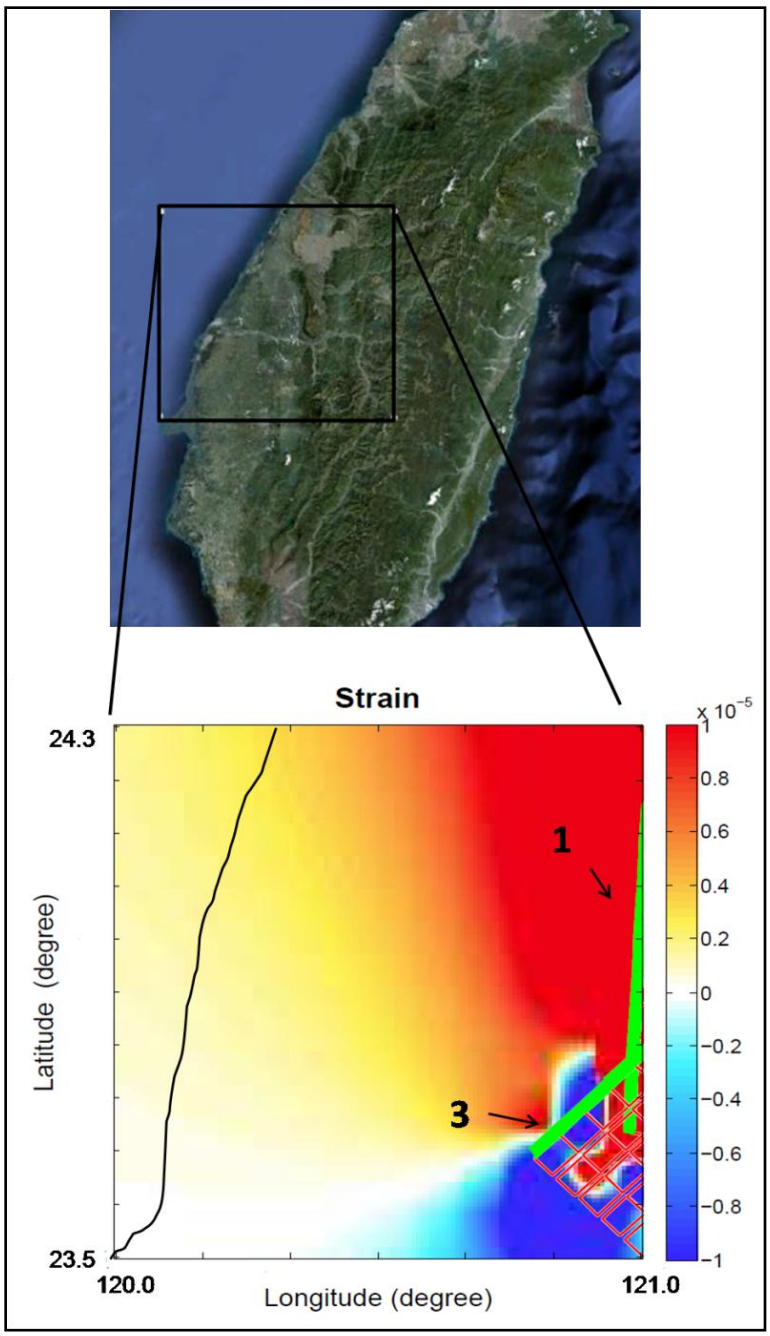

Figure 40. The Choshui River alluvial fan resides in west-central Taiwan and borders the southern terminus of the Chelungpu fault. Fault model of Ji et al. (2005) produces compressional strain (blue) in the southeastern section of the fan. The remaining portion of the fan underwent dilatation (red). The fault is highlighted by a green line. The footwall is located west of the fault plane. Black line indicates coastline.

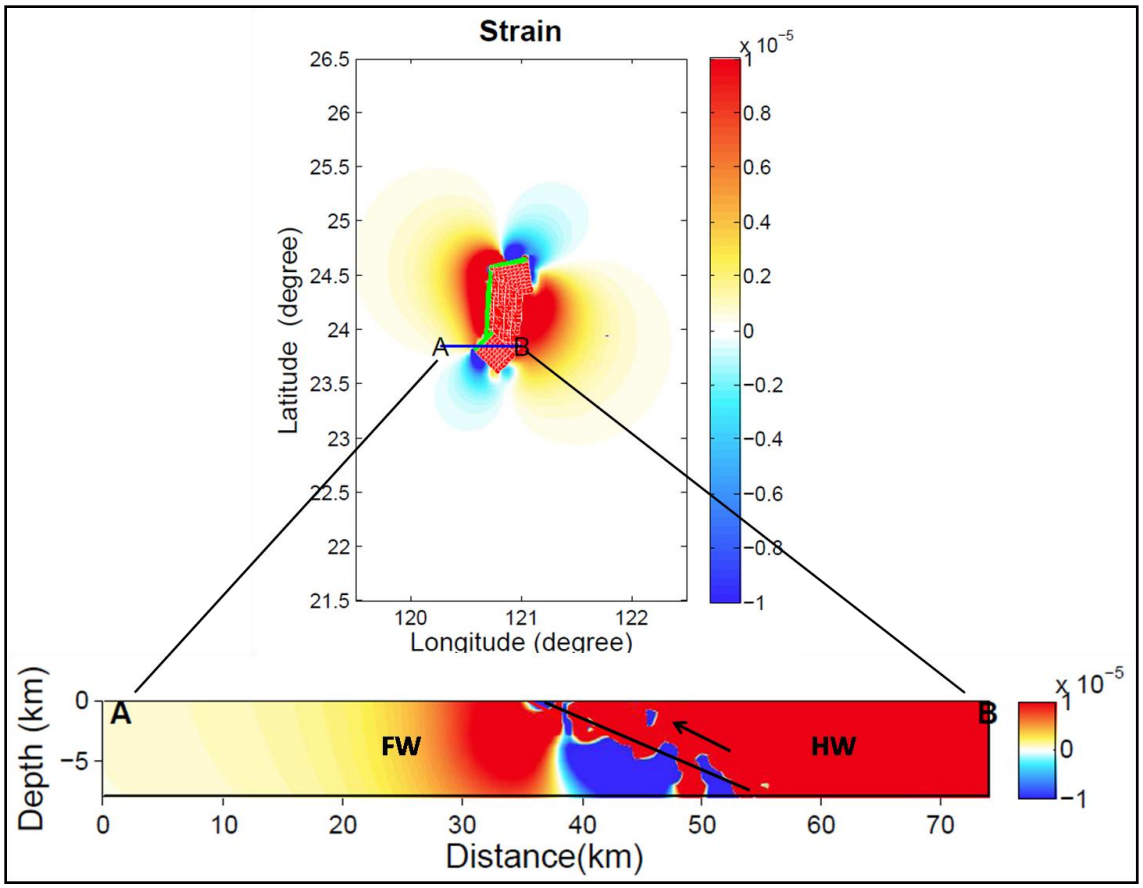

Figure 41. Coseismic strain map (top) and cross-section (bottom) for the Choshui River alluvial fan shows that the hanging-wall is dilated by rupture. The footwall is subjected to compressional strain near the fault plane. West of the footwall, the fan is in the dilatational field. Black line represents fault plane at depth. Black arrow indicates sense of motion.

Choshui Pore-Pressure Modeling

To represent the interfingering aquifers and aquitards of the Choshui River alluvial fan, the model incorporates eight distinct layers (Table 2). The upper 50 m was assigned a hydraulic conductivity value of 2.74×10^{-4} m/d (consistent with a sandy layer). The second layer extends down to 75 m and represents a clay aquitard ($K = 1 \times 10^{-6}$ m/d). The third layer represents a more conductive sand layer and extends to a depth of 150 m. ($K = 2.5 \times 10^{-3}$ m/d). The fourth layer extends down to 180 m and once again represents a clay aquitard ($K = 1 \times 10^{-7}$ m/d). The fifth layer represents a sand layer extending to a depth of 230 m ($K = 2 \times 10^{-4}$ m/d). The sixth layer has a thickness of 20 m, extending down to 250 m ($K = 2 \times 10^{-7}$ m/d). The seventh layer represents an average of sand and clay sediments and extends down to 9 km. The last layer extends down to 10 km and represents a more consolidated bedrock ($K = 1 \times 10^{-8}$ m/d). Part of this model was synthesized from the work of Lai et al. (2004).

The complex layering of the Choshui River alluvial fan creates a complex pore pressure recovery pattern. Overall, the coseismic pore-pressure response of the alluvial fan is consistent with the calculated strain field (Fig. 42). The southeastern portion of the fan shows elevated fluid-pressure, while the rest of the fan became underpressured (Fig 42). Peak induced excess fluid-pressure reaches approximately 1.0×10^{4} Pa, while zones of underpressure reach -6.0×10^{4} Pa.

Table 2. Geologic layering assigned to the Choshui River alluvial fan model. Depth is in meters below the surface.

Layer ID	Depth (m)	Unit	Hydraulic Conductivity (m/d)
1	0 to 50	Aquifer	2.74×10^{-4}
2	50 to 75	Aquitard	1.0×10^{-6}
3	75 to 150	Aquifer	2.5×10^{-3}
4	150 to 180	Aquitard	1.0×10^{-7}
5	180 to 230	Aquifer	2.0×10^{-4}
6	230 to 250	Aquitard	2.0×10^{-7}
7	250 to 9000	Mix of sand and clay	2×10^{-5}
8	9000 to 10000	Bedrock	1.0×10^{-8}

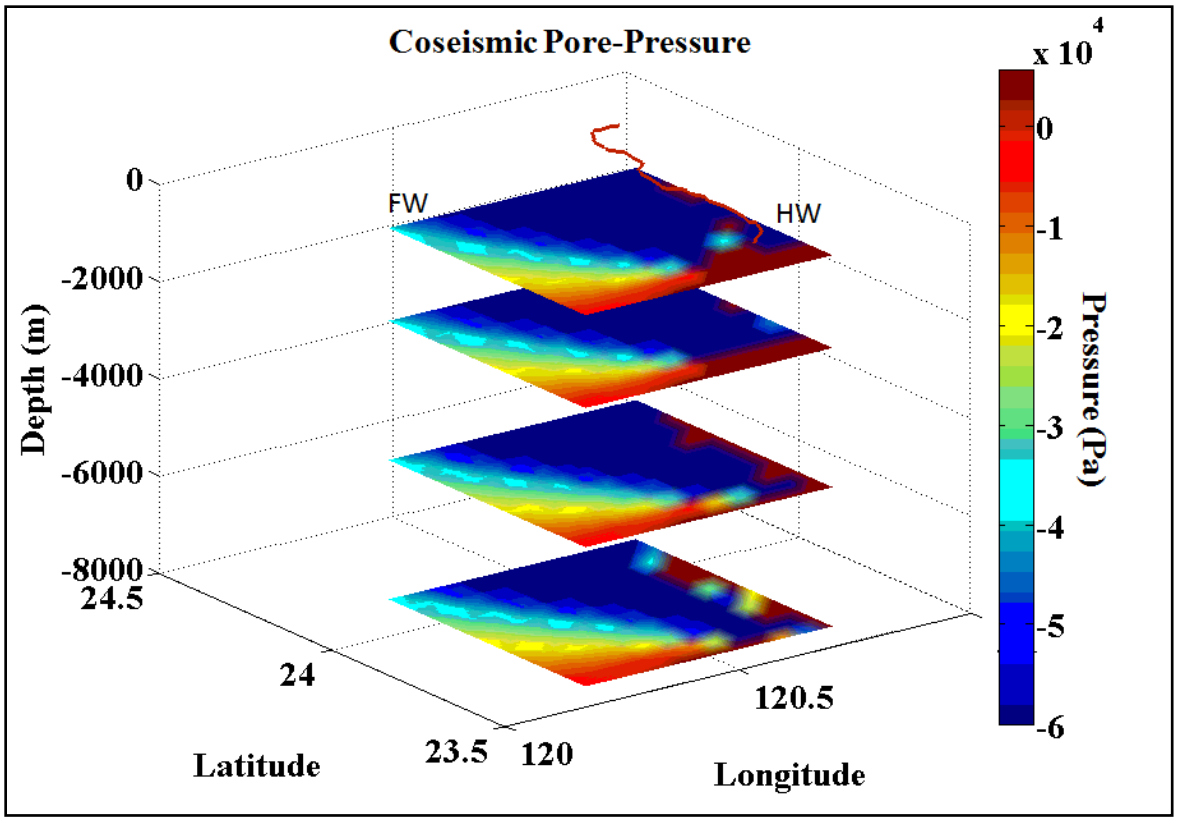

Figure 42. Coseismic pore-pressure reveals that the majority of the Choshui River alluvial fan was under-pressured (blue) by dilatational strain. The southeastern and southwestern portions underwent compression (red). Chelunpgu fault is marked by red line. Hanging-wall is located to the east of the fault plane. Boundary conditions allow for flow out of the surface.

After 25 days (Fig. 43), most of the induced excess pressure had been dissipated near the surface. At 2 km depth some excess pressure existed directly beneath fault segments 1 and 3. These zones correspond to the compression of the footwall at depth (Fig. 41). Zones of under-pressure persist with increasing depth. These zones have a maximum value of -2.5×10^4 Pa. Pressure in these zones are consistent greater strain at depth and less conductive layers above and below that prevent equilibration of the pressure field to pre-seismic conditions (Fig. 43). Over the next 25 days, pore-pressure continues to dissipate. After 50 days (Fig. 44), excess pressure has been completely relieved. Zones of decreased pore-pressure do not equilibrate as fast as those in excess pressure zones, possibly because zones of coseismic underpressure were greater in size and extent than overpressured zones. However, dissipation has reduced under-pressured zones to -2.5×10^3 Pa at 8 km depth.

Pore-pressure fields after 100 days (Fig. 45) show the same trend. With increasing depth, zones of underpressure remain, but only reaching a maximum of -50 Pa. After 200 days (Fig. 46), all remaining zones of underpressure have dissipated back to pre-seismic conditions (zero pressure).

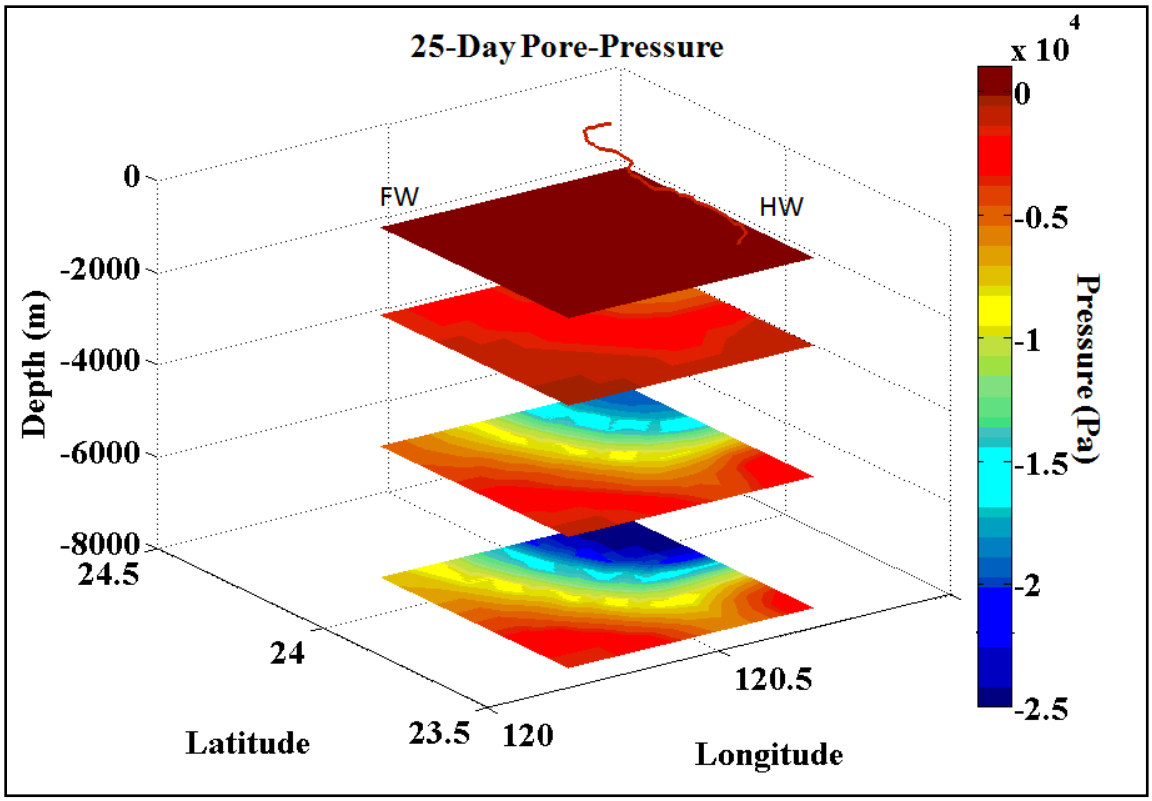

Figure 43. Pore-pressure field after 25 days shows that most zones of over-pressure have dissipated. However, zones of dilatation continue to show underpressure with increasing depth. Red line marks the Chelunpgu fault. The hanging-wall is located to the east of the fault plane. Boundary conditions allow for flow out of the surface.

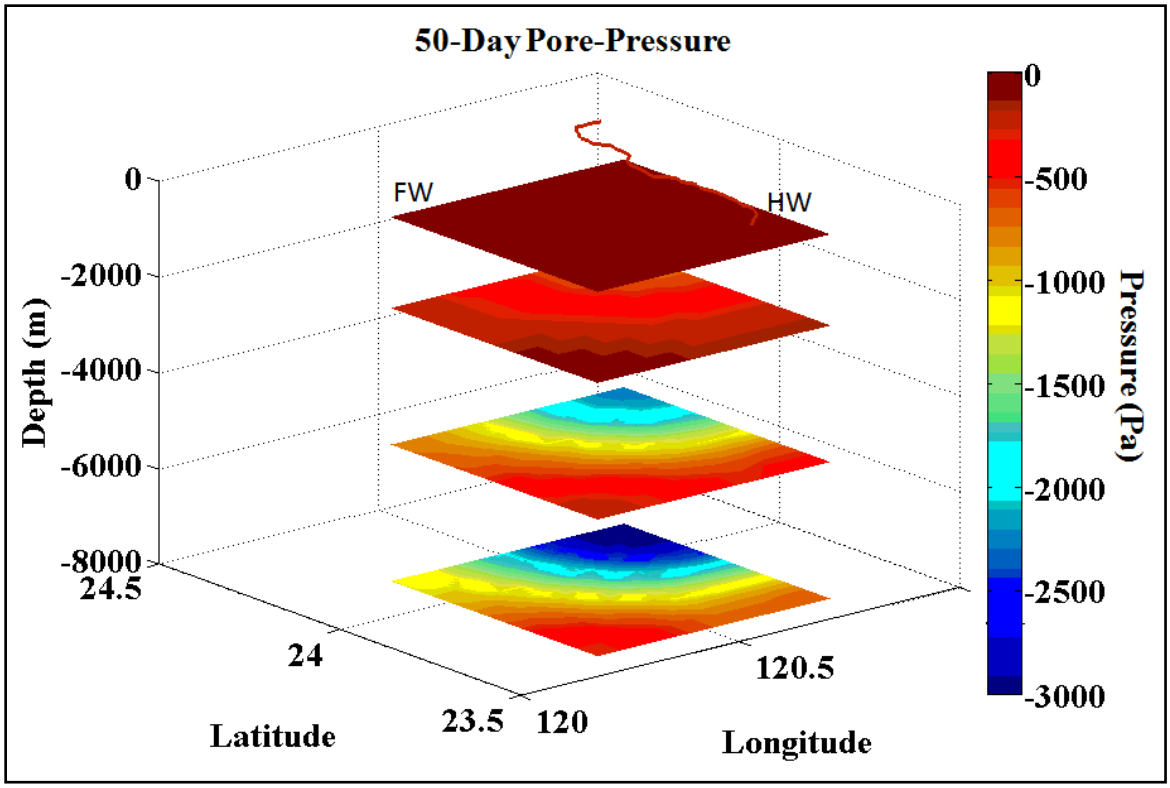

Figure 44. Pore-pressure field after 50 days shows that most zones of over-pressure have dissipated. However, zones of dilatation continue to show underpressure with increasing depth. Red line marks the Chelunpgu fault. The hanging-wall is located to the east of the fault plane. Boundary conditions allow for flow out of the surface.

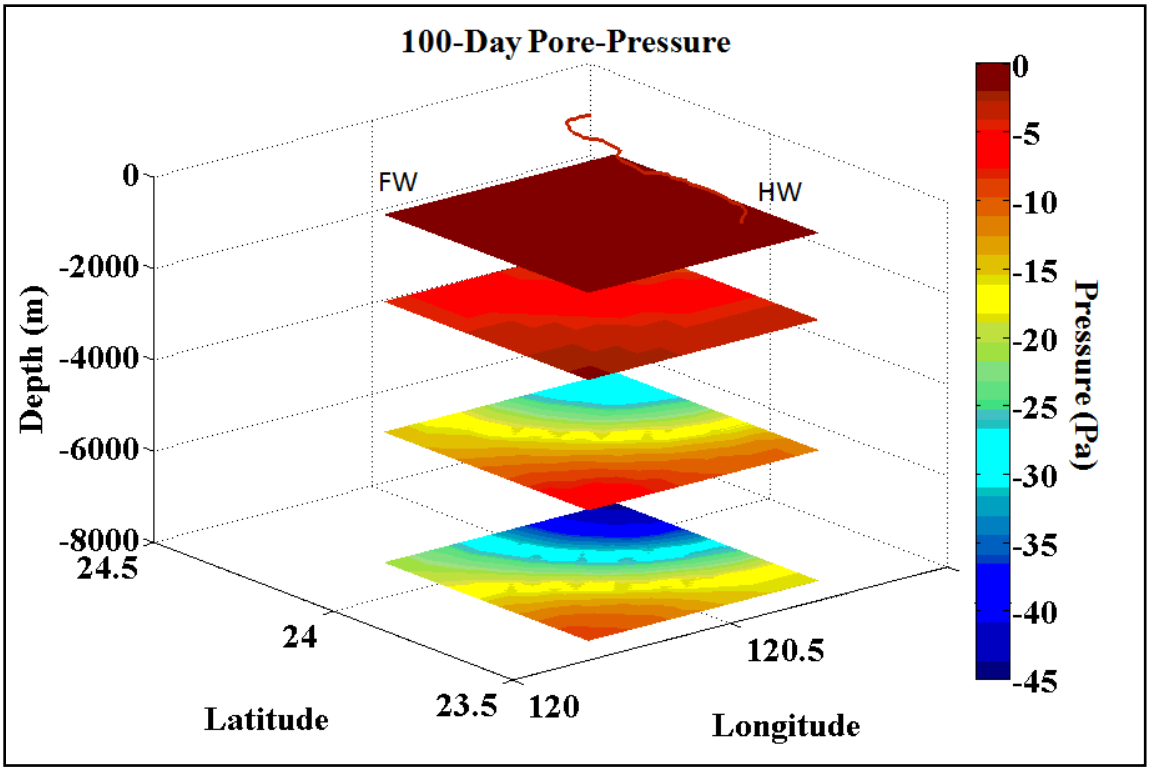

Figure 45. Pore-pressure field after 100 days shows that most zones of overpressure have dissipated. However, zones of dilatation continue to show underpressure with increasing depth. Red line marks the Chelunpgu fault. The hanging-wall is located to the east of the fault plane. Boundary conditions allow for flow out of the surface.

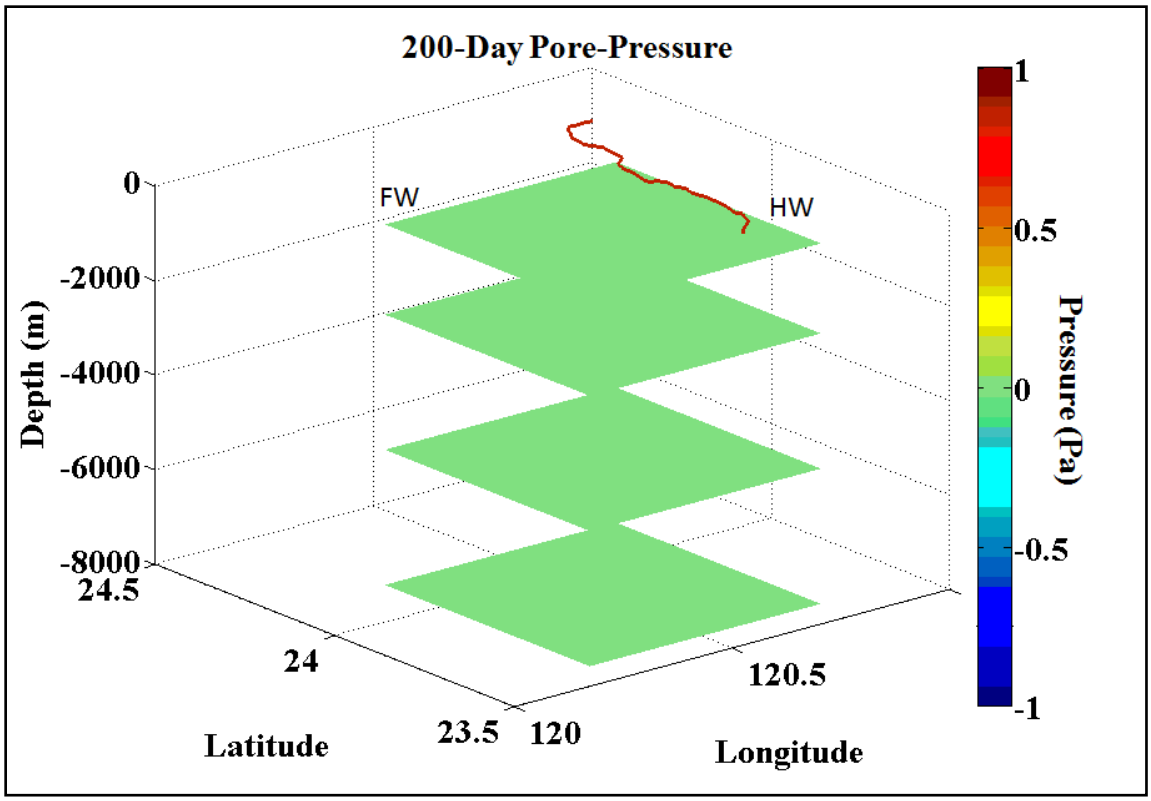

Figure 46. Pore-pressure field after 200 days shows all induced pressure changes have dissipated completely. Red line marks the Chelunpgu fault. The hanging-wall is located to the east of the fault plane. Boundary conditions allow for flow out of the surface.

Table 3. Input parameters for strain models used in this research.

Case ID	Fault Type	Slip Specifice	Poisson's Ratio (ν)	Young's Modulus	Coefficient of friction	Strike	Dip	Strain Field
Simplifed Right-lateral	Pure Strike-Slip	3 m	0.25	8×10^{-5}	0.4	0°	30° W	Fig. 15
Chi-Chi earthquake	Mostly pure reverse, some left-	Allowed to vary from 0 to 24 m	0.25	8×10^{-5}	0.4	Seg.1 = 3° Seg. 2= 80°	29° E	Fig. 23

Discussion

Factors Influencing Well Response

The most important factors influencing well responses during earthquakes events are thought to be proximity of the well to the fault zone, local geology, and mechanisms controlling hydrologic changes (e.g., Muir-Wood and King, 1993; Rojstaczer and Wolf, 1994; Manga et al., 2003). Secondary factors contributing to well responses are tidal or barometric pressure variations as well as local irrigation or pumping conditions. In this research, responses to tidal influences or barometric pressure deviations are not examined. These variations are typically very small and thus should not play a large role in quantitatively determining the response of each individual well. Local pumping and irrigation in the Choshui river alluvial fan is quite extensive. Thus, accounting for these variations is complex and requires data beyond that available for this study. Therefore, anthropogenic changes are not regarded in this research.

The proximity of the well to the seismic zone can have a large impact on the coseismic response. Regions closest to a fault rupture zone undergo the most extensive crustal deformation and are subjected to the greatest peak ground acceleration. If ground acceleration is significant for producing widespread hydrologic anomalies, some of the largest magnitude anomalies should be witnessed in the proximal regions. Lai et al. (2004) noted that some of the largest magnitude changes occurred near the rupture zone. In comparing magnitude of change and distance to the Chelungpu fault, however, they

found that this correlation broke down after a distance of approximately 10 km. They offered no specific explanation for this observation.

The local geology can play an important role in how the water-table responds to stress generated by large magnitude earthquakes. Unconfined or partly confined aquifers typically show less change and shorter lag times in recovery than do more confined aquifers. This is due to the ease of groundwater flow and diffusion in these unconfined aquifers. Unconfined aquifers in the Choshui River alluvial fan (F1) generally recovered to their steady-state conditions within a few hours of disturbance (Chia et al., 2008). Confined aquifers (F2, F3, and F4), however, showed a step-wise change in water-table elevation following the Chi-Chi earthquake and lag times of weeks to months for recovery.

The nature of unconsolidated sediment in the Choshui River alluvial fan plays an important role in influencing coseismic and postseismic responses. Variations in particle size influence the hydraulic properties of the aquifers. As a general rule, aquifers consisting mainly of gravel would be more conductive and permeable than aquifers consisting mainly of sand and silt. Overall the sediment type tends to grade from coarse gravels and sands nearest the Western Foothills to silt and mud-sized particles in distal zones, with interfingering aquifers and confining units down to a few hundred meters depth. Sediment sizes and permeability generally decrease from north to south within the fan and thus could also play a role in governing differing magnitudes of hydrologic response.

Field observations appear to quantitatively show that zones of higher hydraulic conductivity correspond to zones of larger coseismic changes. In general, slightly larger

changes in well levels are associated with the northern and central portions (Δh= 3 to 5 m) of the Choshui river alluvial fan (K = 1.0 x 10^{-3} m/d) than the southern fan (K = 10^{-4} m/d) where coseismic changes in hydraulic head averaged only around 1 to 2 m. Several other factors, however, may have influenced the change in well levels. These changes may also be attributed to small differences in compressibility (α). The higher values of hydraulic conductivity also correspond to faster diffusion rates for well recovery as fluid flow is more easily permitted. Towards the south, hydraulic conductivity values decrease and water-table changes recover more slowly.

Coseismic Response

Of the 58 total wells analyzed from the Choshui River alluvial fan and Western Foothills slope region, only nine wells demonstrate a decrease in water-table elevation in response to the Chelungpu fault rupture (Figs. 47 and 48). The majority of these wells (7) occurred within 10 km of the fault zone. The proximal zone (<10 km) is dominated by consolidated sedimentary sequences, drastically differing from the rest of the alluvial fan, which is comprised of thick unconsolidated Holocene fluvial deposits (Lai et al., 2004). The remaining two wells reside within 15 km of the fault zone. The rest of the wells analyzed (49) illustrate coseismic increases in response to the Chi-Chi earthquake, with the largest positive shifts corresponding to areas within the middle zone of the Choshui River alluvial fan.

The one-way coupled models generated in this study indicate that most of the Western Foothills slope region and alluvial fan were subjected to tensional strain by the rupturing of the Chelunpgu fault. In response, these areas should have seen a widespread

reduction in pore-pressure (Figs. 47 and 48), consistent with the coseismic volumetric strain hypothesis (Muir-wood and King, 1993). Wells within the slope and alluvial fan regions should likewise show a decrease in water-table elevation. These predicted results agree fairly well with observations from Figure 48 and suggest that coseismic strain may be responsible for the hydraulic anomalies observed in wells near the Chelungpu fault, at least in the F2 aquifer. Pore pressure decreased (-2 to -10 Bar) beneath hydrostatic pressure in these regions, indicating that large decreases in pressure head could lead to a significant coseismic lowering of the water table.

An alternate explanation for the observed water-table responses in the Western Foothills and upper slope regions is that fracturing generated by seismic shaking could have led to a downward gradient for fluid-flow. Rojstaczer and Wolf (1994) proposed a causal inducing of hydrologic change by fracturing created by the passing of strong seismic waves through a geologic media. Prevalent vertical to sub-vertical fracturing was observed in the Western Foothills following the Chi-Chi mainshock (Lee et al., 2002). Furthermore, a significant amount of water was found pouring down into tunnels running beneath the Western Foothills following the earthquake (Lin, 2000). Both observations indicate that fractures created by tensile stresses or intense seismic shaking may have facilitated an induced coseismic flow downwards from perched aquifers located in the upper aquifers of the Western Foothills. This hypothesis could explain the reduction in water-table elevation within the consolidated sedimentary rocks of the slope and Western Foothills region.

Similarly, most other areas in the Choshui River alluvial fan are associated with dilatational strain (Fig. 47). Pore-pressure modeling reveals that these areas should correspond with decreases in water-level (Fig. 48). However, field observations show that water-levels generally displayed a coseismic increase (Fig. 48). Therefore, a coseismic volumetric strain mechanism (Muir-Wood and King, 1993) cannot be used to explain a majority of the observed coseismic water-table responses in the Choshui River alluvial fan. Seismic fracturing (Rojstaczer and Wolf, 1994) requires the presence of consolidated rock, which is inconsistent with the unconsolidated sediments found in the rest of the Choshui River alluvial fan. Therefore, this mechanism can be eliminated as a possible explanation for the widespread increase in hydraulic head throughout the middle and distal zones of the alluvial fan.

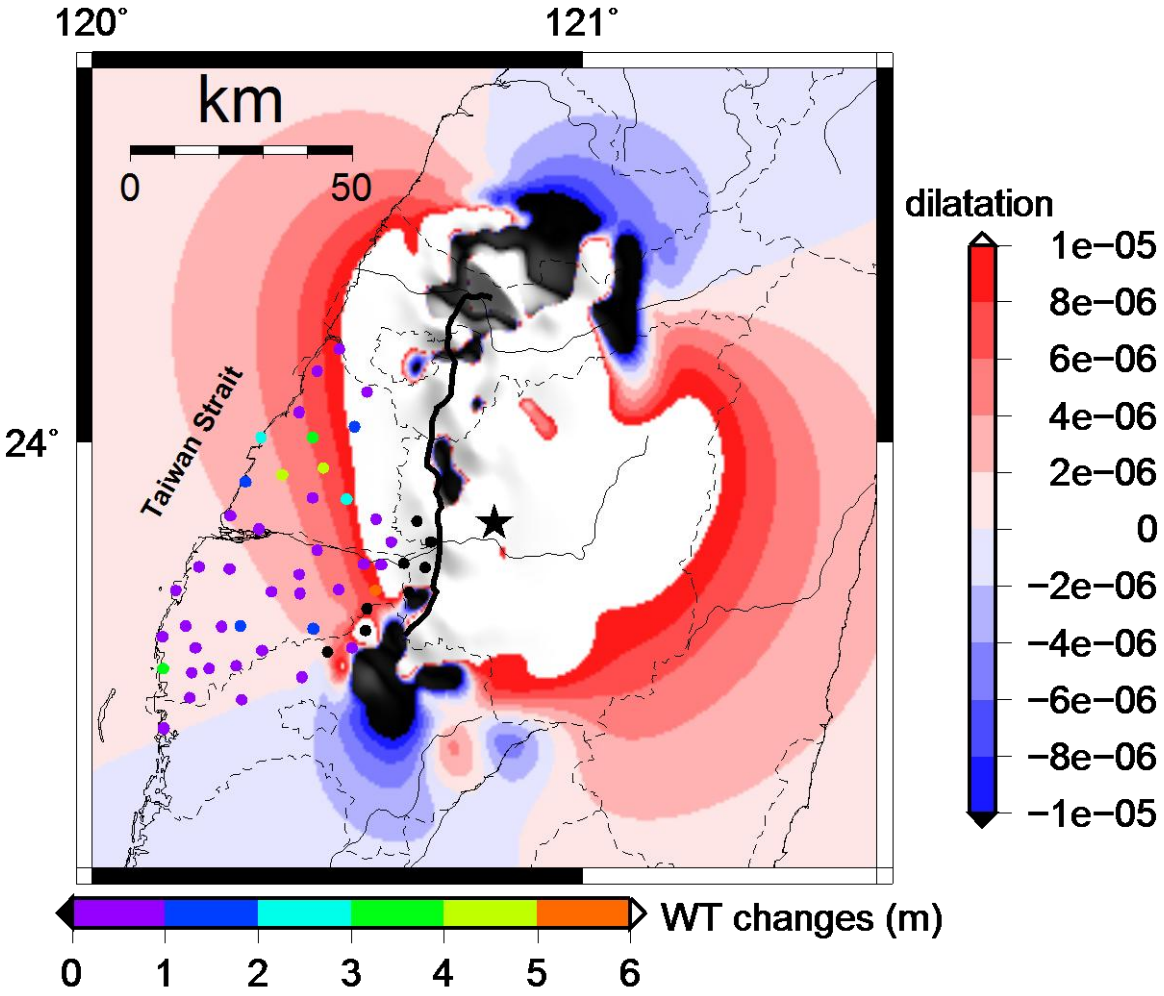

Figure 47. Widespread coseismic increases (49 wells) in water-table elevation were observed to occur in zones that underwent tensional strain (grey to red colored zones) in contrast to the coseismic strain hypothesis. Decreases in water-table elevation (9 wells) were observed within 15 km of the fault plane and correspond to areas of tensional strain (grey to red colored zones in the model). Well locations are represented by round dots; black dots correspond to decreases in water-table elevation. The Chelungpu fault is demarcated by a black line. Black star indicates focal point for fault rupture. Calculation depth was set to 0 m.

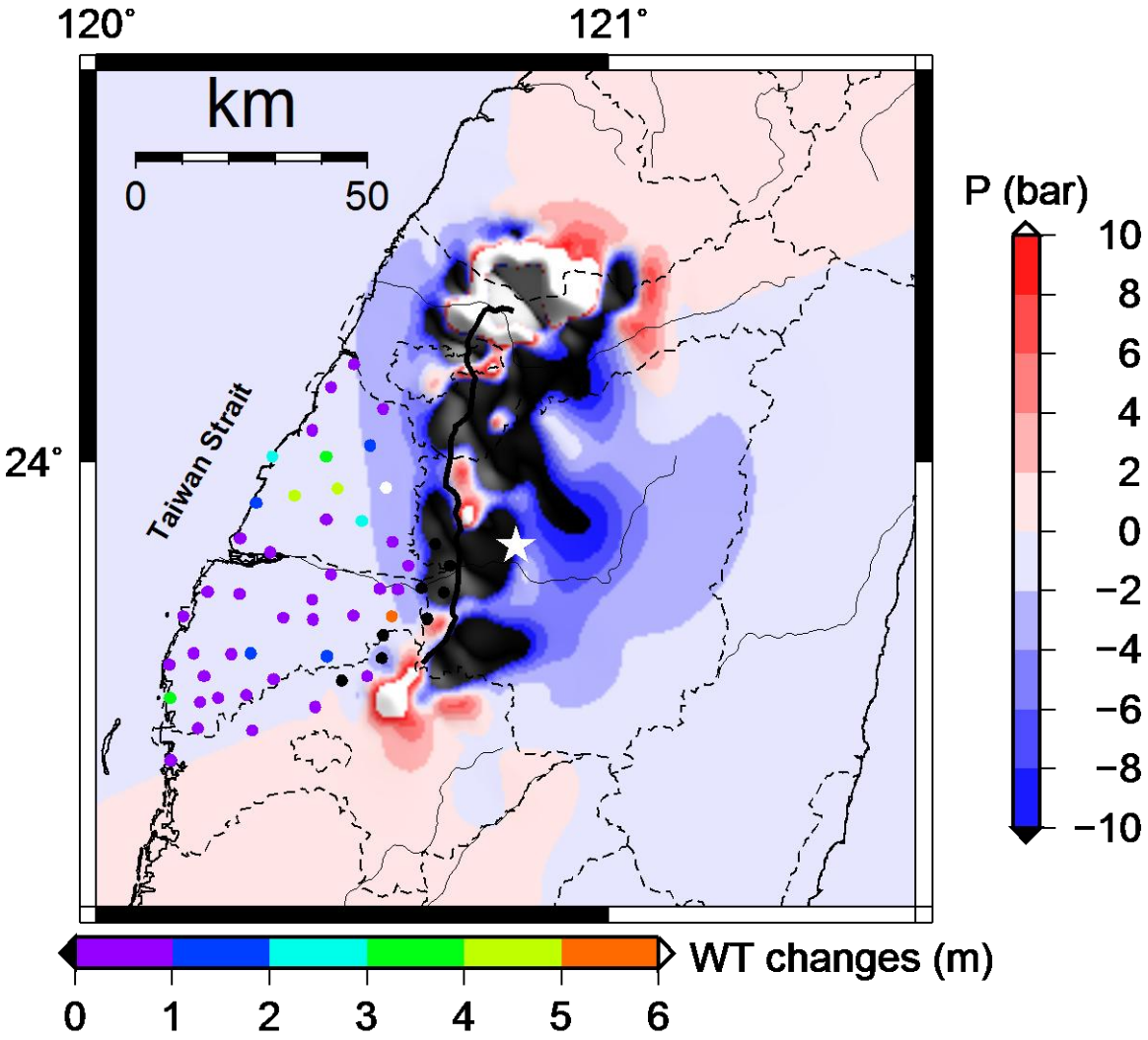

Figure 48. Widespread increases (49 wells) in water-table elevation were observed to occur in zones that were calculated to have decreases in pore-pressure (grey to blue colored zones), contrasting with the coseismic strain hypothesis. Decreases in water-table elevation (9 wells) were observed to occur within 15 km of the fault plane and correspond to areas of decreased pore-pressure (grey to blue colored zones in the model). Well locations are represented by round dots; black dots correspond to decreases in water-table elevation. The Chelungpu fault is demarcated by a black line. White star indicates focal point for fault rupture. Calculation depth was set to 0 m.

Manga (2001) postulated a third mechanism for invoking hydrologic change. This hypothesis states that strong seismic shaking could preferentially re-arrange unconsolidated sediments into a tighter packing scheme (compaction). Although, this mechanism cannot be applied to more consolidated sedimentary sequences in the proximal zone, it could be applied to the more unconsolidated Alluvial Plain sediments. The compaction of grains coincident with the passing of seismic waves leads to a sudden reduction of primary porosity. A sudden reduction in primary porosity by seismic shaking could therefore produce an expulsion of pore-fluids out the pore-spaces and lead to the elevated water-tables that were observed (Wang et al., 2004). Although this hypothesis was not tested directly by this study, moderate to severe amounts of liquefaction (75 sites) within the fan and small degrees of hill slope failure were observed (Wang et al., 2003). Both of these observations could lend evidence to coseismic compaction as the dominant mechanism for invoking hydrologic anomalies within the fan.

Post-seismic Pore Pressure Diffusion

Generally, the wells studied recovered sporadically over the 100 days following the Chi-Chi earthquake (Appendices A to C). Only 16 of the 41 wells with complete data illustrated a relatively smooth and continuous dissipation pattern over the 100 day time-span. One (KC) of the six wells analyzed in the proximal zone showed a smooth and continuous recovery (Appendix A); 10 out of 19 wells analyzed in the middle zone displayed a continuous recovery back to pre-seismic levels (Appendix B), and 5 of 16 wells in the distal zone displayed a smooth recovery (Appendix C). The majority of the other wells showed an oscillating style of recovery. A few of the wells (Fig 49) that

showed coseismic drops in water-level continued to drop with time, perhaps indicating a permanent change in hydraulic conductivity (*K*) in the aquifer, or permeability enhancement generated by seismic fracturing (Rojstaczer and Wolf, 1994). A significant amount of the oscillating recovery patterns took place in wells that showed minimal coseismic changes. These small variations could be caused by seasonal or daily factors (i.e., local pumping, tidal response, or barometric pressure).

It is difficult to properly analyze the diffusion patterns observed over the 100 days following the Chi-Chi earthquake. Unlike the coseismic response of the wells, in which there appears to be correlations among the piezometric response, proximity to the fault, and the type of geology, the well recoveries show no strong correlation with proximity to the fault zone or type of geology.

Of the 5 monitoring wells located near the Chelungpu fault that registered coseismic drops (Fig. 49), only one well (LY) showed a continuous decline in water-level over the 100-day period. One well (TH) followed with an extreme rise in water-table in the 50 days following the earthquake (Fig. 50). The other three wells registered an oscillating style pattern in which there was a recovery back towards pre-earthquake levels followed by another drop in water-table. This irregular recovery pattern indicates that the local groundwater system may have been permanently altered by the deformation generated by the earthquake and perhaps a new steady-state condition will be established slowly in concordance with new aquifer properties.

Another possible explanation for the variances seen in the water-level data is that aftershocks generated by the transfer of stress and also possibly changes in pore-pressure could have resulted in another series of deformation induced water-table changes. Chi

and Dreger (2004) show that two M_w = 6.2 or greater aftershocks occurred in the week following the Chi-Chi mainshock (Table 4). In total there were a total of 5 M_w = 5.8 or greater aftershocks following the Chi-Chi earthquake. Of these five, four were observed to be reverse-slip earthquakes. These findings make a simple analysis of water-table recoveries even more difficult. Regardless of possible permanent changes to the aquifers or impacts created by aftershocks, simple pore-pressure diffusion and resulting groundwater flow does not restore all water-tables to previous levels and thus is probably not the logical mechanism governing the post-seismic response.

Table 4. Aftershocks may play a factor in the sporadic water-table patterns following the Chi-Chi mainshock. Two large magnitude aftershocks occur in the week following the Chi-Chi earthquake

Aftershock ID	Date	M_w
0014	9/22/99	6.2
2352	9/25/99	6.3

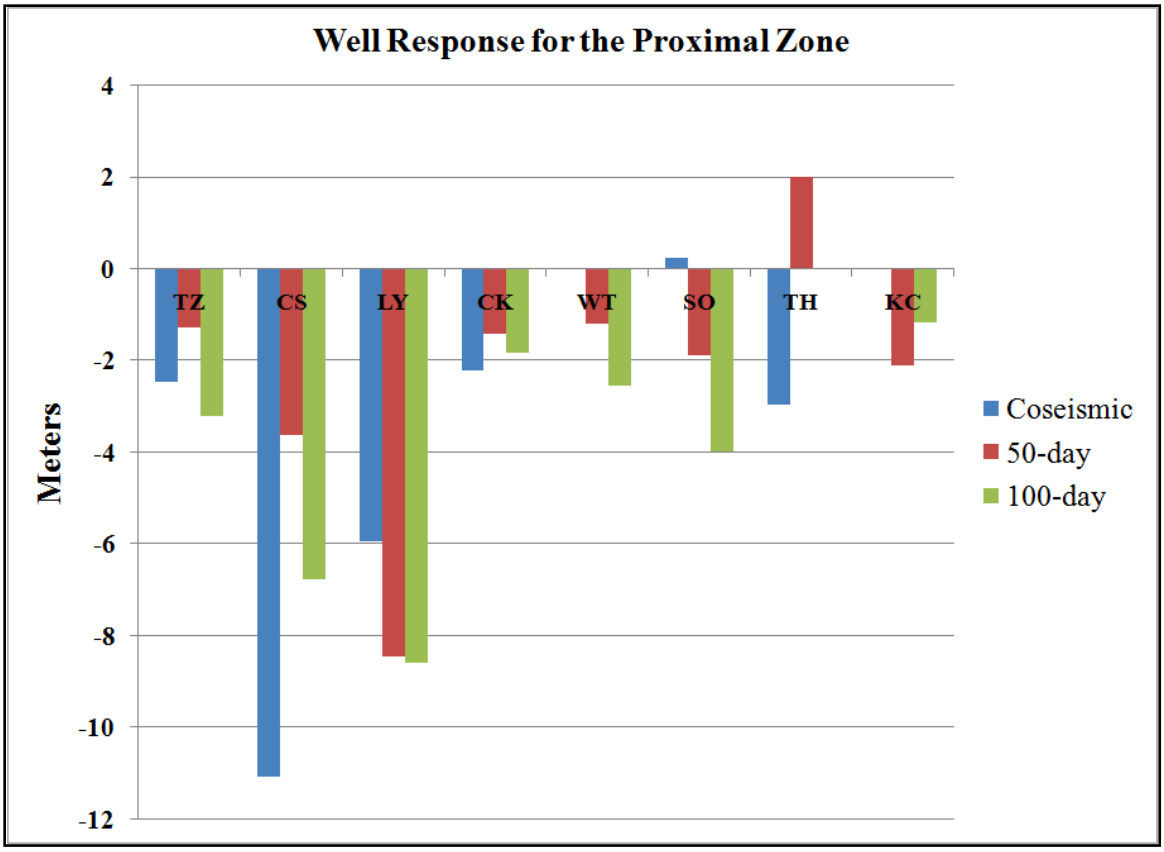

Figure 49. Observed post-seismic recovery of proximal wells (<15 km) shows a general coseismic decrease in water-level. The recovery pattern plotted over 100 days is sporadic. Wells do not generally recover back to pre-seismic levels (0 m). This suggests that volumetric strain and subsequent diffusion are not the dominant mechanism for inducing these changes.

The remaining wells were examined with regard to regional context (Fig. 50 to 53) and 100-day responses. The monitoring wells located in the northern portion of the middle and distal fans showed very large coseismic rises and similar declines in the time period following the earthquake. Prevalent oscillating recovery patterns were found especially within wells that showed small coseismic changes. These oscillations can most likely be attributed to daily and seasonal variations. Several prominent up-up responses, in which coseismic increases were followed with continued water-level increase, were found along the coastal region (Fig. 52 to 53). However, it is unknown as to why these responses occurred mainly along the coastal region. Increasing water-table elevations indicate these regions could be induced groundwater sinks or perhaps local irrigation may play a large role in the 100-day response.

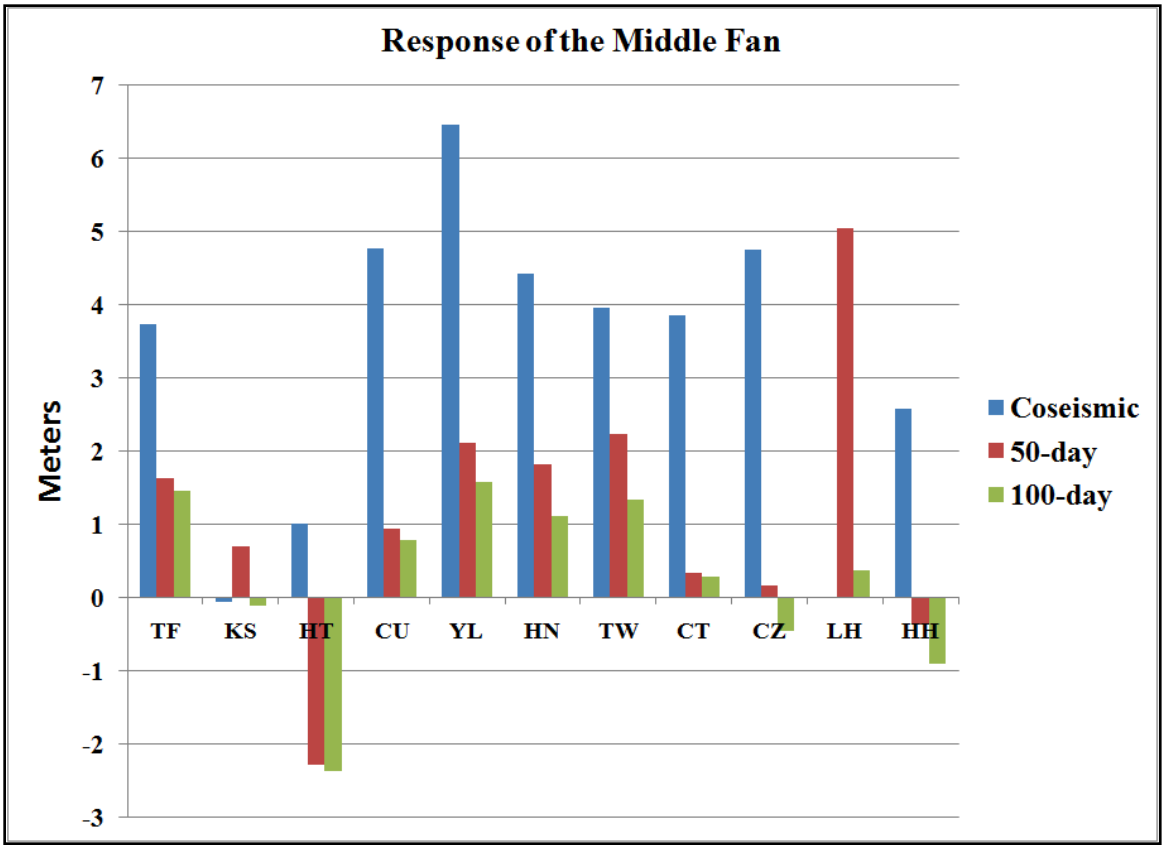

Figure 50. Observed post-seismic recovery patterns for wells located within the middle of the Choshui River alluvial plain (15-30 km from fault).Strong coseismic increases in water-table are found, eliminating coseismic volumetric strain as an inducing mechanism. Some of the recoveries show a step-wise decrease back to a pre-seismic levels; however, others show very irregular recoveries.

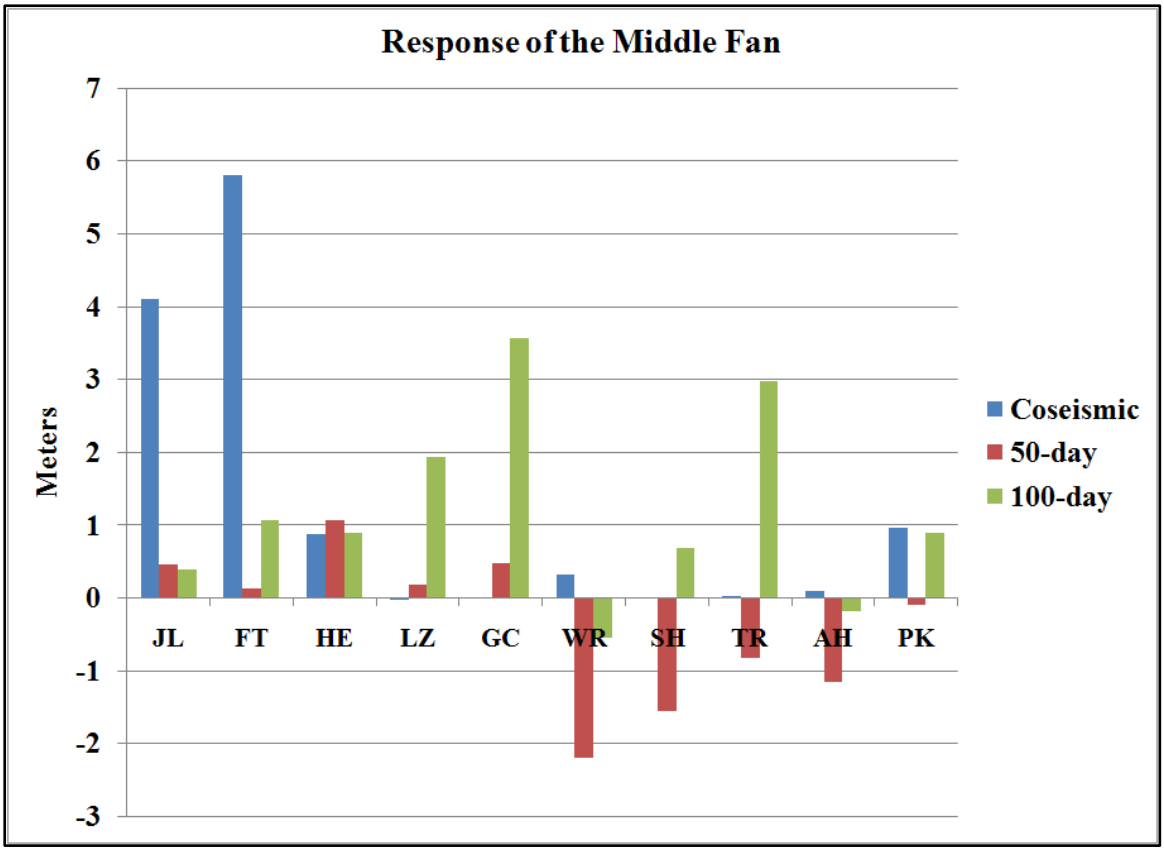

Figure 51. Observed post-seismic recovery patterns for wells located within the middle of the Choshui River alluvial plain (15-30 km from fault).Strong coseismic increases in water-table are found, eliminating coseismic volumetric strain as an inducing mechanism. One of the recoveries show a step-wise decrease back to a pre-seismic levels (JL); however, most show very irregular recoveries.

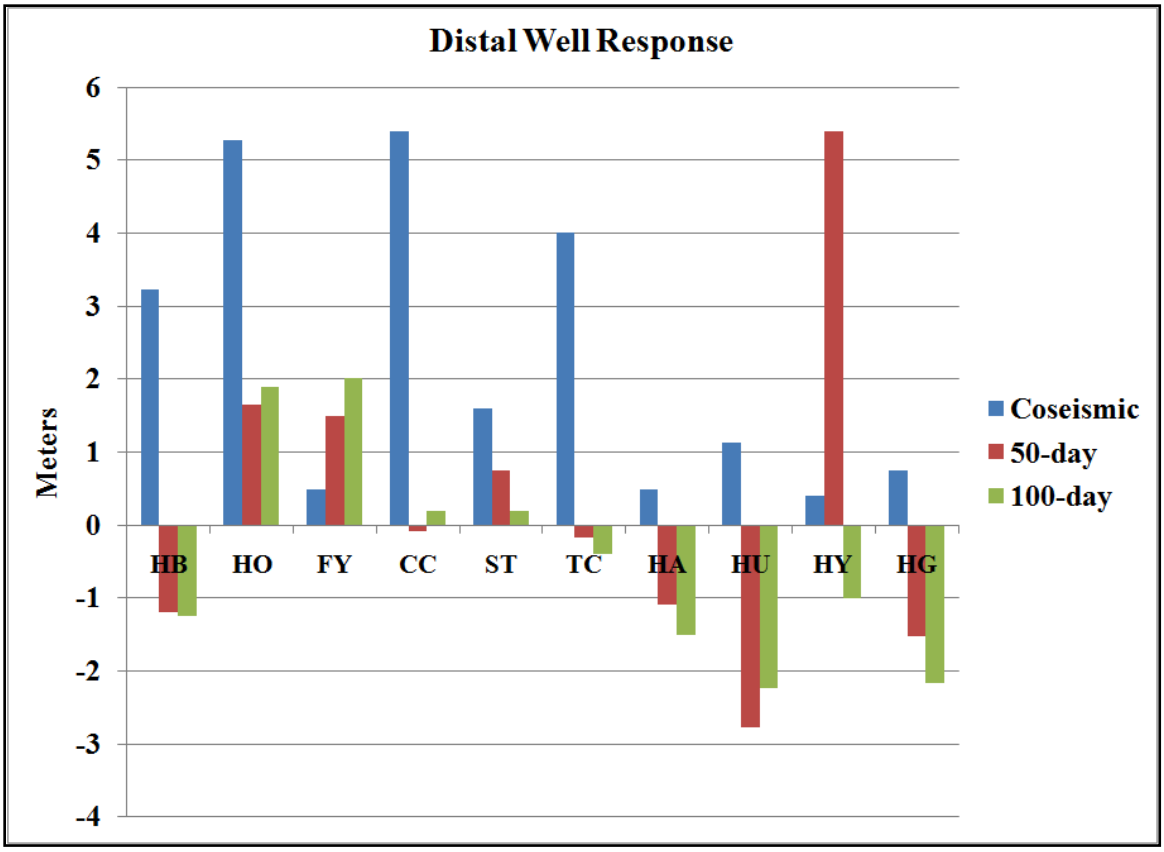

Figure 52. Observed post-seismic recovery patterns for wells located within the distal portion of the Choshui River alluvial plain (< 30 km).Strong coseismic increases in water-table are found, eliminating coseismic volumetric strain as an inducing mechanism. One of the recoveries (ST) shows a step-wise decrease back to pre-seismic level.

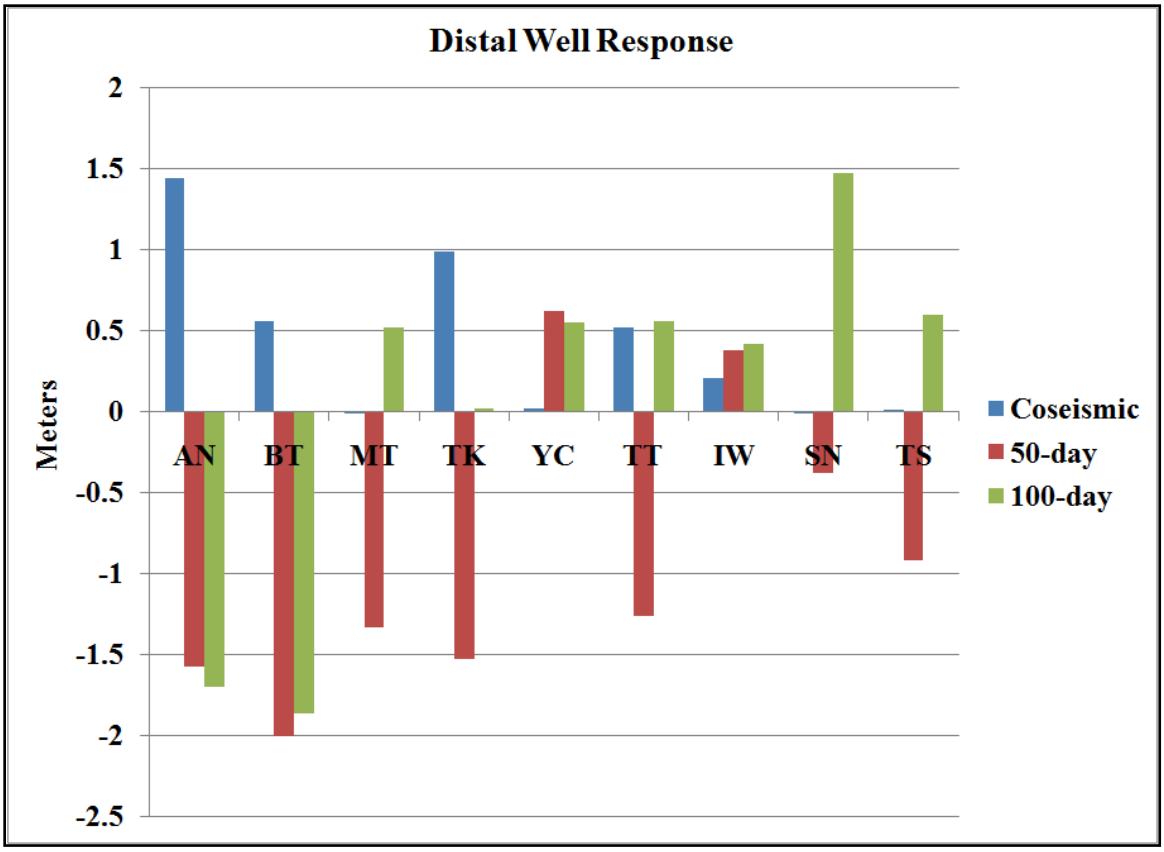

Figure 53. Observed post-seismic recovery patterns for wells located within the distal portion of the Choshui River alluvial plane (< 35 km). Weak coseismic increases in water-table are found, eliminating coseismic volumetric strain as an inducing mechanism. The recovery pattern for every well is sporadic.

Rainfall events in the Changhua and Yunlin counties over the 100 days (Fig. 54) following the Chi-Chi earthquake were found to produce relatively small and localized amounts of precipitation. From the 0 to 50 day time span, both counties reported approximately 25 millimeters of rainfall. In the time span from 50 days to 100 days, the counties reported precipitation totaling slightly more than 25 millimeters. Only incremental changes in water-table could be attributed to these events.

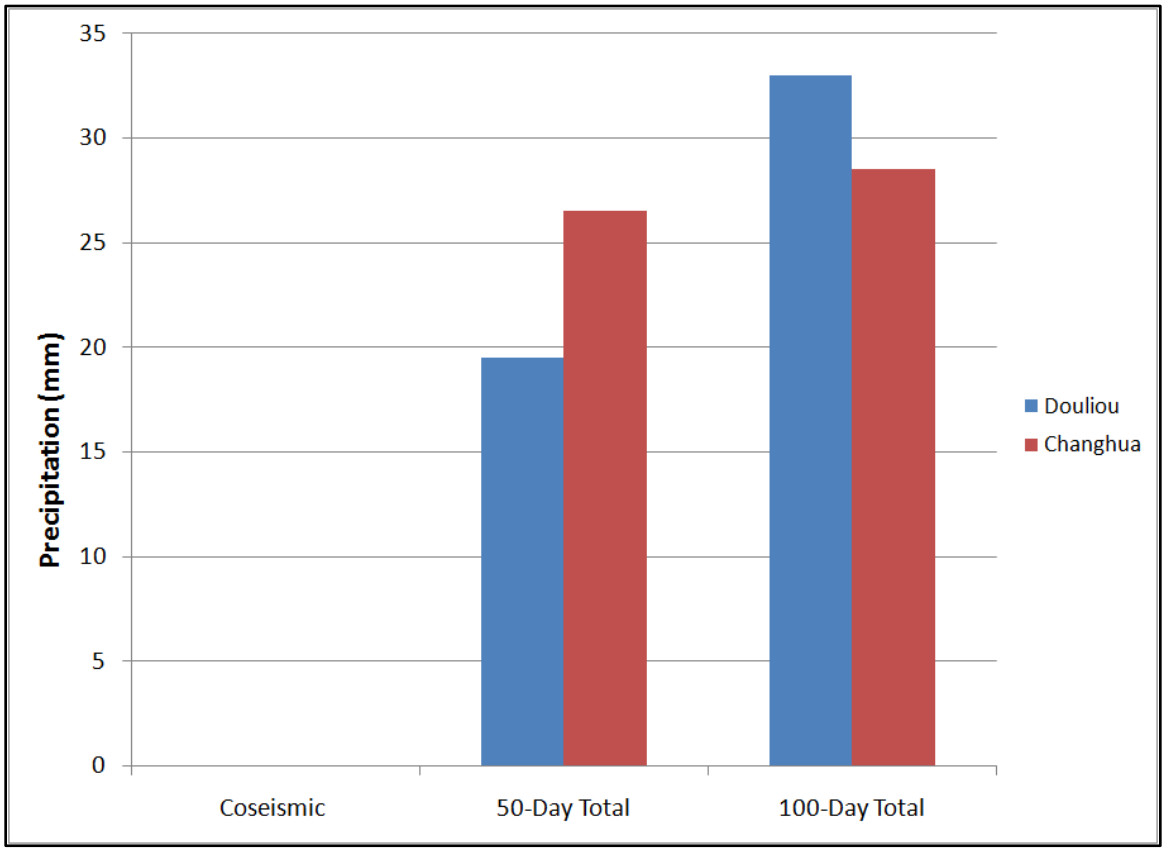

Figure 54. Rainfall for the cities of Douliou and Changhua show marginal rainfall (around 2 inches total or 55 mm). These amounts are not significant enough to produce widespread variations in the water tables.

The chaotic well recovery pattern observed within the Western Foothills slope region and Choshui River alluvial fan may help to shed light on the mechanisms responsible for invoking anomalous hydrologic changes following the Chi-Chi earthquake. PFLOW modeling of the Choshui River alluvial fan and slope show that regions of induced excess or decreased pore-pressure change gradually returned to a pre-seismic steady state condition following the earthquake. Furthermore, these results show that after 100 days, most anomalous fluid-pressure had dissipated. The time period in which the pressure returned back to steady state was dependent upon the magnitude and spatial variation of hydraulic conductivity (K) for the slope and fan regions. However, relatively few to no oscillations in pressure where found to occur over the course of diffusion back to steady-state in the respective PFLOW models. This predicted diffusion pattern is in contrast with to the observed sporadic recovery patterns.

In addition, only 16 of the 41 wells recovered back to a pre-existing state, and oddly, one of the wells continued to show decreases in water-level over a 100-day span. If coseismic volumetric strain and elastic deformation was the only mechanism controlling the hydrologic response of these wells, then there should be a relatively smooth, continuous recovery of hydraulic head through pore-pressure diffusion with time.

Results from this study essentially point to two likely mechanisms for hydrologic changes observed in the alluvial fan: fracture-induced permeability enhancement and coseismic compaction. Fracture-induced permeability could significantly alter the dissipation patterns. Strong ground motion generated by the earthquake led to wide-scale fracturing within the Western Foothills (Lin et al., 2004). In this region, the passing of

seismic waves could have also cleared sediments from the pre-existing fractures and cracks. Both of these factors could create new conduits or close others for fluid flow and thus, could explain why some of the wells continued to show decreases in hydraulic head after the seismic waves had passed, while others showed a sporadic response with time.

Rojstaczer and Wolf (1994) suggested that fracturing of perched aquifers associated with the Loma Prieta earthquake could have contributed to increases in stream discharge at lower elevations. Fluids within perched aquifers located in the upper slope and Western Foothills could have been breached downslope, as confining beds located beneath the aquifer became fractured. Since groundwater located at higher elevations also has a higher potential (hydraulic head) than the surrounding regions, water would flow in the direction of the induced gradient (downhill). This coseismic and post-seismic release of water from higher elevations to zones down-gradient could explain the delayed discharges at lower elevations. Similarly, the flow of the fluids down gradient could also be used to explain abrupt coseismic decreases in the discharge of the Choshui River near the fault zone.

Prior discussion shows that a coseismic compaction mechanism is most likely the dominant factor for invoking wide-spread increases in water-level within the Choshui River alluvial fan, but can this model be used to explain the observed dissipation patterns? The consequent coseismic re-packing of sediments alters the permeability of the sediments and results in changed hydraulic conductivity. This could serve to significantly alter the diffusion rates. Instead of seeing a smooth and continuous diffusion back to a steady-state, changes in permeability and conductivity could also alter pre-existing flow paths or lead to new migratory pathways altogether. Thus dissipation would occur, but

would be dictated by the new hydraulic properties of the fan. The observed recovery rate for well JL was modeled against the theoretical (calculated) recovery rates using different values of hydraulic conductivity (Fig. 55). Modeling results for this well show that recovery took place much slower than with its pre-seismic hydraulic conductivity value, providing strong evidence of decreased conductivity caused by coseismic compaction.

Furthermore, coseismic compaction may also contribute to the observed stream discharge values in the alluvial fan (Baird, 2002; Manga et al., 3003). The expulsion of pore-fluids from the upper aquifers could increase the amount of base-flow to the streams and explain observed increases (Fig. 12).

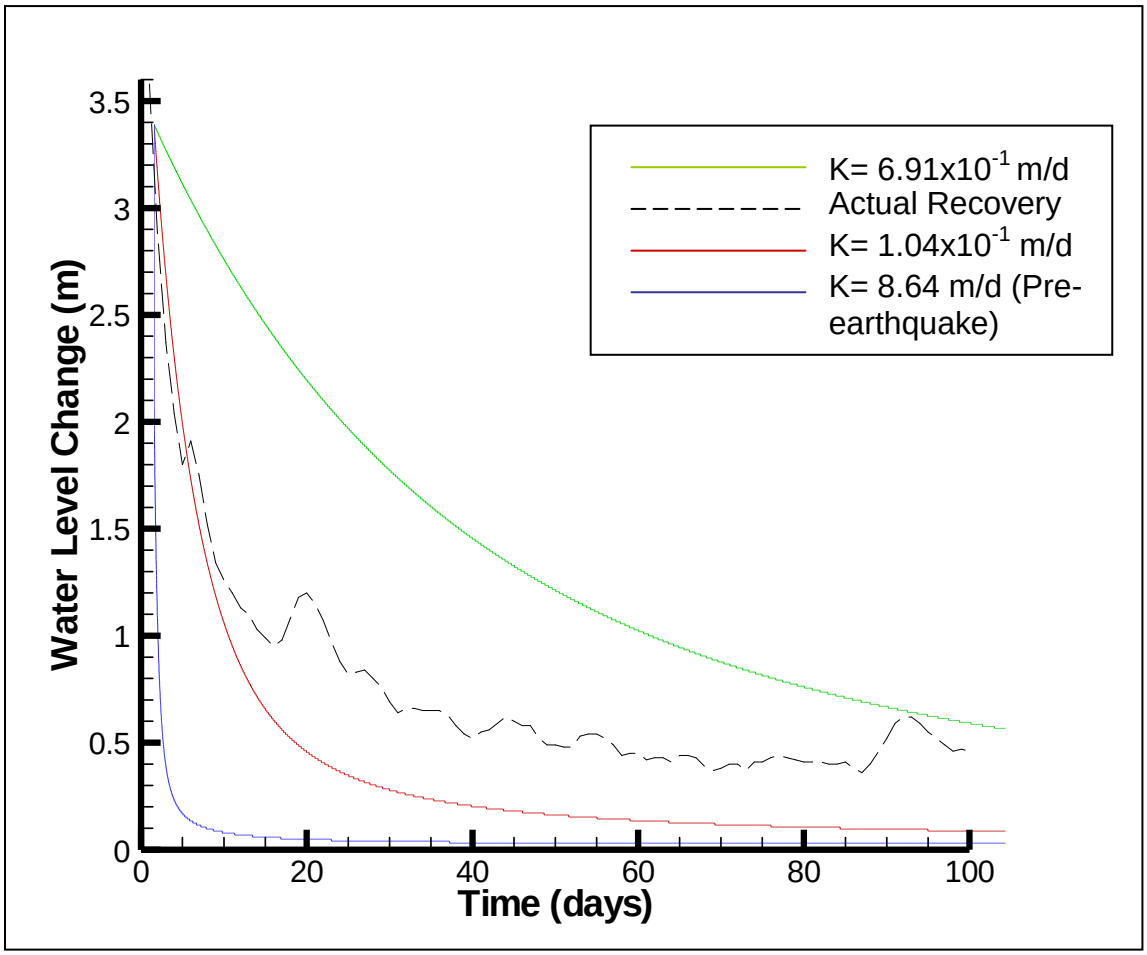

Figure 55. Observed water-table dissipation for well JL. The observed recovery (dashed-line) does not match the recovery modeled with pre-seismic hydraulic conductivity values. This suggest that seismic waves decreased the hydraulic conductivity value of the alluvial fan sediments in this region from 8.64 m/d to between 6.9 x 10^{-1} m/d and 1.04 x 10^{-1} m/d. Black dashed-line indicates observed recovery. Blue line indicates recovery with pre-seismic hydraulic conductivity. Green and red lines are modeled recoveries.

Importance of Hydraulic Conductivity

The importance of hydraulic conductivity as a dominant factor for controlling diffusion patterns was evident from the pore-pressure models. In general, rocks and sediments with intrinsically higher hydraulic conductivity values were found to accommodate the diffusion of excess pressure with much greater ease. Formations that are comprised mainly of gravels, coarse-sands, or coarse-grained sandstones will allow for faster diffusion rates when compared to those dominated by silt, mud, or similar lithologies. Similarly, rocks and sediments with intrinsically low hydraulic conductivities (i.e., shale, crystalline bedrock) will maintain pore-pressure changes longer, because pressure does not propagate quickly into adjacent formations. Results from this study show that by decreasing the magnitude of hydraulic conductivity (K) by one order of magnitude, the corresponding time to diffuse excess pressure on the order of 1×10^6 Pa by 95% increases from 30 days to almost 200 days. Such strong a correlation between diffusion time and hydraulic conductivity highlights the type of geologic media (i.e., geologic layering) as the dominant variable for determining diffusion rates following a large magnitude earthquake.

Summary and Conclusions

This study integrates numerical modeling with the analysis of hydrogeologic field data to explore the hydrodynamic response of the Choshui River alluvial fan and upper slope region to crustal deformation generated by the 1999 Chi-Chi earthquake. Piezometric data were gathered from the Water Resources Bureau (WRB) of Taiwan to study the observed co- and post-seismic response of aquifers in the alluvial plain. Strain modeling was integrated with a pore-pressure diffusion model to create a one-way coupled model that investigates coseismic volumetric strain (Muir-Wood and King, 1993) as a tenable mechanism for inducing the observed hydrologic anomalies and subsequent diffusion.

Strong declines in water-level were found to occur within the calculated dilatational zone near the southern edge of the Chelungpu fault, specifically located within the upper slope region of the Western Foothills. These drops were also modeled to have occurred within a corresponding zone of decreased pore-pressure and thus, the coseismic hydrologic response can be explained by coseismic volumetric strain. However, widespread increases in water-table were found to have occurred within the Choshui River alluvial fan. These increases occurred in zones of dilatational strain and decreased pore-pressure. Therefore, coseismic volumetric strain cannot explain the hydrodynamic response of the Choshui River alluvial fan. A coseismic compaction

mechanism generated by strong seismic-shaking, provides the best explanation for the hydrologic response of the wells in the alluvial fan.

The post-seismic recovery of the 41 wells analyzed generally displayed a sporadic and chaotic recovery pattern, suggesting post-seismic changes in the sediment or rock properties. Wells showing coseismic declines were found to occur within 15 km of the Chelungpu fault can be explained by either coseismic strain or fracture-induced permeability. However, the post-seismic recovery of the proximal region did not recover smoothly, as would be the case if coseismic strain and elastic deformation was the only controlling factor. This favors fracture induced permeability enhancement (Rojstaczer and Wolf, 1994) as the dominant mechanism for controlling the post-seismic hydrodynamic response in this region. Fracture induced permeability enhancement may also explain the coseismic decrease of stream discharge for streams located in the Western Foothills and the increases in stream discharge down-slope in the Choshui River alluvial fan. At best it can be surmised that a combination of coseismic volumetric strain and fracture induced permeability could be used to explain the coseismic response of fluids contained within the upper slope near the fault rupture.

Coseismic compaction may explain the chaotic post-seismic response of fluids contained within the Choshui River alluvial fan. Compaction leading to a reduction in primary porosity could alter the hydraulic conductivities (K) of the aquifers. Modeling suggests that in some areas, conductivity may have been reduced by the effects of the earthquake and thus, supports a coseismic compaction mechanism. The resultant fluid expulsion generated by compaction could also be used to explain the coseismic increases of discharge within streams of the alluvial fan.

Pore-pressure modeling did however highlight the importance of hydraulic conductivity as the dominant factor contributing to the speed of diffusion of induced excess pore-pressure. Layers with low conductivity values maintained induced excess pressure longer and delayed re-equilibration of the pressure field. Contrastingly, higher conductivity accommodates groundwater flow and pressure dissipation; allowing faster recovery.

References

Baird, P., Hydrologic changes with the 1999 Chi-Chi earthquake, Taiwan: A Numerical study. M.S. Thesis. Dept of Geol. and Geog., Auburn University, Auburn, 2002.

Biot, M. (1941), General Theory of Three-Dimensional Consolidation, *J. of Applied Physics*, 12(2), 155-164

Bosl, W.J., and Nur, A. (2000), Crustal Fluids and Earthquakes, *in* GeoComplexity and the Physics of Earthquakes, *Geophysical monograph 120*, American Geophysical Union, 267-284.

Briggs, R.O., 1991, Effects of Loma Prieta earthquake on surface waters in Waddell Valley: *Water Resources Bulletin*, 27, 991-999

Central Geological Survey (2000), Survey report of earthquake geology in the 9/21 Chi-Chi earthquake: Taiwan, Central Geological Survey, 315 (in Chinese).

Chai, B.H.T. (1972), Structure and tectonic evolution of Taiwan. *American Journal of Science*, 272, 389-422

Chen, C.-H., Wang, W.-H., Teng, T-1. (2001), 3D velocity structure around the source area of the 1999 Chi-Chi, Taiwan, Earthquake: Before and after the main shock, *Bull. Seis. Soc. Am*., 91(5), 1013-1027.

Chen, Y.-G., Chen, W.-S., Less, J.-C., Lee, Y.-H., Lee, C.-T., Chang,H.-C., and Lo, C.-H. (2001), Surface rupture of the 1999 Chi-Chi earthquake yields insight on active tectonics of central Taiwan, *Bull. Seis. Soc. Am.*, 91(5), 977-985.

Chi, W.-C., and Dreger, D., 2004, Crustal deformation in Taiwan: Results from finite source inversions of six Mw > 5.8 Chi-Chi aftershocks, *J. Geophys. Res.*, 109, 1-19

Chia, Y., Wang, Y.-S., Chui, J.J., and Liu, C.-W., 2001, Changes of groundwater level due to the 1999 Chi- Chi earthquake in the Choshui River Alluvial fan in Taiwan, *Bull. Seis. Soc. Am.*, 91(5), 1062-1068.

Chia, Y., J. J. Chiu, Y. H. Jiang, T. P. Lee, Y. M. Wu, and M. J. Horng (2008), Implications of coseismic groundwater level changes observed at multiple-well monitoring stations, Geophys. J. Int., 172, 293– 301.

Chiang, C.-S., Yu, H.-S. and Chou, Y.-W. (2004), Characteristics of the wedge-top depozone of the southern Taiwan foreland basin system. Basin Research, 16, 65–78. doi: 10.1111/j.1365-2117.2004.00222.x

Chou , J. T. (1973), Sedimentology and paleogeography of the upper Cenozoic System of western Taiwan: Geol. Soc. China Proc.,16, 111-143

Covey, M. (1986), The evolution of foreland basins to steady state: evidence from the western Taiwan foreland basin, In: Allen, P. A. and Homewood, P. (Eds), *Foreland Basins*, International Association of Sedimentologists, Special Publication 8, 77-90

Healy, J., H., Rubey, W., W., Griggs, D., T., and Raleigh, C., B. (1968), the Denver Earthquakes, *Science*, 161, 1301-1310.

Ho, C.-S. (1975), Taiwan-di-zhi-gai-lun, Ministry of Economic Affairs, R.O.C., p. 118.

Ho, C.-S. (1986), Taiwan-di-zhi-gai-lun, Central Geological Survey, p. 164

Hsu, S. K., C. V. Chin, and L. H. Cheng (2000), The result of first stage of "Groundwater Monitoring Network Plan in Taiwan". Proceedings of water resources management in 21st century, 177–197.

Huang, H.-C. and Tseng, Y.-S. (2002), Characteristics of soul liquefaction using H/V of Microtremors in Yuan-Lin area, Taiwan, *TAO*, 13(3), 325-338.

Haung. C.-Y., Wu, W.-Y., Chang, C.-P., Tsa, S., Yuan, P.-B., Lin, C.-W., Xia, K.-Y. (1997), Tectonic evolution of accretionary prism in the arc-continent collision terrane of Taiwan, *Tectonophysics*, 281, 31-51.

Katsumata, M. and Sykes, L.R. (1969), Seismicity and tectonics of the Western Pacific: Izu-Mariana-Caroline and Ryukyu-Taiwan regions. *Journal of Geophysical Research*, 74, 5923-5948

Lai, W.-C., Koizumi, N., Matsumoto, N., Kitagawa, Y., Lin, C.-W., Shieh, C.-L., and Lee, Y.-P. (2004), Effects of seismic ground motion and geological setting on the coseismic groundwater level changes caused by the 1999 Chi-Chi earthquake, Taiwan. *Earth Planets Space*, 56, 873-880

Lee, M., Liu, T.-K., Mai, K.-F., and Chang, Y.-M. (2002), Coseismic hydrological changes associate with dislocation of the September 21, 1999 ChiChi earthquake, Taiwan, *Geophysical Research Letter*, 29(17), 1824.

Lee, M.-K., Wang, C., Kao, H., and Wolf, L., W. (2001), Numerical analysis of coseismic and postseismic changes of 1999 Chi-Chi Earthquake, Taiwan, *AGU Annual Meeting*, San Francisco.

Lee, M.-K. and Wolf, L., W. (1998), Analysis of fluid pressure propagation in heterogeneous rocks: Implications of hydrologically-induced earthquakes, *Geophysical Research Letters*, 25(13), 2329-2332.

Lin. A., Ouchi, T., Chen, A., and Maruyama, T. (2001), Nature of the fault jog inferred from a deformed well in the northern Chelungpu surface rupture zone, related to the 1999 Chi-Chi, Taiwan, ML 7.3 earthquake, *Bull. Seis. Soc. Am*., 91(5), 959-965.

Lin, A.T., A.B. Watts, and S.P. Hesselbo (2003), Cenozoic stratigraphy and subsidence history of the South China Sea margin in the Taiwan region., *Basin Research, 15*, 453-478.

Lin, J. and R.S. Stein (2004), Stress triggering in thrust and subduction earthquakes, and stress interaction between the southern San Andreas and nearby thrust and strike-slip faults, J. Geophys. Res., 109, B02303, doi:10.1029/2003JB002607.

Liu, K.-S., Shin, T.-C., and Tsai, Y.-B. (1999), A free-field strong motion network in Taiwan: TSMIP, *TAO*, 10(2), 377-396.

Lo, C.-H., and 24 other Co-authors (1999), A comprehensive summary of the hazards caused by the 9/21 Chi-Chi earthquake: Taipei, Taiwan National Center for Research on Earthquake Engineering, NRCEE – 99 – 033 (In Chinese).

Ma, K.-F., Lee, C.-T., and Tsai,Y.-B. (1999), The Chi-Chi, Taiwan earthquake: largest surface displacements on an inland thrust fault, *EOS Transactions*, American Geophysical Union, 80, 605-606.

Ma, K.-F., C.-H. Chan, and R. S. Stein (2005), Response of seismicity to Coulomb stress triggers and shadows of the 1999 M_w = 7.6 Chi-Chi, Taiwan, earthquake, *Journal of Geophysical Research*, 110, B05S19, doi:10.1029/2004JB003389.

Manga, M. (2001), Origin of postseismic streamflow changes inferred from baseflow Recession and magnitude-distance relation: *Geophysical Research Letters*, 28, 2133-2136.

Manga, M., Brodsky, E.E., and Boone, M., 2003, Response of streamflow to multiple Earthquakes and implications for the origin of postseismic dischanges: *Geophysical Research Letters*, 30(5), 1214, doi: 10.1029/2002Gl016618

Montgomery, D. and Manga, M. (2003), Stream flow and Water Well Responses to Earthquakes, *Science*, 300, 2047-2049

Muir- Wood, R., and King, G.C.P. (1993), Hydrological signature of earthquake strain, *J. Geophys. Res*., 98, 22035-22068.

Nur, A., and Booker, J.R. (1972), Aftershocks Caused by Pore Fluid Flow? *Science*, 175 (4024), 885-887

Page, B. and Suppe, J. (1981), The Pliocene Lichi Melange of Taiwan: its olistrostromal and plate-tectonic origin. *Amer. Jour. Sci.*, 281, 193-227.

Roeloffs, E. (1988), Hydrologic precursors to earthquakes: A review, *Pure Appl. Geophys.*, 126, 177–209.

Okada, Y. (1992), Internal deformation due to shear and tensile faults in half-space, *Bull. Seis. Soc. Am*., 28, 1018-1040.

Rojstaczer, S. and Wolf, S. (1994), Hydrologic changes associated with the earthquakes in the San Lorenzo and Pescadero drainage basins, in the Loma Prieta, California, Earthquake of October 17, 1989- Hydrologic disturbance, Rojstaczer S. (ed.), *U.S. Geological Survey Prof. Paper*, 1551-E, E51-E64.

Seed, H.B., and Lee, K.L. (1966), Liquefaction of Saturated Sands during cyclic loading: *Journal of Soil and Mechanic Foundation Division, American Society of Civil Engineers*, 92, 105-134.

Simpson, D.W. (1986), Triggered Earthquakes, *Annual Review of Earth and Planetary Sciences*, 14, 21-42.

Shih, R.-C., Ho, S.-J., Chang, H.-C., and Lin, C.-W. (2000), Preliminary subsurface images of the Chelungpu fault by using shallow seismic reflection, *Proceedings of International Workshop of Annual Commemoration of Chi-Chi Earthquake*, September 18-20, 2000, Taipei, Loh, C.-H., Liao, W.-I., 123-132.

Shin, T.-C. and Teng, T.-L. (2001), An Overview of the 1999 Chi-Chi, Taiwan, earthquake, *Bull. Seis. Soc. Am*., 91(5), 895-913.

Sibson, H.H. (1994), Crustal stress, faulting, and fluid flow, Geofluids: Origin, Migration, and Evolution of Fluids in Sedimentary Basins, Parnell, J. (ed.), *Geophysical Society Special Publication*, 78, 69-84.

Skempton, A. W. (1954), The pore-pressure coefficients A and B, *Geotechnique*, 4, 143-147.

Teng, L. S. (1987a), Stratigraphic records of the late Cenozoic Penglai Orogeny of Taiwan: *Acta Geol. Taiwan*., 25, 205-224.

Teng, L.S. (1990), Geotectonic evolution of late Cenozoic arc-continent collision in Taiwan, *Tectonophysics*, 183, 57-79

Toda, S., R. S. Stein, K. Richards-Dinger and S. Bozkurt (2005), Forecasting the evolution of seismicity in southern California: Animations built on earthquake stress transfer, *J. Geophys. Res*., B05S16, doi:10.1029/2004JB003415. earthquakes,

Wang, H.,F. and Anderson, M., P. (1982), Introduction to groundwater modeling: Finite difference and Finite element methods, W.H. Freeman and Company, New York.

Wang, C,-Y., Li, C.-L., Su, F.-C., Leu, M.-T., Wu, M.-S., Lai, S.-H., and Chern, C.-C. (2002), Structural mapping of the 1999 Chi-Chi earthquake fault, Taiwan by seismic reflection methods, Tao, 3, 211-226

Wang, C.-H., Peng, T.-R., Chen, W.-F., Lee, M.-K., and Chiang, C.-J. (2001), Hydrogen and oxygen isotopic variations of Choshuichi ground water before and after the Cho-Cho earthquake, *Proceeding of the Third Symposium on Ground water Resources and water Protection*, Pintug Technology University, Pintug, Taiwan

Wang, C.-Y., Cheng, L.-H., Chin, C.-V., and Yu, S.-B. (2001), Coseismic hydrologic response of an alluvial fan to the 1999 Chi-Chi earthquake, Taiwan, *Geology*, 29, 831-834.

Wang, C.-Y., Dreger, D.S., Wang, C.-H., Mayeri, G., and Berryman, J.G. (2003), Field Relations among coseismic ground motion, water level change and liquefaction for the 1999 Chi-Chi (Mw=7.5) earthquake, Taiwan, *Geophysical Research Letters*, 30.

Wang, C.-Y., Wang, C.-H, Manga, M., 2004, Coseismic release of water from the mountains: Evidence from the 1999 (M_w = 7.5) Chi-Chi, Taiwan, earthquake, Geological Society of America, 32.

Wong, A. and Wang, C.-Y., 2007, Field relations between the spectral composition of Ground motion and hydrological effects during the 1999 Chi-Chi (Taiwan)Earthquake, *J. of Geophys. Res.*, 112, B10305, doi: 10.1029/2006JB004516.

Water Resources Bureau, 2000, Survey report of surface water and groundwater level fluctuations during the 1999 Chi-Chi earthquake, Taiwan, *Water Resource Bureau*, 37. (in Chinese).

Wolf, L.W., Rowe, C.A., and Horner, R.B., 1997 Periodic Seismicity near Mt. Ogden on the Alaska-British Columbia border: A case for Hydrologically-triggered earthquakes? *Bull. Seis. Soc. Am*, 87, 1473-1483.

Yu, S.-B., and 12 other Co-Authors, 2001, preseismic deformation and coseismic displacements associated with the Chi-Chi, Taiwan, Earthquake, *Bull. Seis. Soc. Am.*, 91(5), 995-1012.

Appendix A: Proximal Well Time-Series Plots

A 100 day time-series was plotted for each well within the proximal zone (< 15 km) using daily averages. The dominant coseismic response was down, however here more interest is expressed in the post-seismic response. Generally, the wells show a sporadic post-seismic response. Outside influences such as local pumping or aftershocks may play major roles in the variations observed within these diagrams. Clearly, simple pore-pressure diffusion modeling cannot explain these patterns (as all curves would show a steady and continuous curve back to pre-seismic levels and maintain this level with some regularity). The timing of the Chi-Chi earthquake is marked by the black arrow. Possible responses caused by aftershocks are marked by red arrows.

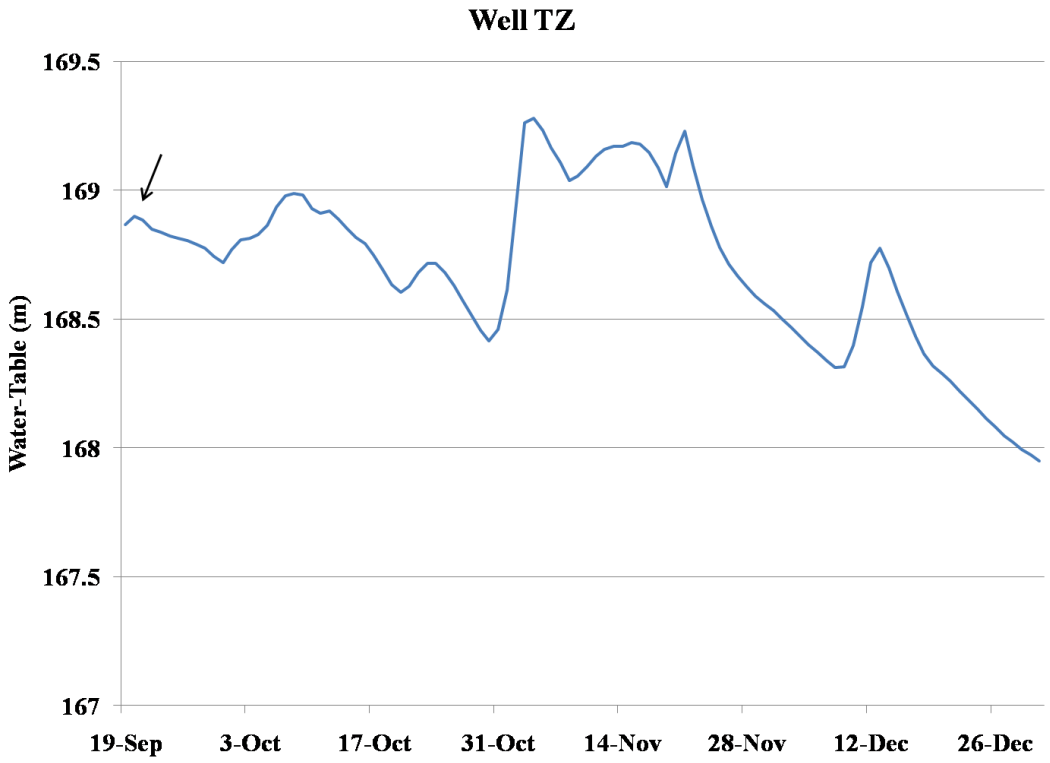

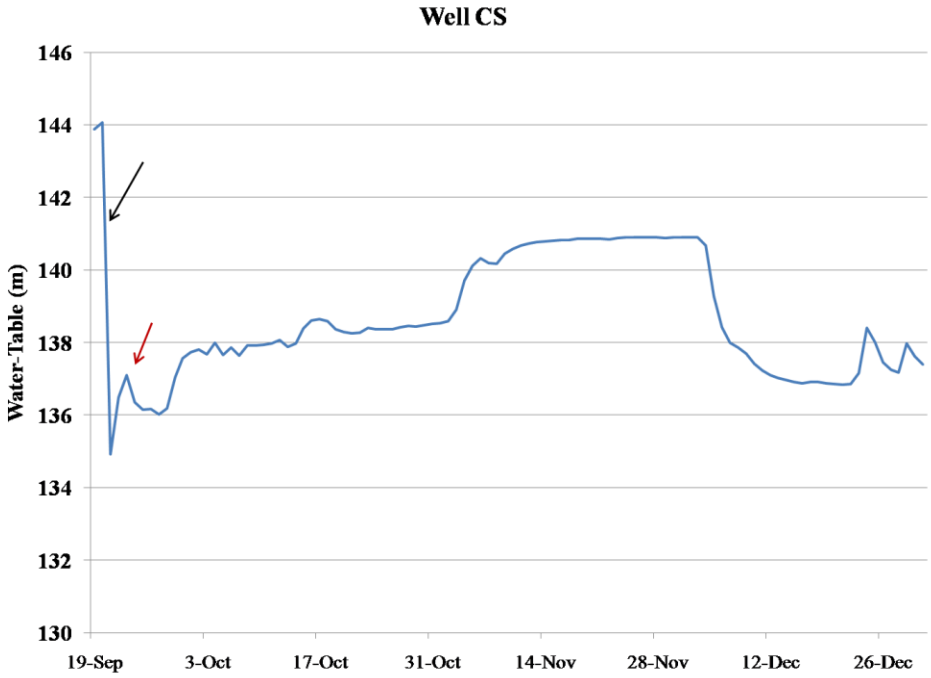
Well CS
Water-Table (m)
146
144
142
140
138
136
134
132
130
19-Sep
3-Oct
17-Oct
31-Oct
14-Nov
28-Nov
12-Dec
26-Dec

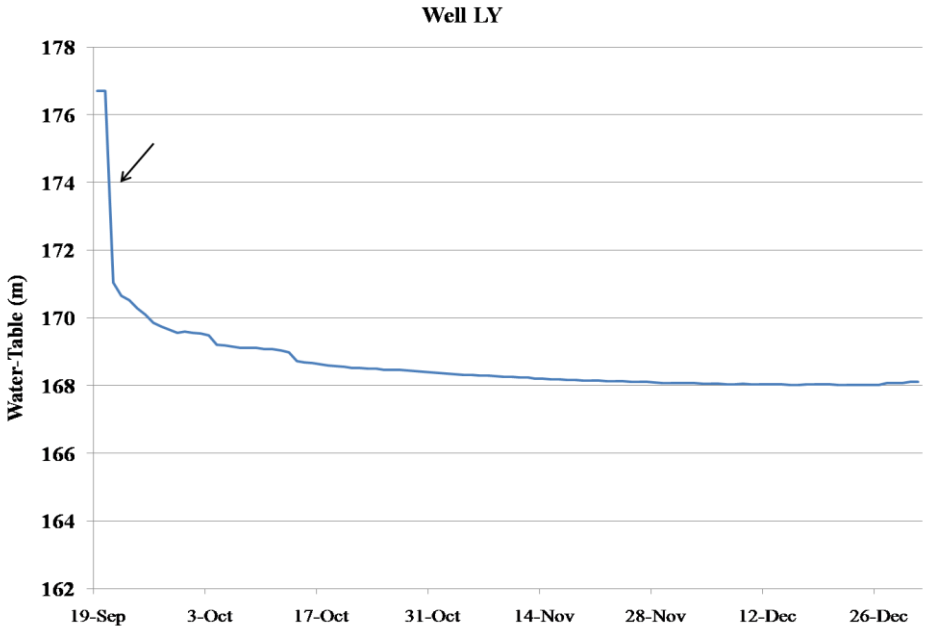
Well LY
Water-Table (m)
178
176
174
172
170
168
166
164
162
19-Sep
3-Oct
17-Oct
31-Oct
14-Nov
28-Nov
12-Dec
26-Dec

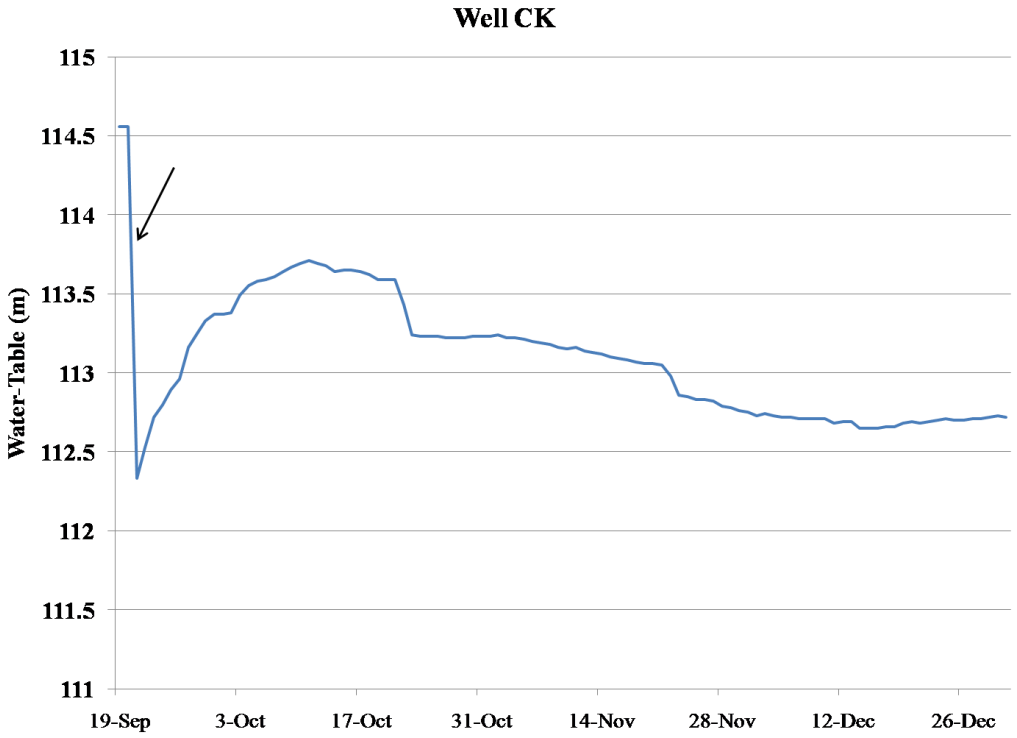
Well CK
Water-Table (m)
115
114.5
114
113.5
113
112.5
112
111.5
111
19-Sep
3-Oct
17-Oct
31-Oct
14-Nov
28-Nov
12-Dec
26-Dec

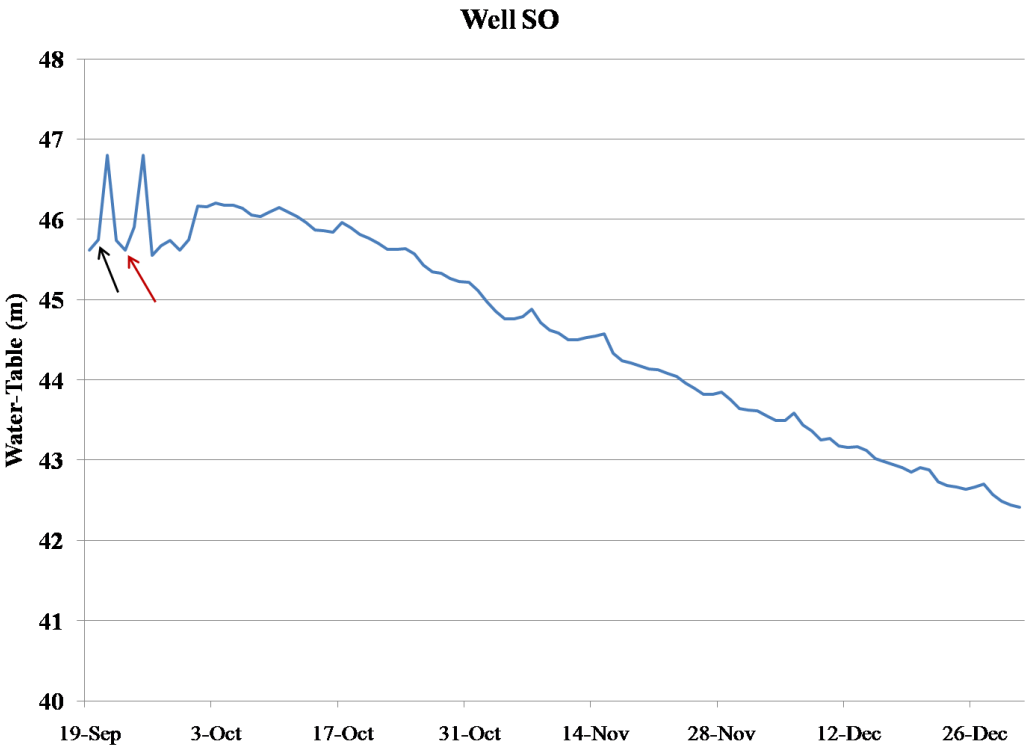
Well SO
Water-Table (m)
48
47
46
45
44
43
42
41
40
19-Sep
3-Oct
17-Oct
31-Oct
14-Nov
28-Nov
12-Dec
26-Dec

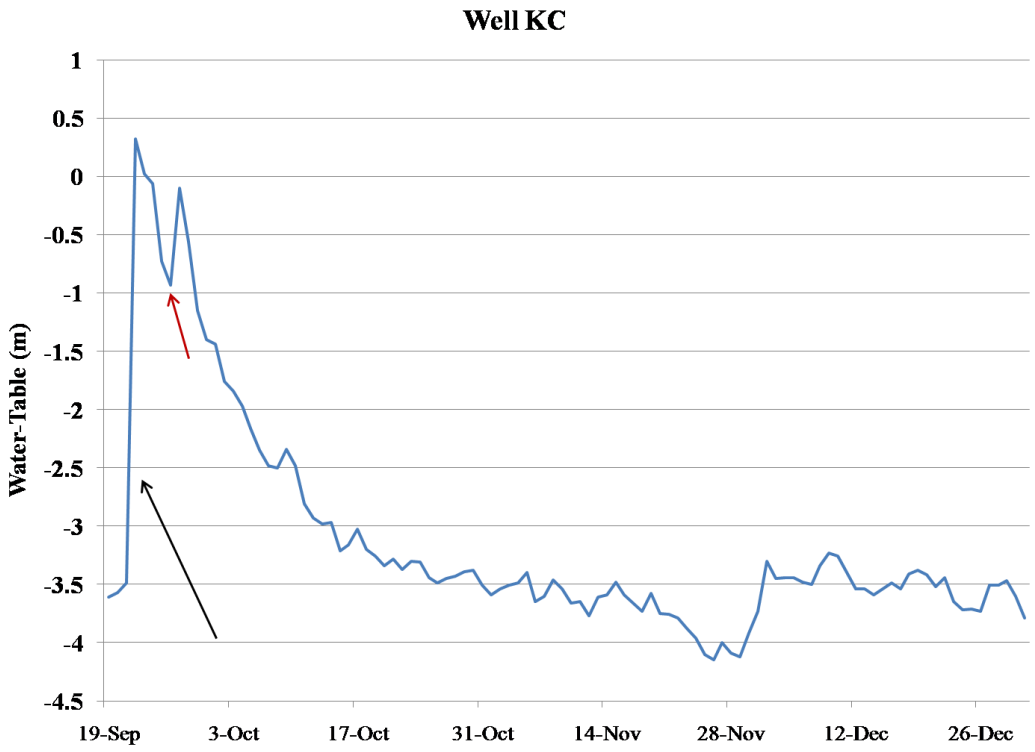
Well KC
Water-Table (m)
1
0.5
0
-0.5
-1
-1.5
-2
-2.5
-3
-3.5
-4
-4.5
19-Sep
3-Oct
17-Oct
31-Oct
14-Nov
28-Nov
12-Dec
26-Dec

Appendix B: Middle-Fan Time-Series

A 100 day time-series was plotted for each well within the middle-fan zone (15-35 km) using daily averages. The dominant coseismic response was up, however here more interest is expressed in the post-seismic response. Generally, the wells show a sporadic post-seismic response. Outside influences such as local pumping or aftershocks may play major roles in the variations observed within these diagrams. Clearly, simple pore-pressure diffusion modeling cannot explain these patterns (as all curves would show a steady and continuous curve back to pre-seismic levels and maintain this level with some regularity). The timing of the Chi-Chi earthquake is marked by the black arrow. Possible responses caused by aftershocks are marked by red arrows.

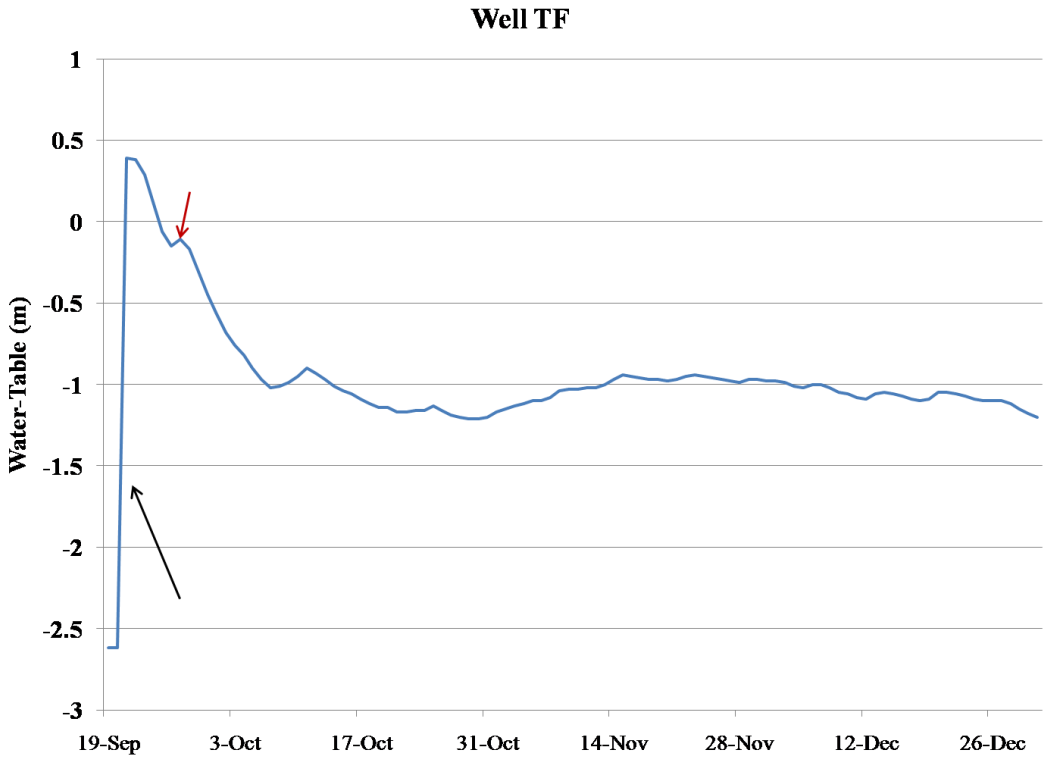

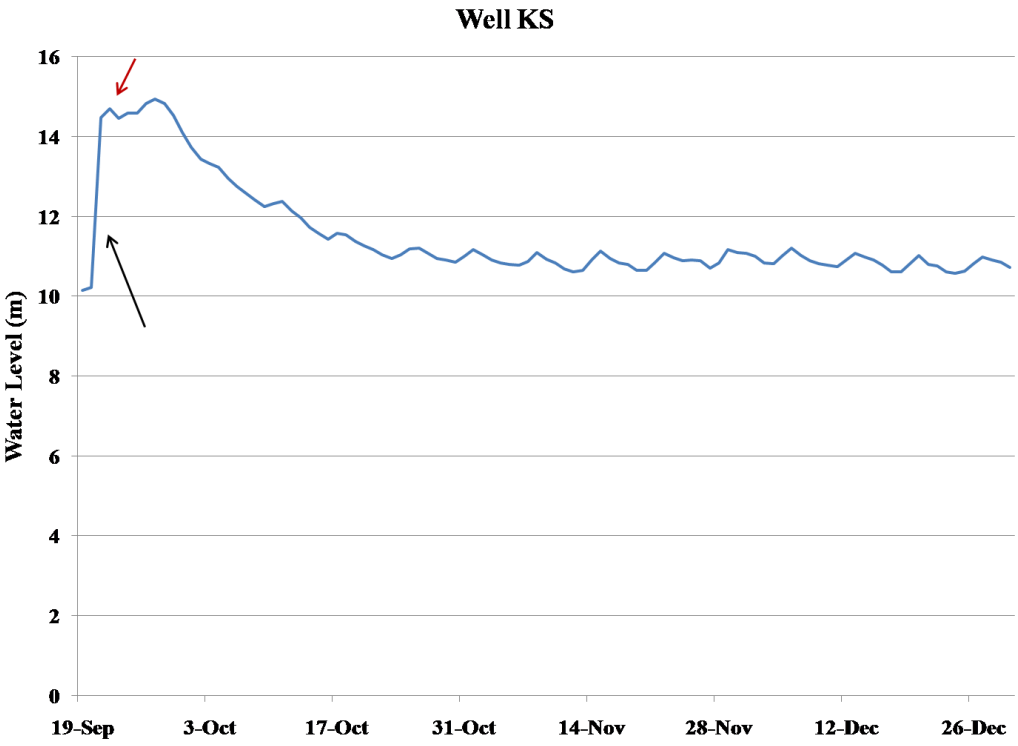
Well KS
Water Level (m)
16
14
12
10
8
6
4
2
0
19-Sep
3-Oct
17-Oct
31-Oct
14-Nov
28-Nov
12-Dec
26-Dec

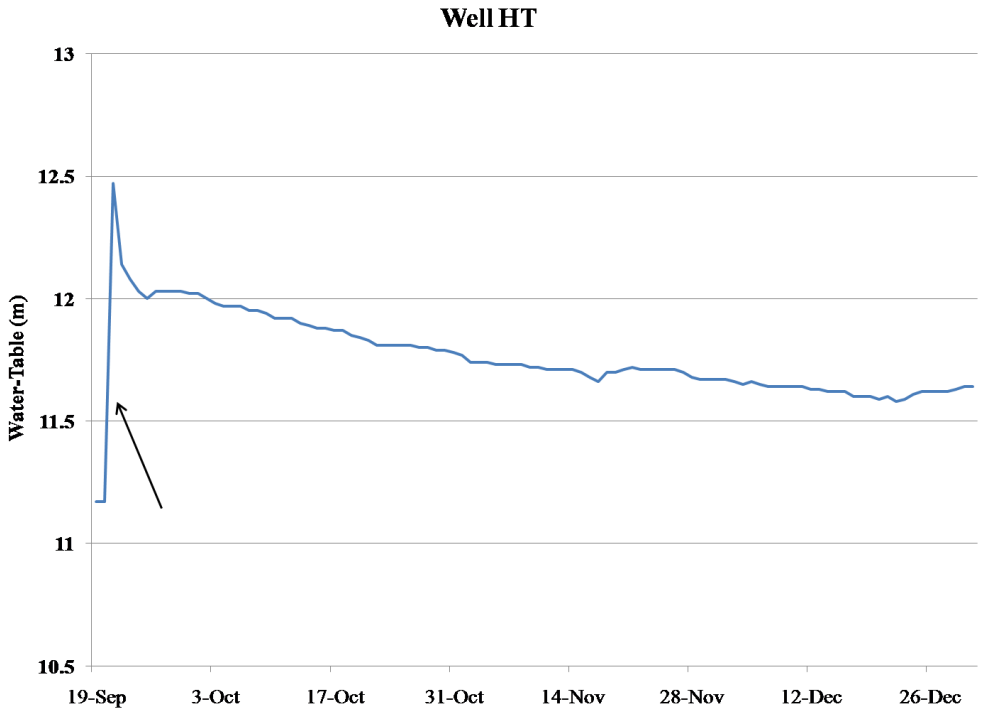
Well HT
Water-Table (m)
13
12.5
12
11.5
11
10.5
19-Sep
3-Oct
17-Oct
31-Oct
14-Nov
28-Nov
12-Dec
26-Dec

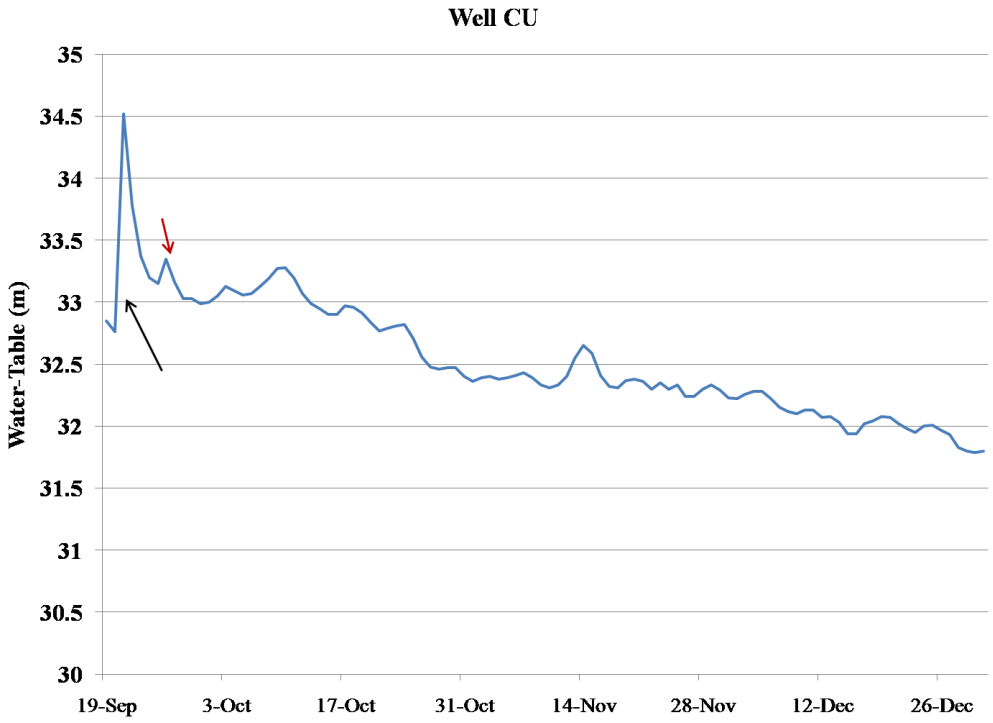
Well CU
Water-Table (m)
35
34.5
34
33.5
33
32.5
32
31.5
31
30.5
30
19-Sep
3-Oct
17-Oct
31-Oct
14-Nov
28-Nov
12-Dec
26-Dec

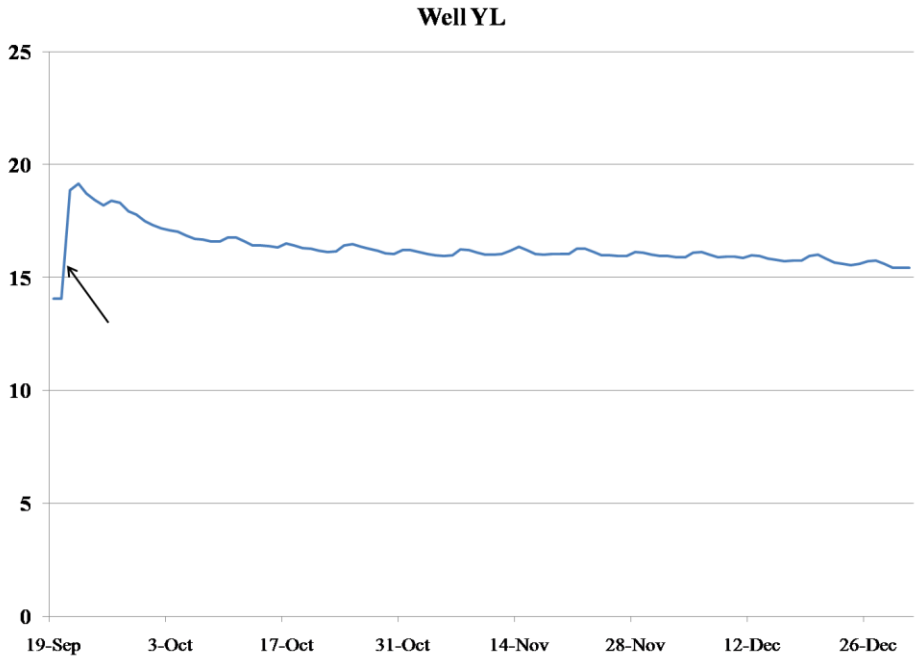
Well YL
25
20
15
10
5
0
19-Sep
3-Oct
17-Oct
31-Oct
14-Nov
28-Nov
12-Dec
26-Dec

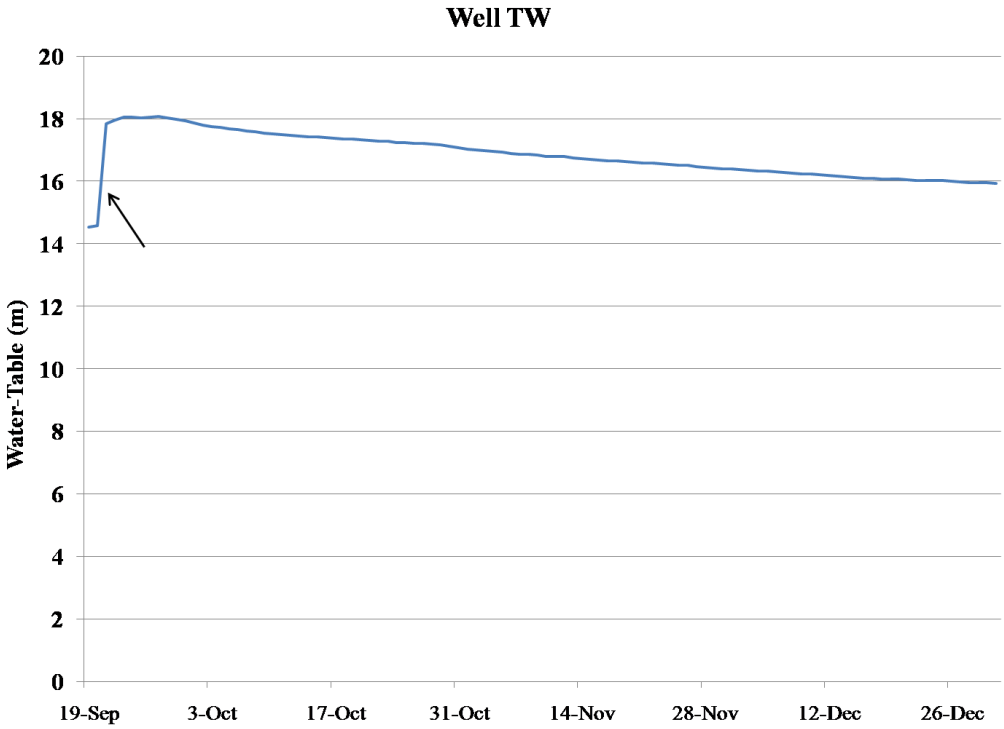
Well TW
Water-Table (m)
20
18
16
14
12
10
8
6
4
2
0
19-Sep
3-Oct
17-Oct
31-Oct
14-Nov
28-Nov
12-Dec
26-Dec

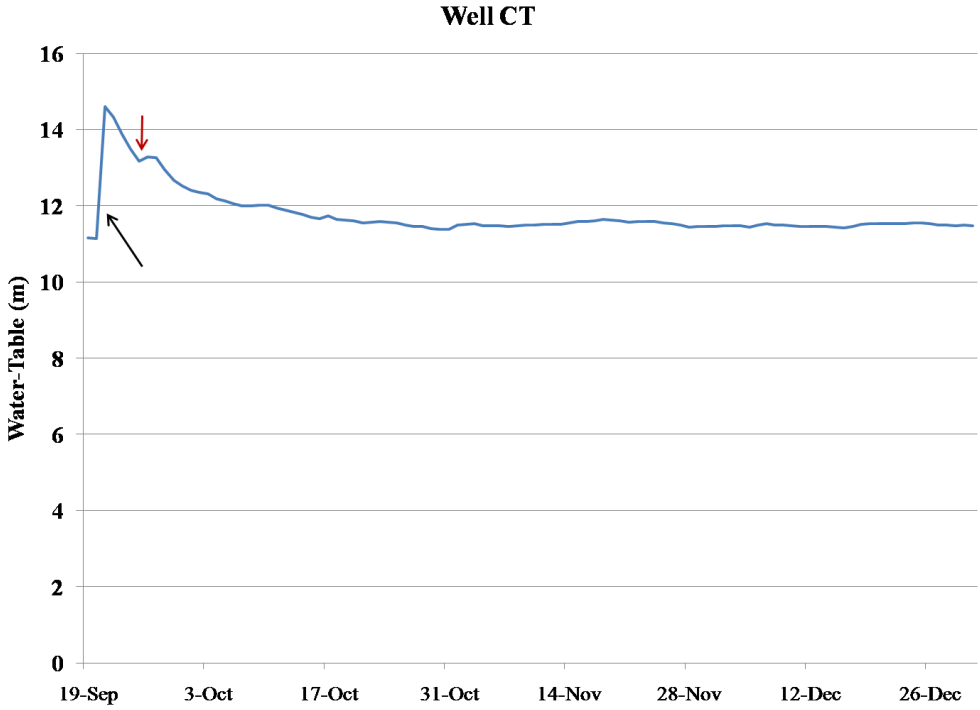
Well CT
Water-Table (m)
16
14
12
10
8
6
4
2
0
19-Sep
3-Oct
17-Oct
31-Oct
14-Nov
28-Nov
12-Dec
26-Dec

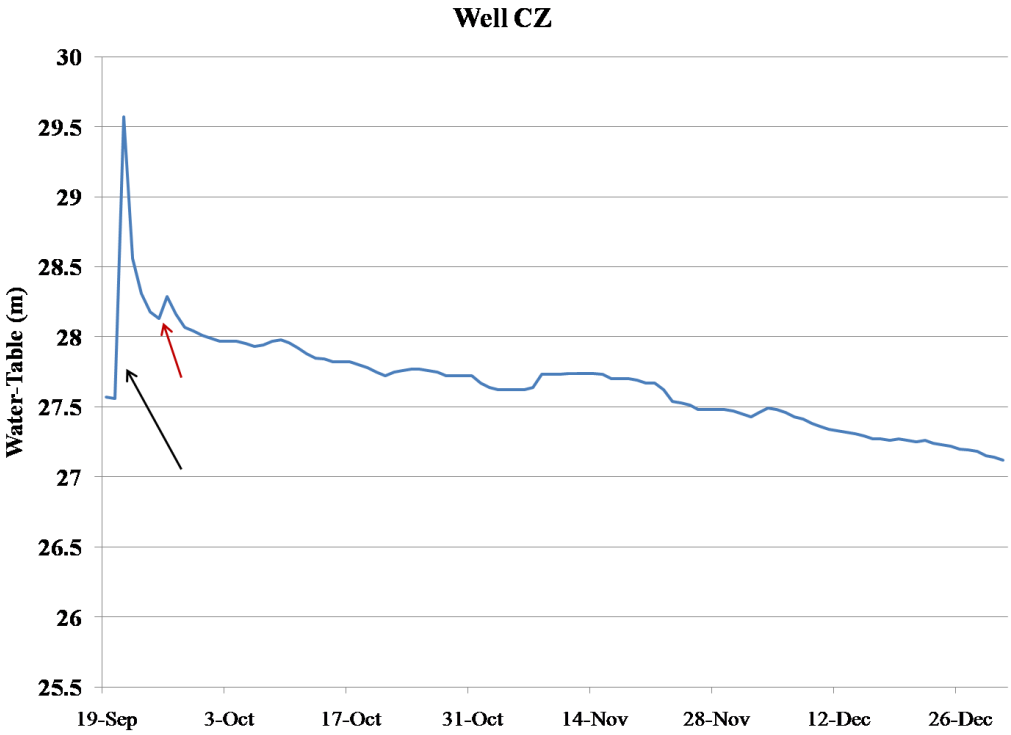
Well CZ
Water-Table (m)
30
29.5
29
28.5
28
27.5
27
26.5
26
25.5
19-Sep
3-Oct
17-Oct
31-Oct
14-Nov
28-Nov
12-Dec
26-Dec


Well HH
Water-Table (m)
35
34.5
34
33.5
33
32.5
32
31.5
31
30.5
30
19-Sep
3-Oct
17-Oct
31-Oct
14-Nov
28-Nov
12-Dec
26-Dec

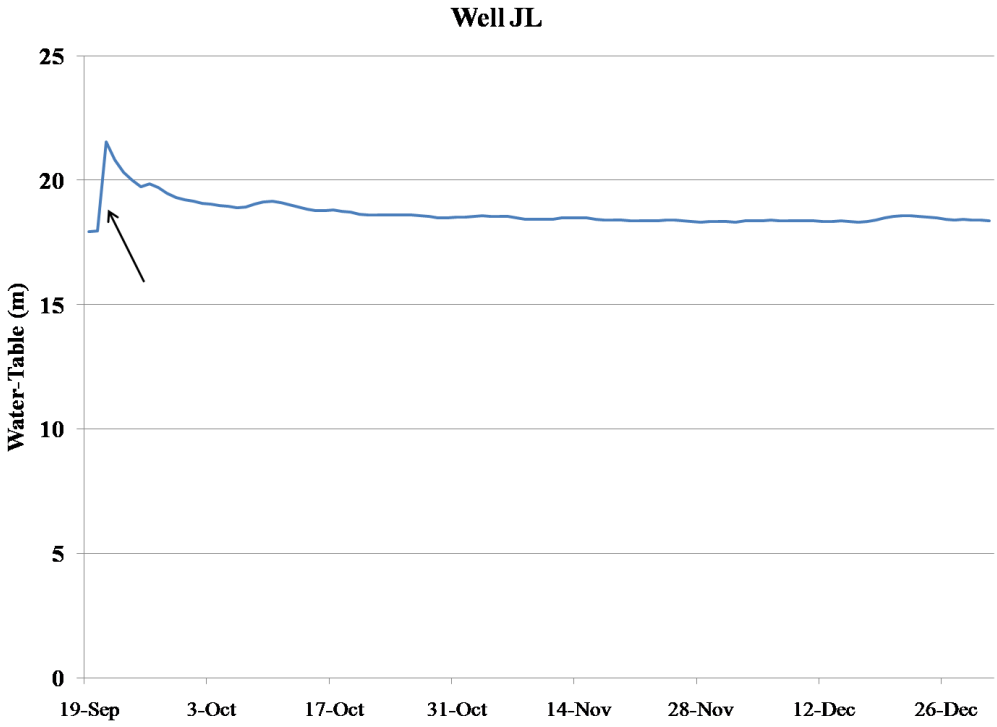
Well JL
Water-Table (m)
25
20
15
10
5
0
19-Sep
3-Oct
17-Oct
31-Oct
14-Nov
28-Nov
12-Dec
26-Dec

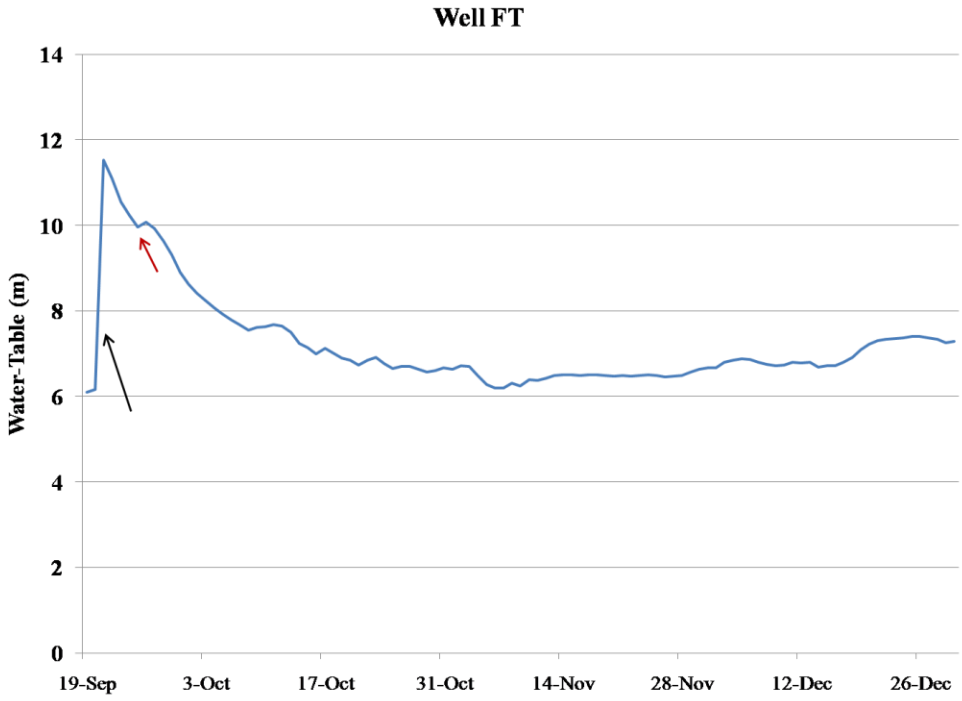
Well FT
Water-Table (m)
14
12
10
8
6
4
2
0
19-Sep
3-Oct
17-Oct
31-Oct
14-Nov
28-Nov
12-Dec
26-Dec

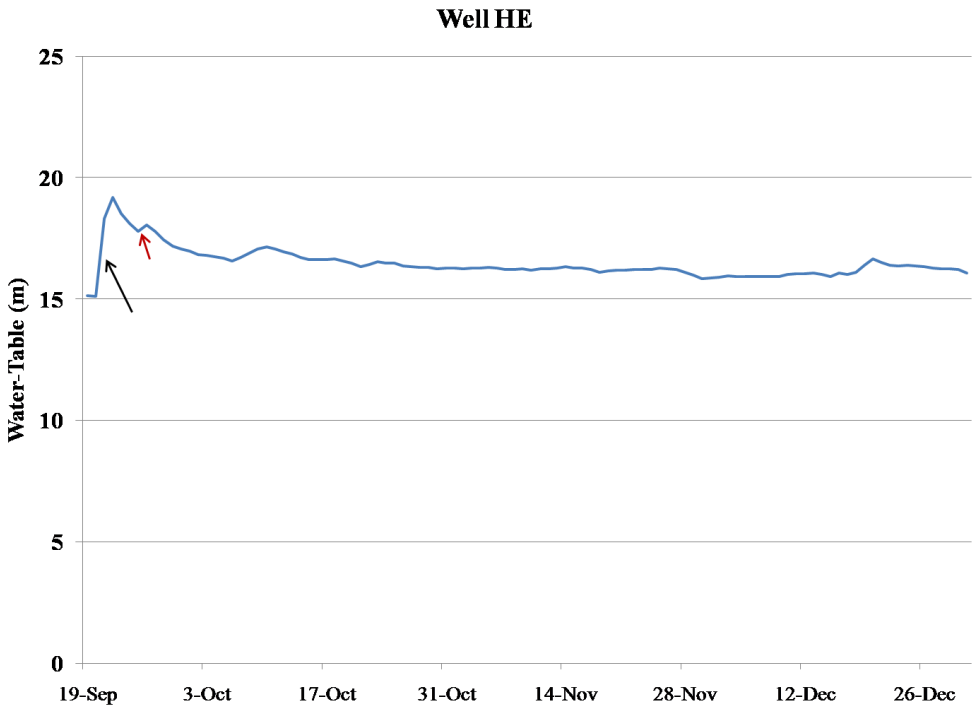
Well HE
Water-Table (m)
25
20
15
10
5
0
19-Sep
3-Oct
17-Oct
31-Oct
14-Nov
28-Nov
12-Dec
26-Dec

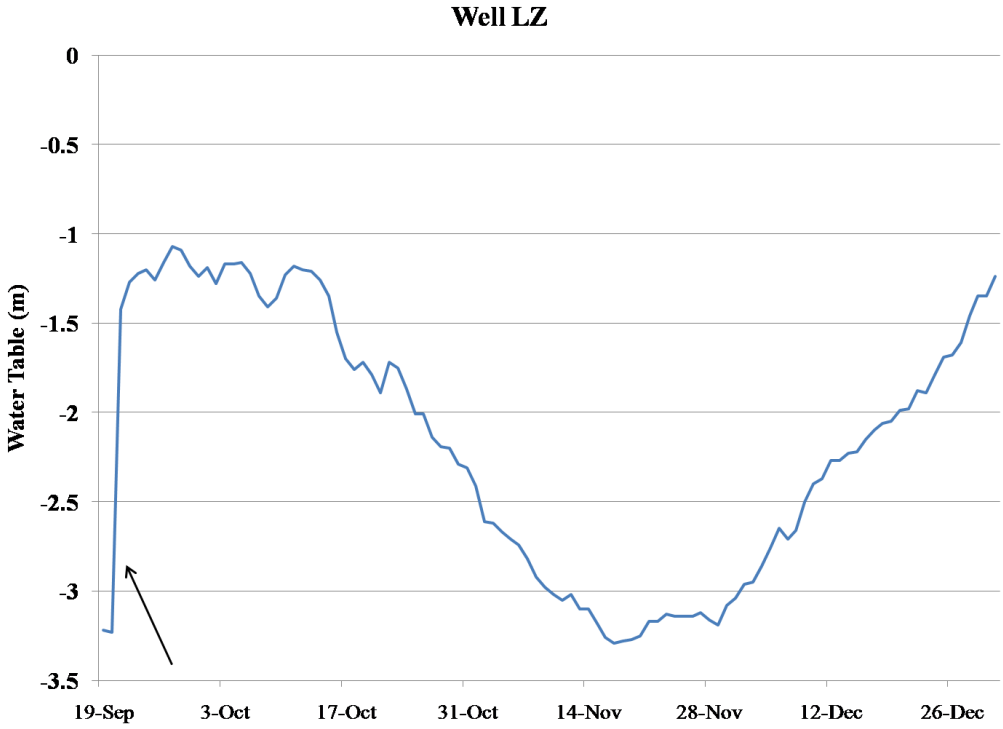
Well LZ
Water Table (m)
0
-0.5
-1
-1.5
-2
-2.5
-3
-3.5
19-Sep
3-Oct
17-Oct
31-Oct
14-Nov
28-Nov
12-Dec
26-Dec

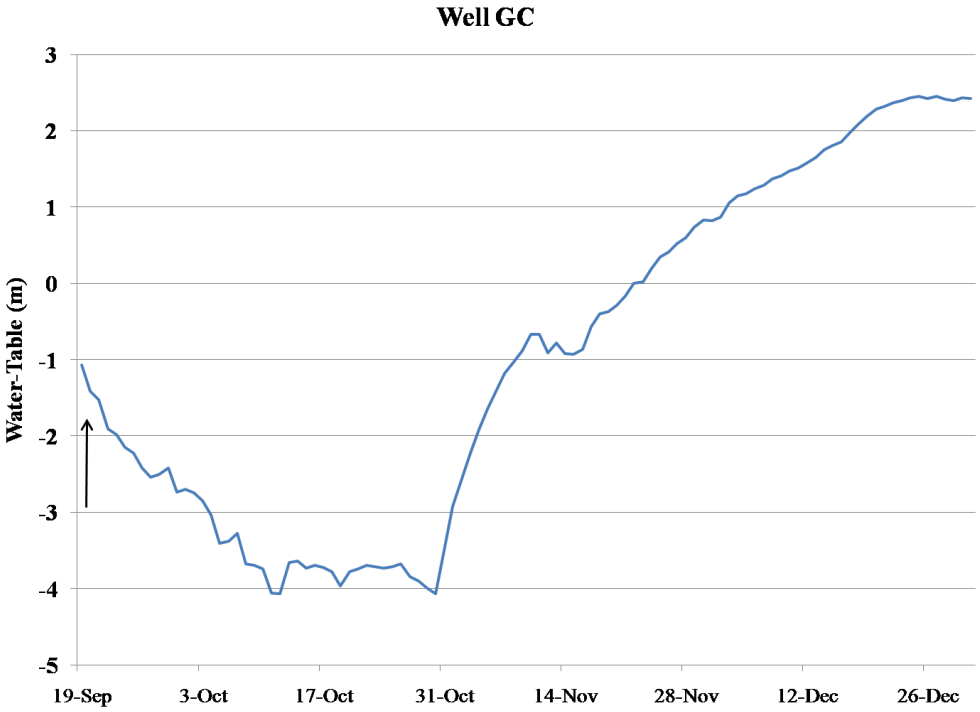
Well GC
Water-Table (m)
3
2
1
0
-1
-2
-3
-4
-5
19-Sep
3-Oct
17-Oct
31-Oct
14-Nov
28-Nov
12-Dec
26-Dec

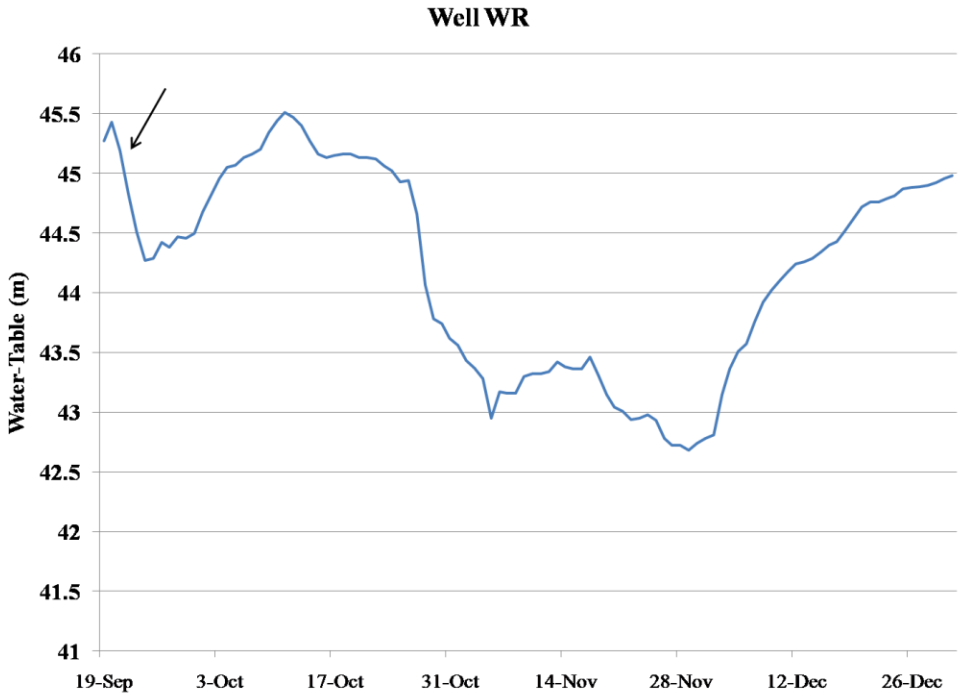
Well WR
Water-Table (m)
46
45.5
45
44.5
44
43.5
43
42.5
42
41.5
41
19-Sep
3-Oct
17-Oct
31-Oct
14-Nov
28-Nov
12-Dec
26-Dec


Well SH
Water-Table (m)
16
14
12
10
8
6
4
2
0
19-Sep
3-Oct
17-Oct
31-Oct
14-Nov
28-Nov
12-Dec
26-Dec


Well TR
Water-Table (m)
0
-1
-2
-3
-4
-5
-6
-7
19-Sep
3-Oct
17-Oct
31-Oct
14-Nov
28-Nov
12-Dec
26-Dec


Well AH
Water-Table (m)
0
-1
-2
-3
-4
-5
-6
-7
-8
19-Sep
3-Oct
17-Oct
31-Oct
14-Nov
28-Nov
12-Dec
26-Dec

Appendix C: Distal Fan Time-Series

A 100 day time-series was plotted for each well within the distal zone (> 35 km) using daily averages. The dominant coseismic response was down, however here more interest is expressed in the post-seismic response. Generally, the wells show a sporadic post-seismic response. Outside influences such as local pumping or aftershocks may play major roles in the variations observed within these diagrams. Clearly, simple pore-pressure diffusion modeling cannot explain these patterns (as all curves would show a steady and continuous curve back to pre-seismic levels and maintain this level with some regularity). The timing of the Chi-Chi earthquake is marked by the black arrow. Possible responses caused by aftershocks are marked by red arrows.

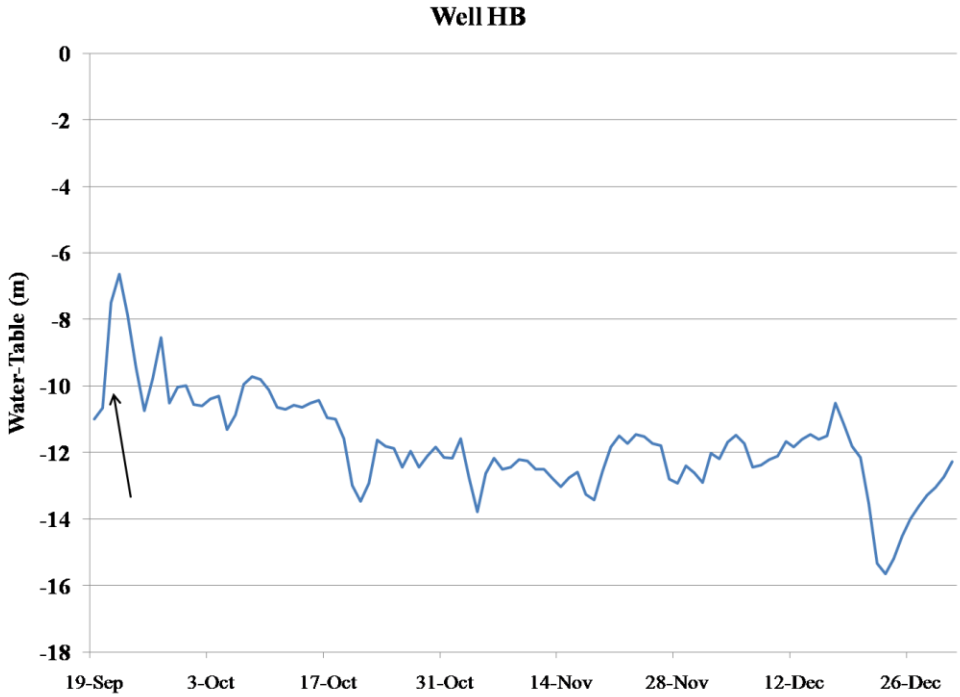

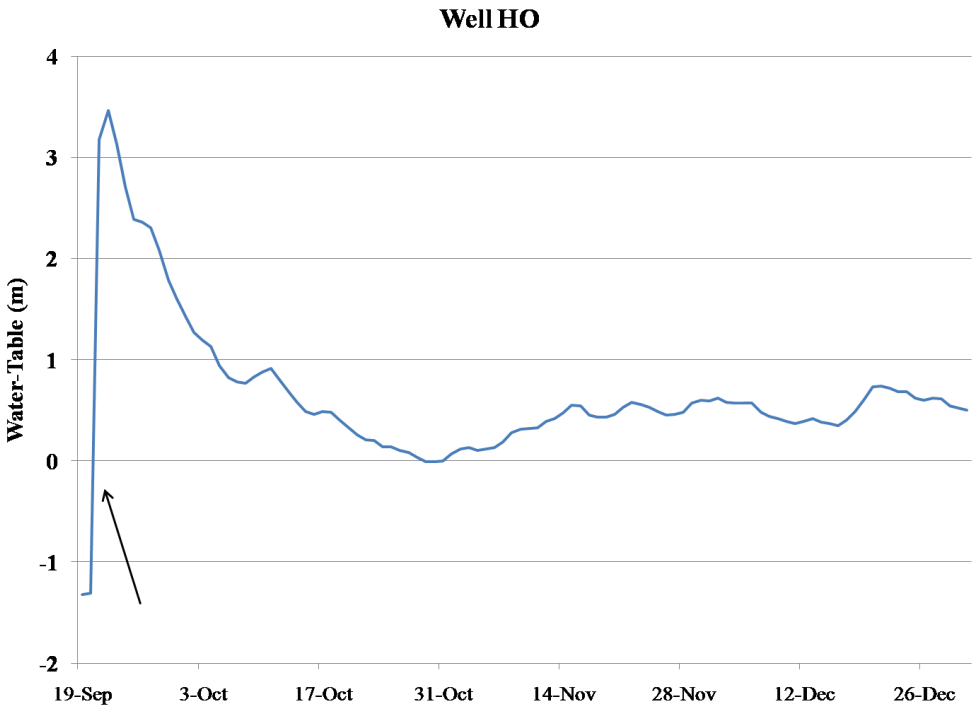
Well HO
Water-Table (m)
4
3
2
1
0
-1
-2
19-Sep
3-Oct
17-Oct
31-Oct
14-Nov
28-Nov
12-Dec
26-Dec

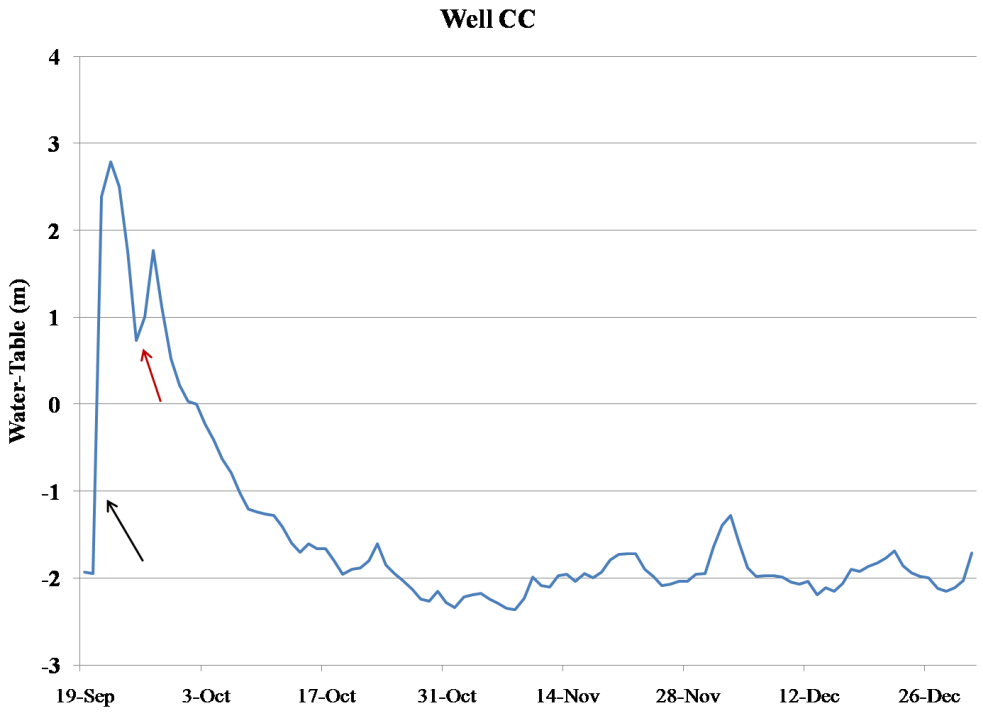
Well CC
Water-Table (m)
4
3
2
1
0
-1
-2
-3
19-Sep
3-Oct
17-Oct
31-Oct
14-Nov
28-Nov
12-Dec
26-Dec

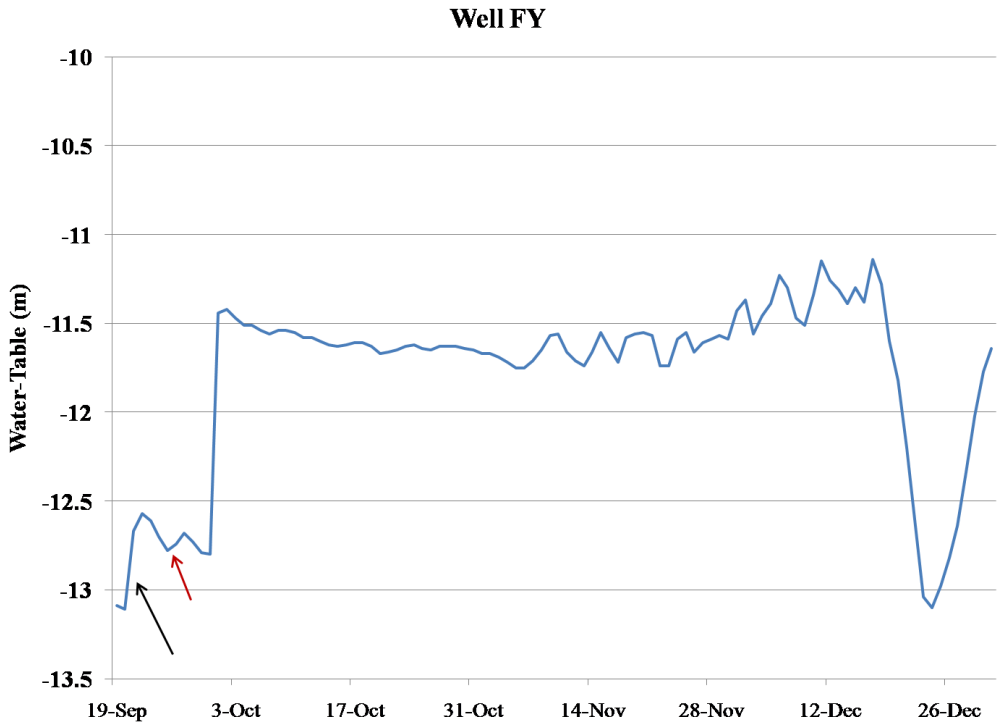
Well FY
Water-Table (m)
-10
-10.5
-11
-11.5
-12
-12.5
-13
-13.5
19-Sep
3-Oct
17-Oct
31-Oct
14-Nov
28-Nov
12-Dec
26-Dec

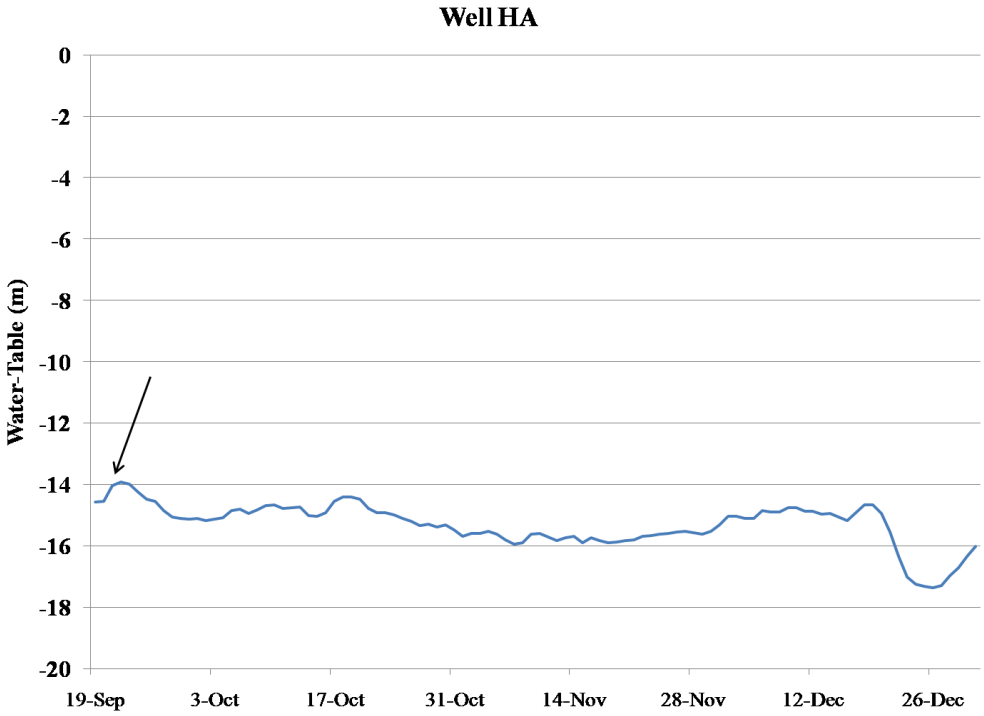
Well HA
Water-Table (m)
0
-2
-4
-6
-8
-10
-12
-14
-16
-18
-20
19-Sep
3-Oct
17-Oct
31-Oct
14-Nov
28-Nov
12-Dec
26-Dec

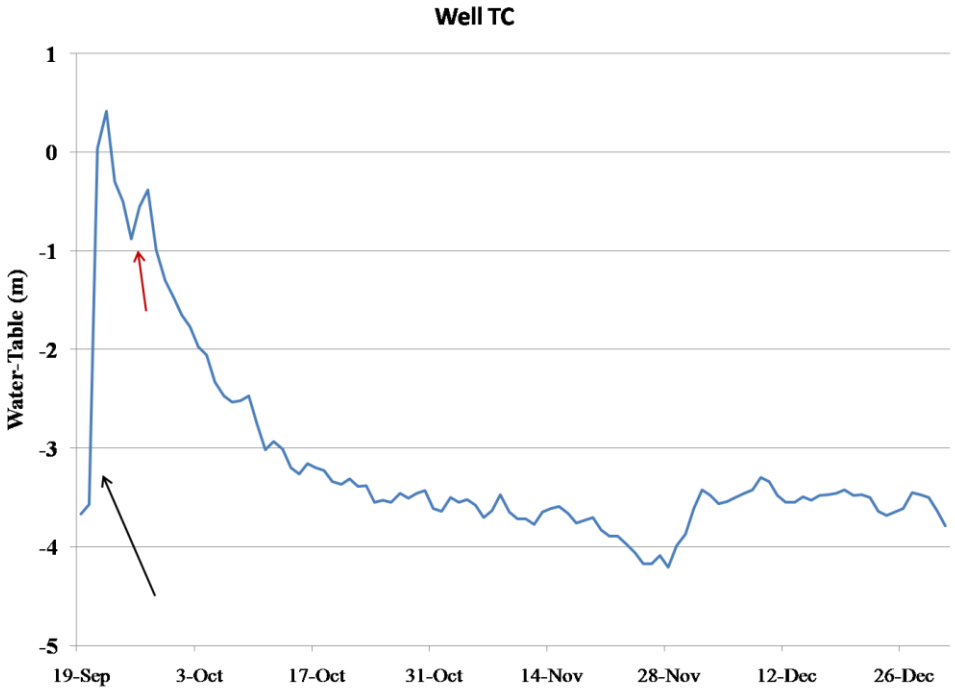
Well TC
Water-Table (m)
1
0
-1
-2
-3
-4
-5
19-Sep
3-Oct
17-Oct
31-Oct
14-Nov
28-Nov
12-Dec
26-Dec


Well HY
0.0
-5.0
-10.0
-15.0
-20.0
-25.0
Water-Table (m)
19-Sep
3-Oct
17-Oct
31-Oct
14-Nov
28-Nov
12-Dec
26-Dec


Well HU
0
-1
-2
-3
-4
-5
-6
-7
Water-Table (m)
19-Sep
3-Oct
17-Oct
31-Oct
14-Nov
28-Nov
12-Dec
26-Dec

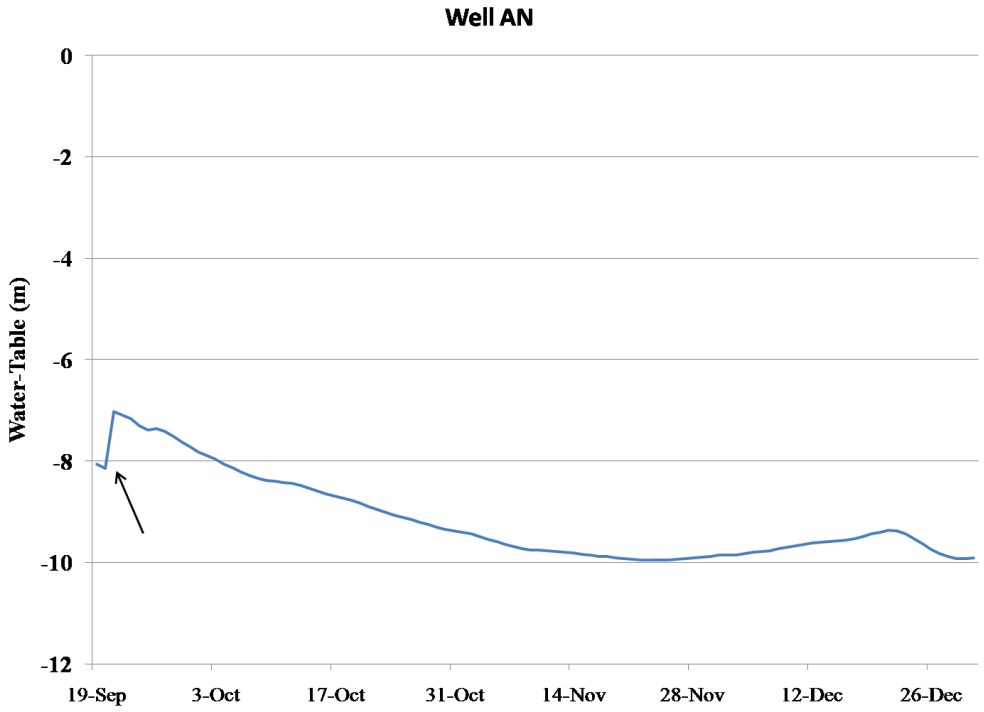
Well AN
Water-Table (m)
0
-2
-4
-6
-8
-10
-12
19-Sep
3-Oct
17-Oct
31-Oct
14-Nov
28-Nov
12-Dec
26-Dec

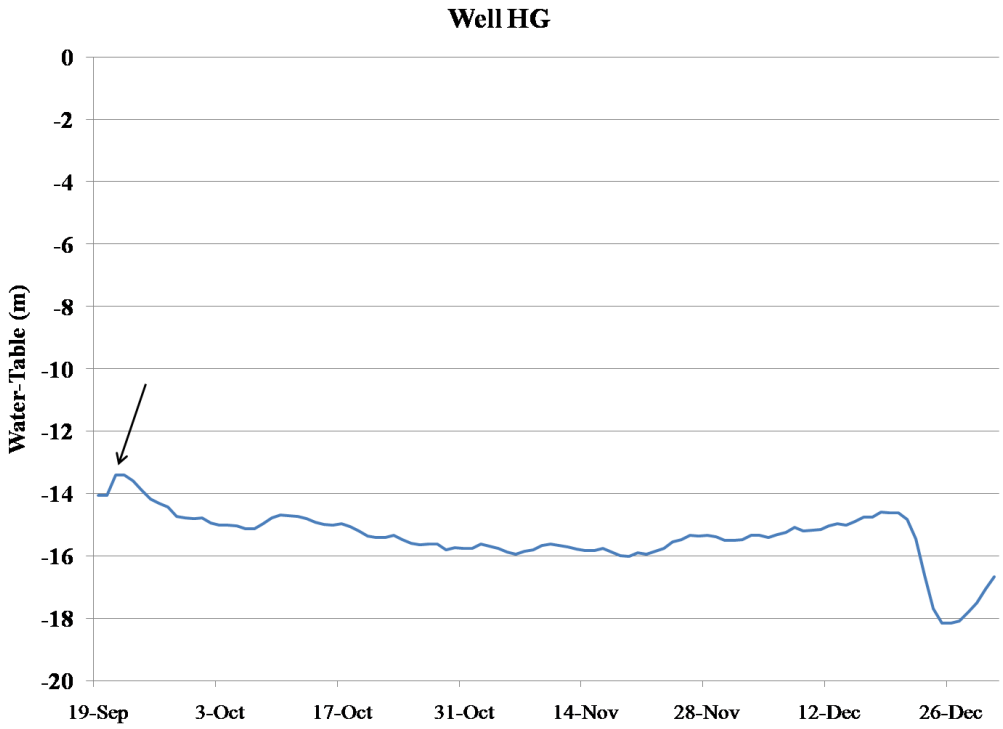
Well HG
Water-Table (m)
0
-2
-4
-6
-8
-10
-12
-14
-16
-18
-20
19-Sep
3-Oct
17-Oct
31-Oct
14-Nov
28-Nov
12-Dec
26-Dec

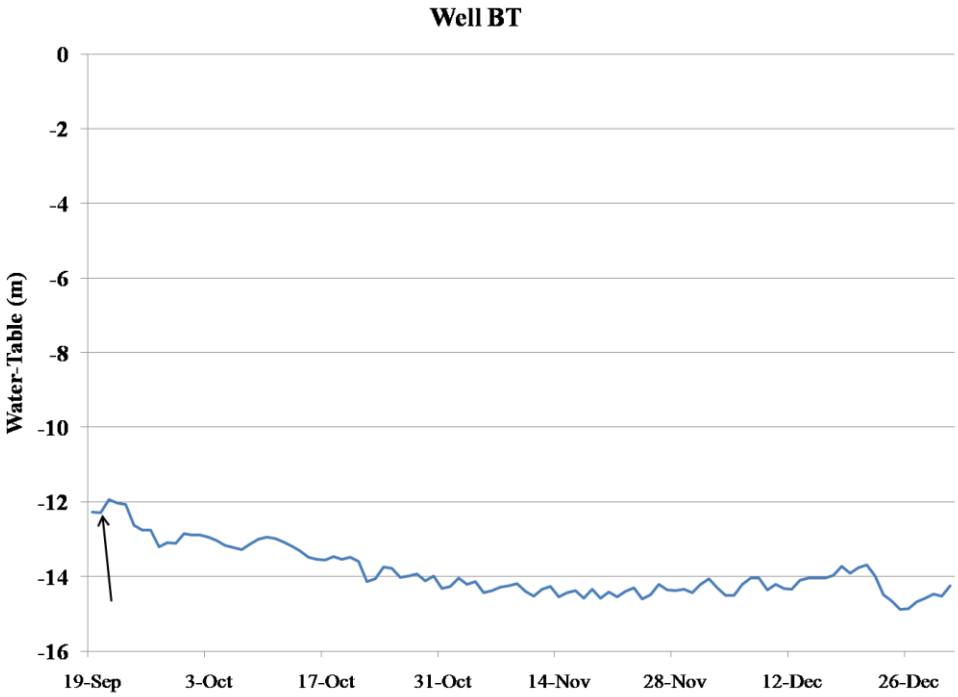
Well BT
Water-Table (m)
0
-2
-4
-6
-8
-10
-12
-14
-16
19-Sep
3-Oct
17-Oct
31-Oct
14-Nov
28-Nov
12-Dec
26-Dec

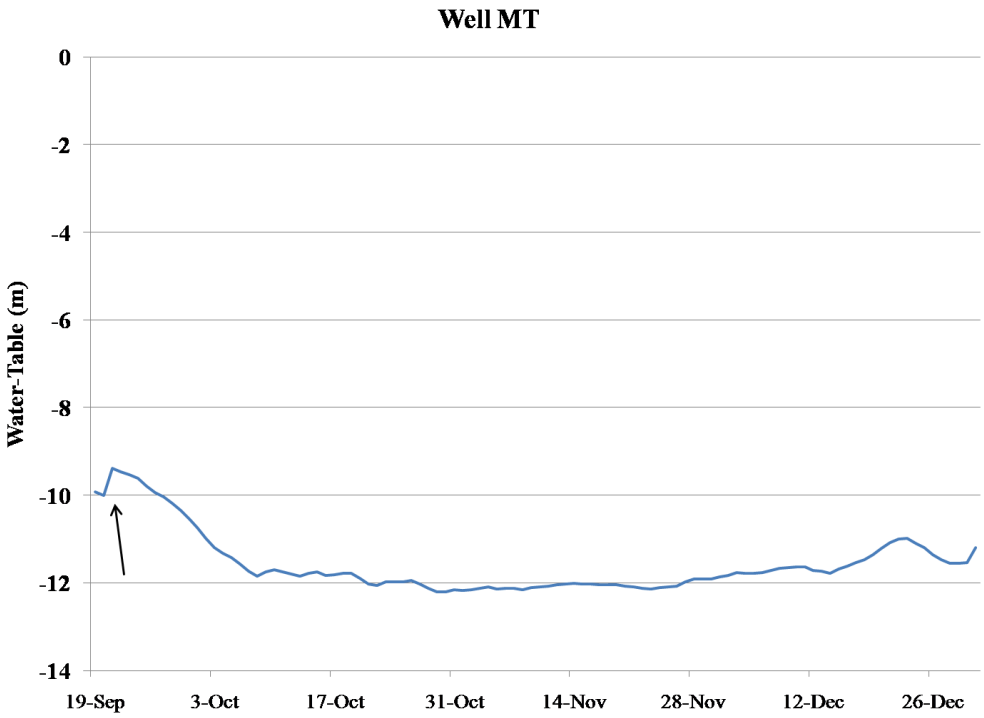
Well MT
Water-Table (m)
0
-2
-4
-6
-8
-10
-12
-14
19-Sep
3-Oct
17-Oct
31-Oct
14-Nov
28-Nov
12-Dec
26-Dec


Well TK
Water-Table (m)
0
-1
-2
-3
-4
-5
-6
-7
-8
-9
-10
19-Sep
3-Oct
17-Oct
31-Oct
14-Nov
28-Nov
12-Dec
26-Dec

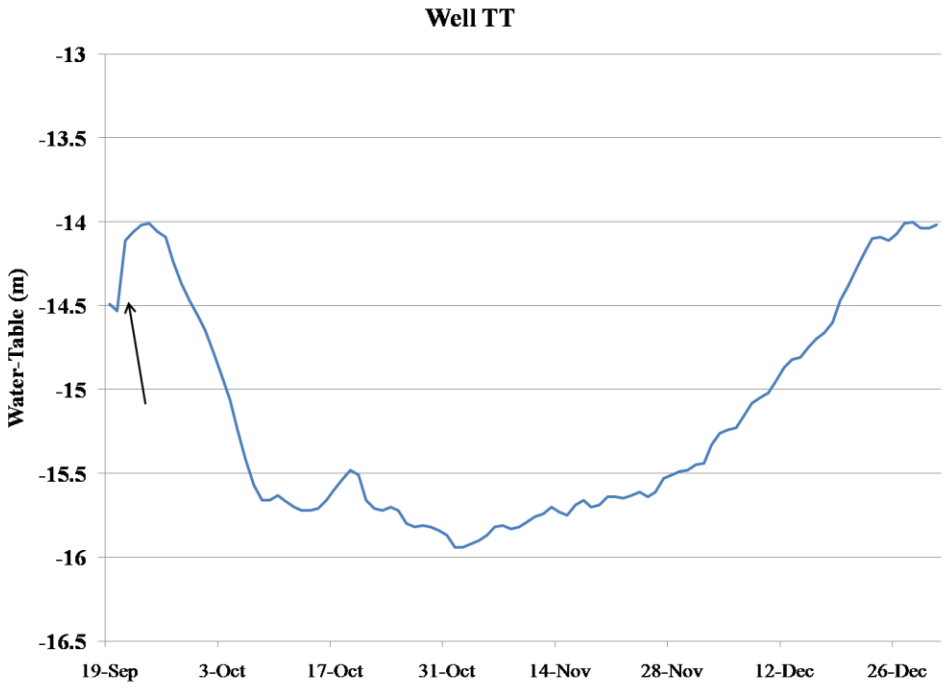
Well TT
Water-Table (m)
-13
-13.5
-14
-14.5
-15
-15.5
-16
-16.5
19-Sep
3-Oct
17-Oct
31-Oct
14-Nov
28-Nov
12-Dec
26-Dec

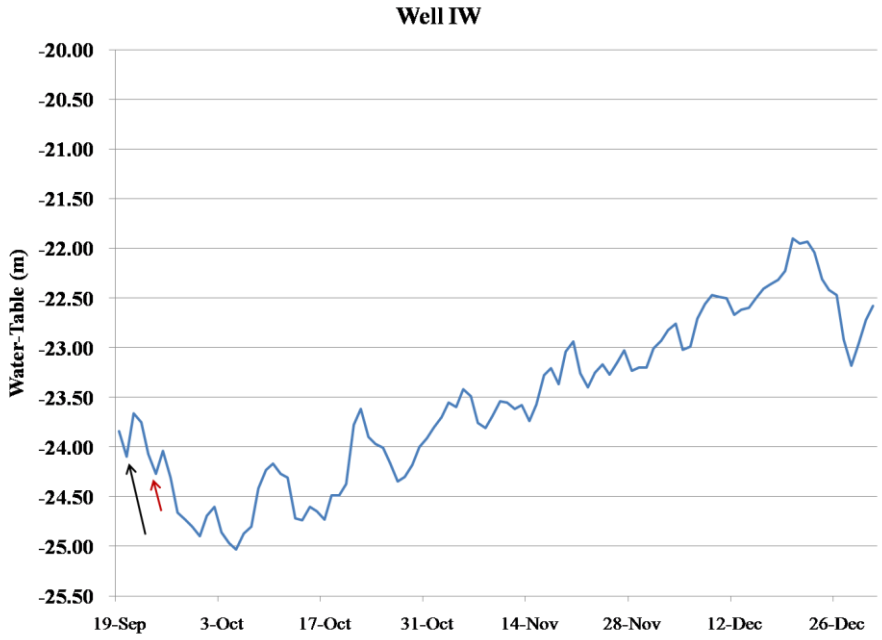
Well IW
Water-Table (m)
-20.00
-20.50
-21.00
-21.50
-22.00
-22.50
-23.00
-23.50
-24.00
-24.50
-25.00
-25.50
19-Sep
3-Oct
17-Oct
31-Oct
14-Nov
28-Nov
12-Dec
26-Dec


Well TS
Water-Table (m)
-22
-23
-24
-25
-26
-27
-28
-29
19-Sep
3-Oct
17-Oct
31-Oct
14-Nov
28-Nov
12-Dec
26-Dec

Appendix D: Strain Input File

(For use: copy into text file and save within Coulomb directory as .inp file)

```
Example for stress changes on specified faults and splitting fault into
some elements.
This example is very simple model for Kobe earthquake like.
#reg1=  0  #reg2=  0   #fixed= 261  sym=  1
 PR1=       .250      PR2=       .250    DEPTH=       1.0
  E1=   0.800000E+06   E2=   0.800000E+06
XSYM=       .000     YSYM=       .000
FRIC=       .400
S1DR=   122.0001     S1DP=      0.0001    S1IN=    100.000     S1GD=
.000000
S2DR=   122.0001     S3DP=     90.0001    S3IN=     30.000     S3GD=
.000000
S3DR=    32.0001     S2DP=      0.0001    S2IN=      0.000     S2GD=
.000000

  #   X-start    Y-start     X-fin      Y-fin   Kode   shear    normal
dip angle     top      bot
xxx xxxxxxxxxx xxxxxxxxxx xxxxxxxxxx xxxxxxxxxx xxx xxxxxxxxxx
xxxxxxxxxx xxxxxxxxxx xxxxxxxxxx xxxxxxxxxx
  1     9.2324    13.9867     9.4364    17.6398 100     1.3413
1.8644    29.0000     0.0000     1.4780   1
  1     9.4363    17.6399     9.6403    21.2930 100     0.2155
1.3846    29.0000     0.0000     1.4780   2
  1     9.6402    21.2929     9.8442    24.9460 100     0.1563
1.0117    29.0000     0.0000     1.4780   3
  1     9.8449    24.9461    10.0489    28.5992 100    -1.5493
2.2211    29.0000     0.0000     1.4780   4
  1     9.9468    28.5991    10.1508    32.2522 100     2.4107
3.4542    29.0000     0.0000     1.4780   5
  1    10.1507    32.3629    10.3547    36.0160 100    -1.2833
5.7722    29.0000     0.0000     1.4780   6
  1    10.3546    36.0159    10.5586    39.6690 100     0.0722
4.3565    29.0000     0.0000     1.4780   7
  1    10.5585    39.6691    10.7625    43.3222 100    -2.4080
7.9490    29.0000     0.0000     1.4780   8
  1    10.7624    43.3221    10.9664    46.9752 100    -6.2396
7.0745    29.0000     0.0000     1.4780   9
  1    10.9662    47.0859    11.1702    50.7390 100     0.0076
4.8641    29.0000     0.0000     1.4780  10
  1    11.1701    50.7392    11.3741    54.3923 100    -3.0204
7.7489    29.0000     0.0000     1.4780  11
  1    11.3748    54.3921    11.5788    58.0452 100    -3.8384
3.7829    29.0000     0.0000     1.4780  12
  1    11.5787    58.0453    11.7827    61.6984 100    -6.7943
6.7744    29.0000     0.0000     1.4780  13
  1    11.7826    61.8092    11.9866    65.4623 100    -4.3821
8.6429    29.0000     0.0000     1.4780  14
  1    11.9865    65.4622    12.1905    69.1153 100    -2.7525
8.8808    29.0000     0.0000     1.4780  15
  1    12.0884    69.1154    12.2924    72.7685 100    -9.1105
5.0744    29.0000     0.0000     1.4780  16
```

```
  1    12.2923    72.7684    12.4963    76.4215 100    -5.6919
2.5499    29.0000     0.0000     1.4780  17
  1    12.4962    76.5322    12.7002    80.1853 100    -9.5533
7.7450    29.0000     0.0000     1.4780  18
  1    12.7008    80.1852    12.9048    83.8383 100   -10.4357
5.9100    29.0000     0.0000     1.4780  19
  1    12.9047    83.8384    13.1087    87.4915 100     1.4356
5.7954    29.0000     0.0000     1.4780  20
  1    12.4962    13.7654    12.7002    17.4185 100     2.3133
2.8858    29.0000     1.9000     3.3780  21
  1    12.7008    17.4184    12.9048    21.0715 100     0.8395
2.9583    29.0000     1.9000     3.3780  22
  1    12.9047    21.0716    13.1087    24.7247 100    -1.3508
2.2288    29.0000     1.9000     3.3780  23
  1    13.1086    24.8352    13.3126    28.4883 100    -4.1872
1.6450    29.0000     1.9000     3.3780  24
  1    13.3125    28.4884    13.5165    32.1415 100     0.9943
1.3276    29.0000     1.9000     3.3780  25
  1    13.5164    32.1414    13.7204    35.7945 100    -1.2645
5.9615    29.0000     1.9000     3.3780  26
  1    13.7203    35.7946    13.9243    39.4477 100    -3.4834
4.5251    29.0000     1.9000     3.3780  27
  1    13.9242    39.5585    14.1282    43.2116 100    -2.5622
3.8976    29.0000     1.9000     3.3780  28
  1    14.0261    43.2115    14.2301    46.8646 100    -4.4989
3.6352    29.0000     1.9000     3.3780  29
  1    14.2308    46.8647    14.4348    50.5178 100    -2.1145
5.0992    29.0000     1.9000     3.3780  30
  1    14.4347    50.5177    14.6387    54.1708 100    -8.1787
7.4813    29.0000     1.9000     3.3780  31
  1    14.6386    54.2815    14.8426    57.9346 100    -4.8359
5.4503    29.0000     1.9000     3.3780  32
  1    14.8424    57.9345    15.0464    61.5876 100    -8.1645
7.2145    29.0000     1.9000     3.3780  33
  1    15.0463    61.5877    15.2503    65.2408 100    -6.0305
6.1019    29.0000     1.9000     3.3780  34
  1    15.2502    65.2407    15.4542    68.8938 100    -5.0800
7.6646    29.0000     1.9000     3.3780  35
  1    15.4549    69.0045    15.6589    72.6576 100    -5.7988
8.9853    29.0000     1.9000     3.3780  36
  1    15.6588    72.6577    15.8628    76.3108 100    -3.8806
4.0930    29.0000     1.9000     3.3780  37
  1    15.8627    76.3107    16.0667    79.9638 100   -13.4257
7.7167    29.0000     1.9000     3.3780  38
  1    15.9646    79.9639    16.1686    83.6170 100   -14.2425
4.8546    29.0000     1.9000     3.3780  39
  1    15.8627    13.5439    16.0667    17.1970 100     0.8195
1.0496    29.0000     3.8000     5.2780  41
  1    15.9646    17.3077    16.1686    20.9608 100     0.0719
0.2005    29.0000     3.8000     5.2780  42
  1    16.1685    20.9607    16.3725    24.6138 100    -0.0731
0.7725    29.0000     3.8000     5.2780  43
  1    16.3724    24.6139    16.5764    28.2670 100    -1.0523
2.1639    29.0000     3.8000     5.2780  44
  1    16.5763    28.2669    16.7803    31.9200 100    -1.9108
2.2028    29.0000     3.8000     5.2780  45
```

```
  1    16.7802    32.0308    16.9842    35.6839 100    -1.9886
7.3496    29.0000     3.8000     5.2780  46
  1    16.9848    35.6840    17.1888    39.3371 100    -3.7391
6.1171    29.0000     3.8000     5.2780  47
  1    17.1887    39.3370    17.3927    42.9901 100    -0.0762
2.6781    29.0000     3.8000     5.2780  48
  1    17.3926    42.9902    17.5966    46.6433 100    -2.0022
4.9448    29.0000     3.8000     5.2780  49
  1    17.5965    46.6432    17.8005    50.2963 100    -0.3480
2.7397    29.0000     3.8000     5.2780  50
  1    17.8004    50.4070    18.0044    54.0601 100    -4.8561
8.1461    29.0000     3.8000     5.2780  51
  1    17.9023    54.0600    18.1063    57.7131 100    -4.3371
8.4900    29.0000     3.8000     5.2780  52
  1    18.1062    57.7132    18.3102    61.3663 100    -6.4030
6.3129    29.0000     3.8000     5.2780  53
  1    18.3109    61.4771    18.5149    65.1302 100    -3.5777
2.5984    29.0000     3.8000     5.2780  54
  1    18.5148    65.1301    18.7188    68.7832 100    -7.1563
5.9950    29.0000     3.8000     5.2780  55
  1    18.7186    68.7833    18.9226    72.4364 100    -6.9885
7.4263    29.0000     3.8000     5.2780  56
  1    18.9225    72.4363    19.1265    76.0894 100    -2.3128
2.9629    29.0000     3.8000     5.2780  57
  1    19.1264    76.2001    19.3304    79.8532 100    -7.6631
4.8123    29.0000     3.8000     5.2780  58
  1    19.3303    79.8533    19.5343    83.5064 100    -7.1948
3.1282    29.0000     3.8000     5.2780  59
  1    19.5342    83.5063    19.7382    87.1594 100     0.0000
0.0000    29.0000     3.8000     5.2780  60
  1    19.1264    13.4333    19.3304    17.0864 100    -0.1864
0.1745    29.0000     5.7000     7.1780  61
  1    19.3303    17.0863    19.5343    20.7394 100    -0.7790
2.0168    29.0000     5.7000     7.1780  62
  1    19.5342    20.7395    19.7382    24.3926 100     1.7535
2.2674    29.0000     5.7000     7.1780  63
  1    19.7389    24.3925    19.9429    28.0456 100     1.2065
1.7967    29.0000     5.7000     7.1780  64
  1    19.8408    28.1563    20.0448    31.8094 100    -1.8346
1.7149    29.0000     5.7000     7.1780  65
  1    20.0447    31.8095    20.2487    35.4626 100    -0.1392
6.1150    29.0000     5.7000     7.1780  66
  1    20.2486    35.4625    20.4526    39.1156 100    -2.9538
4.2606    29.0000     5.7000     7.1780  67
  1    20.4525    39.2263    20.6565    42.8794 100    -0.3162
1.3221    29.0000     5.7000     7.1780  68
  1    20.6564    42.8793    20.8604    46.5324 100    -1.2044
2.0538    29.0000     5.7000     7.1780  69
  1    20.8603    46.5325    21.0643    50.1856 100     0.3843
1.0348    29.0000     5.7000     7.1780  70
  1    21.0641    50.1855    21.2681    53.8386 100    -3.9704
0.0721    29.0000     5.7000     7.1780  71
  1    21.2688    53.9494    21.4728    57.6025 100    -3.9603
5.2540    29.0000     5.7000     7.1780  72
  1    21.4727    57.6026    21.6767    61.2557 100    -6.1404
7.5931    29.0000     5.7000     7.1780  73
```

```
  1    21.6766    61.2556    21.8806    64.9087 100    -3.8671
2.7360    29.0000     5.7000     7.1780  74
  1    21.8805    64.9088    22.0845    68.5619 100    -5.4887
5.6068    29.0000     5.7000     7.1780  75
  1    21.9824    68.5618    22.1864    72.2149 100    -7.7812
7.4434    29.0000     5.7000     7.1780  76
  1    22.1863    72.3256    22.3903    75.9787 100    -3.7464
5.7804    29.0000     5.7000     7.1780  77
  1    22.3902    75.9786    22.5942    79.6317 100    -2.3879
2.5455    29.0000     5.7000     7.1780  78
  1    22.3902    13.2118    22.5942    16.8649 100    -0.8181
0.4993    29.0000     7.6000     9.0780  81
  1    22.5949    16.8650    22.7989    20.5181 100    -0.4261
2.8136    29.0000     7.6000     9.0780  82
  1    22.7987    20.6286    23.0027    24.2817 100     1.9106
2.5133    29.0000     7.6000     9.0780  83
  1    23.0026    24.2818    23.2066    27.9349 100     1.7419
2.4929    29.0000     7.6000     9.0780  84
  1    23.2065    27.9348    23.4105    31.5879 100    -1.1005
1.1636    29.0000     7.6000     9.0780  85
  1    23.4104    31.5880    23.6144    35.2411 100     0.8354
1.1561    29.0000     7.6000     9.0780  86
  1    23.6143    35.3519    23.8183    39.0050 100    -0.9538
0.6436    29.0000     7.6000     9.0780  87
  1    23.8182    39.0049    24.0222    42.6580 100     0.1810
0.5646    29.0000     7.6000     9.0780  88
  1    23.9201    42.6581    24.1241    46.3112 100    -1.8690
0.9655    29.0000     7.6000     9.0780  89
  1    24.1248    46.3111    24.3288    49.9641 100    -0.6225
1.0974    29.0000     7.6000     9.0780  90
  1    24.3287    50.0749    24.5327    53.7280 100    -0.6953
1.1402    29.0000     7.6000     9.0780  91
  1    24.5326    53.7281    24.7366    57.3812 100     0.4077
7.6938    29.0000     7.6000     9.0780  92
  1    24.7365    57.3811    24.9405    61.0342 100     0.4046
11.7388    29.0000     7.6000     9.0780  93
  1    24.9403    61.0343    25.1443    64.6874 100    -0.1907
6.8862    29.0000     7.6000     9.0780  94
  1    25.1442    64.7979    25.3482    68.4510 100    -4.8420
4.4077    29.0000     7.6000     9.0780  95
  1    25.3481    68.4511    25.5521    72.1042 100    -8.4452
5.7905    29.0000     7.6000     9.0780  96
  1    25.5528    72.1041    25.7568    75.7572 100    -2.3707
3.6889    29.0000     7.6000     9.0780  97
  1    25.7567    13.1011    25.9607    16.7542 100    -0.0707
0.1438    29.0000     9.5000    10.9780 101
  1    25.8586    16.7541    26.0626    20.4072 100    -1.2899
1.7043    29.0000     9.5000    10.9780 102
  1    26.0625    20.4073    26.2665    24.0604 100     0.8894
1.9634    29.0000     9.5000    10.9780 103
  1    26.2664    24.0603    26.4704    27.7134 100     0.7986
1.6212    29.0000     9.5000    10.9780 104
  1    26.4703    27.8242    26.6743    31.4773 100     0.2934
0.5488    29.0000     9.5000    10.9780 105
  1    26.6742    31.4774    26.8782    35.1305 100    -0.0180
0.0037    29.0000     9.5000    10.9780 106
```

```
  1    26.8788    35.1304    27.0828    38.7835 100     0.2065
0.4977    29.0000     9.5000    10.9780 107
  1    27.0827    38.7836    27.2867    42.4367 100    -0.0188
0.0445    29.0000     9.5000    10.9780 108
  1    27.2866    42.5472    27.4906    46.2003 100    -0.6852
0.0856    29.0000     9.5000    10.9780 109
  1    27.4905    46.2004    27.6945    49.8535 100    -2.3484
0.7970    29.0000     9.5000    10.9780 110
  1    27.6944    49.8534    27.8984    53.5065 100    -0.2946
1.0616    29.0000     9.5000    10.9780 111
  1    27.7963    53.5066    28.0003    57.1597 100    -0.6094
2.3330    29.0000     9.5000    10.9780 112
  1    28.0002    57.2705    28.2042    60.9236 100    -0.8848
6.3717    29.0000     9.5000    10.9780 113
  1    28.2049    60.9234    28.4089    64.5765 100    -2.5618
3.7693    29.0000     9.5000    10.9780 114
  1    28.4088    64.5767    28.6128    68.2298 100    -5.0420
0.6951    29.0000     9.5000    10.9780 115
  1    28.6127    68.2296    28.8167    71.8827 100    -7.5802
2.7648    29.0000     9.5000    10.9780 116
  1    29.0204    12.8796    29.2244    16.5327 100    -0.0182
0.1196    29.0000    11.4000    12.8780 121
  1    29.2243    16.5329    29.4283    20.1859 100    -0.5781
0.0581    29.0000    11.4000    12.8780 122
  1    29.4282    20.2967    29.6322    23.9498 100     0.4607
0.7399    29.0000    11.4000    12.8780 123
  1    29.6329    23.9497    29.8369    27.6028 100    -0.5637
0.3756    29.0000    11.4000    12.8780 124
  1    29.7348    27.6029    29.9388    31.2560 100     0.0893
0.2763    29.0000    11.4000    12.8780 125
  1    29.9387    31.2559    30.1427    34.9090 100     0.0411
0.1338    29.0000    11.4000    12.8780 126
  1    30.1426    35.0197    30.3466    38.6728 100     0.2027
0.2985    29.0000    11.4000    12.8780 127
  1    30.3465    38.6727    30.5505    42.3258 100    -0.2493
0.0861    29.0000    11.4000    12.8780 128
  1    30.5504    42.3259    30.7544    45.9790 100     0.0208
0.0274    29.0000    11.4000    12.8780 129
  1    30.7543    45.9789    30.9583    49.6320 100    -0.6949
0.5215    29.0000    11.4000    12.8780 130
  1    30.9582    49.7428    31.1622    53.3959 100    -0.1658
0.0269    29.0000    11.4000    12.8780 131
  1    31.1628    53.3960    31.3668    57.0491 100    -0.3909
0.1531    29.0000    11.4000    12.8780 132
  1    31.3667    57.0490    31.5707    60.7021 100    -3.1725
1.0051    29.0000    11.4000    12.8780 133
  1    31.5706    60.7022    31.7746    64.3553 100    -7.0166
2.4241    29.0000    11.4000    12.8780 134
  1    31.7745    64.4658    31.9785    68.1189 100    -6.0071
2.7163    29.0000    11.4000    12.8780 135
  1    31.8764    68.1190    32.0804    71.7721 100    -5.3549
3.3256    29.0000    11.4000    12.8780 136
  1    32.2842    12.7690    32.4882    16.4221 100    -0.2242
0.3228    29.0000    13.3000    14.7780 141
  1    32.4889    16.4220    32.6929    20.0751 100     0.6854
0.8873    29.0000    13.3000    14.7780 142
```

```
  1    32.6928    20.0752    32.8968    23.7283 100     1.5415
2.4744    29.0000    13.3000    14.7780 143
  1    32.8966    23.7282    33.1006    27.3813 100    -1.2909
1.4906    29.0000    13.3000    14.7780 144
  1    33.1005    27.3814    33.3045    31.0345 100    -0.2003
0.8281    29.0000    13.3000    14.7780 145
  1    33.3044    31.1452    33.5084    34.7983 100    -0.0583
0.2112    29.0000    13.3000    14.7780 146
  1    33.5083    34.7982    33.7123    38.4513 100    -1.0880
0.0030    29.0000    13.3000    14.7780 147
  1    33.7122    38.4514    33.9162    42.1045 100    -1.7469
0.0781    29.0000    13.3000    14.7780 148
  1    33.8141    42.1044    34.0181    45.7575 100     0.0135
0.0194    29.0000    13.3000    14.7780 149
  1    34.0188    45.8683    34.2228    49.5214 100     0.7337
1.3146    29.0000    13.3000    14.7780 150
  1    34.2227    49.5215    34.4267    53.1746 100     0.3842
0.8418    29.0000    13.3000    14.7780 151
  1    34.4266    53.1745    34.6306    56.8276 100     0.5745
1.1867    29.0000    13.3000    14.7780 152
  1    34.6305    56.9383    34.8345    60.5914 100    -1.3403
1.0754    29.0000    13.3000    14.7780 153
  1    34.8344    60.5913    35.0384    64.2444 100    -4.5599
2.0394    29.0000    13.3000    14.7780 154
  1    35.6507    12.5475    35.8547    16.2006 100     0.0049
0.0343    29.0000    15.2000    16.6780 161
  1    35.7526    16.2007    35.9566    19.8538 100     0.5617
1.3183    29.0000    15.2000    16.6780 162
  1    35.9565    19.9646    36.1605    23.6177 100     1.1132
1.6378    29.0000    15.2000    16.6780 163
  1    36.1604    23.6176    36.3644    27.2707 100    -1.2532
1.4355    29.0000    15.2000    16.6780 164
  1    36.3643    27.2708    36.5683    30.9239 100    -0.4535
0.3373    29.0000    15.2000    16.6780 165
  1    36.5682    30.9238    36.7722    34.5769 100    -0.8759
0.9496    29.0000    15.2000    16.6780 166
  1    36.7729    34.6876    36.9768    38.3407 100    -2.4920
1.4279    29.0000    15.2000    16.6780 167
  1    36.9767    38.3408    37.1807    41.9939 100    -1.7855
2.9120    29.0000    15.2000    16.6780 168
  1    37.1806    41.9938    37.3846    45.6469 100     1.1842
4.9724    29.0000    15.2000    16.6780 169
  1    37.3845    45.6470    37.5885    49.3001 100     3.2175
4.1147    29.0000    15.2000    16.6780 170
  1    37.5884    49.3000    37.7924    52.9531 100     2.2544
2.9747    29.0000    15.2000    16.6780 171
  1    37.7923    53.0638    37.9963    56.7169 100     0.6771
2.4577    29.0000    15.2000    16.6780 172
  1    37.8942    56.7168    38.0982    60.3699 100    -0.6265
1.7035    29.0000    15.2000    16.6780 173
  1    38.0981    60.3700    38.3021    64.0231 100    -4.8504
0.2992    29.0000    15.2000    16.6780 174
  1    13.0575    88.1833    16.7295    88.8475 100     5.8241
3.2205    29.0000     0.0000     1.4780   1
  1    16.7298    88.8476    20.4018    89.5118 100     3.4808
10.4071    29.0000     0.0000     1.4780   2
```

```
  1    20.4013    89.5118    24.0733    90.1760 100    14.9460
13.2669    29.0000     0.0000     1.4780   3
  1    24.0736    90.0652    27.7456    90.7294 100     0.4583
10.7601    29.0000     0.0000     1.4780   4
  1    27.7452    90.7295    31.4172    91.3937 100     0.0684    -
0.8480    29.0000     0.0000     1.4780   5
  1    31.4175    91.3937    35.0895    92.0579 100     2.3190   -
10.3626    29.0000     0.0000     1.4780   6
  1    35.0898    92.0578    38.7618    92.7220 100     1.4169    -
6.6687    29.0000     0.0000     1.4780   7
  1    38.7613    92.6114    42.4333    93.2756 100     1.1699    -
0.2321    29.0000     0.0000     1.4780   8
  1    42.4337    93.2757    46.1057    93.9399 100    -1.0634
3.2834    29.0000     0.0000     1.4780   9
  1    17.2395    85.6373    20.9115    86.3015 100     1.1250
2.6583    29.0000     1.9000     3.3780  11
  1    20.9118    86.1907    24.5838    86.8549 100     6.2128
5.8789    29.0000     1.9000     3.3780  12
  1    24.5833    86.8550    28.2553    87.5192 100    -2.3763
7.4124    29.0000     1.9000     3.3780  13
  1    28.2557    87.5193    31.9277    88.1835 100    -0.6227
2.4030    29.0000     1.9000     3.3780  14
  1    31.9272    88.1833    35.5992    88.8475 100     3.0039    -
5.9571    29.0000     1.9000     3.3780  15
  1    35.5995    88.8476    39.2715    89.5118 100     1.4206    -
2.7480    29.0000     1.9000     3.3780  16
  1    39.2718    89.4012    42.9438    90.0654 100    -0.8335
2.4951    29.0000     1.9000     3.3780  17
  1    42.9434    90.0652    46.6154    90.7294 100    -0.3629
1.1915    29.0000     1.9000     3.3780  18
  1    17.8512    82.3163    21.5232    82.9805 100     0.8612    -
0.0678    29.0000     3.8000     5.2780  20
  1    21.5235    82.9805    25.1955    83.6447 100     4.6433
3.3160    29.0000     3.8000     5.2780  21
  1    25.1958    83.6448    28.8678    84.3090 100     0.8444
6.5789    29.0000     3.8000     5.2780  22
  1    28.8673    84.3088    32.5393    84.9730 100    -1.8847
6.2606    29.0000     3.8000     5.2780  23
  1    32.5396    84.9731    36.2116    85.6373 100     3.1054
2.2248    29.0000     3.8000     5.2780  24
  1    36.2112    85.5265    39.8832    86.1907 100     2.1115
3.5110    29.0000     3.8000     5.2780  25
  1    39.8835    86.1907    43.5555    86.8549 100     2.6453
3.7115    29.0000     3.8000     5.2780  26
  1    43.5558    86.8550    47.2278    87.5192 100     0.8992    -
1.6320    29.0000     3.8000     5.2780  27
  1    22.1351    79.7701    25.8071    80.4343 100     2.8938
0.4897    29.0000     5.7000     7.1780  30
  1    25.8074    80.4343    29.4795    81.0985 100     1.8543
3.8615    29.0000     5.7000     7.1780  31
  1    29.4798    81.0986    33.1518    81.7628 100     0.8610
6.0668    29.0000     5.7000     7.1780  32
  1    33.1513    81.6520    36.8233    82.3162 100     2.1464
5.5105    29.0000     5.7000     7.1780  33
  1    36.8236    82.3163    40.4956    82.9805 100     2.0459
5.4223    29.0000     5.7000     7.1780  34
```

```
  1    40.4952    82.9805    44.1672    83.6447 100     3.2273
4.9382    29.0000     5.7000     7.1780  35
  1    44.1675    83.6448    47.8395    84.3090 100     2.1154
0.3790    29.0000     5.7000     7.1780  36
  1    26.3172    77.2241    29.9892    77.8883 100     1.6052
1.8468    29.0000     7.6000     9.0780  40
  1    29.9895    77.7775    33.6615    78.4417 100     2.3305
6.0755    29.0000     7.6000     9.0780  41
  1    33.6618    78.4418    37.3338    79.1060 100     2.2507
6.9517    29.0000     7.6000     9.0780  42
  1    37.3333    79.1060    41.0053    79.7702 100     2.0305
5.6839    29.0000     7.6000     9.0780  43
  1    41.0057    79.7701    44.6777    80.4343 100     1.4382
4.1089    29.0000     7.6000     9.0780  44
  1    44.6772    80.4343    48.3492    81.0985 100     1.6736    -
0.3024    29.0000     7.6000     9.0780  45
  1    30.6012    74.5673    34.2732    75.2315 100     0.8433
3.6015    29.0000     9.5000    10.9780  50
  1    34.2735    75.2316    37.9455    75.8958 100     4.3688
5.9138    29.0000     9.5000    10.9780  51
  1    37.9458    75.8956    41.6178    76.5598 100     3.1951
5.9409    29.0000     9.5000    10.9780  52
  1    41.6173    76.5599    45.2893    77.2241 100     3.3909
3.3225    29.0000     9.5000    10.9780  53
  1    45.2896    77.1135    48.9616    77.7777 100     3.8704    -
1.5355    29.0000     9.5000    10.9780  54
  1    34.8851    72.0211    38.5571    72.6853 100     3.5601
2.8825    29.0000    11.4000    12.8780  60
  1    38.5574    72.6854    42.2295    73.3496 100     5.9234
6.2636    29.0000    11.4000    12.8780  61
  1    42.1278    73.3496    45.7998    74.0138 100     3.6884
6.0104    29.0000    11.4000    12.8780  62
  1    45.7994    73.9030    49.4714    74.5672 100     4.0120
1.8142    29.0000    11.4000    12.8780  63
  1    39.0672    69.4752    42.7392    70.1394 100     4.9147
3.8167    29.0000    13.3000    14.7780  70
  1    42.7395    70.0286    46.4115    70.6928 100     2.7376
3.5571    29.0000    13.3000    14.7780  71
  1    46.4118    70.6928    50.0838    71.3570 100     2.9124
2.9724    29.0000    13.3000    14.7780  72
  1    39.6796    66.1541    43.3516    66.8183 100     4.1555
1.6523    29.0000    15.2000    16.6780  79
  1    43.3512    66.8183    47.0232    67.4825 100     3.6841
1.3920    29.0000    15.2000    16.6780  80
  1    47.0235    67.4824    50.6955    68.1466 100     4.1546
2.1555    29.0000    15.2000    16.6780  81
  1    -1.0953    11.1639     1.5567    13.7654 100     0.8599
0.2678    29.0000     0.0000     1.4780   1
  1     1.5568    13.8207     4.2088    16.4222 100     1.3243
0.4899    29.0000     0.0000     1.4780   2
  1     4.2089    16.3667     6.8609    18.9682 100     2.1507
0.7350    29.0000     0.0000     1.4780   3
  1     6.8610    19.0235     9.5130    21.6250 100    -0.2609
1.3538    29.0000     0.0000     1.4780   4
  1     9.4112    21.6804    12.0632    24.2818 100     0.4833
0.4405    29.0000     0.0000     1.4780   5
```

```
  1    12.0633    24.2265    14.7153    26.8280 100     1.9984
0.9457    29.0000     0.0000     1.4780   6
  1     1.2510     8.8392     3.9030    11.4407 100     0.7608
0.7723    29.0000     1.9000     3.3780   7
  1     3.9031    11.4958     6.5551    14.0973 100     2.3114
0.6838    29.0000     1.9000     3.3780   8
  1     6.5552    14.0420     9.2072    16.6435 100     0.4506
1.0849    29.0000     1.9000     3.3780   9
  1     9.1054    16.6988    11.7574    19.3003 100    -0.6185
3.1578    29.0000     1.9000     3.3780  10
  1    11.7567    19.3557    14.4087    21.9571 100     1.3282
4.0819    29.0000     1.9000     3.3780  11
  1    14.4088    21.9018    17.0608    24.5033 100     0.2074
0.9030    29.0000     1.9000     3.3780  12
  1     3.5973     6.6252     6.2493     9.2266 100     0.2249
0.0723    29.0000     3.8000     5.2780  13
  1     6.2494     9.1712     8.9014    11.7726 100     1.9550
0.9830    29.0000     3.8000     5.2780  14
  1     8.9007    11.8280    11.5527    14.4294 100     1.6076
0.4720    29.0000     3.8000     5.2780  15
  1    11.4508    14.3742    14.1028    16.9756 100     1.3026
0.6923    29.0000     3.8000     5.2780  16
  1    14.1029    17.0310    16.7549    19.6324 100     0.7295
2.1167    29.0000     3.8000     5.2780  17
  1    16.7550    19.5772    19.4070    22.1786 100     1.5614
2.4159    29.0000     3.8000     5.2780  18
  1     5.9428     4.3005     8.5948     6.9020 100     0.2307
0.7439    29.0000     5.7000     7.1780  19
  1     8.5949     6.8465    11.2469     9.4479 100     0.2587
0.2500    29.0000     5.7000     7.1780  20
  1    11.1450     9.5033    13.7970    12.1047 100     0.2172
0.6420    29.0000     5.7000     7.1780  21
  1    13.7971    12.0495    16.4491    14.6509 100     0.6006
1.3243    29.0000     5.7000     7.1780  22
  1    16.4492    14.7063    19.1012    17.3077 100     1.6601
1.2185    29.0000     5.7000     7.1780  23
  1    19.1013    17.2523    21.7533    19.8537 100     1.3233
2.2221    29.0000     5.7000     7.1780  24
  1     8.2890     1.9758    10.9410     4.5773 100     0.0626
1.4456    29.0000     7.6000     9.0780  25
  1    10.9411     4.5218    13.5931     7.1232 100     0.5337
0.4546    29.0000     7.6000     9.0780  26
  1    13.4913     7.1786    16.1433     9.7800 100     0.8918
0.3744    29.0000     7.6000     9.0780  27
  1    16.1434     9.7248    18.7954    12.3262 100    -0.2080
1.0387    29.0000     7.6000     9.0780  28
  1    18.7947    12.3816    21.4467    14.9830 100     1.2601
0.9080    29.0000     7.6000     9.0780  29
  1    21.3449    14.9276    23.9969    17.5290 100     0.5614
0.9906    29.0000     7.6000     9.0780  30
  1    10.6353    -0.3489    13.2873     2.2526 100     0.5173
0.2618    29.0000     9.5000    10.9780  31
  1    13.1847     2.1971    15.8367     4.7985 100     0.0685
1.0385    29.0000     9.5000    10.9780  32
  1    15.8368     4.8539    18.4888     7.4554 100     0.0159
0.0316    29.0000     9.5000    10.9780  33
```

```
  1    18.4889     7.4001    21.1409    10.0015 100     0.4298
0.3264    29.0000     9.5000    10.9780  34
  1    21.1410    10.0569    23.7930    12.6584 100     0.2501
0.4694    29.0000     9.5000    10.9780  35
  1    23.6911    12.6029    26.3431    15.2043 100     0.3142
0.1870    29.0000     9.5000    10.9780  36
  1    12.9808    -2.6736    15.6328    -0.0721 100     1.8746
0.8497    29.0000    11.4000    12.8780  37
  1    15.5309    -0.1276    18.1829     2.4738 100     1.0630
1.3299    29.0000    11.4000    12.8780  38
  1    18.1830     2.5292    20.8350     5.1307 100    -0.4306
1.6400    29.0000    11.4000    12.8780  39
  1    20.8351     5.0754    23.4871     7.6768 100     0.4587
0.6433    29.0000    11.4000    12.8780  40
  1    23.3853     7.7322    26.0373    10.3337 100     0.8180
1.1324    29.0000    11.4000    12.8780  41
  1    26.0366    10.2782    28.6886    12.8796 100     0.3933
0.7954    29.0000    11.4000    12.8780  42
  1    15.2251    -4.9983    17.8771    -2.3968 100     2.8672
1.5363    29.0000    13.3000    14.7780  43
  1    17.8772    -2.4523    20.5292     0.1492 100     1.1866
1.7584    29.0000    13.3000    14.7780  44
  1    20.5293     0.2045    23.1813     2.8060 100     0.1964
0.5458    29.0000    13.3000    14.7780  45
  1    23.1806     2.7507    25.8326     5.3522 100    -0.2569
1.3407    29.0000    13.3000    14.7780  46
  1    25.7308     5.4075    28.3828     8.0090 100     0.0314
0.4687    29.0000    13.3000    14.7780  47
  1    28.3829     7.9535    31.0349    10.5549 100     0.0279
0.0140    29.0000    13.3000    14.7780  48
  1    17.5714    -7.3229    20.2234    -4.7215 100     3.1591
1.6352    29.0000    15.2000    16.6780  49
  1    20.2227    -4.7770    22.8747    -2.1755 100     1.7745
1.8217    29.0000    15.2000    16.6780  50
  1    22.8748    -2.1202    25.5268     0.4813 100     0.0382
0.1195    29.0000    15.2000    16.6780  51
  1    25.4249     0.5367    28.0770     3.1381 100    -0.3367
1.3104    29.0000    15.2000    16.6780  52
  1    28.0770     3.0828    30.7290     5.6843 100    -0.0380
1.8403    29.0000    15.2000    16.6780  53
  1    30.7291     5.7397    33.3811     8.3411 100    -0.4672
1.9956    29.0000    15.2000    16.6780  54

    Grid Parameters
  1  ----------------------------  Start-x =    -111.0000
  2  ----------------------------  Start-y =    -220.0000
  3  ---------------------------   Finish-x =     195.0000
  4  ---------------------------   Finish-y =     278.0000
  5  ------------------------  x-increment =       5.0000
  6  ------------------------  y-increment =       5.0000
    Size Parameters
  1  --------------------------  Plot size =     1.000000
  2  --------------  Shade/Color increment =     0.100000
  3  ------  Exaggeration for disp.& dist. =     10000.00

Cross section default
```

```
1  ----------------------------  Start-x =     -6.70000
2  ----------------------------  Start-y =     34.66000
3  --------------------------   Finish-x =     33.58000
4  --------------------------   Finish-y =     34.66000
5  -----------------  Distant-increment =     0.500000
6  ----------------------------  Z-depth =     11.00000
7  ------------------------  Z-increment =     0.500000
   Map info
1  ---------------------------- min. lon =      119.5000000
2  ---------------------------- max. lon =      122.5000000
3  ---------------------------- zero lon =      120.5882000
4  ---------------------------- min. lat =       21.5000000
5  ---------------------------- max. lat =       26.5000000
6  ---------------------------- zero lat =       23.4869000
```